The Dynamics of Thermals and Their Contribution to Mixed Layer Processes

By
George S. Young

Department of Atmospheric Science
Colorado State University
Fort Collins, Colorado

Colorado State University

Department of Atmospheric Science

Paper No. 402

THE DYNAMICS OF THERMALS AND THEIR CONTRIBUTION TO MIXED LAYER PROCESSES

by

George S. Young

Research supported by the

National Science Foundation under grants
ATM-8507961 and ATM-8206808

Department of Atmospheric Science
Colorado State University
Fort Collins, CO 80523

September, 1986

Atmospheric Science Paper No. 402

ABSTRACT

The dynamics of thermal updrafts and compensating environmental downdrafts in the Convective Boundary Layer are examined using observations from the Phoenix 78 field experiment.

A new conditional sampling technique based upon the universal mixed layer spectra of vertical velocity is developed and used to distinguish thermals from their environment. The spectra show that the buoyant production of vertical velocity variance occurs primarily at horizontal scales of from 0.1 to 10.0 times the depth of the boundary layer. Therefore, thermals are defined as those regions in which the vertical velocity is upwards at these horizontal scales. Thus, the contribution of mesoscale and inertial subrange eddies to the vertical velocity are eliminated from the determination of the thermal-environmental boundaries. This technique is not limited to conditions of large upwards heat or moisture fluxes as were previous methods.

A new diagnostic model is developed which permits the determination, from observations, of the lateral mass exchange between thermal updrafts and environmental downdrafts and the pressure forces acting on the vertical velocity in these two regions. This model consists of the budget equations for horizontal averages of virtual potential temperature, convective mass flux and vertical velocity. These averages are computed separately for the updraft and downdraft

regions so that the processes affecting the two legs of the convective circulation can be examined separately. Therefore, the lateral exchanges between the two regions enter into the budgets. These exchanges are commonly referred to as lateral entrainment and detrainment.

The time tendency terms in the budgets are small while the effects of lateral mixing and pressure are large. The importance of lateral mixing and pressure effects is shown to result from the large imbalance between the observed gradient production of buoyancy and vertical buoyancy flux divergence.

The lateral mixing into thermals is small relative to that out of thermals in the upper boundary layer. Therefore, the proportion in downdrafts of a nonbuoyant contaminant released in the upper boundary layer should increase with time. This result supports the observed initial descent of plume centers in large eddy simulation models.

Acknowledgements

My advisor, Dr. Richard H. Johnson, has fostered this work with that delicate balance of freedom and support so essential to scientific research.

I gratefully acknowledge the efforts and suggestions of my committee, Dr. Jack E. Cermak, Dr. Peter H. Hildebrand, Dr. Thomas B. McKee and Dr. Roger A. Pielke. Their questions have opened the way to many new ideas.

The staff of the Research Aviation Facility of the National Center for Atmospheric Research provided the knowledge and experience in airborne data collection and analysis upon which this work was built. Their patience and skill in training scientists to use the NCAR aircraft is extraordinary.

The research reported in this work was funded by the National Science Foundation through Grants ATM-8507961 and ATM-8206808.

Dedication

This work is dedicated to the late E.C. Huffaker who pioneered the investigation of thermals. His ability to draw reasoned insights from limited observational data has been a constant source of inspiration.

TABLE OF CONTENTS

1. Introduction

1.1 Goals and motivations

The objective of this work is to advance the understanding of the structure and dynamics of thermals in the convective boundary layer (CBL). Turbulence statistics computed from the aircraft observations of the Phoenix 78 field experiment are used meet these objectives. The buoyancy, vertical velocity and turbulence structure of the thermal updrafts and their environment are determined from these data. The size and spacing of these features are also found. The contribution of thermals to various statistics of CBL turbulence and the validity of the "Top Hat" approximation to the structure of thermals are discussed as well. The dynamics of thermals are examined through their budgets of buoyancy, mass flux and vertical velocity. All of the terms in these budgets including the pressure effects and lateral exchanges between thermals and their environment are measured or diagnosed.

The convective circulations of which arise when buoyancy is supplied to the lower boundary of the atmosphere are commonly called thermals. These circulations are composed of updrafts and downdrafts with a dominant horizontal scale of approximately 1.5 times depth of the boundary layer, z_i (Caughey and Palmer, 1979). The thermal updrafts and compensating environmental downdrafts span the depth of the convective boundary layer as either bubbles or plumes extending

from the surface layer to the capping inversion (Richter et al., 1977; Emmitt, 1978; Gaynor and Mandics, 1978; Caughey and Palmer, 1979; Taconet and Weill, 1983). These are the circulations which support fair weather cumulus and many other important phenomena of the CBL.

Thermals occur whenever the boundary layer is unstable enough for buoyant production of turbulence kinetic energy to dominate shear production throughout most of the depth of the CBL. Such conditions occur over land during the warm season days, in the trade wind regions and during cold air outbreaks over any relatively warm or moist surface. These synoptic situations are very common so thermals and the phenomena they support are common features of the planetary boundary layer.

Knowledge of the dynamics of thermals can be applied in a number of fields. Dispersion theory for the CBL is very dependent on an accurate description and understanding of theramls. So too are mesoscale models which must parameterize or otherwise handle the temperature and momentum mixing of thermals in the CBL. In addition, understandings derived from convection in the atmospheric boundary layer may be applicable to convection between the surface and the thermocline in the ocean. This oceanic convection can be an important control on sea surface temperature and thus upon climate.

1.2 Outline

Turbulence data were collected with two Queenair aircraft operated by the National Center for Atmospheric Research (NCAR) during the Phoenix 78 field experiment. This experiment was conducted during September, 1978. Only the data collected on days with nearly calm and clear conditions were analyzed for this study. These limitations were

imposed to eliminate some of the potential departures from ideal CBL structure. Surface fluxes and virtual potential temperature profiles measured at the 300 m tower of the Boulder Atmospheric Observatory (BAO) were also used in the analysis.

The author participated in the planning and direction of similar aircraft operations during the Phoenix 84 field experiment. This experience provided insight into the data collection procedures and the quality of the data. The resulting knowledge of uncertainties in determination of the CBL depth was particularly useful during the analysis of the Phoenix 78 data.

Mixed layer scaling is used throughout this study as a method of combining turbulence data collected under different but qualitatively similar conditions. This method was proposed in Deardorff (1970) and has been extended by Kaimal et al., (1976) and others. This scaling has been found useful for collapsing CBL turbulence data onto universal profiles or families of such profiles. As with any similarity theory, mixed layer scaling works only when the assumptions upon which it is based are valid. The light winds and nearly clear skies of the Phoenix 78 experiment contribute to the validity of these assumptions.

The terrain of the study area is rolling farmlands with the foothills of the Rocky Mountains 25 km to the west. The possible influences of this terrain on the validity of mixed layer scaling are examined by comparison of the scaled profiles turbulence statistics from Phoenix 78 with those reported for studies conducted over smoother terrain and over water. No systematic bias exists between the Phoenix 78 turbulence profiles and those of previous studies.

Most of the profiles changed little from study to study. However, some features of the CBL turublence structure do seem to be sensitive to factors which are ignored in mixed layer scaling. The variances of the horizontal wind components, for example, exibit large scatter between and within experiments even after scaling. Temperature variance in the capping inverion is also poorly normalized. Even for these features the Phoenix 78 observations are typical of those observed in locations with more uniform topography.

The turbulence spectra of vertical velocity, horizontal wind speed, temperature and specific humidity are examined to determine the dominant scales for CBL eddies. The spectral range observed can be separated into three subranges. The inertial subrange exists at horizontal scales of less than a tenth the boundary layer depth as found in previous studies (Kaimal et al., 1976). The energy containing subrange for boundary layer convective eddies extends from the long wavelength limit of the inertial subrange out the short wavelength limit of the mesoscale. The transition from CBL convective eddies to mesoscale eddies occurs at the wavelength where the eddies become two dimensional. There is a spectral minimum at scales near ten times the boundary layer depth which separates these two eddy regimes. At scales longer than this so called spectral gap, the ratio of the spectral densities of vertical velocity and horizontal wind speed is much lower than at shorter scales. Thus, the gap marks the transition from the three dimensional convective eddies to the larger quasi two dimensional mesoscale eddies.

This understanding of the spatial scales of boundary layer turbulence provides the basis for separating the contributions of the

different eddy types. A form of conditional sampling is developed which can be used to distinguish the effects of thermal updrafts and environmental downdrafts. Because of its foundation in the spectral dynamics of CBL turbulence, the conditional sampling method developed for this work is more general and less arbitrary than those used previously. The methods developed by Manton (1977), Lenschow and Stephens (1980), Greenhut and Khalsa (1982) and others have all depended on the existence of a significant unidirectional flux of temperature or moisture throughout the region of interest. These methods worked well in the cases reported but lacked general applicability. Hence the need to develop the present method which uses upward motion on the size scale of thermals as a conditional sampling criteria.

This conditional sampling technique is applied to the aircraft measured turbulence data from Phoenix 78. Once thermals have been distinguised from their environment the size, spacing and turbulence structure can be determined. This classic approach to the study of thermals has been used by Manton (1977), Lenschow and Stephens (1980, 1982), Greenhut and Khalsa (1982), Khalsa and Greenhut (1985) and others. The results of these studies are compared with those of the present study. A general agreement is found between the observations of thermals from greatly differing synoptic situations.

The conditional sampling approach is extended by examining the budgets of mass flux, buoyancy and vertical velocity for thermals and for their environment. Budget equations for these quantities are solved separately for the thermal updrafts and the environmental downdrafts. The Phoenix 78 observations provide the information

needed to measure or diagnose every term in these equations. As a result, the two components of lateral mass exchange between thermals and their environment can be examined quantitatively. The pressure effects can also be diagnosed quantitatively. The separation of these quantities requries the use of budget equations for all three quantities. Previous analysis by Lenschow and Stephens (1982) used only a simplified version of the vertical velocity budget and so gave only the net effect of these terms.

The present approach to diagnosing the unmeasured terms in the dynamic and thermodynamic equations governing thermals provides considerable insight in to the workings of boundary layer convection. The importance of lateral exchanges between thermals and their environment and of pressure forcing is shown.

These results suggest several further lines of research.

The implications of the diagnosed profiles of lateral exchange between thermals and their environment for the dispersion of contaminants needs to be examined. These results may improve our understanding of the dispersion results of large eddy simulations (LES) and test the validity of the LES results.

If the diagnosed profiles of lateral exchange could be related to the bulk characteristics of the CBL and of thermals and their environment then a better dynamical understanding of this mixing process would result. Further, it would then be possible to derive a fairly simple dynamical model of the CBL which could be used to examine the effects of entrainment and inversion rise rate on the structure of the CBL.

The past work on thermals is outlined in section 1.3. The Phoenix 78 data used in this study and its acquisition are discussed in some detail in Chapter 2 as are the weather and terrain conditions for the experiment. The theory of mixed layer scaling is reviewed in Chapter 3. The values of the scaling parameters for Phoenix 78 are also presented and discussed in that chapter. Chapter 4 covers the theory, observations and applications of turbulence spectra for the CBL. An intercomparison of the profiles of bulk CBL turbulence statistics from various experiments is conducted in Chapter 5. This is done to evaluate the representativeness of Phoenix 78 results. Chapter 6 contains the Phoenix 78 observations of thermal size and structure and a comparison with past observations of this type. The budgets of mass, buoyancy and vertical velocity for thermal updrafts and their environment are developed in Chapter 7. The terms in these budgets are either measured directly or diagnosed. The chapter concludes with an evaluation of the importance of lateral exchanges and pressure effects to the dynamics of thermals and to the mean structure of the CBL.

1.3 Past Research on the Dynamics of Thermals

The dynamics of thermals and their importance to turbulence processes in the CBL have been studied since before the turn of the century. Huffaker (1897) reported on a major field program conducted by the Smithsonian Instiution to study these phenomena. Observations of the flight of vultures, measurements of lapse rate from the Washington monument and manned balloons and a variety of physical experiments were discussed. An essentially correct qualitative description of the CBL structure and the dynamics of thermals emerged

from this study. However, the sensing systems available at that time limited the quantitative results of this study.

Research on the dynamics of thermals and on CBL turbulence in general has since focused on improving quantitative description and theory. Woodcock (1940, 1975) and Deardorff (1976) were able to use observations of seagulls, wind speed and thermodynamic stability and similarity theories to derive criteria for the transition from three dimensional thermals to two dimensional convective rolls. These two phenomena are sufficiently different dynamically and energetically to require separate study. Two dimensional convective rolls are known to draw much of their energy from the wind shear (Lemone, 1973) while three dimensional thermals do not. This work will focus on the dynamics of three dimensional thermal convection.

Thermals can be observed or modelled in a number of ways. Thermals have been remotely sensed by lidar (Kunkel et al., 1977; Lopez, 1977), radar (Hardy and Ottersten, 1969; Konrad, 1970; Konrad and Robinson, 1973; Roland, 1973, 1976; Richter et al., 1974; Noonkester, 1976) and sodar (Hall et al., 1975; Lopez, 1977; Gaynor and Mandics, 1978; Noonkester, 1976; Taconet and Weill, 1983).

Direct observations from insturments carried by balloons (Betts, 1976; Kaimal et al., 1973; Emmitt, 1978; Caughey and Palmer, 1979) or towers (Wilczak and Tillman, 1980) have also been made. Observations from instrumented aircraft have proved to be very useful for studying the dyanmics of thermals. Vul'fson (1961), Grant (1965), Warner and Telford (1963, 1967), Roland (1973), Lopez, (1977), Manton (1977), Lenschow and Stephens (1980, 1982), Greenhut and Khalsa (1982), Khalsa and Greenhut (1985) and others have reported aircraft observations of

thermals. Until the advent of mixed layer similarity theory in the 1970s, little quantitative use could be made of these aircraft observations because it was impossible to adequately scale out the variations in conditions from flight to flight. The more resent studies have all taken advantage of mixed layer scaling to combine data from several horizontal flight legs into vertical profiles.

Conditional sampling has been used in a number of studies to separate the turbulence data collected in thermals from that collected in their environment. Taconet and Weill (1983) applied conditional sampling to doppler sodar data to determine the updraft structure of thermals. Manton (1977), Lenschow and Stephens (1980, 1982), Greenhut and Khalsa (1982) and Khalsa and Greenhut (1985) used conditonal sampling on aircraft turbulence data. They were able to describe quantitatively the thermal and trubulence structure of thermals as well as their contribution to the CBL turbulence processes.

The criteria for distinguishing thermals from their environment have varied from study to study depending on the instrumentation available and on the nature of the scalar fluxes in the region studied. The criteria were selected so as to be related to some variable which varied significantly between thermals and their environment. This procedure has lead to the use of different criteria for studies in different synoptic conditions and at different levels in the CBL. Temperature based schemes have been used at low levels in the CBL (Manton, 1977; Greenhut and Khalsa, 1982) while moisture based schemes have been used over oceans (Lenschow and Stephens, 1980; Greenhut and Khalsa, 1982).

The current study advances the use of conditional sampling by developing a technique based on the universal vertical velocity spectra. This technique can be used in any experiment where high quality vertical velocity data is available.

Not all of the dynamically important quantities for CBL convection can be measured by presently avialable sensor systems. The diagnosis of these unmeasured but dynamically important quantities has been studied by Betts (1976) and Lenschow and Stephens (1982). Betts used highly parameterized static energy budgets and balloon sounding data to diagnose the convective mass flux profile for thermals. The diagnosed profile compares well with direct observations made with more sophisticated measurement systems. Lenschow and Stephens (1982) used a form of the vertical velocity budget for thermals to compute the net effect of lateral exchange with the environment and pressure. The current study advances this approach by using the budgets for convective mass flux and buoyancy as well. These budgets can be solved simultaneously to diagnose the two components of lateral mass exchange and the pressure effects separately.

Scorer (1957) studied bubbles of buoyant fluid as analogies to thermals. Since then, the understanding the intermittent plume structure of thermals has increased. More recent laboratory tank experiments have forcused on the statistical properties of the CBL as a whole rather than the structure and dynamics of thermals (Willis and Deardorff, 1974).

The same has generally been true of the analysis of the results of LES models (Deardorff, 1974ab; Moeng, 1984; Moeng and Wyngaard, 1984; Wyngaard and Brost, 1984). Lamb (1978) did use conditional

sampling of the results of Deardorff's LES model to study the vertical velocity structure of thermals as it relates to dispersion. The full potential of LES models for the study of thermals has not yet been realized.

2. Description of Phoenix Data Set

2.1 NCAR Aircraft Data Set

2.1.1 NCAR Aircraft Instrumentation

Two NCAR Queen Air instrumented aircraft were the primary data collection platforms for this study. The capabilities and instrumentation of these aircraft are described in the remainder of this subchapter. The flight patterns flown are described in the next subchapter.

The capabilities and instrumentation of these aircraft are outlined in Burris et al. (1973) and NCAR (1977, 1981). The aircraft instrumentation was used to measure the three components of wind velocity, temperature, humidity, static pressure, refractive index and aircraft position. The instrumentation used in this study will be described below. More detailed information is available in the technical references given for each instrument. The data reduction procedures used at NCAR are described in Kelley and Lackmon (1976).

Details of the wind sensing system are provided in Lenschow et al. (1978) and Lenschow and Spyers-Duran (1985). Basically, the three components of wind velocity are determined by subtracting the motion of the aircraft from the motion of the air relative to the aircraft. The aircraft motion is sensed by an inertial navigation system (INS) while the motion of the air relative to the aircraft is sensed by fixed vanes mounted on a gust probe ahead of the nose. Error growth

in the vertical velocity is limited by combining pressure altitude with the vertical acceleration to provide a long-term reference altitude. Thus, the changes in pressure altitude determine the long period vertical velocity while the INS-fixed vane system determines the short period vertical velocity. The velocities are sampled at 20 Hz and are accurate to 0.3 m/s.

The wing mounted Rosemont thermometer provided the temperature data used in this study. This sensor was used because it exhibited less damping of temperature variations than did the other available sensors. The Rosemont thermometer is of the platinum resistance wire type. The accuracy is $\pm$ 0.14°C and the response time is near 0.1 sec. More details of this instrument are indcluded in Spyers-Duran and Baumgardner (1983).

A microwave refractometer provided the humidity measurements used in this study. This sensor provided the fastest response humidity data available during the Phoenix experiment. The fast response is important for turbulence studies. The microwave refractometer and its limitations are described in more detail in NCAR (1976).

The static pressure data came from the fuselage static pressure port.

Further information on instrument response can be obtained by examining the variance spectra of their output. These spectra are shown and discussed in the chapter on turbulence spectra. The effects of instrument response on the spectra are discussed there.

2.1.2 Phoenix Aircraft Flight Patterns

Two types of flight patterns were used in this study (Hildebrand, 1979). Horizontal patterns were flown to measure turbulence

statistics for a given level and ascending box soundings were flown to measure the vertical profiles of the mean variables. Figure 2.1 shows these patterns as seen from the side.

The horizontal flight legs were about 30 km long and were flown at various levels throughout the boundary layer and the capping inversion. The lowest flight levels were 150 m above the ground because of legal constraints on the low altitude flight over inhabited areas. Figure 2.2 shows the L shaped flight track of a pair of horizontal flight legs superimposed on a contour map of the area. Generally, an aircraft would fly both legs of the L pattern at the same level before descending to fly at the next lower level. Each aircraft would fly these horizontal patterns at several levels between each pair of sounding ascent patterns. The two aircraft often worked in conjunction to cover the entire depth of the PBL in a minimum amount of time. Such a set of horizontal flight patterns and a sounding ascent pattern took about one hour to complete.

Table 2.1 lists the times and altitudes relative to the inversion height ($z_* = z/z_i$) for each of the horizontal flight legs analyzed. The turbulence statistics used in this study were derived from these 58 horizontal flight legs. These flight legs are distributed throughout the altitude range $0.1 \leqq z_* \leqq 1.3$. There are 13 horizontal flight legs at altitudes between 0.1 and 0.3 z_i, 9 between 0.3 and 0.5, 8 between 0.5 and 0.7, 13 between 0.7 and 0.9, 11 between 0.9 and 1.1 and 4 between 1.1 and 1.3. Thus capping inversion and the entire depth of the CBL above the surface layer were well covered by horizontal flight legs.

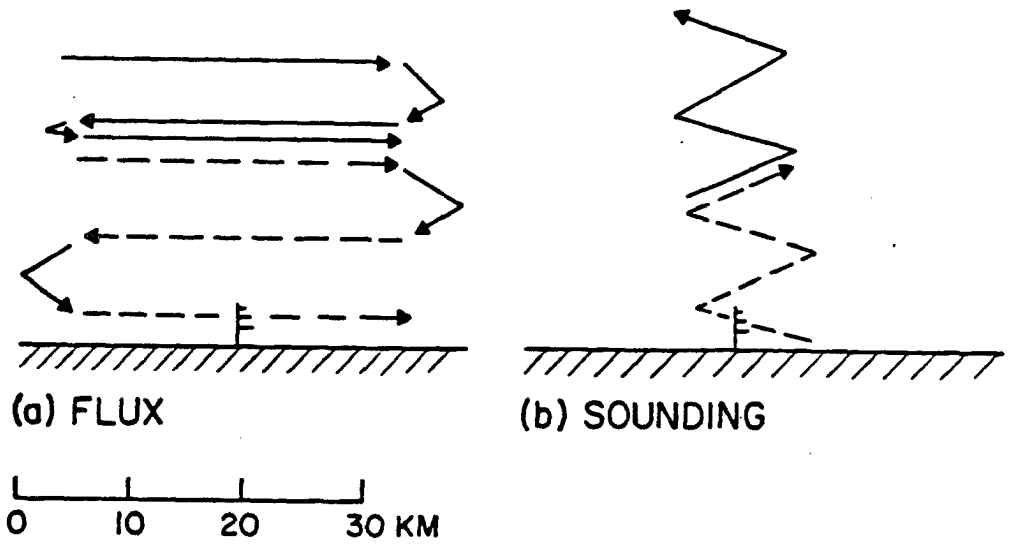

Fig. 2.1 Side view of the two aircraft flight patterns used in this study. A set of horizontal flight legs is shown in part A and a sounding ascent pattern is shown in part B.

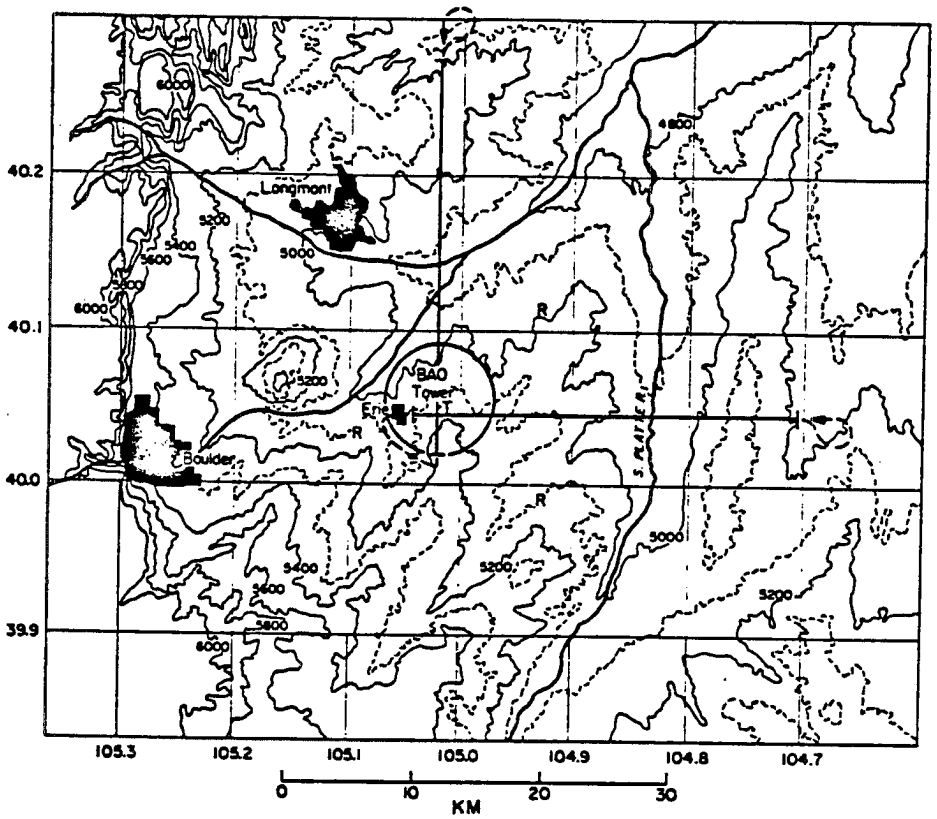

Fig. 2.2 The L shaped pattern formed by two horizontal flight legs at the same level is shown superimposed on a contour map of the terrain of the study area.

This study is aimed at investigation of the large three dimensional buoyantly driven eddies of the CBL. Therefore, only those horizontal flight legs flown during nearly clear and nearly calm conditions with definite upward surface temperature fluxes were selected for analysis.

A general description of the weather on each of the Phoenix 78 data collection days can be found in Wolfe (1979). The descriptions below cover only those times for which data were analyzed in this study. September 9, 1978, had an average surface wind speed of 1.9 m/s and a maximum of 3.2 m/s. Cloud cover increased from zero in the morning to 6/10 of Cu, Ac, and Cb by evening. The horizontal flight legs analyzed for this day were flown during the times of clear skies or scattered Cu. September 21, 1978, had an average surface wind speed of 1.0 m/s with a maximum of 1.8 m/s. Cloud cover ranged from zero to 1/10 Ci. The horizontal flight legs analyzed for this day were flown in clear boundary layers. The weather on September 22, 1978, was similar to that on September 21, 1978. Both days had surface anticyclones over the region. The average surface wind speed was 1.3 m/s and the maximum was 2.2 m/s. The sky remained clear all day. September 29, 1978, had an average surface wind of 1.5 m/s with a maximum of 3.7 m/s. The cloud cover increased from 0/10 in the morning to 7/10 of Cu, Ac and Ci by evening. The horizontal flight legs analyzed for this day were flown during the morning and early afternoon under clear skies or scattered Cu.

Thus the horizontal flight legs analyzed for this study were all flown in clear skies or in scattered Cu conditions. The wind speeds were less then half of those needed to align CBL convective elements

into longitudinal rolls. These conditions are representative of those in which randomly located three dimensional convection dominates the PBL (LeMone, 1973).

The sounding ascent flight legs were flown in a box pattern from ground level to a level above that of the highest horizontal flight pattern. The ascent rate was held at 150 m/min during this pattern. The data from the sounding ascent flight patterns were used to determine the inversion height when it was above the 300 m limit of the BAO tower.

2.2 BAO Tower Data Set

2.2.1 BAO Tower Site

The 300 m instrumented tower of the National Oceanic and Atmospheric Administration's Boulder Atmospheric Observatory (Kaimal and Gaynor, 1983) was the primary source of temperature and flux data at the surface for this study. The BAO tower is located on the Colorado high plains 25 km east of the first foothills of the Front Range of the Rocky Mountains as shown in Figure 2.3. Figure 2.4 is a contour map of the immediate area of the BAO tower. The gently rolling terrain around the BAO site is typical of that throughout the Phoenix experimental area. The land use is predominantly agricultural with some small towns and clusters of houses and trees. By September, most of the crops have been harvested leaving the land in short grass pasture, stubble and bare soil.

2.2.2 BAO Tower Instrumentation

The BAO tower has eight primary instrumentation levels (10, 22, 50, 100, 150, 200, 250, 300 m). For this study, data from all eight levels were used. Each level is equipped with both sonic and

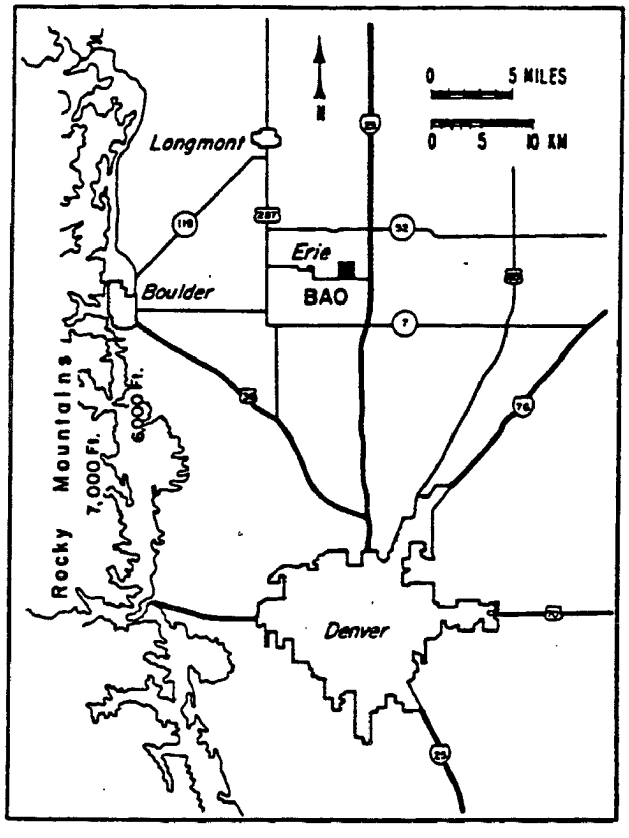

Fig. 2.3 Map of the surroundings of the Boulder Atmospheric Observatory and study area.

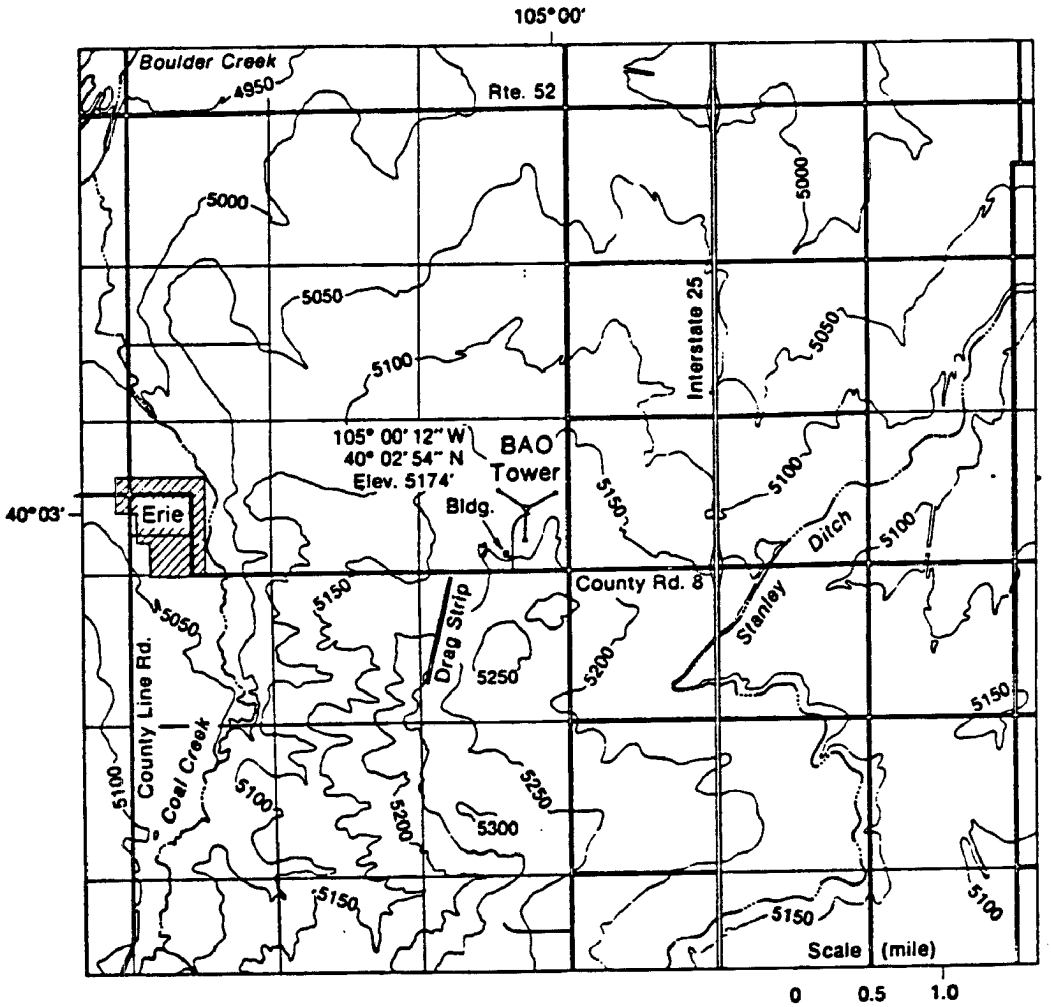

Fig. 2.4 Contour map of the vicinity of the Boulder Atmospheric Observatory

prop-vane anemometers. The sonic anemometers are used to compute the temperature and momentum fluxes because of their rapid response and full 3 axis wind sensing.

Temperature at each level is measured by both a high accuracy quartz thermometer and a fast response platinum wire thermometer. The quartz thermometers have a one-minute time constant and a 0.05° C absolute accuracy. They are thus very well suited to measuring accurately the mean temperatures and temperature profiles. The platinum wire thermometers provide temperature data with a 5 to 10 Hz cutoff and so are used in conjunction with the sonic anemometers to compute temperature fluxes.

All of the BAO tower data used in this study are in the form of 20 minute averages supplied by NOAA. Further details of the BAO instrumentation can be found in Kaimal and Wolfe (1979) and Kaimal and Gaynor (1983).

3. Determination of Nondimensionalizing Parameters

3.1 Theory of Convective Boundary Layer Similarity

Vertical profiles of turbulence statistics are valuable tools for describing and explaining turbulence processes in the CBL. They will be used extensively for this purpose in subsequent sections. Therefore, the dimensional analysis procedure used to generate vertical profiles of turbulence statistics from aircraft data will be discussed in this chapter. The theory of dimensional analysis will be discussed in the first subchapter. The application of this theory to the Phoenix 78 data will be discussed in the second subchapter. The time series of the scaling parameters, which are used in the application of dimensional analysis to CBL turbulence, will be presented and discussed in the third subchapter.

The vertical profiles are composed of a number of data points, each representing one sample of CBL turbulence. Because an aircraft can collect turbulence data at only one altitude at a time, the samples making up the vertical profiles must be collected at different times. Thus, the controlling weather conditions can vary between samples. Similarity theory and dimensional analysis (Li and Lam, 1964) provide a method of scaling turbulence statistics from different weather conditions so that they can be compared in a meaningful way.

The Pi theorem of dimensional analysis (Li and Lam, 1964) states that when turbulence statistics from different weather conditions are

nondimensionalized by the controlling parameters, they become functions of only those nondimensional products which can be formed from the controlling parameters. The Pi theorem is the basis for the procedures of dimensional analysis which are described below. In the literature, there is some disagreement concerning nomenclature with many of the results of dimensional analysis being reported as results of similarity theory. This is not a problem in interpreting the literature as long as the mathematical methods used are described as well as named.

Application of the Pi theorem to analysis of turbulence statistics requires several steps. The first is to hypothesize the controlling parameters. Use of inappropriate controlling parameters will invalidate the results and is made apparent by the consequent scatter of the results. The second step is to define a scaling parameter for each of the fundamental quantities in the data. For CBL turbulence studies the fundamental quantities are velocity, temperature and height. Each scaling parameter is defined as the product of the hypothetical controlling parameters which has the dimensions of the appropriate fundamental quantity. There may be more then one product with the correct dimensions, in which case the most convenient form may be selected without affecting the results. The third step in application of the Pi theorem to data analysis is to nondimensionalize the data by the scaling parameters. Each data point is nondimensionalized by the values of the scaling parameters appropriate to the time and place of it's collection. The fourth step is to create, from the hypothetical controlling parameters, the complete set of nondimensional products upon which the non-dimensionalized data should depend. This step completes the

requirements for applicability of the Pi theorem. If the hypothetical controlling parameters are the true controlling parameters then the Pi theorem guarantees that the nondimensionalized data will be a function of only those nondimensional products which were formed in step four.

Having completed the requirements for application of the Pi theorem, the nondimensionalized data are plotted against the nondimensional products. If the hypothetical controlling parameters are the true controlling parameters, the points will fall along curves. If the not, the points will be scattered. This provides a test of the validity of the hypothetical controlling parameters. Instrument error and sampling errors can also induce scatter in the results. Therefore, the existence of a large amount of scatter in the results does not necessarily mean the hypothetical controlling parameters are invalid. The sources of scatter will be discussed in more detail in Chapter 5.

If the nondimensionalized data points fall along a curve when plotted against the nondimensional products then this curve defines the functional relationship between them. Nondimensional height is usually one of the nondimensional products when dimensional analysis is applied to CBL turbulence. Thus, the curves formed by plotting the nondimensionalized data against the nondimensional products define the functional form of the desired vertical profiles.

This dimensional analysis method is derived and described in detail in Li and Lam (1964). Wyngaard et al. (1971) and Kaimal et al. (1976) provide explanations of the application of this method to CBL turbulence observations. These latter authors, however, use the term similarity theory to describe the method. Thus, a group of

controlling external parameters which is valid for some set of conditions is called a similarity. Useful similarities have been found for three sublayers of the CBL: the surface layer, the local free convection layer and the mixed layer. These three layers and the applicable similarities are described in detail below.

Surface layer similarity applies in the height range from z_o to L (Kaimal et al. 1976) where z_o is the surface roughness length and $|L|$ is the Monin-Obukhov length (Obukhov, 1946; Monin and Obukhov, 1954). The controlling parameters in the surface layer are z, τ_o, Q_o and $g/\bar{T}$ where z is the height above the surface, τ_o is the surface stress divided by density, Q_o is the surface virtual temperature flux, g is the gravitational acceleration and $\bar{T}$ is the average temperature. These controlling parameters can be combined to form four scaling parameters, u_*, T_*, L and z where

$$u_* = (\tau_o)^{1/2}$$
$$T_* = Q_o/u_*$$
$$L = -\bar{T}u_*^3/kgQ_o$$

and k is the von Karman constant. According to the theory of dimensional analysis any surface layer turbulence statistics which are nondimensionalized by u_*, T_* and L will become functions of z/L only.

The local free convection layer similarity applies to the next higher layer from $|L|$ to about $0.1\ z_i$ (Wyngaard et al. 1971). Within the local free convection layer the surface stress ceases to be a controlling parameter. As a result no nondimensional groups can be formed from the controlling parameters. Therefore, by dimensional

analysis, any turbulence statistics which are nondimensionalized by the controlling parameters are constant in this layer.

The scaling parameters for the free convection layer are

$$u_f = (Q_o z g/\bar{T})^{1/3}$$
$$T_f = Q_o/u_f$$
$$z$$

It will be shown below that the local free convection scaling parameters can be related to the mixed layer scaling parameters in a simple way.

The mixed layer similarity, proposed in Deardorff (1970), applies to the bulk of the convective boundary layer. Within the mixed layer the controlling external parameters are z, z_i, Q_o, and $g/\bar{T}$ where z_i is the height of the capping virtual potential temperature inversion. The nondimensional group z/z_i can be formed from these controlling parameters as can the following scaling parameters

$$w_* = (Q_o z_i g/\bar{T})^{1/3}$$
$$\theta_* = Q_o/w_*$$
$$z_i$$

By dimensional analysis, any mixed layer turbulence statistics which are nondimensionalized by these scaling parameters will become functions of z/z_i only. In addition to the usual scaling parameters, q_*, the humidity mixing ratio scaling parameter, can be defined in a way analogous to that in which θ_* is defined.

The mixed layer similarity is valid from about 0.1 z_i up to the level where entrainment across the capping inversion becomes important. In the entrainment layer, at the top of the CBL, stability and shear within the capping inversion may be added to the list of controlling parameters. No really adequate entrainment layer similarity has yet been tested.

The mixed layer and local free convection layer scaling parameters can be related as follows

$$u_f = (z/z_i)^{1/3} w_*$$
$$T_f = (z/z_i)^{-1/3} \theta_*$$
$$z = (z/z_i) z_i$$

These relationships allow one to apply mixed layer similarity down into the free convection layer. The results will become functions of z/z_i rather then constants but the validity of the analysis will not be decreased. Because the Phoenix aircraft data are all from above 0.1 zi, mixed layer scaling is appropriate. However, the relationships between mixed layer and local free convection layer parameters will be used to ensure that the profile formulations derived do not violate free convection similarity in the lower limit.

3.2 Calculation of Nondimensionalizing Parameters

Nondimensionalization of the Phoenix aircraft turbulence data requires the mixed layer scaling parameters, z_i, w_*, θ_*, q_* for each horizontal flight leg. These parameters were derived from data collected by the BAO tower and the NCAR aircraft. Surface layer scaling parameters were also calculated so that $z_i/|L|$ could be used

as a measure of the validity of the mixed layer similarity assumptions. The remainder of this subchapter will describe the method used to calculate these nondimensionalizing paramters. The time series for each of the paramters will be presented in the next subchapter.

The tower provided 20 minute average measurements of Q_o, τ_o, and $\bar{T}$ while the aircraft measured z_i and $\overline{w'q'_o}$ approximately once an hour. The procedures by which these quantities are obtained from the data are described below. The first step in deriving the surface layer scaling parameters was to compute τ_o from $\overline{u'w'}$ and $\overline{v'w'}$. The resulting time series of τ_o as well as those for $\overline{w'T'}$ had considerable variation between adjacent times. This was particularly true of $\overline{w'T'}$ at the higher levels. These variations occurred because the 20 minute averaging time of the tower is comparable to the interval between passage of large eddies. Use of a 3 point triangular filter on τ_o, $\overline{w'T'}$and $\bar{T}$ resulted in smooth time series. The filitered series are more representative of the BAO region as a whole because, at any given time, this region includes areas of both large and small fluxes. The diurnal cycles were preserved by this filtering. Even with this filtering, the surface temperature flux determined from the BAO tower failed to match that obtained by extrapolating the temperature flux profile measured by the aircraft to the surface for half the flight legs. The ratio of these two measures of the surface temperature flux ranged from 0.4 to 1.5 with half the values being indistinguishable from 1.0. Thus, the temperature flux values measured at a fixed point on the surface are not always representative of the average surface temperature flux for the surrounding few 10's of kilometers. Because

the surface temperature fluxes determined from the aircraft data are averages along L shaped transects through the BAO area they are probably more representative of the regional average surface temperature fluxes than are the surface temperature fluxes determined from measurements at a single point. The surface temperature fluxes determined from the aircraft are certainly more representative of conditions along the fixed flight track than are those taken at the tower. Therefore, the surface heat flux values derived from the aircraft data will be used in the nondimensionalization of the other aircraft data. The diurnal cycles presented in the next subchapter will be based on the tower data, however, because of the greater temporal resolution and coverage of that data set.

The largest value of $\overline{w'T'}$ in the lowest 50 m of the BAO tower was selected as $\overline{w'T'_o}$ so that $\overline{w'T'_o}$ would be representative of the temperature flux at the top of the surface layer. Profiles of $\overline{w'T'}$ indicated that while this quantity decreased approximately linearly with height in the mixed layer, it increased with height in the surface layer. Therefore the maximum value in the lowest 50 m is the value of flux into the bottom of the mixed layer.

The surface moisture flux, $\overline{w'q'_o}$, was determined by extrapolating aircraft $\overline{w'q'}$ profiles to the surface, fitting by eye a smooth curve to the resulting time series and picking points off the curve at 20 minute intervals. $\overline{w'T'_o}$ and $\overline{w'q'_o}$ were combined to give $\overline{w'T'_{vo}}$ which is Q_o.

Twenty minute average values of the surface layer parameters, u_*, T_*, $g/\bar{T}$ and L were computed from these series using the formulae given in the previous subchapter. Von Karman's constant was taken as 0.35

in keeping with BAO practice. If one favors another value of k, such as the currently popular value of 0.4, one can easily adjust the values of these parameters accordingly. The mixed layer scaling parameters derived were z_i, w_*, θ_*, q_* z_i/L. Each of these parameters was calculated for every 20 minute period for which surface layer, z_i and $\overline{w'q'_o}$ data were available.

The boundary layer depth, z_i was taken from a smooth curve drawn by eye through the available z_i estimates. When z_i was less then 300 m, the tower data were used to estimate its value. The curve was drawn to pass through the levels of tower instrumentation at the times the inversion passed through those levels. When z_i was greater then 300 m, yet still well defined, and aircraft soundings were available, z_i was taken to be the level where vertical velocity and temperature variance decreased sharply. This level was associated with the temperature inversion and marked the top of the entrainment layer. Late in the day, the top of the boundary layer sometimes became undefined and variable and so z_i could not be estimated. Data from flight legs with poorly defined z_i could not be analyzed.

The mixed layer scaling parameters, w_*, θ_* and q_* were determined from the Q_o, z_i and $\overline{w'q'}_o$ data described above and the surface layer nondimensionalizing parameters. The formulae used for w_* and θ_* were given in the previous subchapter. The parameter q_* is the humidity mixing ratio scaling parameter analogous to θ_*.

$$q_* = \overline{w'q'_o}/w_*$$

3.3 Observations of Nondimensionalizing Parameters

The time series of the surface fluxes and the mixed layer scaling parameters provide a general picture of PBL development for each day in the Phoenix experiment. The time series are qualitatively alike for each of the four days studied. There are, however, considerable quantitative differences from day to day.

The time series for surface virtual temperature flux, Q_o, are shown in Figures 3.1 A through 3.1 D. Q_o is equal to the surface buoyancy flux for dry convection. This flux remains near zero until after sunrise and then rises to a reach of maximum within an hour of midday. By midafternoon, the surface buoyancy flux begins to decrease rapidly and is generally near zero by sunset. This cycle is in phase with solar insolation. This timing was also observed on the undisturbed days 12 and 33 of the Wangara experiment reported by Clark et al. (1971). Kaimal et al. (1976), however, report a two hour lag between midday and the time of maximum surface heat flux as typical of the Minnesota experiment. This lag could be caused either by heat storage in the soil or by a latent heat flux which decreases as the soil drys after noon. Either of these effects could compete with the surface heat flux for the energy of the noon time solar radiation. A wet soil surface would contribute to both effects. Daily maximum values of Q_o range form .22 to .28 degrees C(m/s).

Time series for surface humidity mixing ratio flux, q_o, are shown in Figures 3.2 A through 3.2 D. The surface humidity mixing ratio flux is a measure of evapotranspiration. These series follow a diurnal cycle similar to that of Q_o although the timing of the maximum flux varies by as much as three hours on either side of midday. This

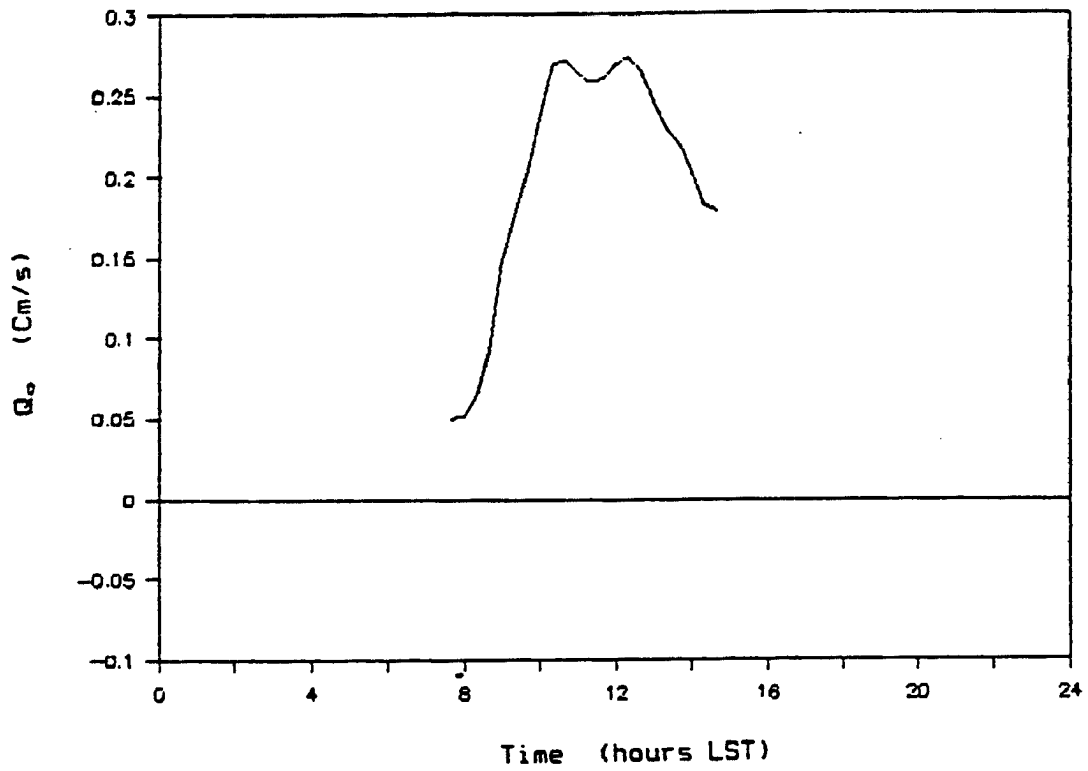

Fig. 3.1A Time series of 20 minute averages of surface buoyancy flux, Q_o, for 9/9/78. Time has units of hours after midnight and Q_o has units of Cm/s.

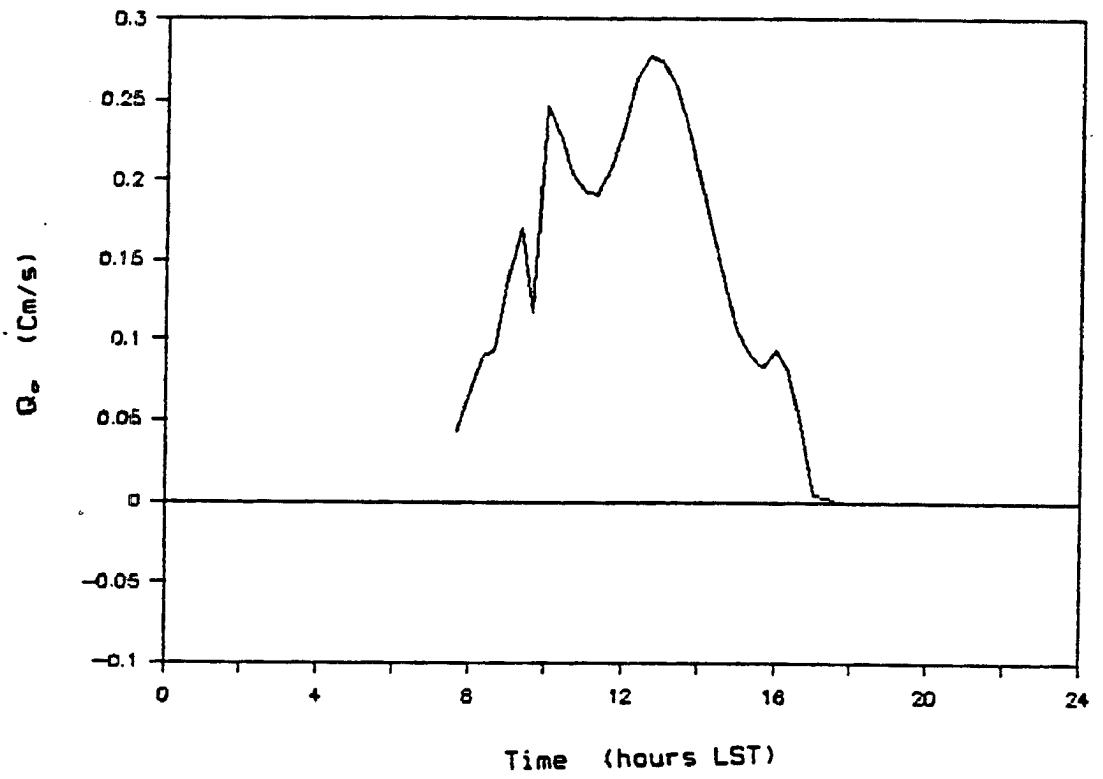

Fig. 3.1B Time series of 20 minute averages of surface buoyancy flux, Q_o, for 9/21/78. Time has units of hours after midnight and Q_o has units of Cm/s.

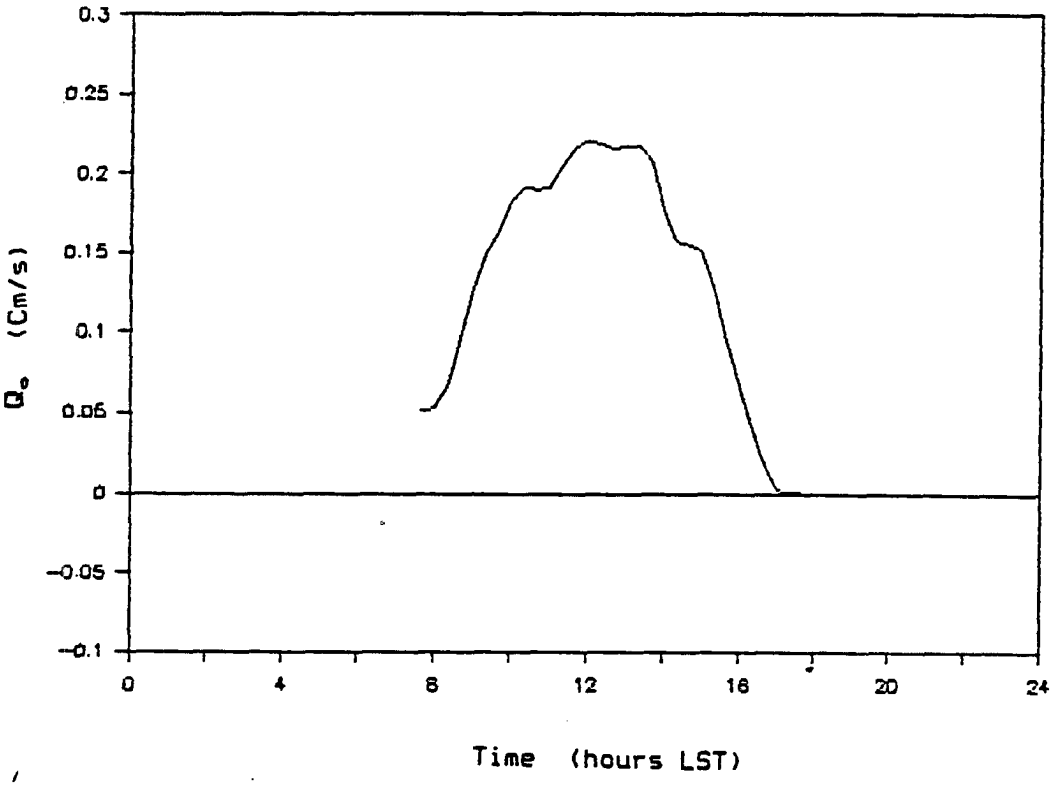

Fig. 3.1C Time series of 20 minute averages of surface buoyancy flux, Q_o, for 9/22/78. Time has units of hours after midnight and Q_o has units of Cm/s.

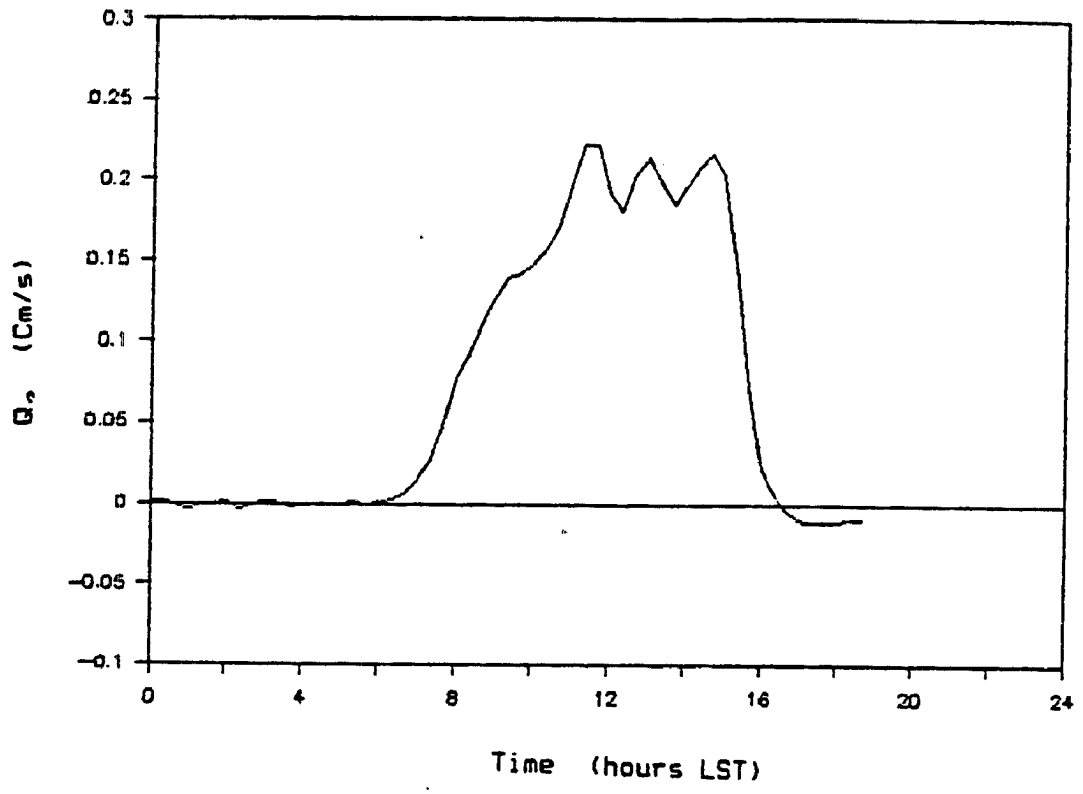

Fig. 3.1D Time series of 20 minute averages of surface buoyancy flux, Q_o, for 9/27/78. Time has units of hours after midnight and Q_o has units of Cm/s.

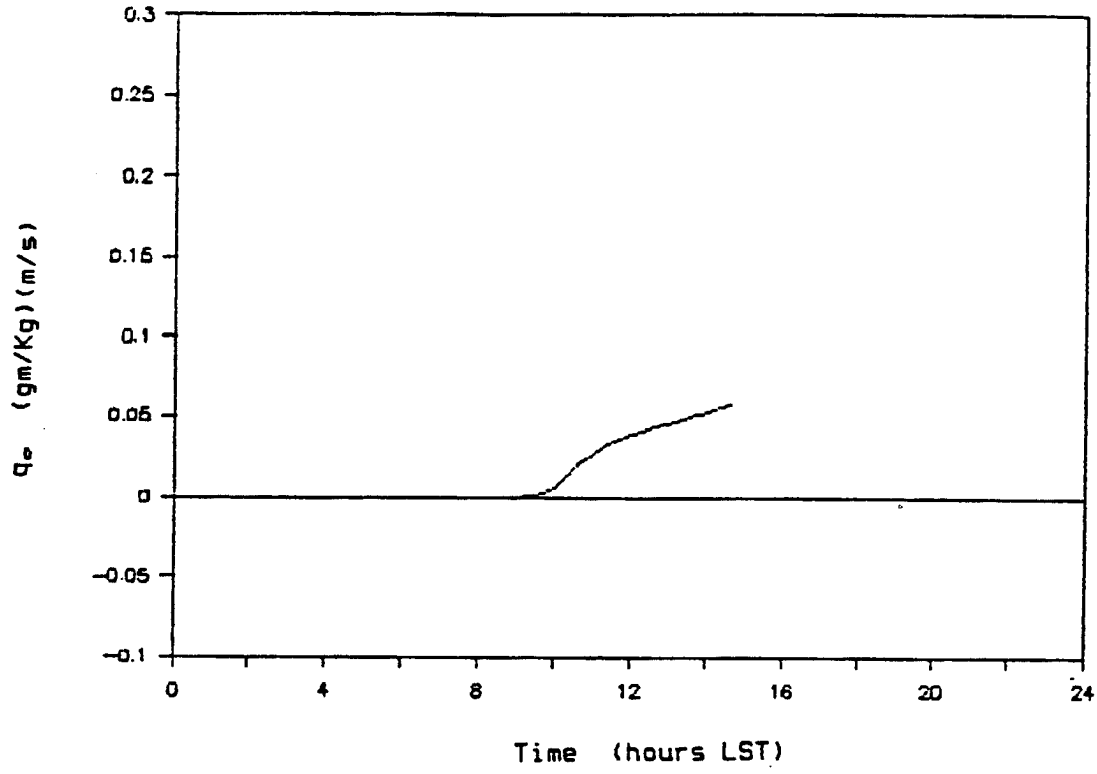

Fig. 3.2A Time series of 20 minute averages of surface humidity mixing ratio flux, q_o, for 9/9/78. Time has units of hours after midnight and q_o has units of (gm/kg)(m/s).

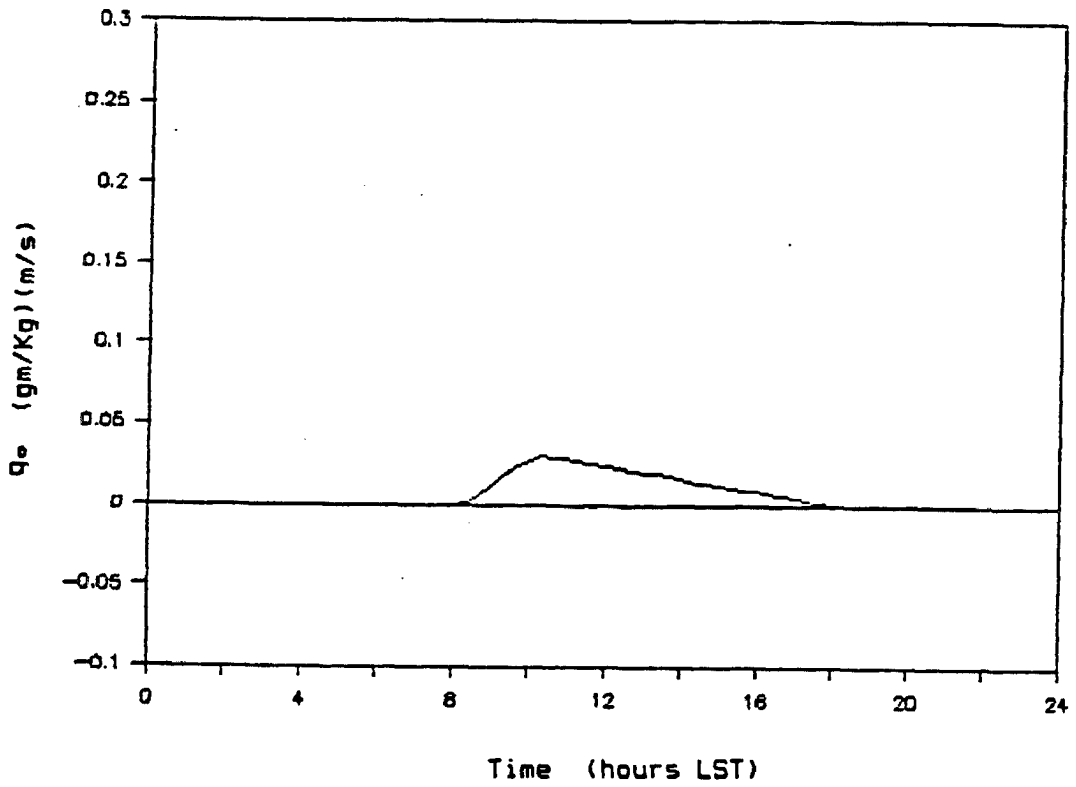

Fig. 3.2B Time series of 20 minute averages of surface humidity mixing ratio flux, q_o, for 9/21/78. Time has units of hours after midnight and q_o has units of (gm/kg)(m/s).

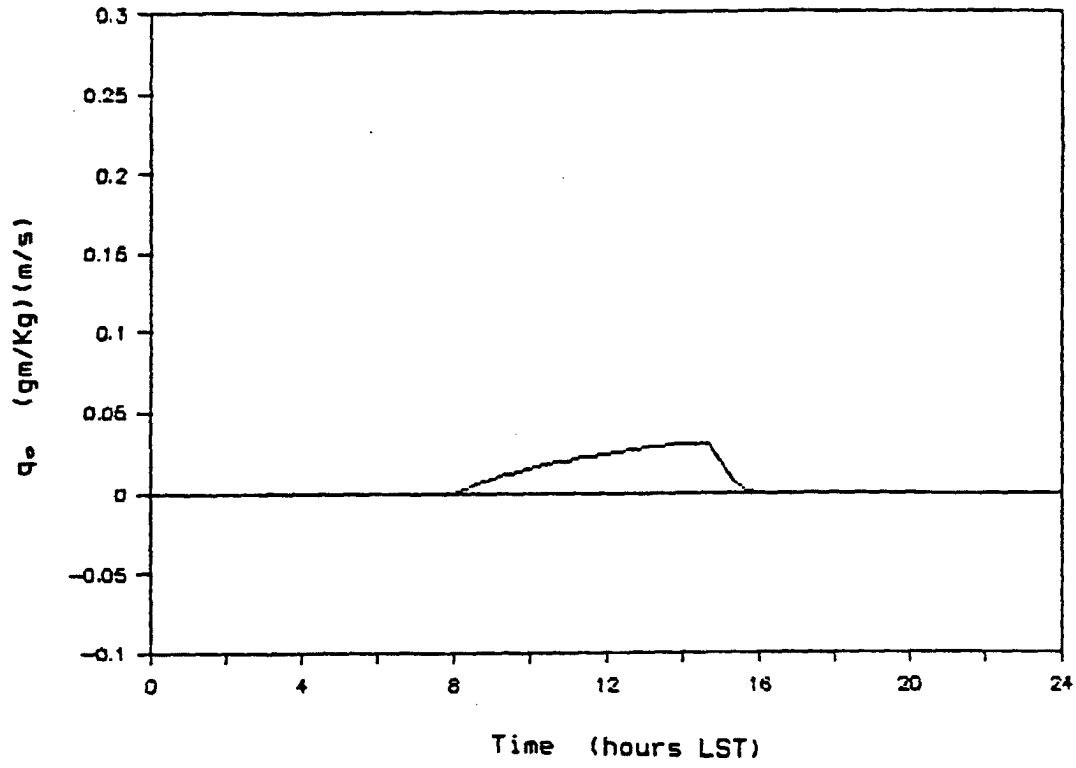

Fig. 3.2C Time series of 20 minute averages of surface humidity mixing ratio flux, q_o, for 9/22/78. Time has units of hours after midnight and q_o has units of (gm/kg)(m/s).

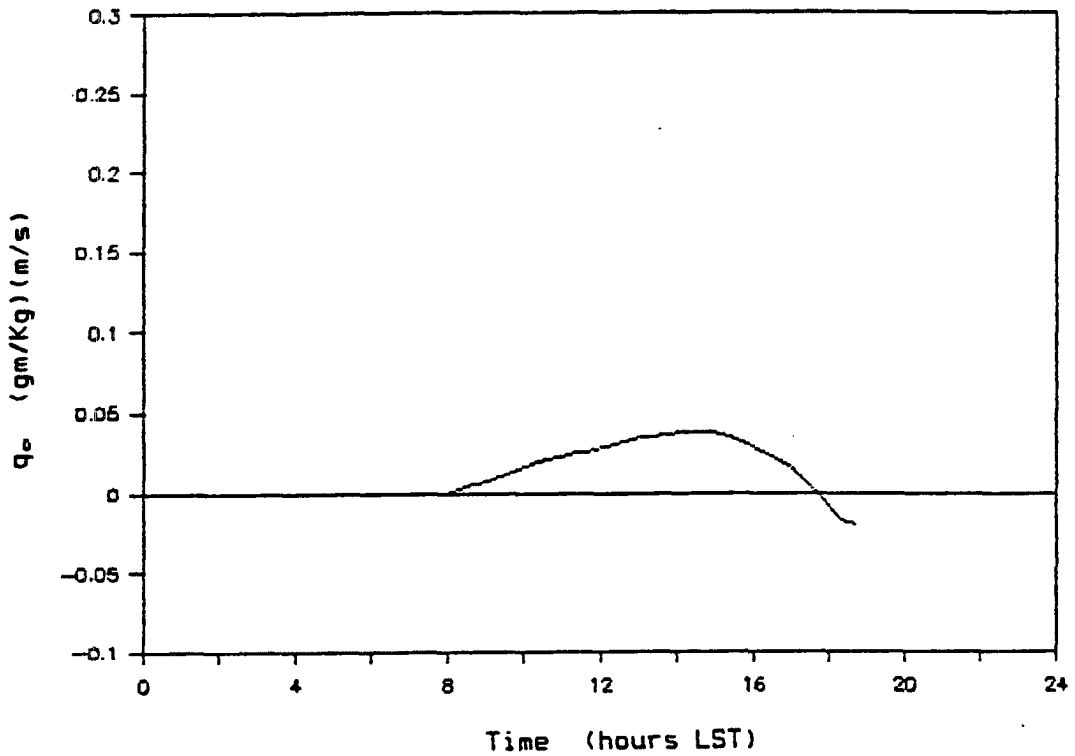

Fig. 3.2D Time series of 20 minute averages of surface humidity mixing ratio flux, q_o, for 9/27/78. Time has units of hours after midnight and q_o has units of (gm/kg)(m/s).

greater variability may be related to the day to day changes in soil moisture. Daily maximum values of q_o range from 0.03 to 0.06 (gm/kg)(m/s). These maximum values correspond to a latent heat flux of from 0.076 to 0.15 degrees C(m/s). Comparison of these values with the daily maximum values of Q_o, 0.22 to 0.28, shows that the contribution of latent heat flux to the surface energy budget can be half as large as that of the sensible heat flux. This is a larger ratio than one would have expected a priori for a climatalogically dry continental location.

The time series for boundary layer depth, z_i, are shown in Figures 3.3 A through 3.3 D. The boundary layer depth increases monotonically with time during the daylight hours, beginning soon after sunrise. The most rapid increase in boundary layer depth occurs between 1000 and 1500 when the surface buoyancy flux is largest. Flights conducted at times of extreme CBL growth rate may have some uncertainties in z/z_i. On the four days studied, the maximum depth of the PBL was reached within an hour of 1600 LST. This maximum depth varied from 1300 to 2200 m. The diurnal cycle of boundary layer depth observed during the Phoenix experiment was the same as that observed during the Wangara (Clark, et al. 1971) and Minnesota experiments (Kaimal et al. 1976). With the reversal of the surface buoyancy flux near sunset, a new inversion forms near the surface. The old inversion remained intact at about the same level as in late afternoon.

Figures 3.4 A through 3.4 D show the time series of w_* while Figures 3.5 A through 3.5 D show the time series of θ_*. Updraft velocity in thermals is closely related to w_* and their buoyancy is

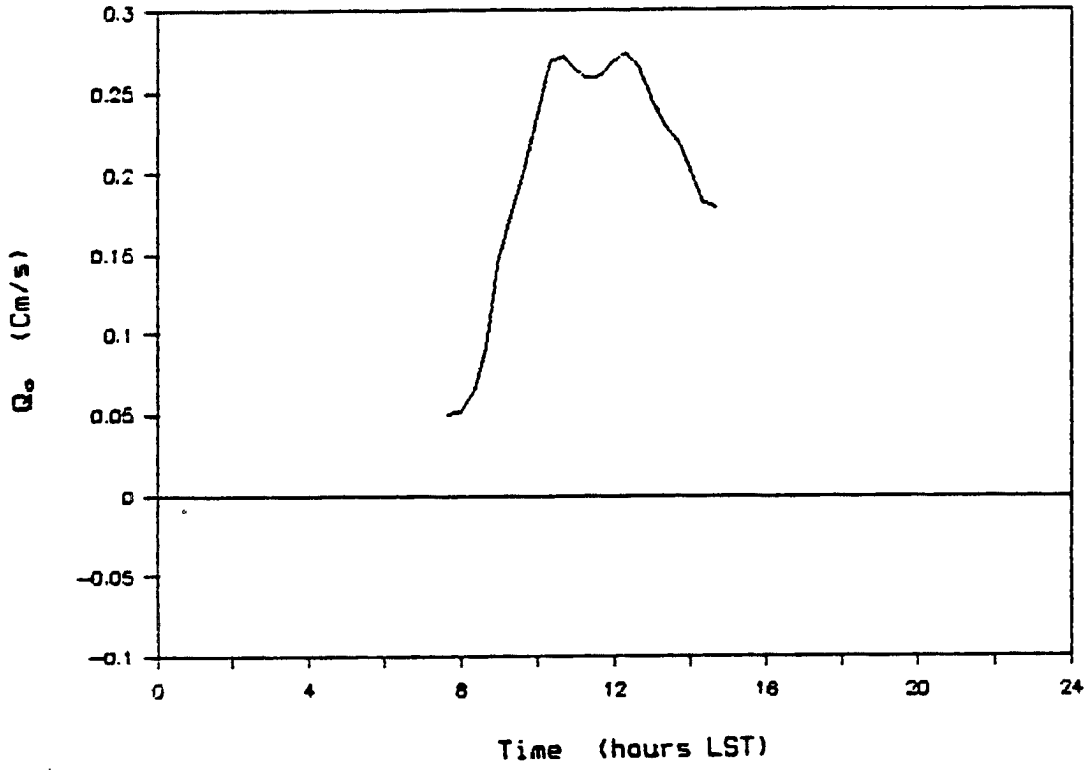

Fig. 3.1A Time series of 20 minute averages of surface buoyancy flux, Q_o, for 9/9/78. Time has units of hours after midnight and Q_o has units of Cm/s.

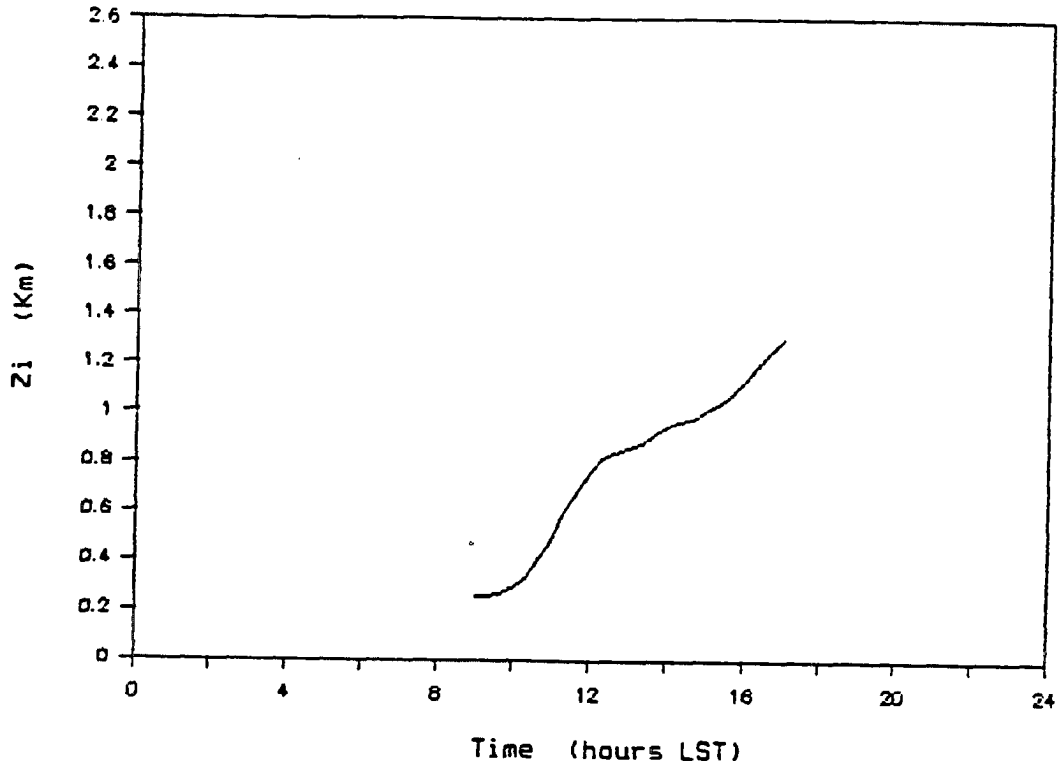

Fig. 3.3B Time series of 20 minute averages of boundary layer depth, z_i, for 9/21/78. Time has units of hours after midnight and $\tilde{z}_i$ has units of km.

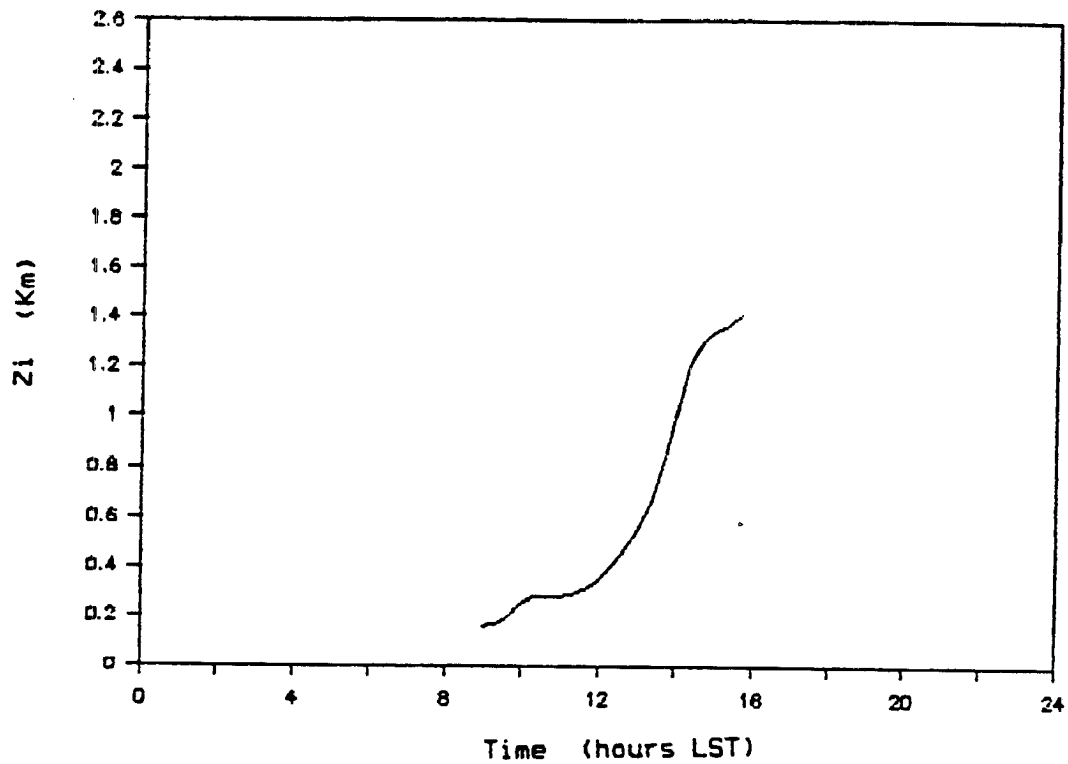

Fig. 3.3C Time series of 20 minute averages of boundary layer depth, z_i, for 9/22/78. Time has units of hours after midnight and z_i has units of km.

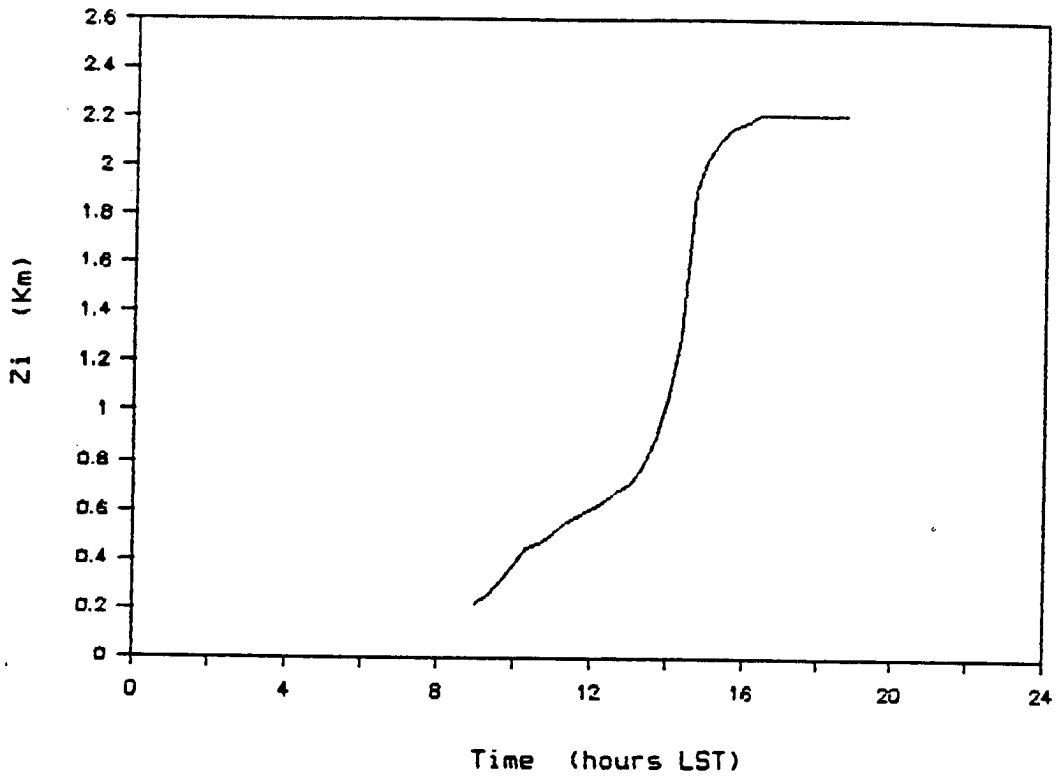

Fig. 3.3D Time series of 20 minute averages of boundary layer depth, z_i, for 9/27/78. Time has units of hours after midnight and z_i has units of km.

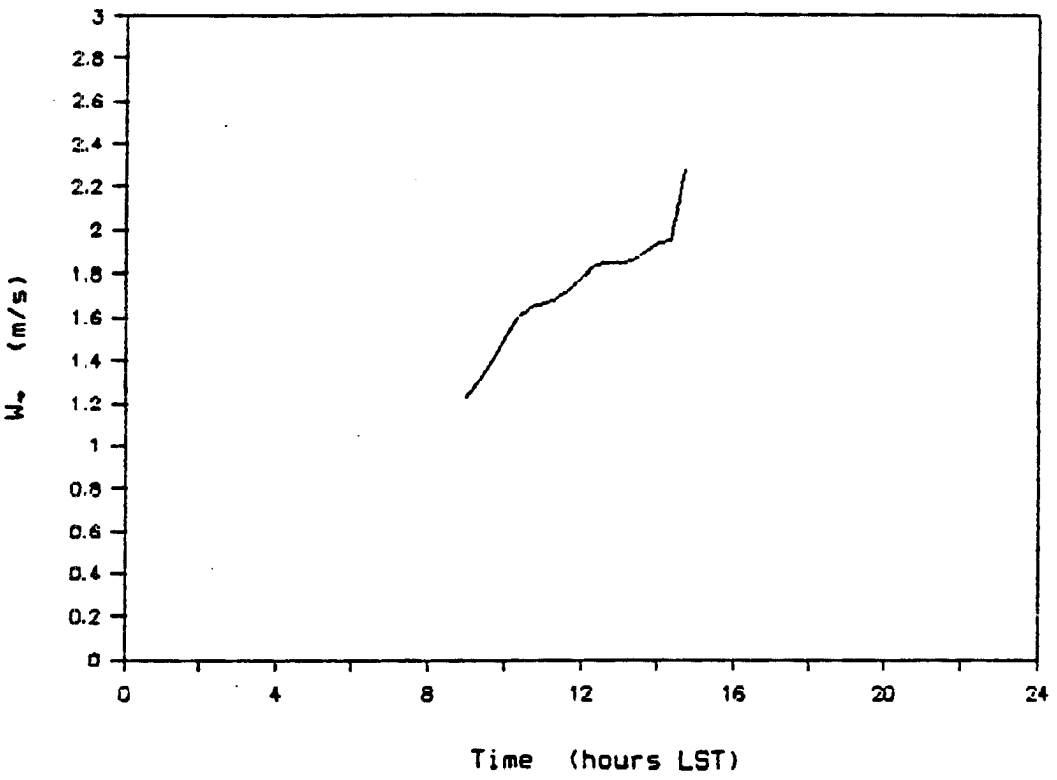

Fig. 3.4A Time series of 20 minute averages of w_* for 9/9/78. Time has units of hours after midnight and w_* has units of m/s.

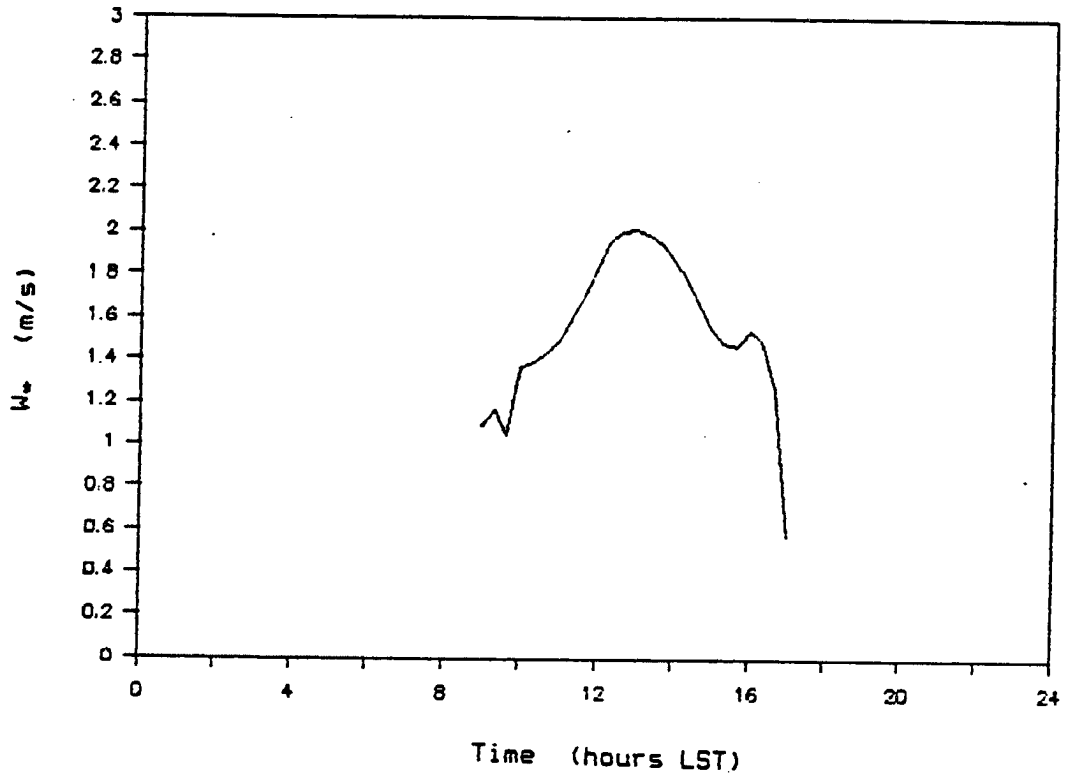

Fig. 3.4B Time series of 20 minute averages of w_* for 9/21/78. Time has units of hours after midnight and w_* has units of m/s.

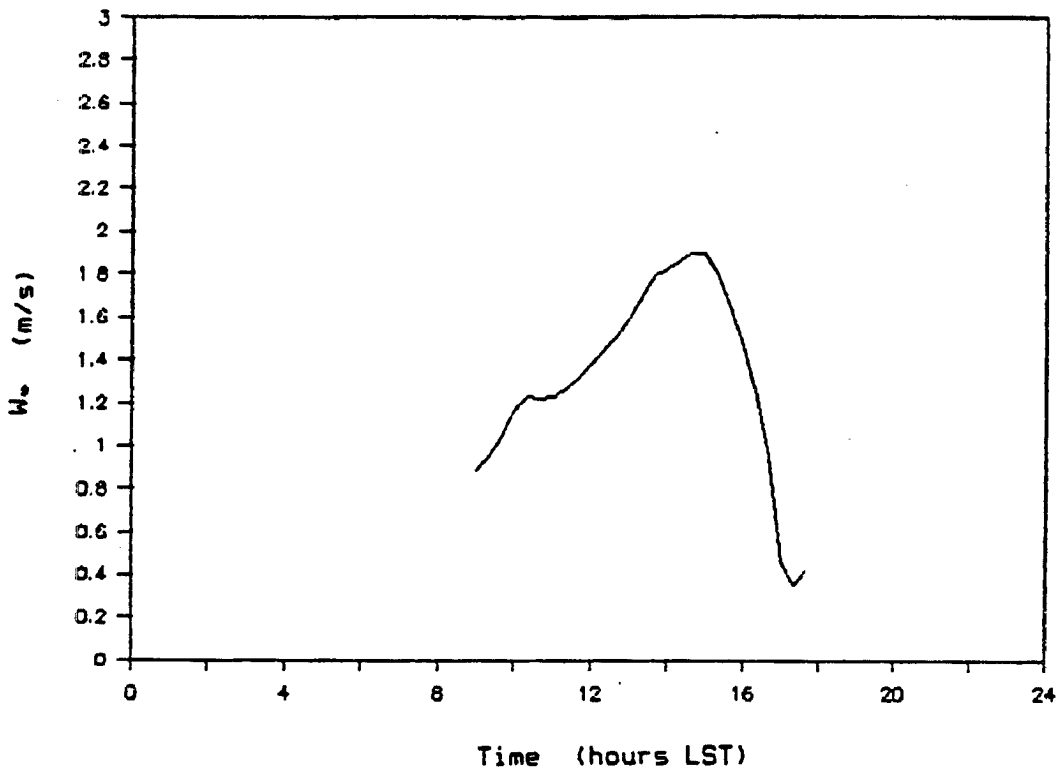

Fig. 3.4C Time series of 20 minute averages of w_* for 9/22/78. Time has units of hours after midnight and w_* has units of m/s.

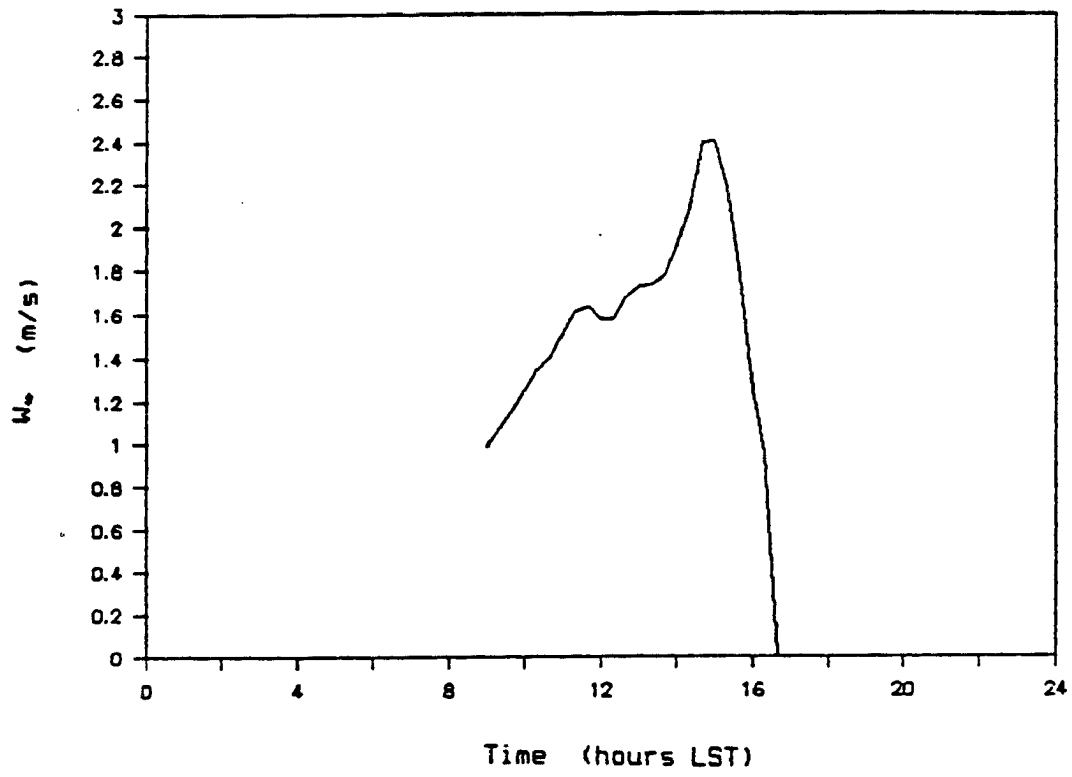

Fig. 3.4D Time series of 20 minute averages of w_* for 9/27/78. Time has units of hours after midnight and w_* has units of m/s.

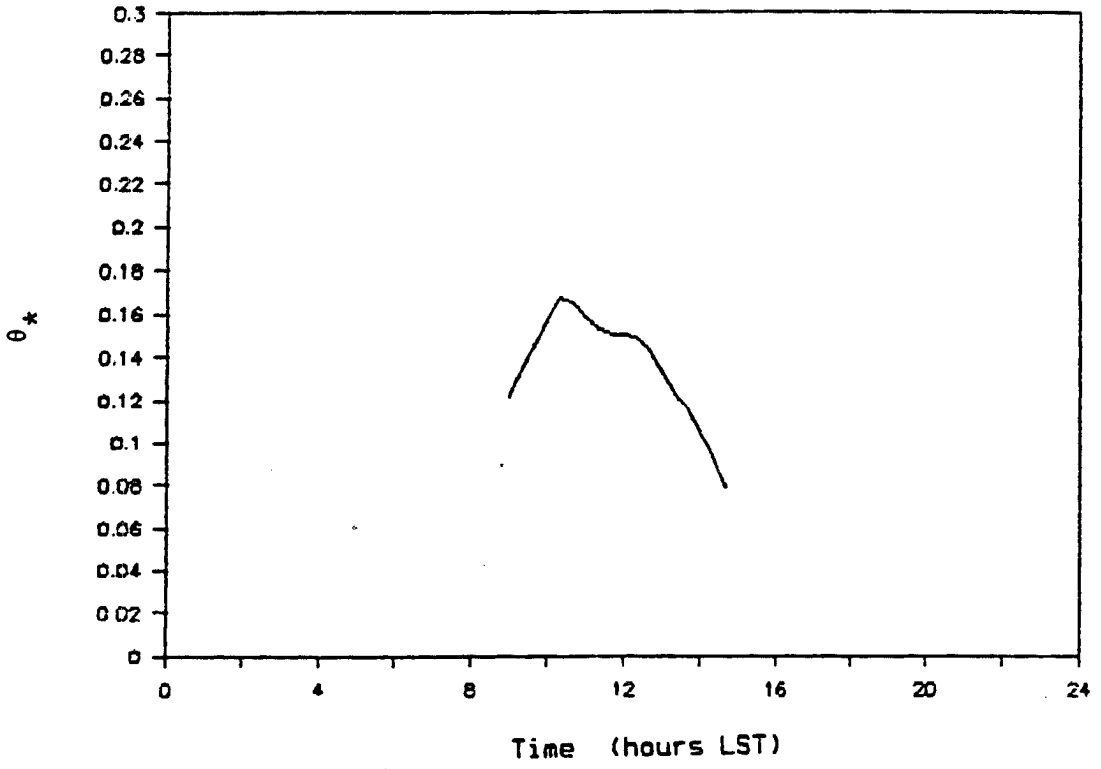

Fig. 3.5A Time series of 20 minute averages of θ_* for 9/9/78. Time has units of hours after midnight and θ_* has units of degrees C.

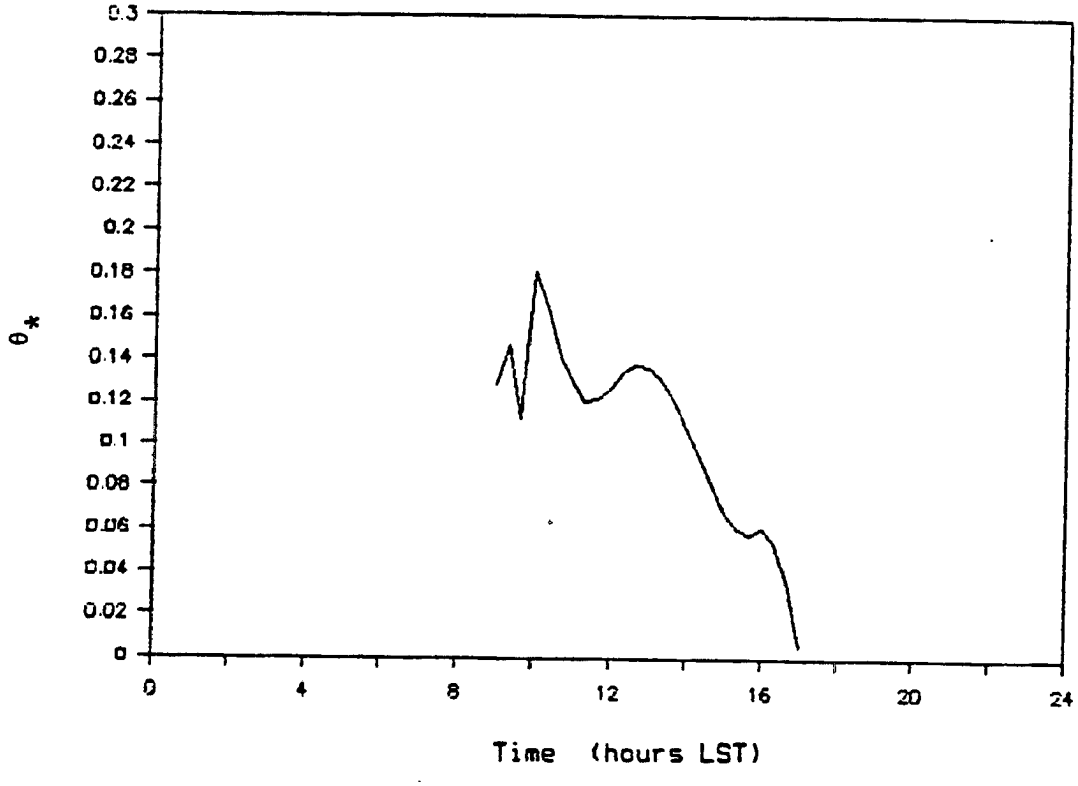

Fig. 3.5B Time series of 20 minute averages of θ_* for 9/21/78. Time has units of hours after midnight and θ_* has units of degrees C.

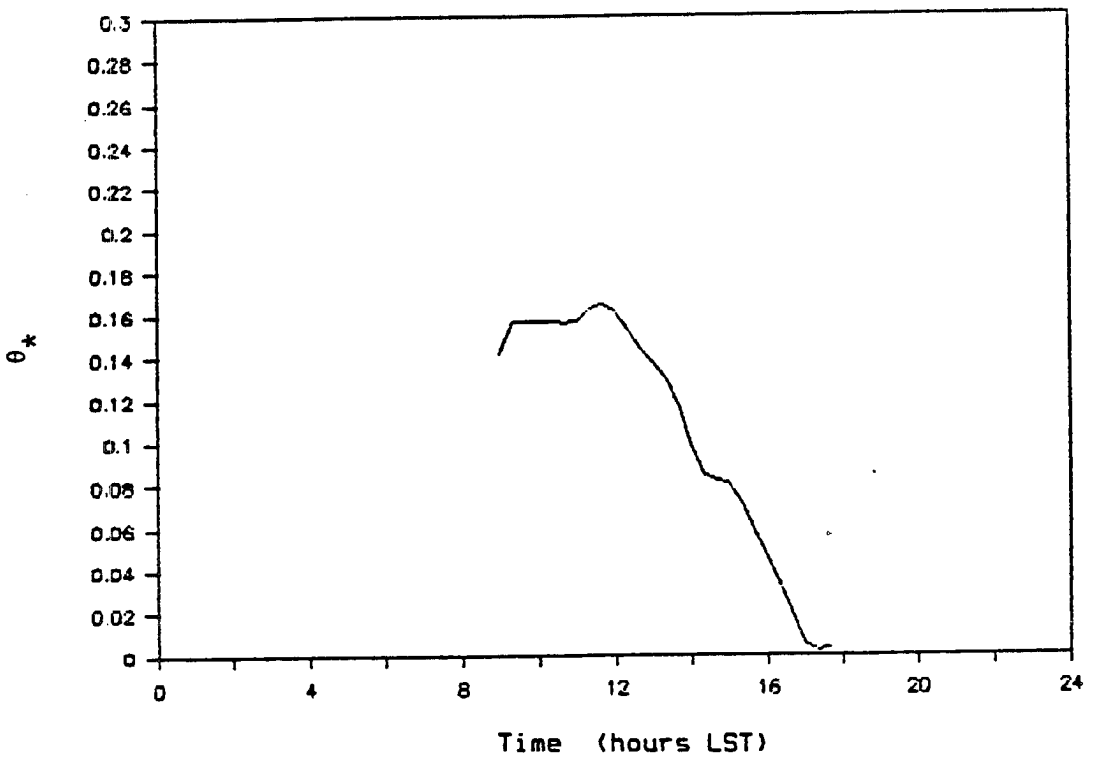

Fig. 3.5C Time series of 20 minute averages of θ_* for 9/22/78. Time has units of hours after midnight and θ_* has units of degrees C.

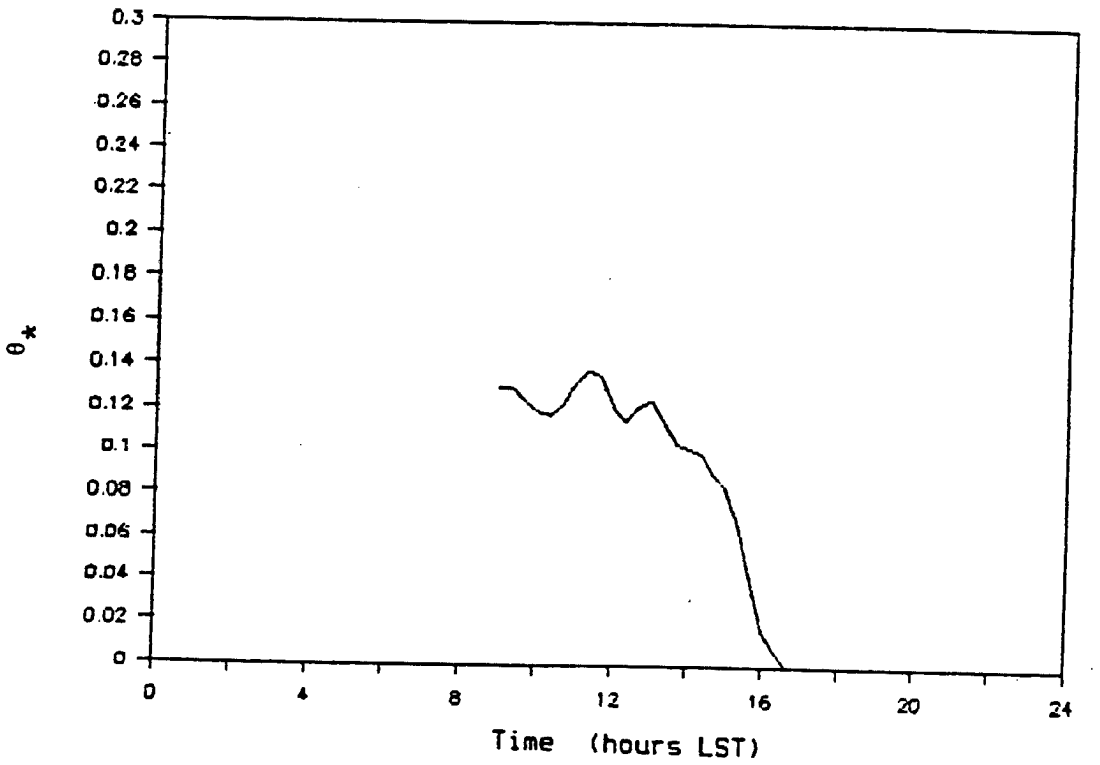

Fig. 3.5D Time series of 20 minute averages of θ_* for 9/27/78. Time has units of hours after midnight and θ_* has units of degrees C.

closely related to θ_*. If mixed layer similarity were perfectly valid, then the w_* and θ_* cycles would be exactly proportional to the updraft velocity and buoyancy of thermals with the constants of proportionality varying only with z/z_i. In fact, an air parcel with buoyancy equal to θ_* and no drag would reach a speed of w_* as it accelerated from the surface to $z_i/2$. [1]

---

[1]This result can be derived from the definitions of w_* and θ_*, and the appropriate equation of motion (Venkatram, 1984).

$$w_* = \left(\frac{Q_o\ g\ z_i}{\bar{T}}\right)^{1/3}$$

$$\theta_* = \left(\frac{Q_o^2\ g}{\bar{T} z_i}\right)^{1/3}$$

$$\frac{dw}{dt} = \frac{g\theta'}{\bar{T}}$$

For a parcal starting at rest of the surface with $\theta' = \theta_*$ the solution to this equation of motion is as follows

$$w = \frac{g\theta_* t}{\bar{T}}$$

$$z = \frac{1}{2}\frac{g\theta_* t^2}{\bar{T}}$$

when t is the elapsed time of buoyant acceleration, the time needed

to accelerate to w_* is $\frac{w_*\bar{T}}{g\theta_*} = \frac{z_i^2\bar{T}}{Q_o g}$

in that time the parcal would reach a hieght of

$\frac{1}{2}\frac{g\theta_*}{\bar{T}}\left(\frac{w_*\bar{T}}{g\theta_*}\right)^2$ which simplifies to $\frac{1}{2}\frac{w_*^2\bar{T}}{\theta_* g}$ or $\frac{z_i}{2}$

The diurnal cycles of w_* and θ_* are controlled mainly by those of z_i and Q_o. Deep boundary layers with large surface buoyancy fluxes are favorable for large w_*. Therefore, the peak values of w_* occur between 1200 and 1500 LST when the boundary layer depth has increased to almost it's maximum and the surface buoyancy flux has not begun to decrease rapidly. Daily maximum values of w_* observed during this study are all between 1.9 and 2.4 m/s.

The diurnal cycle of θ_* is particularly interesting because it reaches a maximum between 1000 and 1200 LST. The occurrence of the θ_* maximum before the maximum of surface buoyancy flux is caused by the inverse relationship between θ_* and z_i. As the boundary layer depth increases, thermals have more room to accelerate and can thus reach higher velocities for the same buoyancy. Therefore, to maintain a given buoyancy flux, a deep boundary layer will require less buoyancy than a shallow one. Daily maximum values of θ_* during this study were 0.16 ± 0.03 degrees C.

Figure 3.6 A through 3.6 D show the time series of q_*. The diurnal cycle of q_* is as variable as that of q_o. Peak values can occur throughout the daylight hours and range from 0.018 to 0.029 g/kg.

Figures 3.7 A through 3.7 D show the time series of $z_i/|L|$. This is the ratio of mixing layer depth to surface layer depth. When this ratio is much greater than 10.0 the effect of surface stress on the bulk of the mixed layer is negligible and mixed layer scaling is valid. The diurnal cycles are irregular but tend to have minima in the evening when the surface wind speeds are still near the daily

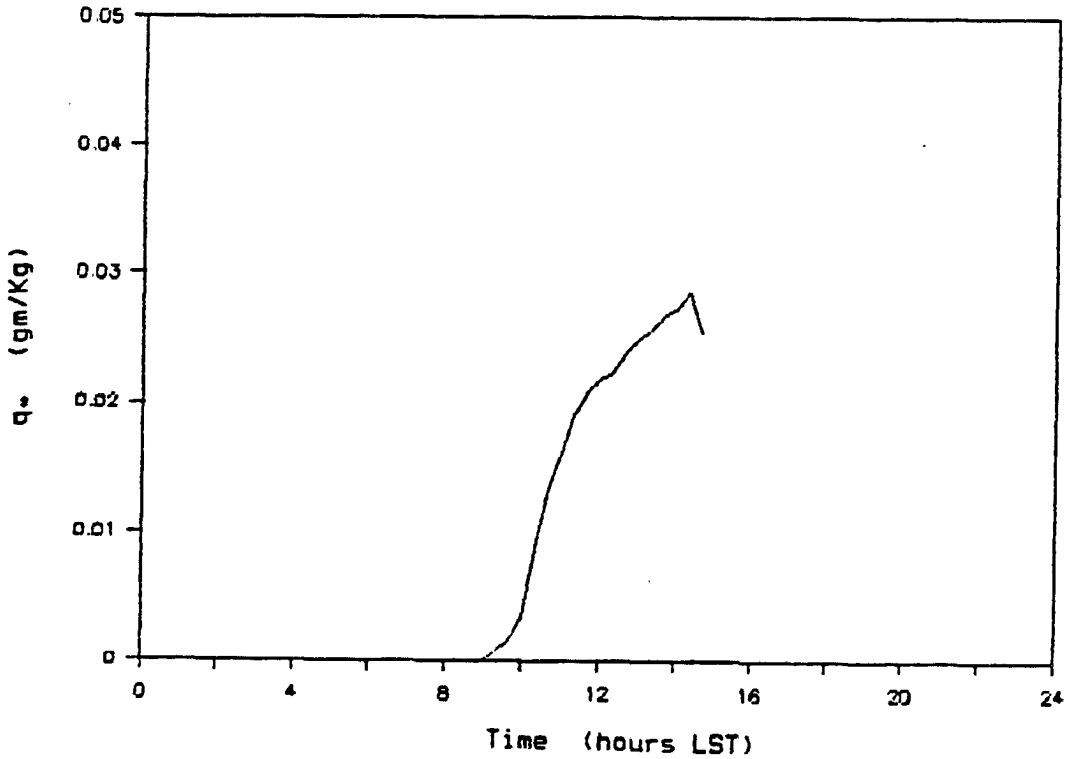

Fig. 3.6A Time series of 20 minute averages of q_* for 9/9/78. Time has units of hours after midnight and q_* has units of gm/kg.

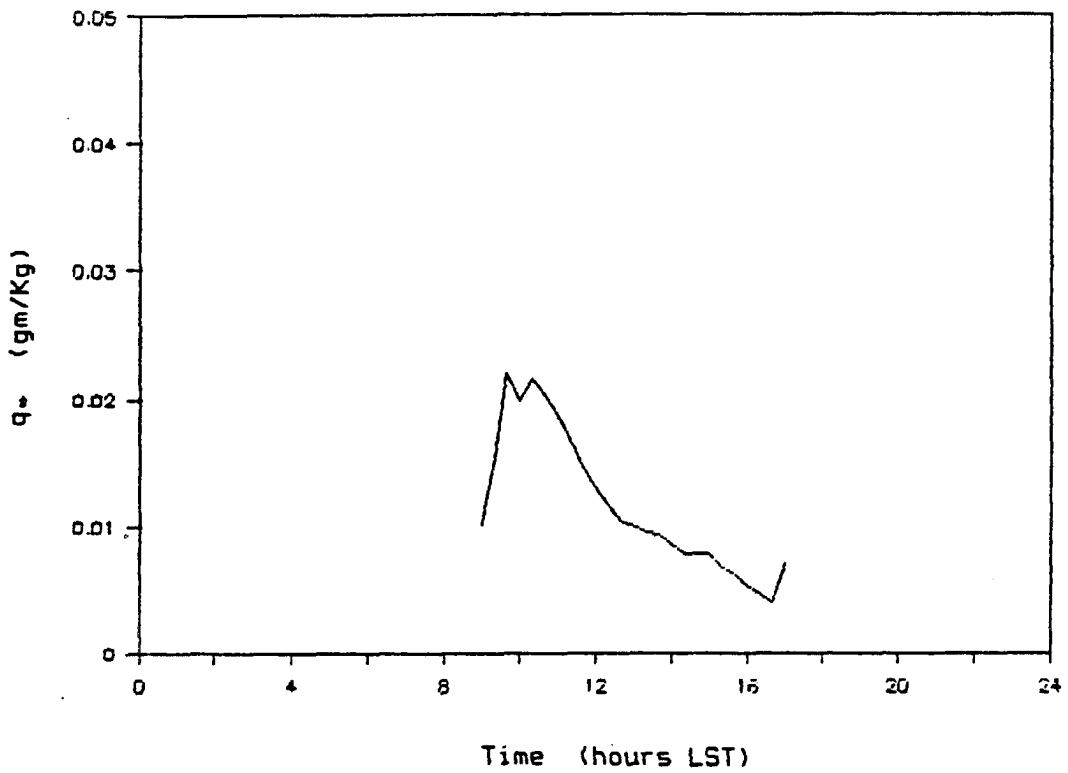

Fig. 3.6B Time series of 20 minute averages of q_* for 9/21/78. Time has units of hours after midnight and q_* has units of gm/kg.

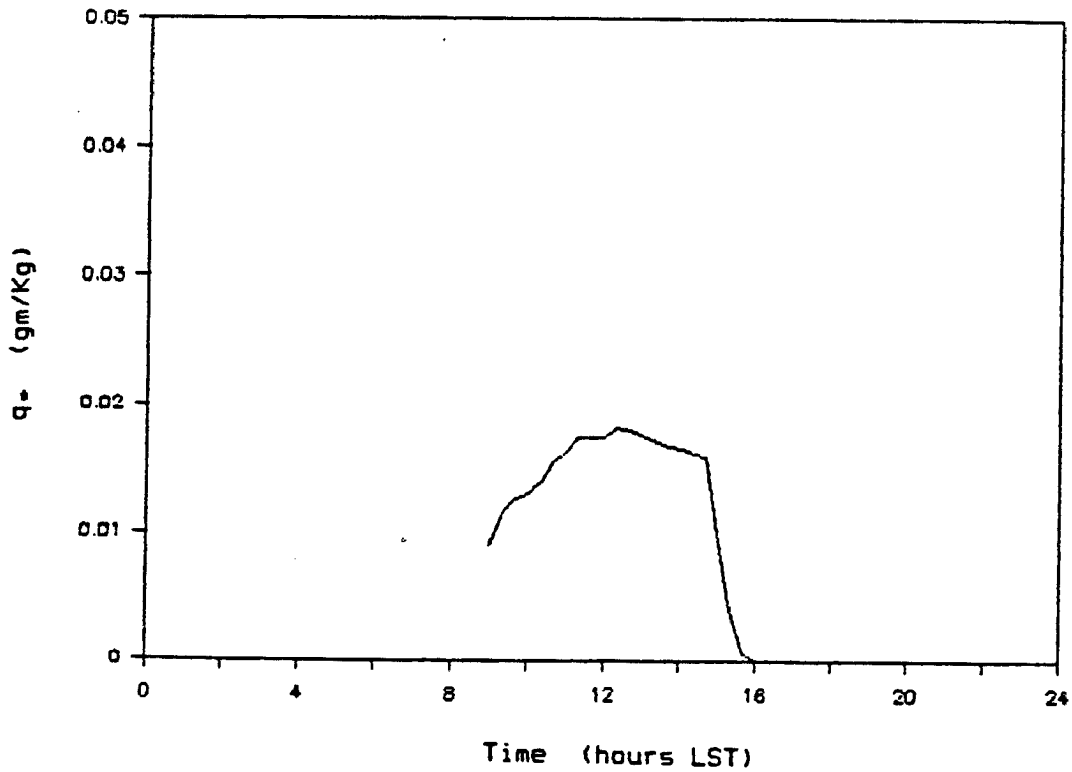

Fig. 3.6C Time series of 20 minute averages of q_* for 9/22/78. Time has units of hours after midnight and q_* has units of gm/kg.

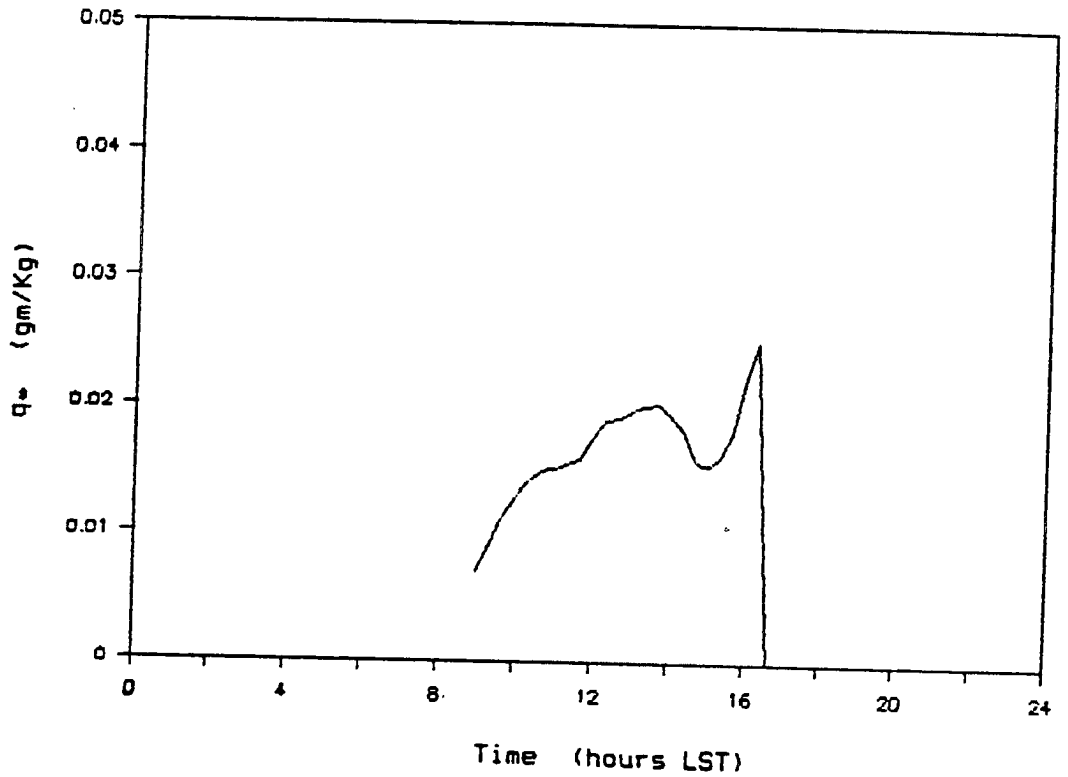

Fig. 3.6D Time series of 20 minute averages of q_* for 9/27/78. Time has units of hours after midnight and q_* has units of gm/kg.

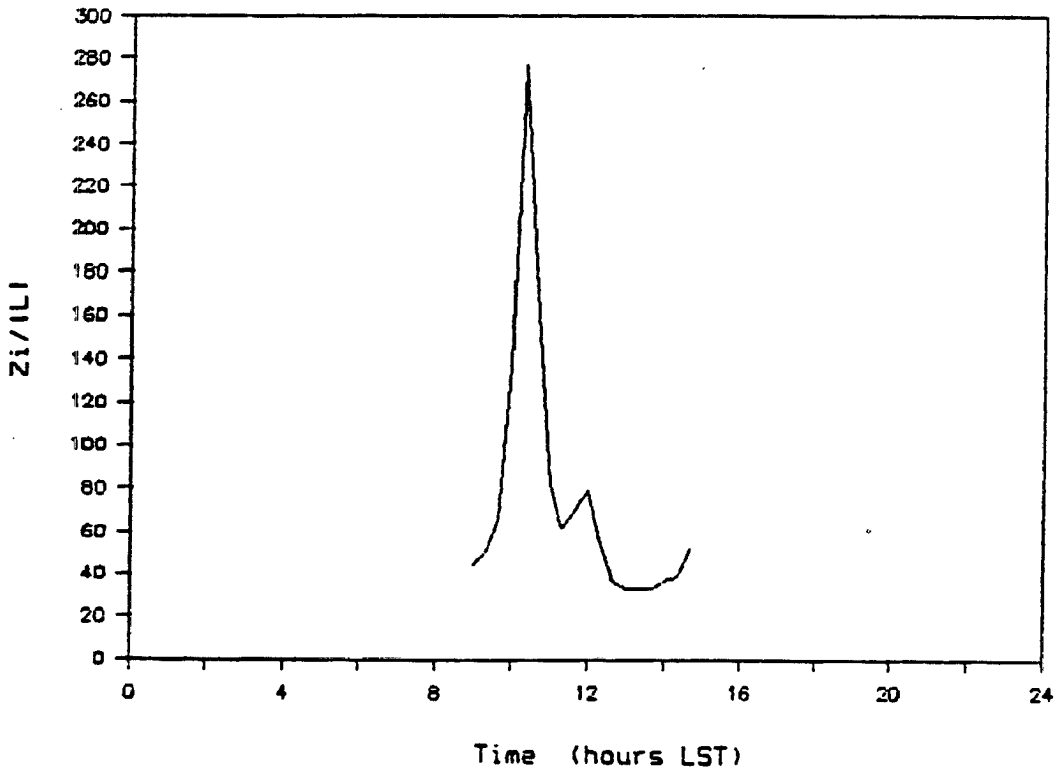

Fig. 3.7A Time series of 20 minute averages of $z_i/|L|$ for 9/9/78. Time has units of hours after midnight and $z_i/|L|$ is non-dimensionless.

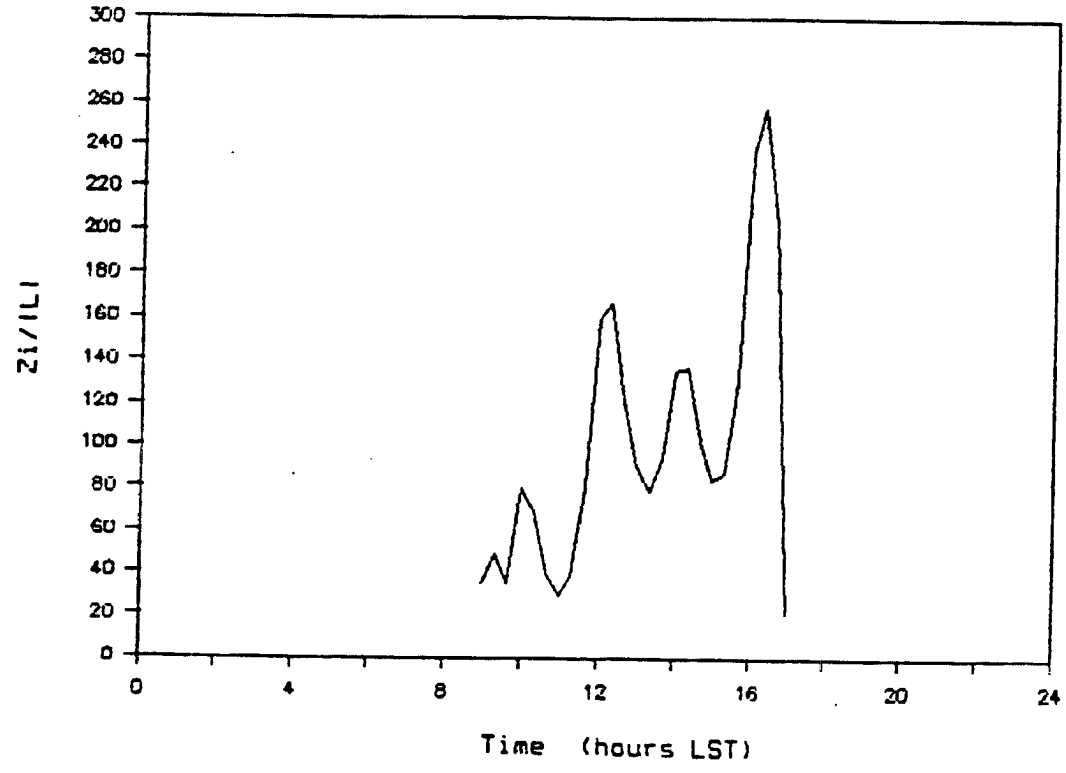

Fig. 3.7B Time series of 20 minute averages of $z_i/|L|$ for 9/21/78. Time has units of hours after midnight and $z_i/|L|$ is non-dimensionless.

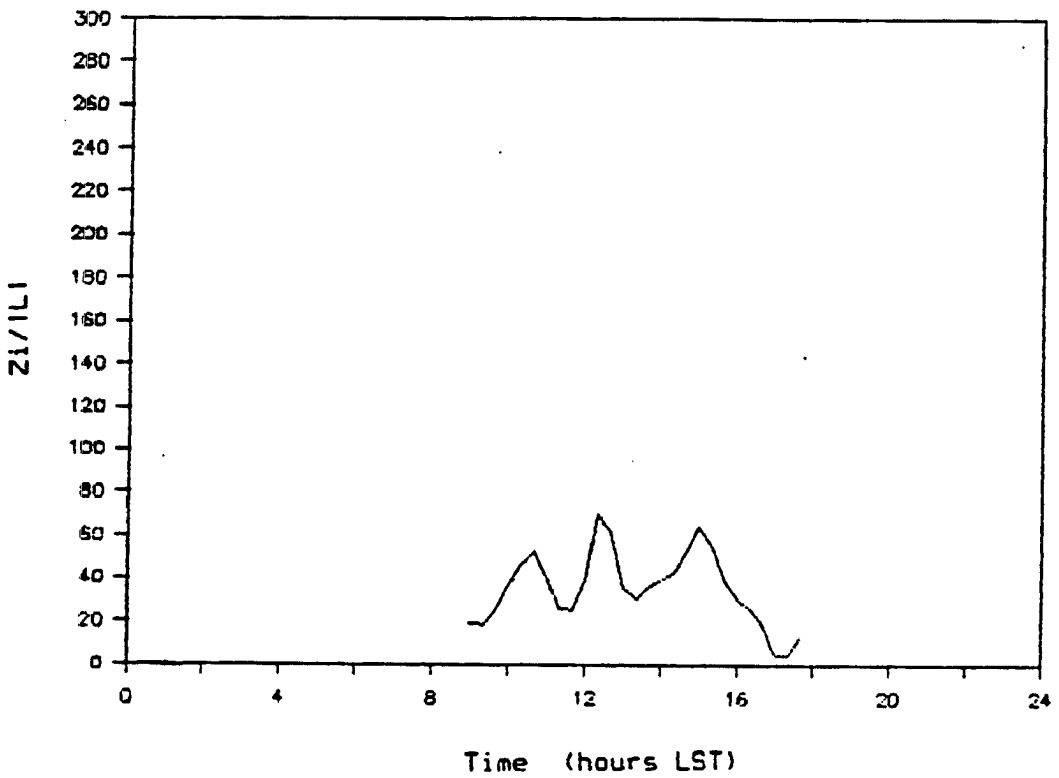

Fig. 3.7C Time series of 20 minute averages of $z_i/|L|$ for 9/22/78. Time has units of hours after midnight and $z_i/|L|$ is non-dimensionless.

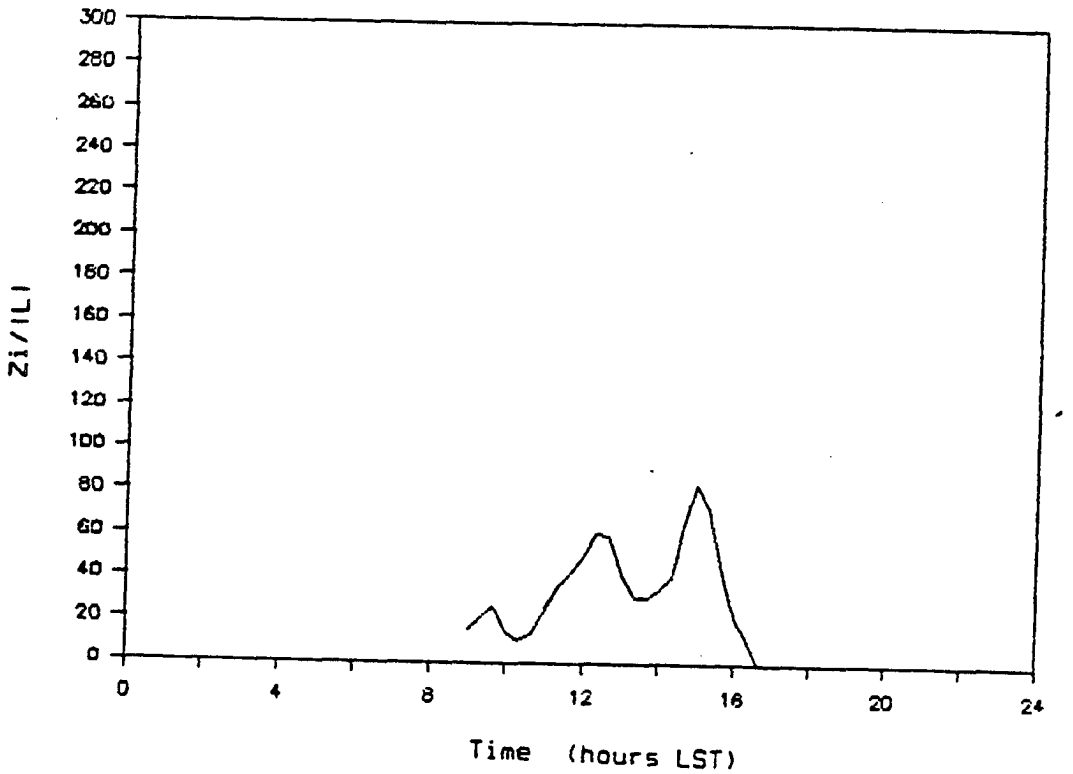

Fig. 3.7D Time series of 20 minute averages of $z_i/|L|$ for 9/27/78. Time has units of hours after midnight and $z_i/|L|$ is non-dimensionless.

maximum and the surface buoyancy fluxes have dropped to near zero. Throughout most of the day, ratio, $z_i/|L|$, ranges from 10.0 to 300.0 for the relatively calm, unstable periods chosen for study in Phoenix. Therefore, mixed layer similarity should be valid for the flight legs analyzed.

4. Turbulence Spectra in the Convective Boundary Layer

4.1 Motivation for Examining Convective Boundary Layer Turbulence Spectra

Fluxes and other turbulence statistics of the convective boundary layer contain contributions from several types of eddy phenomena. Mesoscale eddies, driven by either terrain or synoptic scale forcing, make contributions at horizontal scales ranging upwards from a few kilometers (Pielke, 1984). The horizontal flight legs flown during the Phoenix experiment were long enough to sample the smaller of these mesoscale eddies. On somewhat shorter horizontal scales, of order one kilometer, are the large three dimensional buoyantly driven eddies of the CBL. These microscale eddies make a major contribution to the turbulence statistics of the CBL (Lenshow and Stephens; 1980, 1982). These eddies are the focus of this research. The large buoyantly driven microscale eddies decay into smaller microscale eddies through the process of vortex stretching (Tennekes and Lumley; 1972). This process leads to an inertial energy cascade to smaller scales and the formation of the so called inertial subrange turbulence. The contribution of these smaller eddies to the turbulence statistics of the CBL is also of interest in this study because they are the decay products of the large buoyantly driven eddies of the CBL. Another reason for interest in these smaller eddies is that they can contribute to mixing between the large eddies and thus exert an important diffusive effect on CBL turbulence.

Turbulence spectra are useful tools for examining the horizontal scales at which these different turbulent phenomena occur. If the dividing scales between these phenomena can be ralated to some external scales, such as z or z_i, then the aircraft data can be filtered to separate the contributions of the different phenomena to the turbulence statistics. The contributions of the two pheonomena of primary interest in this study, large buoyantly driven eddies and the smaller energy cascading eddies, could then be studied separately and compared.

There are several ways to distinguish the different physical phenomena which contribute to a turbulence spectra. Distinct spectral peaks, local maxima in spectral variance density, are associated with sources of variance at distinct horizontal scales. Each of these distinct sources of variance is a different physical phenomena. The large buoyantly driven three dimensional eddies of the CBL are a source of variance in the larger microscale wavelengths. The existence of a spectral peak at these wavelengths can confirm the existence of a significant microscale source of variance. The lack of such a peak indicates that any microscale source of variance is insignificant relative to the variance cascaded downscale from larger scales into the microscale. There is always some source of atmospheric variance at some scale larger than the microscale. This source corresponds to a spectral peak at a wavelengths too long to be resolved by the Phoenix aircraft horizontal flight legs. However, the short wavelength tail of this peak should be detectible. The spectral subrange between these two peaks is generally called a spectral gap because of it's relatively smaller contribution to total variance.

The existence of the spectral gap depends directly on the existence of a significant microscale variance source. Numerous cases with and without such spectral gaps have been reported in the literature. Bush and Panofsky (1968) and Smedman-Hogstrom and Hogstrom (1975) provide reviews of work in this field. The scale at which this spectral gap is located is the dividing scale between the mesoscale eddies and the large buoyantly driven eddies of the CBL. Knowledge of this scale is necessary for separating the contributions of mesoscale and microscale eddies to the total turbulence statistics.

The knowledge of the spectral slope in the subranges in which there is no variance source can also make a major contribution to the understanding of turbulence dynamics. Often a particular physical process is associated with a particular spectral slope. Dimensional analysis plays an important role in discovering such associations. For example, an inertial energy cascade to smaller scales in three dimensional turbulence can be shown by dimensional analysis to result in a -5/3 spectral slope (Tennekes, 1978). The spectral subrange of the microscale which has been found to have this slope is therefore called the inertial energy cascade subrange or, more often, simply the inertial subrange. This is the spectral subrange in which the decay of the large buoyantly driven eddies of the CBL occurs. The scale at which the slope first departs from -5/3 towards zero because of the effects of buoyant production of variance separates the inertial subrange from the subrange in which buoyant production of variance occurs. Knowledge of this scale is necessary for separating the contributions to the turbulence statistics of the two phenomena of interest, large buoyantly driven eddies of the CBL and inertial subrange turbulence.

For two dimensional turbulence, such as occurs at the larger atmospheric scales, an upscale reverse cascade of energy leads to a -5/3 spectral slope while a downscale cascade of enstrophy (the mean squared vorticity) leads to a -3 spectral slope. The Phoenix horizontal flight legs are not long enough to sample these scales well. Therefore, these phenomena would be reflected only as moderately steep spectral slopes at the long wavelength end of the Phoenix spectra.

Thus, the turbulence spectra of the CBL can be expected to provide information about the scales at which buoyant production of variance occurs and those at which the inertial cascade of energy occurs. These spectra should also provide information about the location and form of the spectral gap which separates microscale eddies from mesoscale eddies.

4.2 Normalization of Convective Boundary Layer Turbulence Spectra

Mixed layer scaling has been successfully applied to the u, v, and w spectra by Kaimal et al. (1976). They used data collected with a tethered balloon during the 1973 atmospheric boundary layer experiment in Minnesota. The velocity spectral power density and frequency were nondimensionalized by w_*, z_*, U and ε. U, the average wind speed past the sensor, was used with Taylor's hypothesis to convert frequency to wavelength. ε, the turbulence kinetic energy dissipation rate, was used to collapse all the spectra onto one curve in the inertial subrange. They found that the spectral forms varied little throughout the depth of the mixed layer.

For aircraft data this mixed layer normalization of vertical velocity spectra takes the following form:

$$\frac{(2\pi)^{2/3}\,\lambda S_w(\lambda)}{4/3\alpha_1 w_*^2 \psi_w^{2/3}} = F_w(z_i/\lambda,\ z/z_i)$$

where α_1, the inertial subrange spectral constant, is taken to be 0.5 following Kaimal et al. (1976). λ is wavelength, ψ_w is the nondimensionalized w variance dissipation rate ($\varepsilon\bar{T}/gQ_o$ or $\varepsilon z_i/w_*^3$), and F_w is a nondimensional empirical function of the nondimensionalized wavelength and the nondimensionalized height. Wind speed spectra could be normalized in the same manner but with the factor $4/3\alpha_1$ replaced by α_1 because the sampling direction has no effect on spectra of an scalar (Panofsky and Dutton, 1984). This method of normalization will be used on the vertical velocity and wind speed spectra calculated from the Phoenix aircraft data. Figure 4.1 shows the effect of the normalization on the w spectra of 15 horizontal legs flown within the middle of the convective boundary layer (CBL). The normalization greatly reduces scatter by acocunting for the effects of variations in boundary layer depth and turbulence intensity. The complete results will be presented in the next subchapter.

Kaimal et al. (1976) presented temperature spectra in an unnormalized format because of the large contamination of the low frequency end of their temporal spectra by the diurnal trend. The horizontal flight legs of the Phoenix aircraft data set are short enough, less then 10 minutes in duration, that this problem did not arise. Nevertheless, as shown in Figure 4.2, there is a significant amount of variance in the potential temperature spectra at wavelengths longer then 10 z_i (i.e. on the mesoscale). However, there is a negligible contribution to Q_o, and therefore w_* and q_*, from these

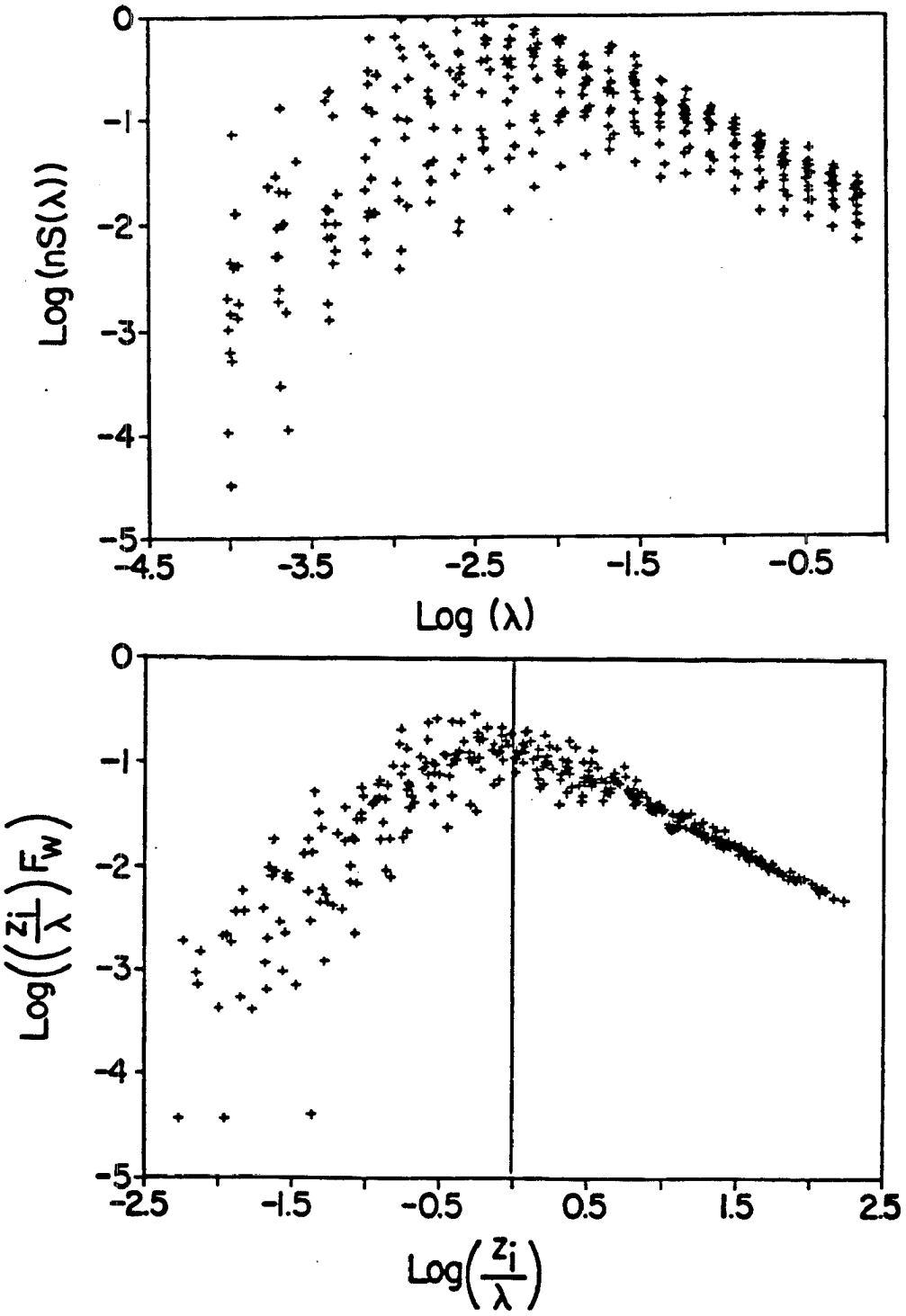

Fig. 4.1 Comparison of 15 vertical velocity spectra before (top) and after (bottom) normalization. The spectra are for the layer from $0.2 < z_* < 0.8$. The scales on all axis are logarithmic.

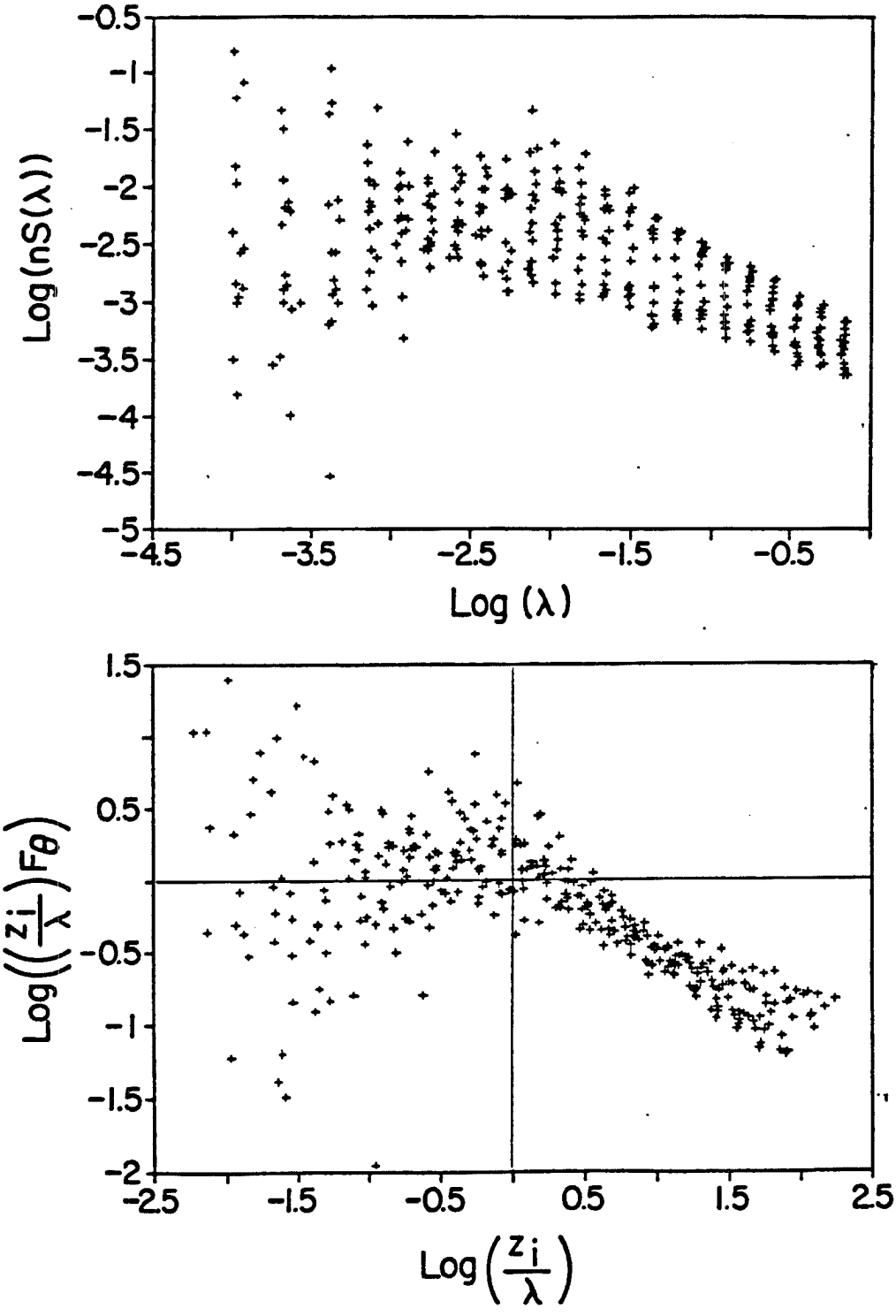

Fig. 4.2 Comparison of 15 potential temperature spectra before (top) and after (bottom) normalization. The spectra are for the layer from $0.2 < z_* < 0.8$. The scales on all axis are logorithmic.

mesoscale potential temperature fluctuations because the surface layer vertical velocities are so small at these wavelengths. Thus w_* and θ_* are representative of the microscale variance and, therefore, may be used to normalize the microscale portion of the mixed layer potential temperature spectra.

Using a mixed layer normalization scheme similar to that used for w (Corrsin, 1951; Kaimal et al., 1972), one gets a potential temperature spectra of the following form:

$$\frac{(2\pi)^{2/3}\lambda S_\theta(\lambda)}{\beta_1 \theta_*^2 \psi_\theta} = F_\theta(z_i/\lambda,\ z/z_i)$$

$$= \left(\frac{z_i}{\lambda}\right)^{-2/3}, \text{ in the inertial subrange}$$

where β_1, the inertial subrange spectral constant is taken to be 0.8 following Kaimal et al., (1972). ψ_θ is the nondimensionalized potential temperature variance dissipation rate, $(\varepsilon_\theta^{-1/3} z_i^{2/3}/(\theta_*^2))$. F_θ is a nondimensional empirical function of nondimensionalized wavelength and nondimensionalized height. A similar scaling could be applied to any scalar spectra. Figure 4.2 shows the effect of this normalization on the θ spectra of 15 horizontal legs flown within the middle of the CBL. As with w, the normalization reduces the scatter by accounting for the effects of variations in boundary layer depth and turbulence intensity. This method of normalization will be used on the potential temperature spectra calculated from the Phoenix aircraft data. An analogous method is used to normalize humidity mixing ratio spectra. The results will be presented in the next subchapter.

In order to derive universal forms for the nondimensionalized microscale spectra, it is necessary to combine spectra from a number of flight legs. This is required because of the randomness in the spectral estimates which can be relatively large toward the long wavelength end of the spectra. Generally this combining of spectra is done separately for each of several ranges of $z_{\star}$. The ranges of $z_{\star}$ are selected such that spectra within each range vary little from one another. For the present study, the ranges $0.0 < z_{\star} < 0.2$, $0.2 < z_{\star} < 0.8$, and $0.8 < z_{\star} < 1.2$ were selected to include the surface layer, the mixed layer and the entrainment layer respectively.

Spectra are commonly smoothed by eye. Envelopes for each of the ranges of $z_{\star}$ are then fit by eye to the ensemble of smoothed spectra (e.g., Kaimal et al., 1976). A more objective method of combining similar spectra is bin averaging. For each predefined wavelength bin, a single average wavelength, spectral density pair, $(\lambda, S(\lambda))$, is computed from all of the pairs whose wavelengths fall within that bin. The resulting average spectra are smooth estimates of the true spectra if enough sample spectra are included in the average. This averaging method was used on the Phoenix aircraft data spectra and yielded average spectra which were centered within the cluster of sample spectra. The bin averaged spectra cover a wavelength band from 0.008 to 200.0 z_i. These results will be presented in the next subchapter.

4.3 Convective Boundary Layer Turbulence Spectra from Phoenix Aircraft Data

The CBL turbulence spectra prepared using the methods described in the previous subchapter are presented below. Spectra for vertical velocity, horizontal wind speed, potential temperature and humidity

mixing ratio were calculated for the subset of the Phoenix horizontal flight legs listed in Table 4.1. These legs were selected to span the available days and the times of day when the CBL was active.

The measured spectra fall into three categories. Those at low enough z_* to be strongly affected by the surface, those at high enough z_* to be strongly affected by entrainment and those within the middle of the CBL which are not strongly affected by either. These regions correspond to $0.1 < z_* < 0.2$, $0.2 < z_* < 0.8$, and $0.8 < z_* < 1.2$ for the relatively calm and unstable days sampled in Phoenix. There are no spectra for levels below $0.1\ z_*$ because the aircraft could not be flown at such low levels over the populated neighborhood of the BAO. The measured spectra will be presented in three formats for each of these z_* regions. The bin averaged spectra will be presented as estimates of the universal spectral form for these regions. Superimposed on these bin averaged spectra will be scatter plots which include all the spectral data from which they were derived. These plots will provide information about the degree and type of scatter of the data about the mean. These data will be plotted on a log-log scale to facilitate the detection of power laws and subsequent analysis of turbulence dynamics. In addition, the bin averaged spectra will be presented in a log-linear format for which area is proportional to variance. This format is particularly well suited for analyzing the contributions of various wavelength bands to the total variance.

The vertical velocity spectra are shown in Figures 4.3 through 4.8. The scatter of the individual points around the bin averaged spectral curves is a result of both the lack of smoothness of the individual spectra and of variations between the individual spectra.

Table 4.1 Subset of Phoenix Horizontal Flight Legs for which Spectra were Computed

Date	Time	z_*	Aircraft
90578	1058	0.954	304
90578	1107	0.474	304
90578	1116	0.455	304
92178	1114	1.081	306
92178	1122	1.008	306
92178	1130	0.63	306
92178	1139	0.6	306
92178	1148	0.213	306
92178	1157	0.203	306
92178	1508	0.541	306
92178	1509	1.136	304
92178	1518	1.122	304
92178	1518	0.533	306
92178	1526	0.144	306
92718	1527	0.819	304
92178	1536	0.805	304
92178	1536	0.142	306
92278	1409	1.005	306
92278	1416	0.736	306
92278	1423	0.458	306
92278	1430	0.199	306
92278	1438	0.124	306
92678	1037	1.031	306
92678	1046	0.59	306
92678	1053	0.42	306
92678	1102	0.31	306
92778	1416	1.043	306
92778	1424	0.768	306
92778	1432	0.566	306
92778	1441	0.173	306

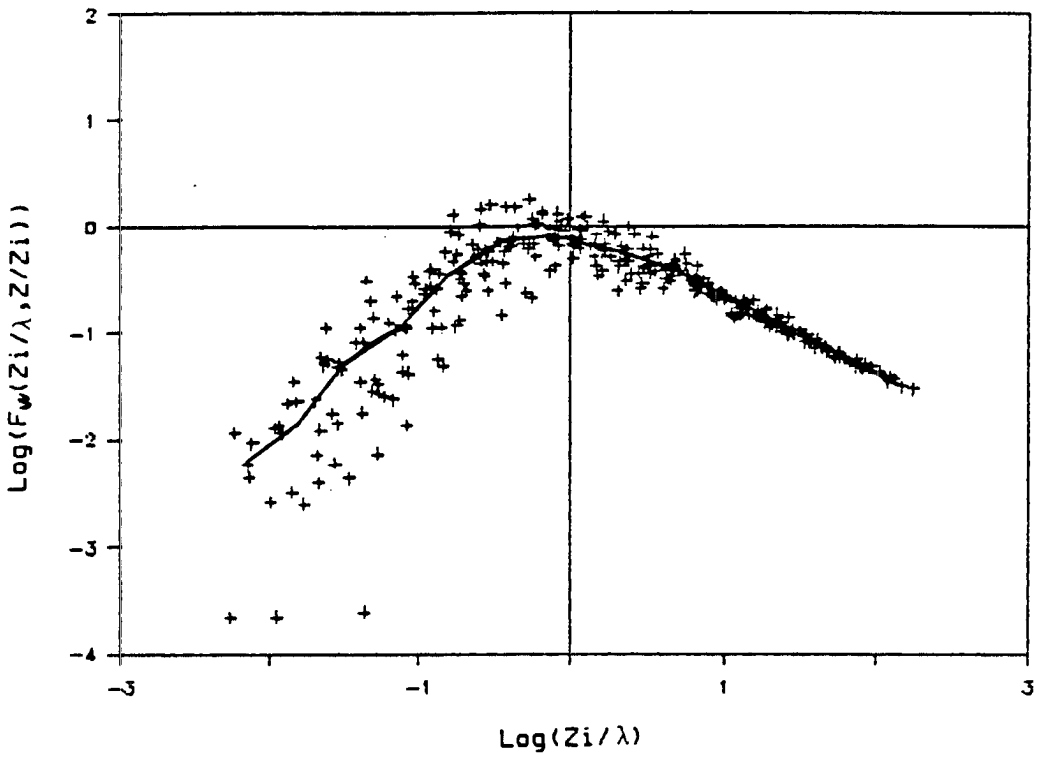

Fig. 4.3 Normalized vertical velocity spectra for the mid CBL layer with z_* from 0.2 to 0.8. The individual spectra are plotted as crosses while the bin averaged spectra is plotted as a solid line. Both axis have logarithmic scales.

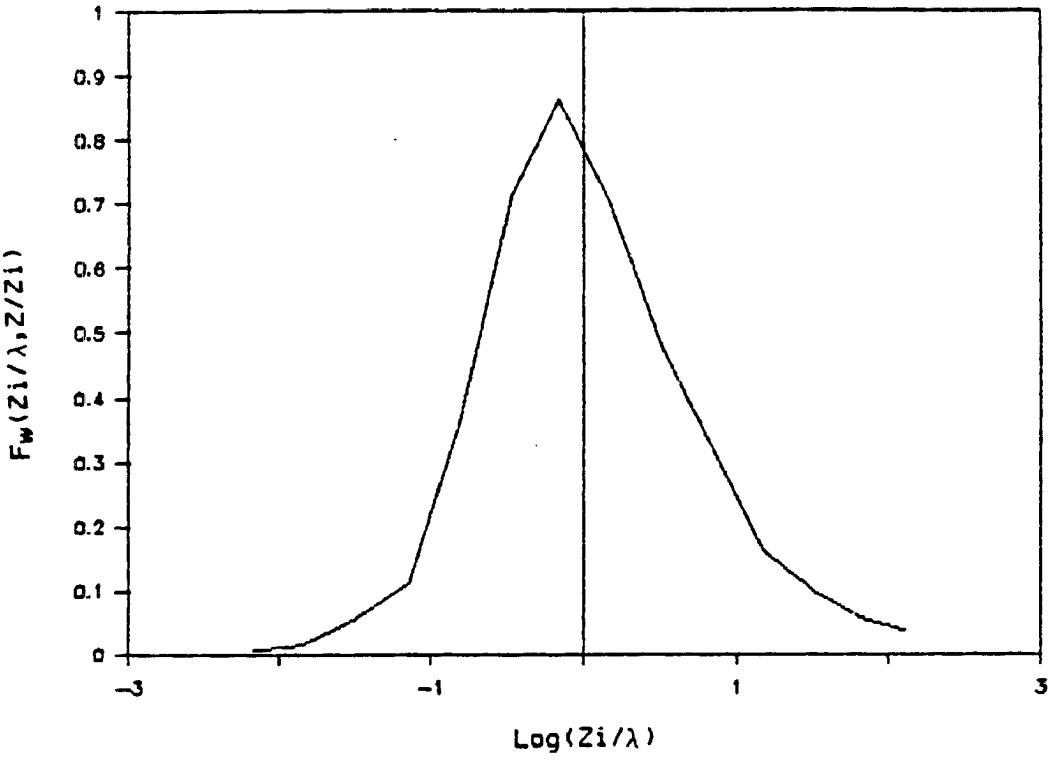

Fig. 4.4 Bin averaged vertical velocity spectra for the mid CBL layer with z_* from 0.2 to 0.8. The scale on the horizontal axis is logarithmic while that on the vertical axis is linear. Area is proportional to variance.

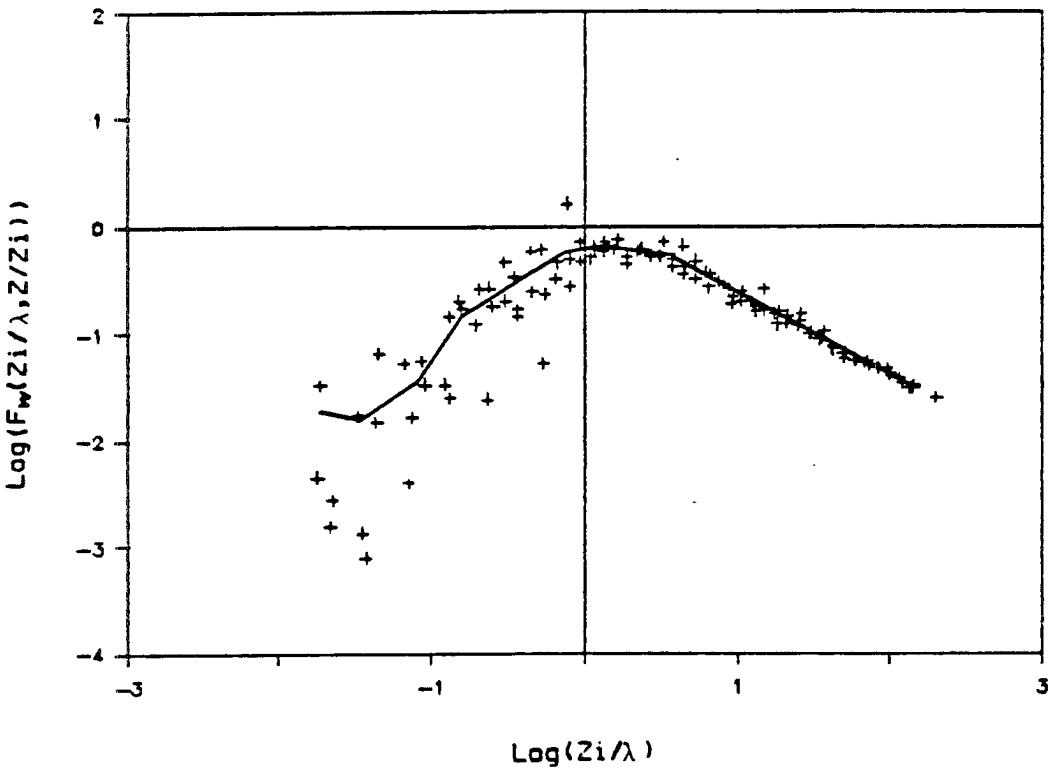

Fig. 4.5 Normalized vertical velocity spectra for the lower CBL layer with $z_{\hat{}}$ from 0.1 to 0.2. The individual spectra are plotted as crosses while the bin averaged spectra is plotted as a solid line. Both axis have logarithmic scales.

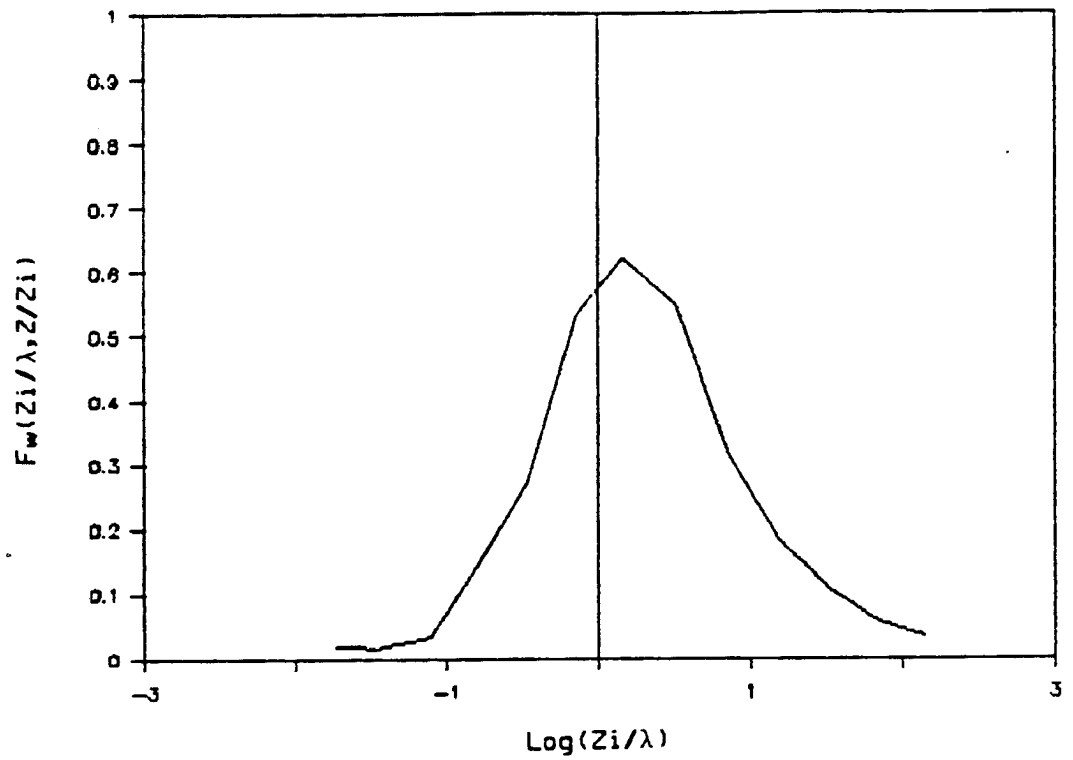

Fig. 4.6 Bin averaged vertical velocity spectra for the lower CBL layer with z_* from 0.1 to 0.2. The scale on the horizontal axis is logarithmic while that on the vertical axis is linear. Area is proportional to variance.

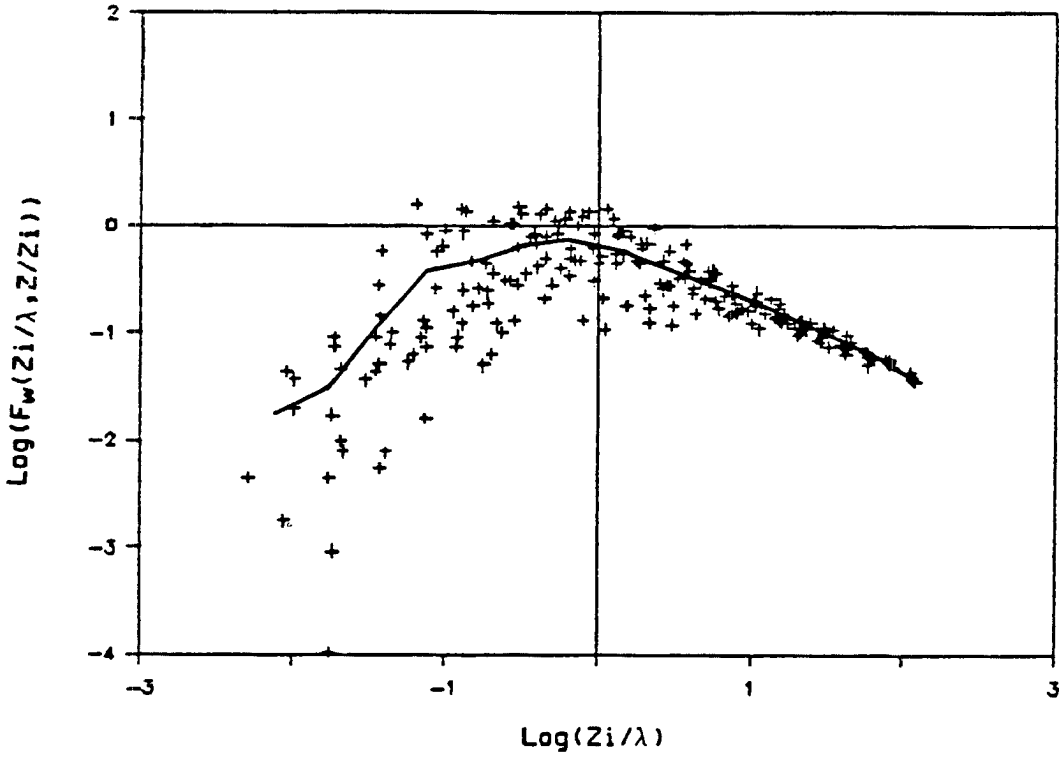

Fig. 4.7 Normalized vertical velocity spectra for the entrainment layer with z_* from 0.8 to 1.2. The individual spectra are plotted as crosses while the bin averaged spectra is plotted as a solid line. Both axis have logarithmic scales.

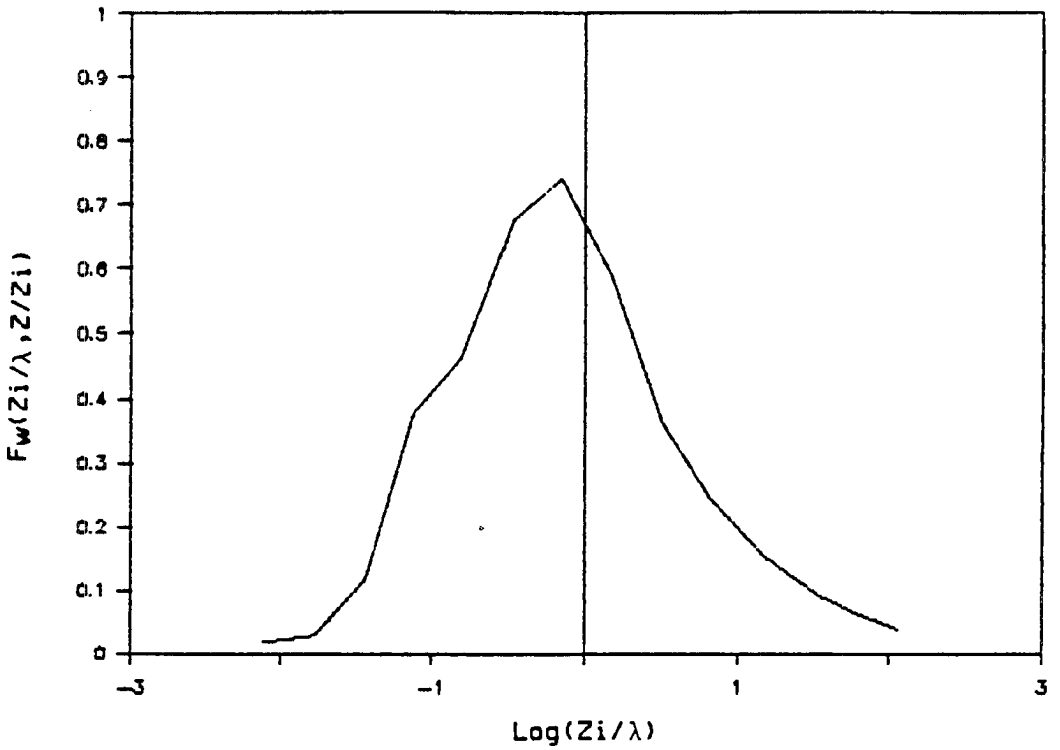

Fig. 4.8 Bin averaged vertical velocity spectra for the entrainment layer with z_* from 0.8 to 1.2. The scale on the horizontal axis is logarithmic while that on the vertical axis is linear. Area is proportional to variance.

Figure 4.3 shows the vertical velocity spectra for the mid CBL layer from 0.2 to 0.8 z_*. Scatter is quite small in the inertial subrange and moderate at longer wavelengths. No systematic variation with z_* is apparent in this layer.

Theory by Kolmogorov suggests the existence of a spectral slope of -2/3 within the inertial subrange (Kaimal et al. 1972). Figure 4.3 shows that such a slope exists for wavelengths less then 0.1 z_i. This slope changes smoothly in the wavelength range form 0.1 to 1.0 z_i where the transition from the inertial energy cascade subrange to the microscale energy production subrange occurs.

The spectral peak corresponding to the microscale energy production subrange is rather broad and occurs at wavelengths of about 1.5 z_i. Spectral power decreases steadily from wavelengths of 3.0 z_i up to the maximum wavelength sampled, 200.0 z_i. The spectral slope for wavelengths between 10.0 and 100.0 z_i is approximately 5/4. The smallness of the the mesoscale contribution to the vertical velocity variance can be attributed to the limitations imposed on the long wavelength vertical velocity variance by the shallowness of the atmosphere (Charney, 1948). Figure 4.4 is also a graph of the vertical velocity spectrum for the layer for 0.2 to 0.8 z_*. However, this figure uses log-linear coordinates so that the area under the spectral curve within a given wavelength band is proportional to the variance contributed by that wavelength band. Most of the vertical velocity variance occurs at wavelengths between 0.1 and 10.0 z_i.

Figure 4.5 is a graph of the vertical velocity spectra in the layer from 0.1 to 0.2 z_i which is strongly affected by the surface. The scatter of the individual spectral estimates about the averaged

spectra is no greater in this layer than in the mid levels of the CBL. This is because the aircraft did not descend into the surface layer where mixed layer scaling fails. The most obvious difference between the lower CBL and mid CBL vertical velocity spectra is the shift in the microscale spectral peak to shorter wavelengths for the lower altitude spectra. This shift has been observed in previous studies including those of Kaimal et al. (1972) and Kaimal et al. (1976). For this average, composed of spectra from 0.1 to 0.2 z_i only, the transition to the -2/3 slope of the inertial subrange occurs by a wavelength of about 0.1 z_i in the lower CBL as it did in the mid CBL. The normalization scheme used results in the inertial subrange vertical velocity spectra collapsing onto a single curve for both the mid and lower CBL. The spectral slope at wavelengths significantly greater then that of the microscale spectral peak is also similar for the two layers. However, because of the shift in wavelengths of the spectral peak the variance contributed by these longer wavelengths is less for the lower levels as can be seen from Figures 4.6 and 4.4.

Kaimal et al. (1976) computed very similar vertical velocity spectral forms for these two CBL layers from tethered balloon data taken during the Minnesota experiment. However, their spectra did not extend to such long wavelengths and had shallower slopes near their long wavelength extremities. This difference in slope may be related to a failure of Taylor's hypothesis for long wavelengths which would result in fixed and moving platforms sampling differently. Taylors hypothesis is that eddies do not have time to evolve significantly as they drift past a fixed point. If true, this hypothesis permits the conversion of a time series to a space series or of frequencies to

wavelengths as Kaimal et al. (1976) did. If, however, the wind speeds are light there may be sufficient time for the largest eddies to evolve as they drift past a fixed point. Thus, in light winds, a data series from a fixed point will reflect the temporal, rather then, the spacial variability of the larger eddies. This may be one reason for the discrepancy between surface temperature fluxes derived form the BAO tower and the NCAR aircraft reported in Chapter 3. The Phoenix data were taken under conditions of light winds when the advective time scale for the large eddies, $z_i/\bar{U}$, was similar to the time scale for the evolution of large eddies, z_i/w_*. Under these circumstances, measurements at a single point represent a sample of the local rather then the regional temperature flux because the large eddies have time to eveolve to fit local forcing as they are advected along.

There are other possible explanations for this difference. Typical wind speeds were higher during the Minnesota experiment than during the Phoenix experiment. The wind speeds during the Minnesota experiment were typically high enough for longitudinal rolls to dominate the convective field while during the Phoenix experiment the wind speeds were low enough for three dimensional thermals to dominate the convective field. Sampling along the wind direction and, thus, nearly along the axis of the longitudinal rolls would have resulted in the observation of more long wavelength variance. There has yet to be a theoretical prediction of spectral slope in this wavelength band.

Vertical velocity spectra for the entrainment layer of z_* from 0.8 to 1.2 are presented in Figure 4.7. The scatter for this layer is significantly greater than for the lower layers. This is to be

expected in a layer where stability changes rapidly and gravity waves can compete with convective elements for turbulence energy. The entrainment layer and the mid CBL vertical velocity spectra collapse onto a single curve in the inertial subrange and have a very similar form in the region of the microscale spectral peak. However, the entrainment layer has more variance at wavelengths longer than the spectral peak. This could be a result of the presence of gravity waves in the stably stratified air at these levels. The Ashchurch results (Caughey and Palmer, 1979) match these in that the vertical velocity inertial subrange spectral slope remains -5/3 in the entrainment layer. However, for Ashchurch, the wavelength of the microscale spectra peak of vertical velocity decreased sharply near z_i. This result is not matched for the Phoenix data set described above. This implies that proximity to the capping inversion was less of a constraint on eddy size for the Phoenix data set than for the Ashchurch data set. If the capping inversion acted as a more rigid surface at Ashchurch than at the BAO site this observation would be explained. This is quite possible because the capping inversions observed during Phoenix were often quite weak.

Figure 4.8 shows that despite the extra long wavelength variance most of the vertical velocity variance is still contributed by wavelengths between 0.1 and 10.0 z_i.

Figures 4.9 through 4.14 show the horizontal wind speed spectra. There are important differences and similarities between these spectra and their counterparts for vertical velocity. These will be described below as will the height related differences in spectral form for horizontal wind speed.

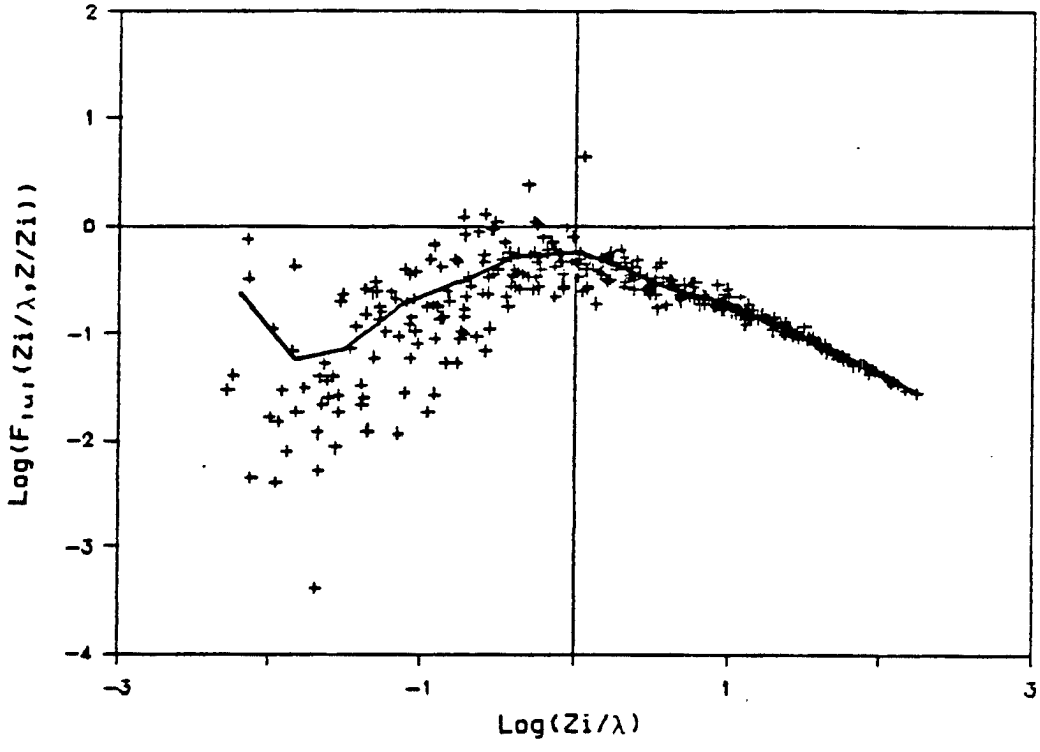

Fig. 4.9 Normalized horizontal wind speed spectra for the mid CBL layer with $z_{\star}$ from 0.2 to 0.8. The individual spectra are plotted as crosses while the bin averaged spectra is plotted as a solid line. Both axis have logarithmic scales.

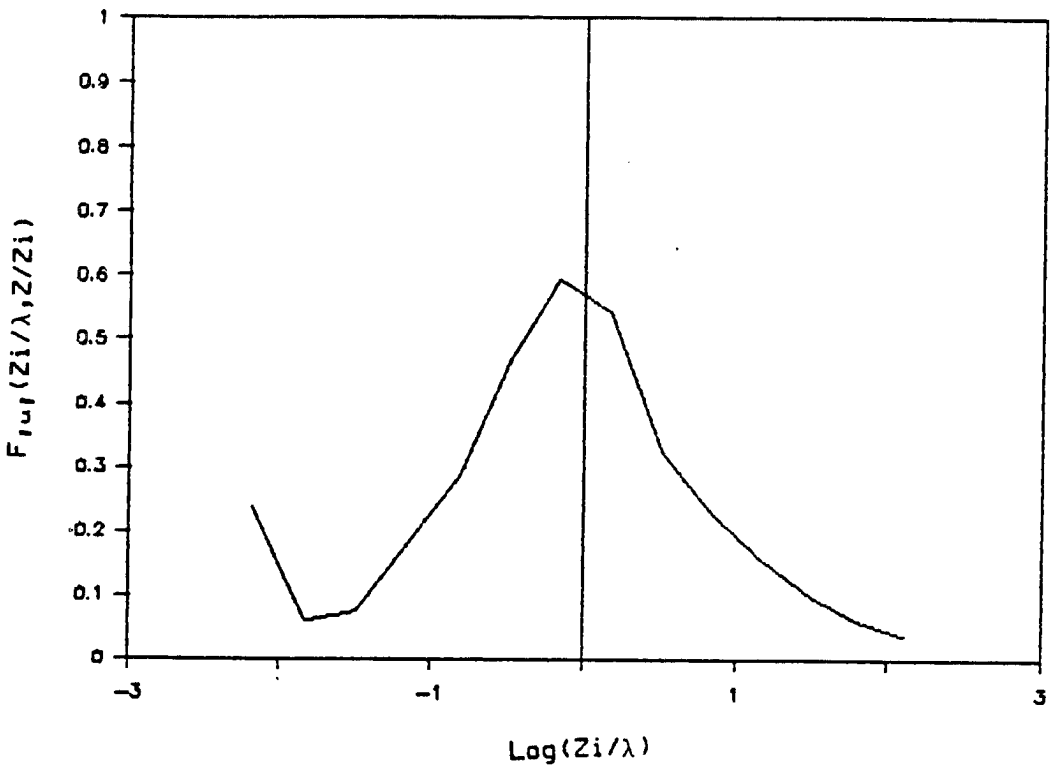

Fig. 4.10 Bin averaged horizontal wind speed spectra for the mid CBL layer with z_* from 0.2 to 0.8. The scale on the horizontal axis is logarithmic while that on the vertical axis is linear. Area is proportional to variance.

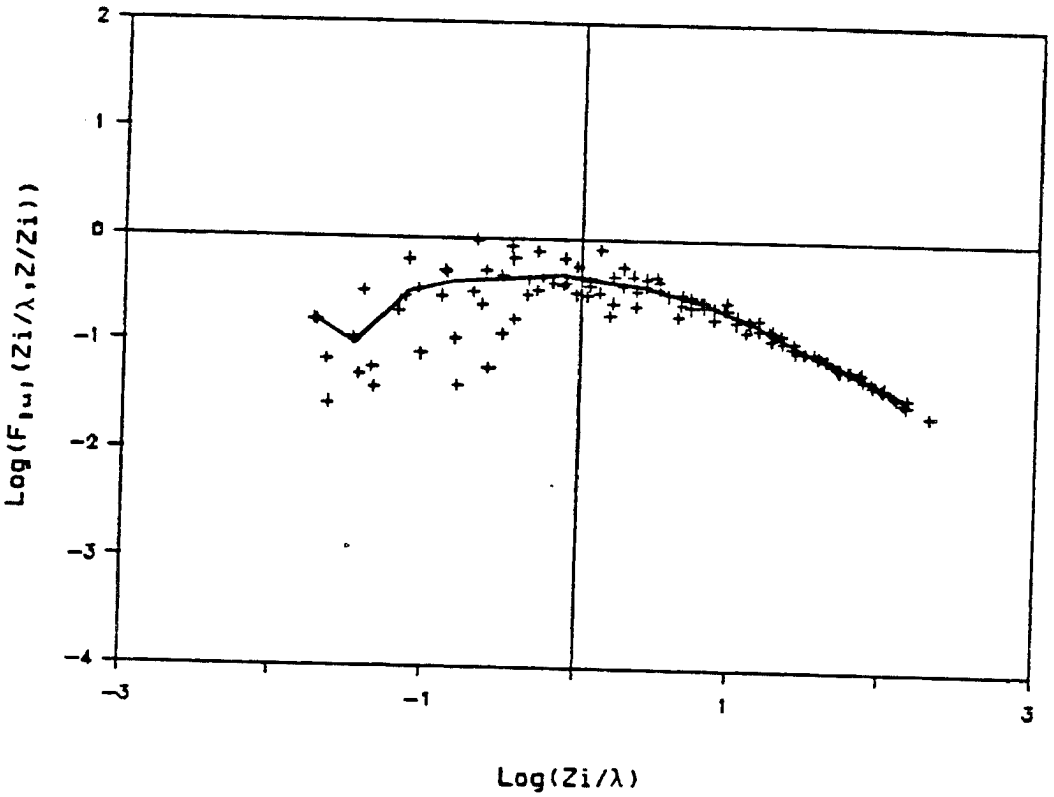

Fig. 4.11 Normalized horizontal wind speed spectra for the lower CBL layer with z_* from 0.1 to 0.2. The individual spectra are plotted as crosses while the bin averaged spectra is plotted as a solid line. Both axis have logarithmic scales.

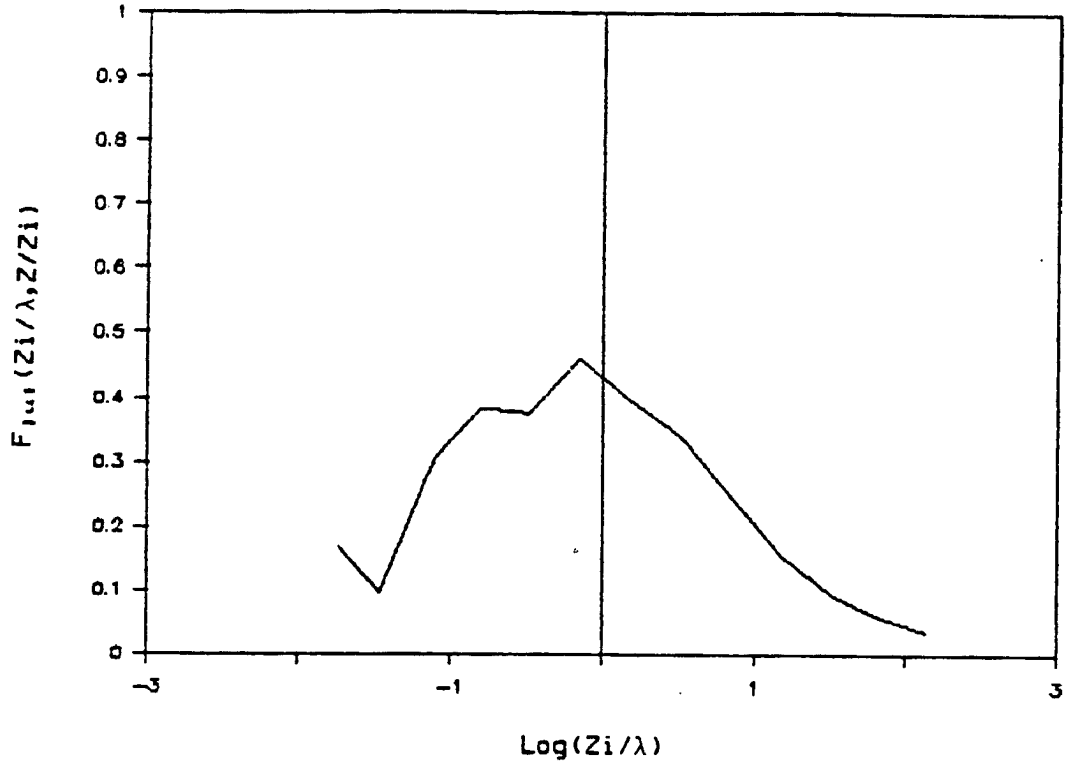

Fig. 4.12 Bin averaged horizontal wind speed spectra for the lower CBL layer with z_* from 0.1 to 0.2. The scale on the horizontal axis is logarithmic while that on the vertical axis is linear. Area is proportional to variance.

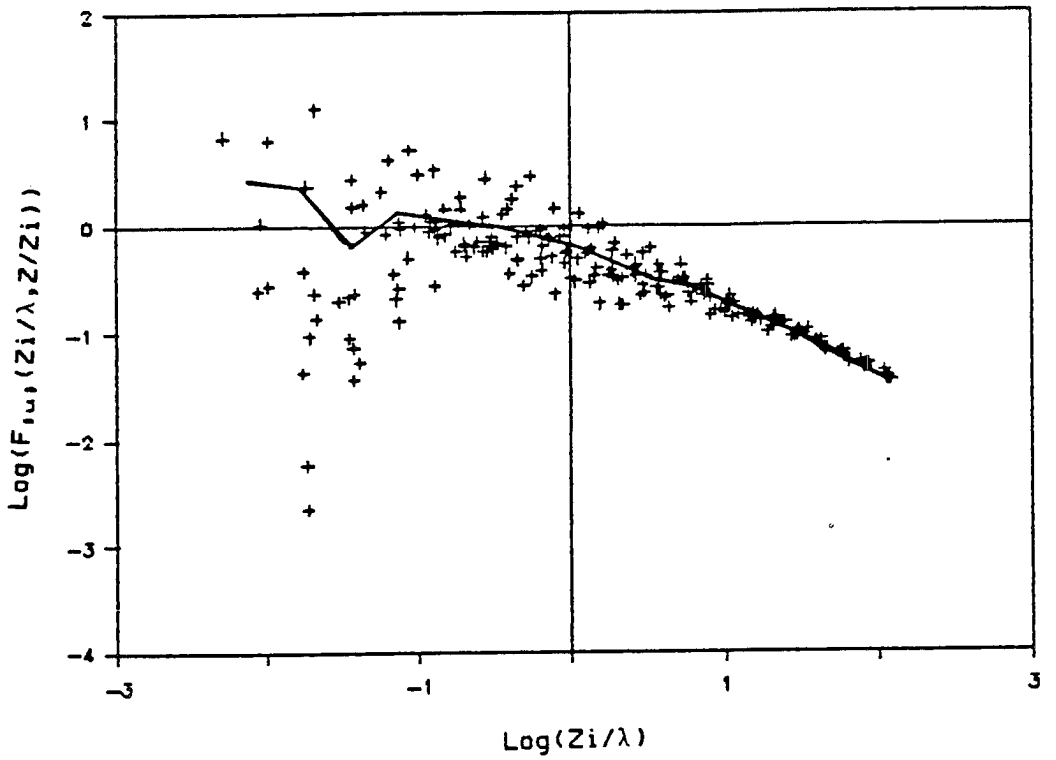

Fig. 4.13 Normalized horizontal wind speed spectra for the entrainment layer with $z_{\star}$ from 0.8 to 1.2. The individual spectra are plotted as crosses while the bin averaged spectra is plotted as a solid line. Both axis have logarithmic scales.

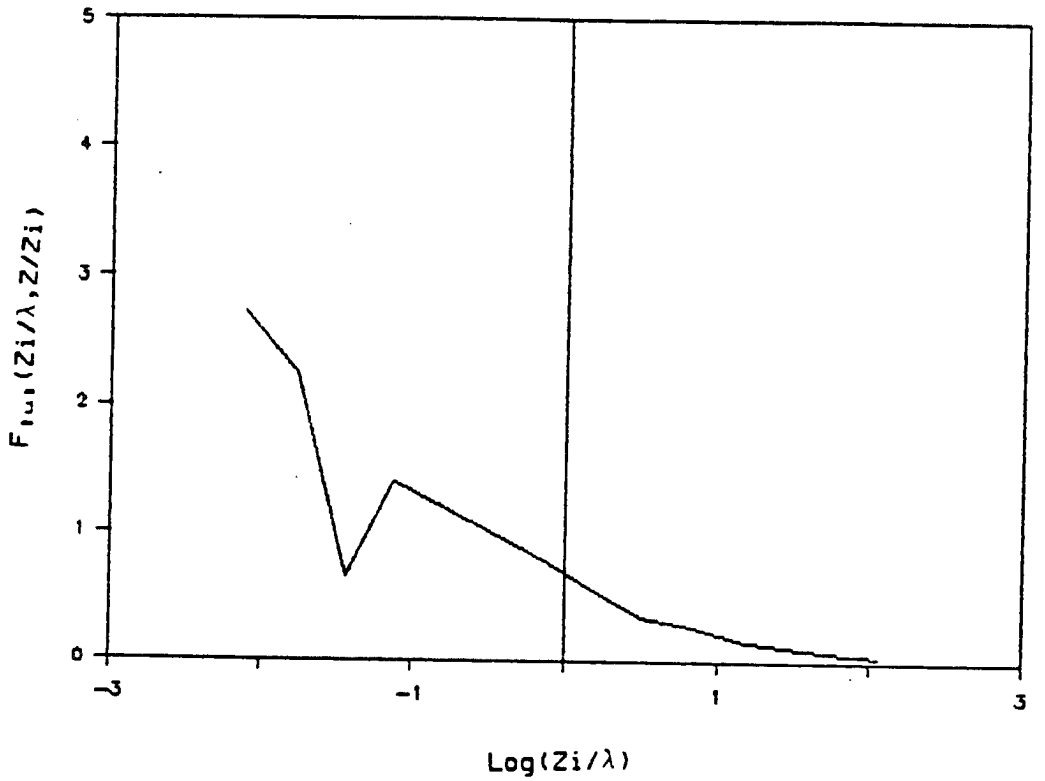

Fig. 4.14 Bin averaged horizontal wind speed spectra for the entrainment layer with $z_{\star}$ from 0.8 to 1.2. The scale on the horizontal axis is logarithmic while that on the vertical axis is linear. Area is proportional to variance.

The horizontal wind speed spectra for the mid CBL layer of z_* from 0.2 to 0.8 is shown in Figure 4.9. Scatter is relatively small in the inertial energy cascade subrange and the microscale energy production subrange. However, it becomes considerably greater at wavelengths longer then that of the microscale spectral peak.

The inertial subrange is identical to that shown in Figure 4.3 for the corresponding vertical velocity spectra. This is to be expected from the isotropy of the inertial subrange turbulence. The inertial subrange extends up to a wavelength of 0.1 z_i above which a gradual transition to the microscale spectral peak occurs. This spectral peak is at a wavelength of about 1.5 z_i as is that for the corresponding vertical velocity spectra. However, it is slightly lower and more rounded then that for vertical velocity.

The spectral slope at wavelengths between 10.0 and 50.0 z_i is shallower than it is for vertical velocity, 4/5 rather then 5/4. At wavelengths longer then 70.0 z_i there is an increase in horizontal wind speed variance as the mesoscale subrange is entered. This increase is a reflection of the enstrophy cascade from the larger scale sources. There is large scatter in the spectral gap and mesoscale subranges because the mixed layer scaling used is not appropriate for these long wavelengths. The location of the spectral gap varies between individual spectra because of the leg to leg changes in the ratio of microscale to mesoscale variance contributions. This effect combined with the limited length of the flight legs and the lack of a scaling system appropriate to the spectral gap and mesoscale subranges of the spectra result in the large scatter observed. Despite these limitations, the data document

the existence of a spectral gap between the microscale and larger scale energy sources. This gap occurs in the 10 to 100 z_i wavelength range.

Smedman-Hogstrom and Hogstrom (1975) observed similar behavior of the spectral gap for horizontal wind speed in a surface layer experiment at Marsta Sweden. As with vertical velocity, most of the microscale horizontal wind variance in the mid CBL is in the 0.1 to 10.0 z_i wavelength range. This can be seen in Figure 4.10.

Figure 4.11 shows the horizontal wind speed spectra for the lower CBL layer of z_* for 0.1 to 0.2. These spectra collapse onto the universal curve in the inertial subrange but exhibit a much broader microscale spectral peak than do the mid CBL horizontal wind speed spectra. The center of this peak is at a wavelength of about 1.5 z_i showing that height above the ground does not produce the limiting effect on horizontal wind speed that it does on vertical velocity. This observation is in agreement with those of Kaimal et al. (1976) and Donelan and Miyake (1973).

The lower CBL horizontal wind speed spectra have a spectral gap in the 10.0 to 100.0 z_i range as did the mid CBL spectra. Figure 4.12 shows that again most of the microscale variance is contributed by wavelengths between 0.1 and 10.0 z_i.

Figure 4.13 depicts the horizontal wind speed spectra for the entrainment layer of z_* from 0.8 to 1.2. The inertial subrange again collapses onto a universal curve but for this layer the transition extends over a much broader wavelength band reaching the microscale spectral peak at a wavelength of about 15 z_i. Thus, there is a considerably greater shift in the microscale spectral peak location

between the mid CBL and the entrainment layer for horizontal wind speed than there is for vertical velocity. This shift in the location of the microscale spectral peak to longer wavelengths could be caused by gravity waves, the merger of the outflow of a number of microscale updrafts or by the aircraft passing through undulations in the capping inversion. The latter explanation would be plausible if the inversion height varied by about 0.1 z_i on a horizontal scale of about 15.0 z_i. This is quite likely the case in the rolling terrain around the BAO. Thus, the shift in the location of the horizontal wind speed microscale spectral peak to longer wavelength as z_i is approached may be a result of either the instrument platform used or the CBL motions themselves.

Figure 4.14 shows that the wavelengths longer than 10.0 z_i make a significant contribution to the horizontal wind speed variance in the entrainment layer. This contribution comes from two sources, mesoscale sources at wavelengths just longer than the spectral gap and microscale sources at wavelengths just shorter than the spectral gap. The individual entrainment layer spectra exhibit very deep and narrow spectral gaps. It is the variation in the location of these gaps from leg to leg which results in smoothness of the gap in the bin averaged spectra.

Figure 4.15 through 4.20 show the Phoenix aircraft potential temperature spectra. The spectral forms for potential temperature have much in common with those for horizontal wind speed. Figure 4.15 shows the potential temperature spectra for the mid CBL layer of z_* from 0.2 to 0.8. The extreme short wavelength end of the spectra is contaminated by instrument noise as the limits of instrument response

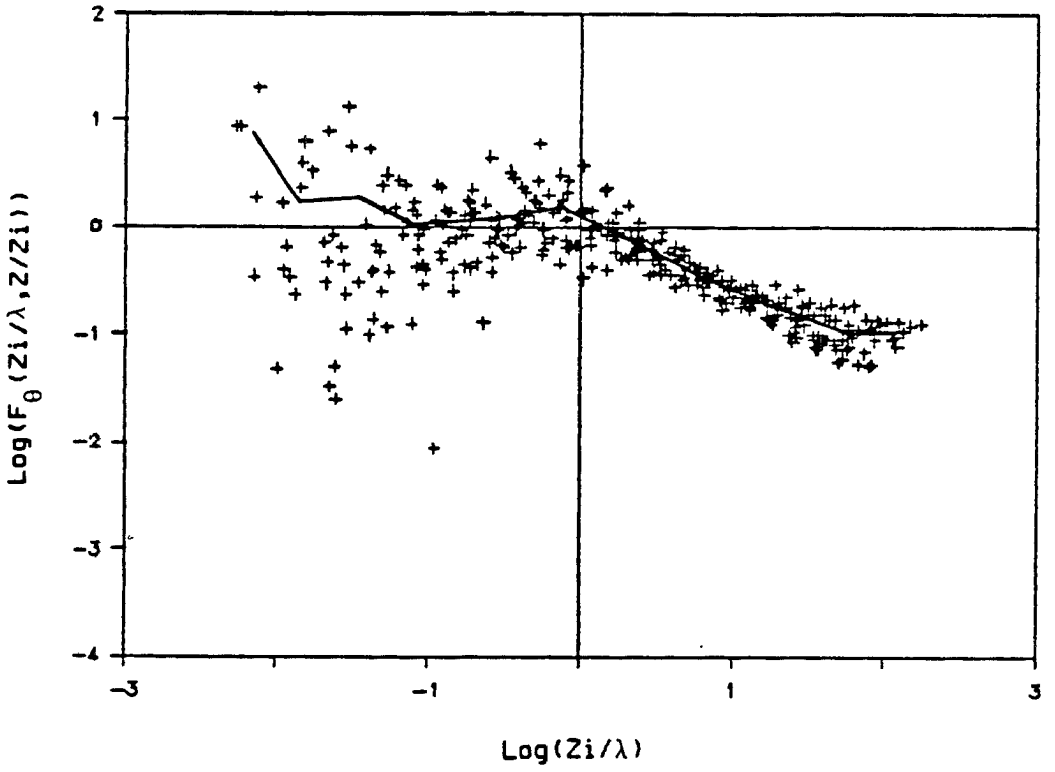

Fig. 4.15 Normalized potential temperature spectra for the mid CBL layer with z_* from 0.2 to 0.8. The individual spectra are plotted as crosses while the bin averaged spectra is plotted as a solid line. Both axis have logarithmic scales.

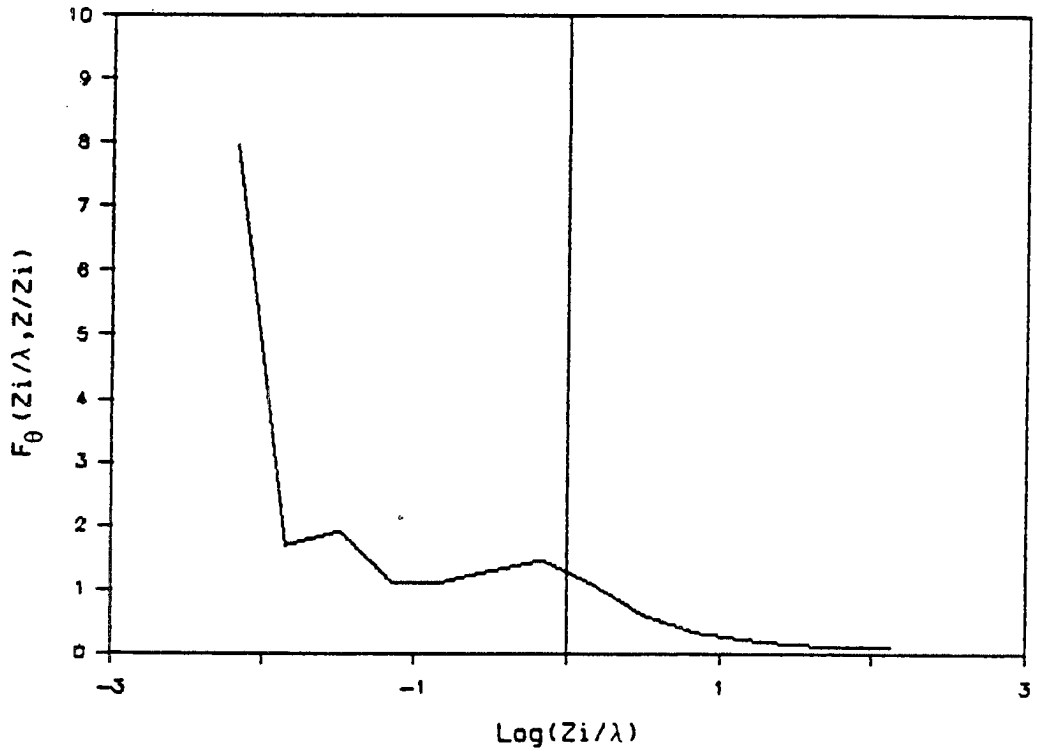

Fig. 4.16 Bin averaged potential temperature spectra for the mid CBL layer with z_* from 0.2 to 0.8. The scale on the horizontal axis is logarithmic while that on the vertical axis is linear. Area is proportional to variance.

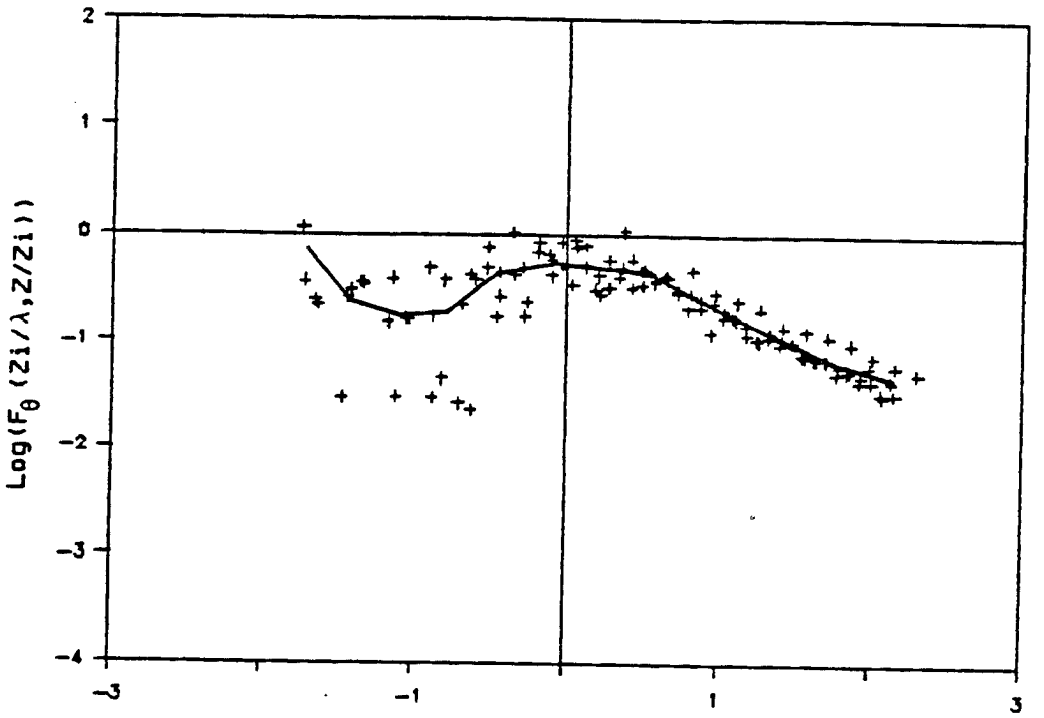

Fig. 4.17 Normalized potential temperature spectra for the lower CBL layer with z_* from 0.1 to 0.2. The individual spectra are plotted as crosses while the bin averaged spectra is plotted as a solid line. Both axis have logarithmic scales.

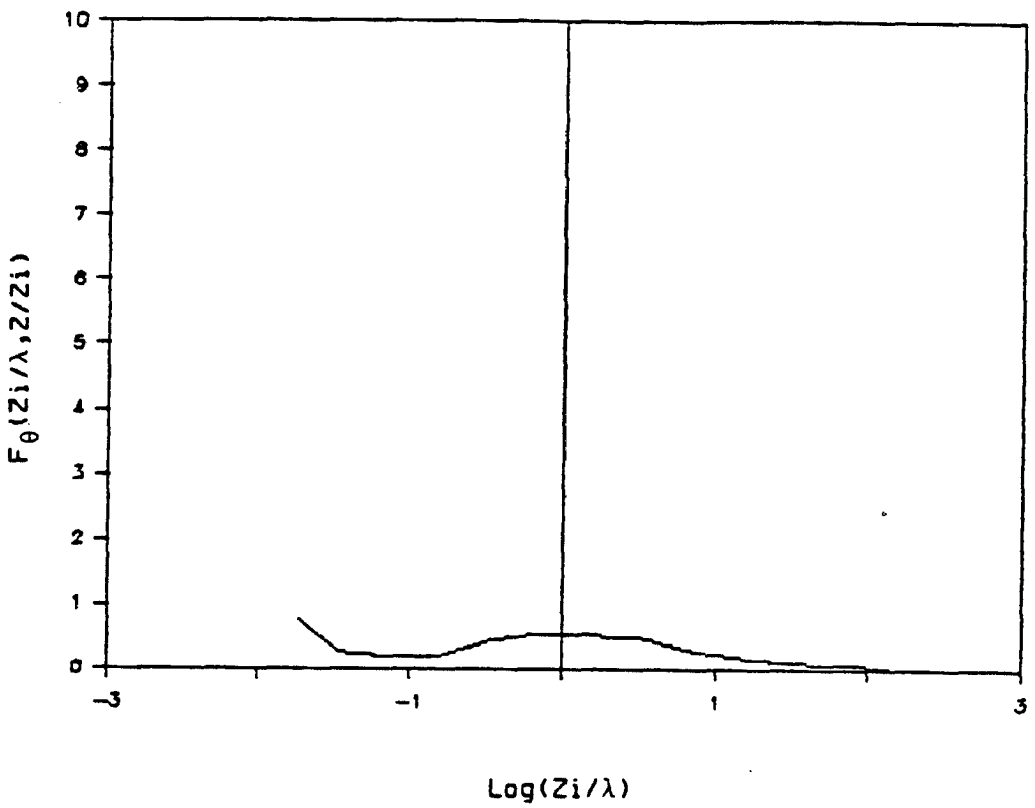

Fig. 4.18 Bin averaged potential temperature spectra for the lower CBL layer with z_* from 0.1 to 0.2. The scale on the horizontal axis is logarithmic while that on the vertical axis is linear. Area is proportional to variance.

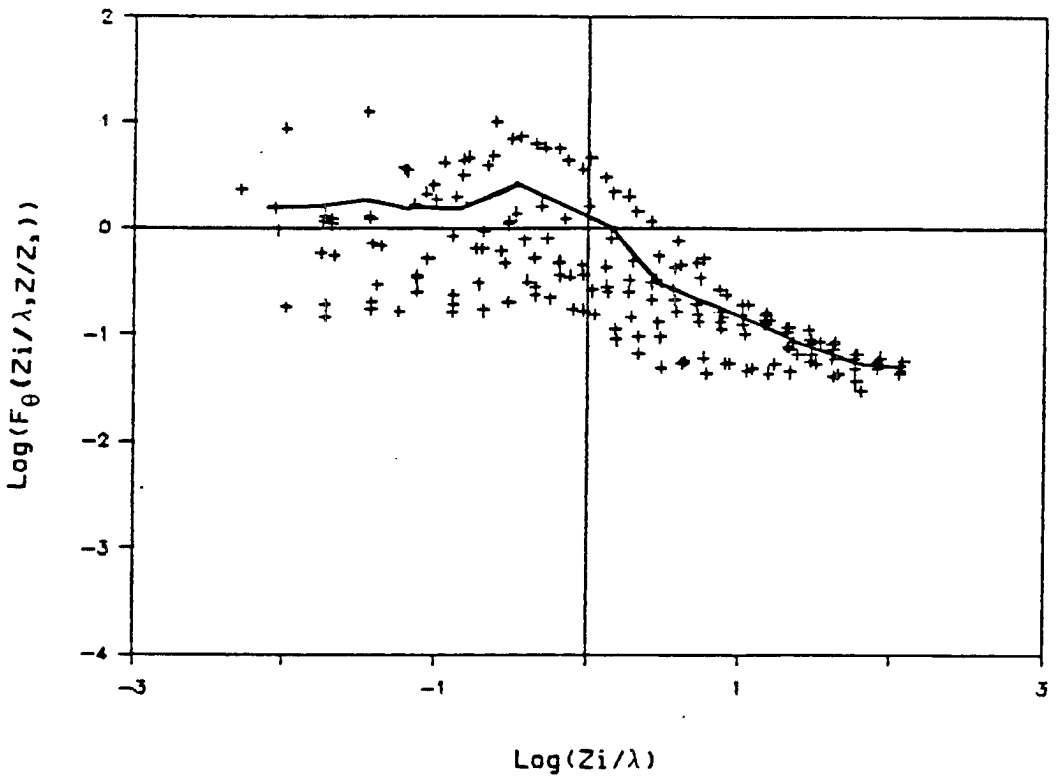

Fig. 4.19 Normalized potential temperature spectra for the entrainment layer with z_* from 0.8 to 1.2. The individual spectra are plotted as crosses while the bin averaged spectra is plotted as a solid line. Both axis have logarithmic scales.

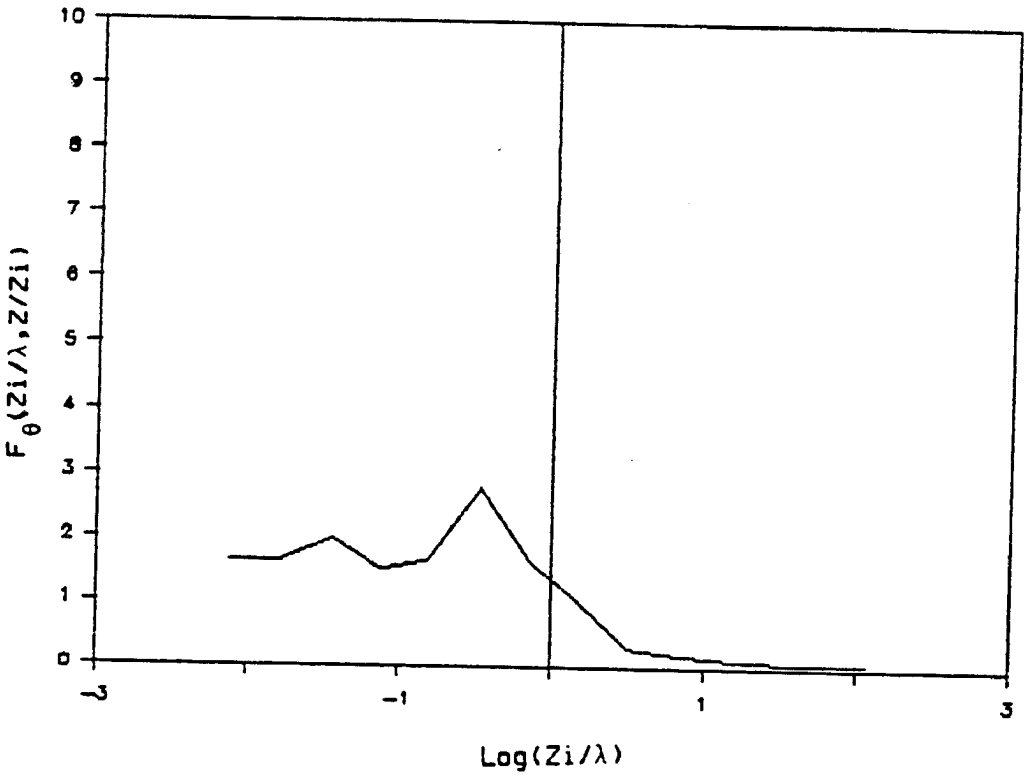

Fig. 4.20 Bin averaged potential temperature spectra for the entrainment layer with z_* from 0.8 to 1.2. The scale on the horizontal axis is logarithmic while that on the vertical axis is linear. Area is proportional to variance.

is reached. The remainder of the inertial subrange is well measured, however, and collapses onto one curve. Scatter becomes large at wavelengths longer than that for the spectral peak. The bin average spectra follows the center of the data cluster despite the scatter. The -2/3 slope of the inertial subrange extends to wavelengths greater the 0.1 z_i from which point the spectra curves smoothly into the microscale peak. This spectral peak occurs at a wavelength of about 1.5 z_i. The shape of this transition and spectral peak is similar to that found in the horizontal wind speed spectra. There is a wide shallow spectral gap in the wavelength band around 10.0 z_i. Beyond the spectral gap there is a steady increase in the spectral level into the mesoscale. The ratio of potential temperature variance to horizontal wind speed variance is observed to be much greater for the mesoscale then for the microscale. Therefore, the spectral gap between these two scales of motion occurs at a shorter wavelength for potential temperature than for horizontal wind speed. The spectral gap is shallower for potential temperature than for horizontal wind speed because the ratios of mesoscale to microscale spectral levels differ between the two variables while the locations of the peaks do not.

Figure 4.16 shows that while most of the microscale potential temperature variance is at wavelengths between 0.1 and 10.0 z_i there is considerable mesoscale potential temperature variance as well.

Figure 4.17 shows the potential temperature spectra for the lower CBL from 0.1 to 0.2 z_*. The inertial subrange is similar to that for the mid CBL potential temperature spectra. However, the microscale spectral peak occurs at a shorter wavelength which agrees with the

results of surface layer studies conducted by Donelan and Miyake (1973), Kaimal et al. (1972) and Kaimal et al. (1976). This shortening of the wavelength of the peak of the temperature spectra near the ground reflects the role of vertical velocity in producing temperature variance from the mean lapse rate and the shortening of the peak wavelength of the vertical velocity spectra near the ground. The ground proximity is the cause of the reduced eddy size of vertical circulations at lower levels.

The spectral gap is deeper as a result of this shift in location of the microscale spectral peak. The gap remains at a wavelength near 10.0 z_i as in the mid CBL.

Most of the microscale potential temperature variance in the lower CBL is contributed by wavelengths between 0.1 and 10.0 z_i. This can be seen in Figure 4.18.

Figure 4.19 shows the potential temperature spectra for the entrainment layer, z_* from 0.8 to 1.2. Although spectra for individual legs are quite smooth, there is considerable leg to leg varition between them. The variation is systematic with z_*. Potential temperature spectra at higher levels tend to have steeper slopes at small wavelengths because stable stratification provides an energy sink which acts throughout the inertial subrange. Caughey and Palmer (1979) observed this steepening of the spectral slopes in at short wavelengths above z_i for the Ashchurch experiment.

The peaks of the individual spectra are at wavelengths greater than 1.5 z_i. This could be the result of the same mechanisms which caused large peak wavelengths for the horizontal wind speed spectra of the entrainment layer. This could also be the result of preferential

damping of the shorter wavelengths by stable stratification. The spectral gap again occurs at wavelengths near 10.0 z_i with a significant mesoscale contribution to the potential tempeature variance. The vertical velocity variance is extremely small at these mesoscale wavelengths. Therefore these mesoscale wavelengths contribute little to the vertical fluxes despite the large horizontal wind speed and potential temperature variances there. This can be seen in Figure 4.20.

Figures 4.21 through 4.26 show the Phoenix aircraft humidity mixing ratio spectra. The mixing ratio spectra exhibit large differences between legs because of differences in the noise level. Spectra with more noise appear lower on the scatter plots of the Figure 4.8 as a result of the dissipation normalization. The analysis was repeated with only the least contaminated mixing ratio spectra included but this produced no major changes in the shapes of the bin averaged spectra. It must be borne in mind while studying these spectra that humidity is by far the least reliable of the variables measured at high frequency. Therefore, the resulting mixing ratio spectra can be considered only as approximations. The complete set of mixing ratio spectra are presented here.

Figure 4.21 shows the mixing ratio spectra for the mid CBL layer of z_* from 0.2 to 0.8. Scatter is large but the extreme lower points are all from two of the 15 spectra and do not effect the average spectral shape. The spectral slope at inertial subrange wavelengths is somewhat shallower than -2/3, probably because of the noise contamination. The microscale spectral peak is at a wavelength of about 7.0 z_i. This is a considerably longer peak wavelength then that

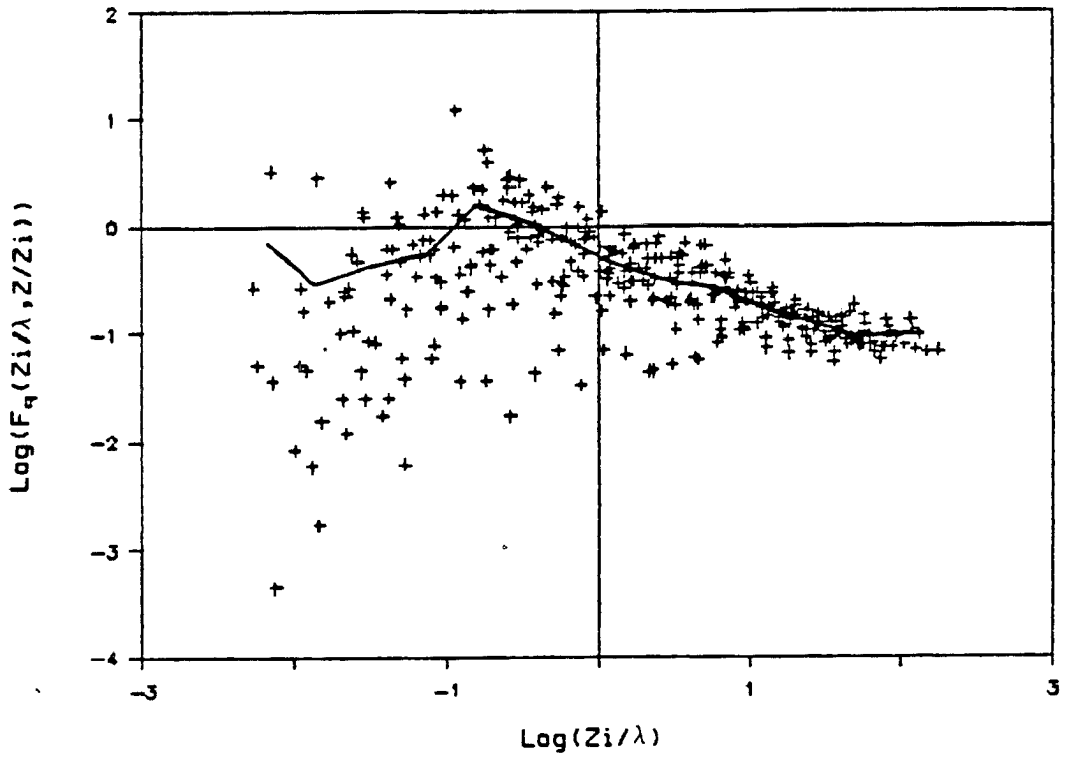

Fig. 4.21 Normalized humidity mixing ratio spectra for the mid CBL layer with z_* from 0.2 to 0.8. The individual spectra are plotted as crosses while the bin averaged spectra is plotted as a solid line. Both axis have logarithmic scales.

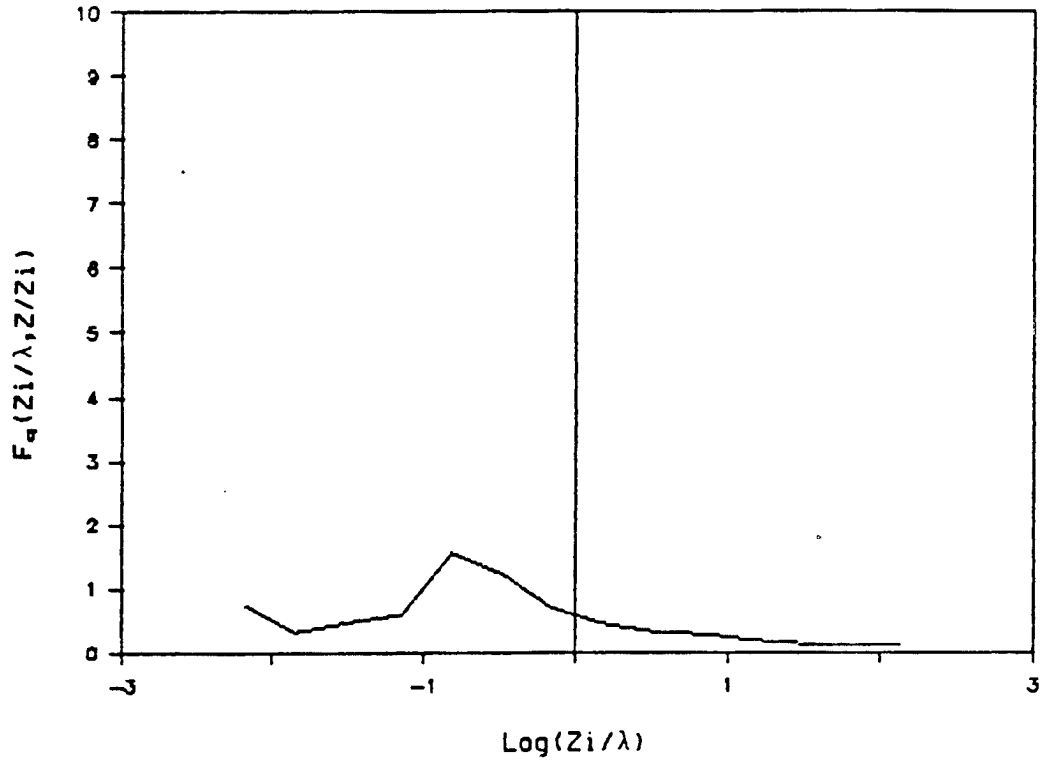

Fig. 4.22 Bin averaged humidity mixing ratio spectra for the mid CBL layer with z_* from 0.2 to 0.8. The scale on the horizontal axis is logarithmic while that on the vertical axis is linear. Area is proportional to variance.

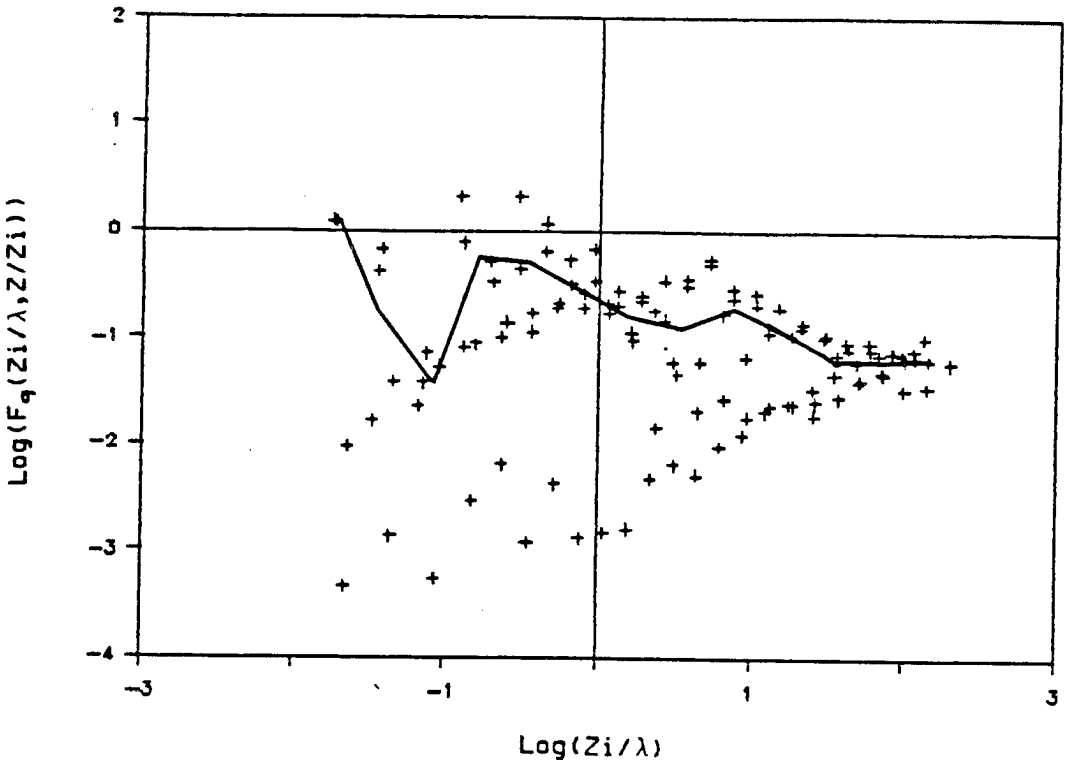

Fig. 4.23 Normalized humidity mixing ratio spectra for the lower CBL layer with z_* from 0.1 to 0.2. The individual spectra are plotted as crosses while the bin averaged spectra is plotted as a solid line. Both axis have logarithmic scales.

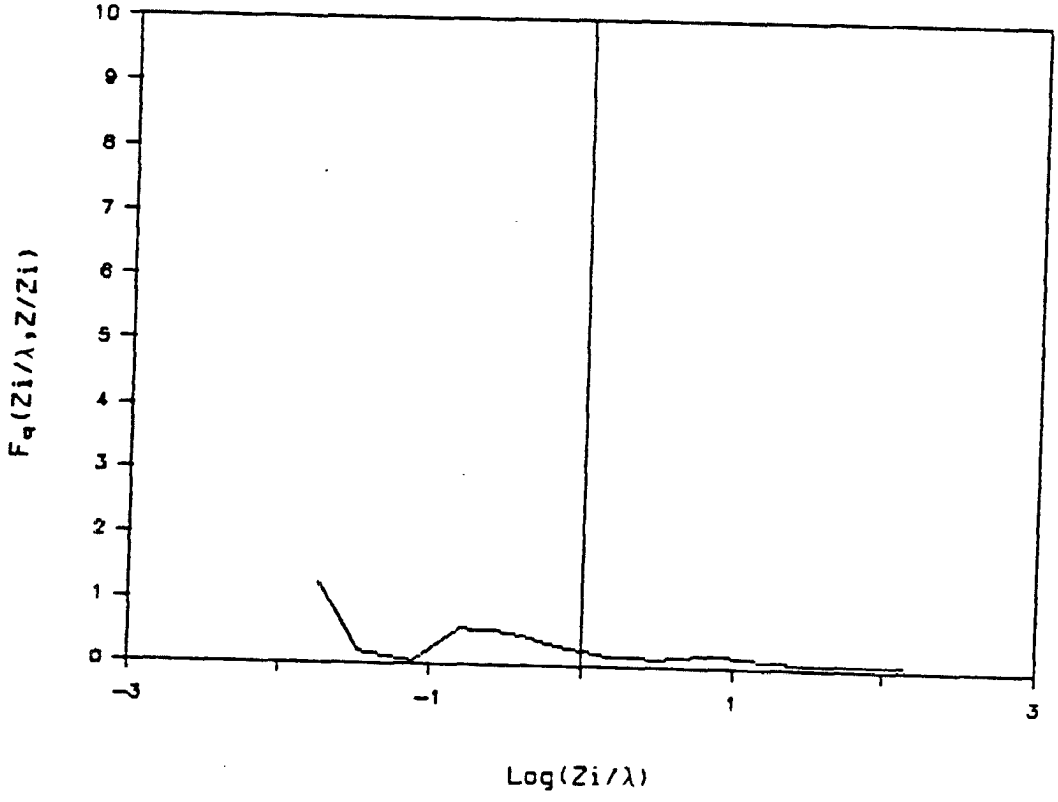

Fig. 4.24 Bin averaged humidity mixing ratio spectra for the lower CBL layer with z_* from 0.1 to 0.2. The scale on the horizontal axis is logarithmic while that on the vertical axis is linear. Area is proportional to variance.

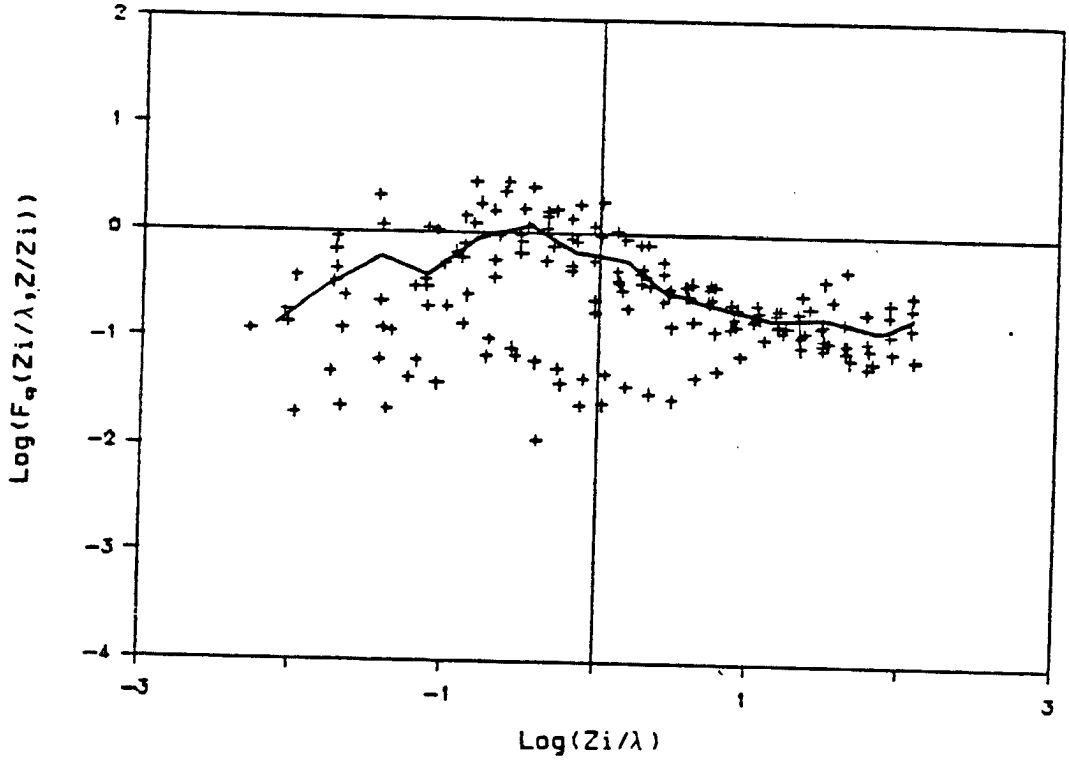

Fig. 4.25 Normalized humidity mixing ratio spectra for the entrainment layer with $z_{\star}$ from 0.8 to 1.2. The individual spectra are plotted as crosses while the bin averaged spectra is plotted as a solid line. Both axis have logarithmic scales.

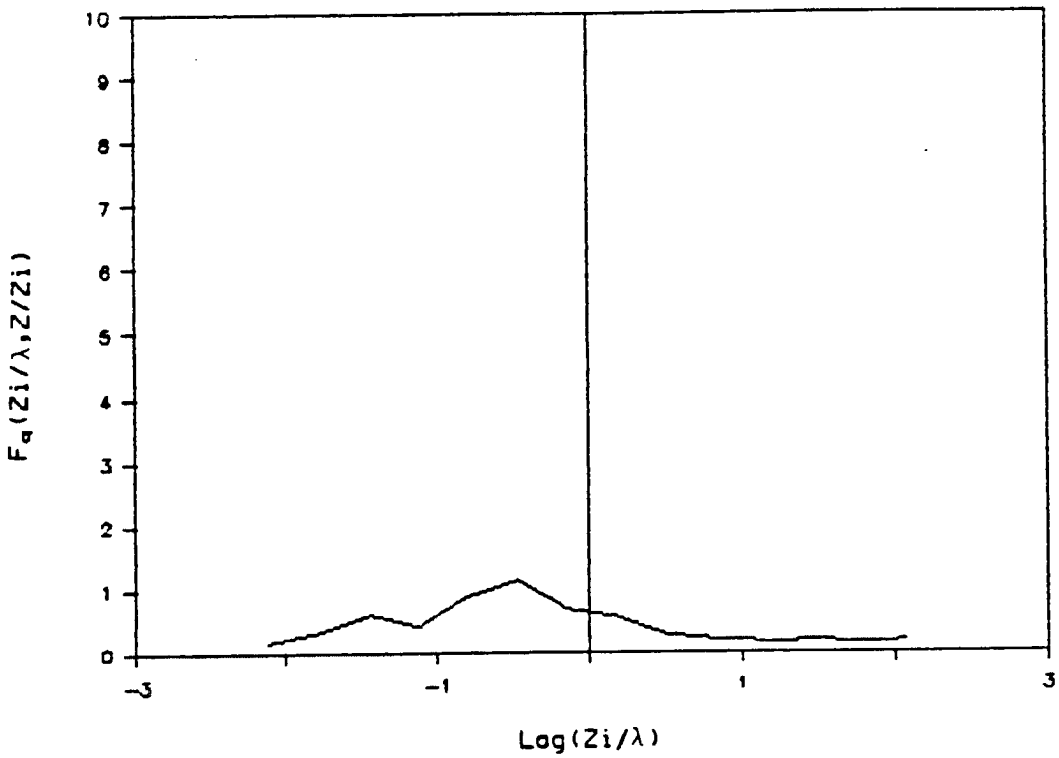

Fig. 4.26 Bin averaged humidity mixing ratio spectra for the entrainment layer with z_* from 0.8 to 1.2. The scale on the horizontal axis is logarithmic while that on the vertical axis is linear. Area is proportional to variance.

found for any of the other variables. The peak wavelength may be more closely related to the spectra of the surface mositure sources such as lakes and rivers than to the microscale turbulence scales. A deep spectral gap occurs in the 10 to 100 z_i wavelength band with some indication of mesoscale variance at extremely long wavelengths. Figure 4.22 shows that most of the microscale mixing ratio variance is in the 0.1 to 10.0 z_i wavelength band.

Figure 4.23 shows the humidity mixing ratio spectra in the lower CBL layer for z_* from 0.1 to 0.2. There are two microscale peaks in this spectra. The highest peak is at a wavelength of about 7.0 z_i, the same as the microscale spectral peak for mid CBL mixing ratio. The second microscale spectral peak is at a wavelength of about 0.15 z_i, a wavelength much shorter than that of any other spectral peak observed in the Phoenix aircraft data set. There is a deep spectral gap at a wavelength of about 10.0 z_i. Figure 4.24 shows the depth of this gap quite clearly. These features are found in the individual spectra as well as in the bin average spectra.

Figure 4.25 shows the humidity mixing ratio spectra for the entrainment layer of z_* from 0.8 to 1.2. All of these spectra are contaminated by noise at short wavelengths and two of them are totally deformed by this contamination. However, removal of the badly contaminated spectra does not alter the general form of the bin average spectra. The bin averaged spectra is rather similar to that for the mid CBL considering the scatter of the points that went into the mean.

Figure 4.26 shows some indication of a spectral gap at wavelengths near 10.0 z_i. The gap is less pronounce than that found in the mid and lower CBL. Not only is there more variance near 10.0 z_i by also less variance at mesoscale wavelengths.

The various spectra described above combine to provide a coherent picture of the variance distributions in the microscale and shorter mesoscale wavelengths. All of the variables except humidity mixing ratio have a mid CBL microscale spectral peak at a wavelength of about 1.5 z_i. This matches the results of Kaimal et al. (1976) for temperature and the three components of velocity. The peak wavelength for humidity mixing ratio is considerably longer for unknown reasons. Within the lower CBL, the microscale spectral peak moves to shorter wavelengths for vertical velocity and potential temperature because of the restriction placed on vertical eddy size by proximity to the ground (Panofsky and Dutton, 1984). For the other variables there is no difference in wavelength of the microscale spectral peak between the mid CBL and those lower CBL that the aircraft was able to reach. The humidity spectra do, however, have a secondary microscale spectral peak at very short wavelengths in the lower CBL. At levels near the capping inversion there is an increase in the wavelengths of the microscale spectral peak for vertical velocity, horizontal wind speed and potential temperature. This may reflect either the presence of gravity waves in the inversion, the merger of outflow from a number of microscale updrafts just as the individual thunderstorm anvils merge to form an MCC's cirrus shield or aircraft penetration of undulations on the inversion.

All of the spectra except vertical velocity spectra show an increase in variance with increasing wavelength in the shorter mesoscale wavelengths measured. The wavelength separation of this mesoscale variance contribution from the microscale spectral peak results in a spectral gap at wavelengths near 10.0 z_i. Spectra for

situations without a microscale energy source would lack this microscale spectral peak and so would not have a spectral gap.

4.4 Definition of Spectral Subranges in the Phoenix Aircraft Data

CBL turbulence spectra can be divided into wavelength subranges based on physical processes. The inertial energy cascade subrange and the microscale energy production subrange are common to all CBL turbulence spectra. The spectra of horizontal wind speed, potential temperature and humidity mixing ratio have significant variance in the mesoscale subrange as well as in the microscale. There is a spectral gap of reduced variance at wavelengths between this mesoscale energy containing subrange and the microscale energy production subrange.

The inertial subrange extends from a wavelength of 0.1 z_i down to the Kolmogorov microscale for turbulence in the CBL above 0.1 z_i. The shortest wavelength sampled by the Phoenix aircraft was approximately 8 meters. This is well above the Kolmogorov microscale and well below 0.1 z_i for the CBL. Thus, the Phoenix aircraft data resolves at least a decade of wavelengths in the inertial subrange. This is sufficient for calculation of dissipation by the method of Kaimal et al. (1976).

The microscale energy production subrange covers the wavelengths in which buoyant production of variance takes place. This subrange thus begins at the wavelength where the spectral slope first becomes shallower then that which results from a purely inertial energy cascade. This wavelength is 0.1 z_i for the CBL at heights above 0.1 z_i. The microscale energy production subrange extends up to the wavelength of the spectral gap between microscale variance and mesoscale variance. This gap is located around a wavelength of 10 z_i. Within the microscale energy production subrange are the buoyantly

driven eddies (thermals), clusters of thermals, and the smaller eddies which form as thermals decay towards isotropic turbulence. The microscale energy production subrange lies entirely within those wavelengths which are well sampled by the Phoenix aircraft flight legs.

The mesoscale energy containing subrange lies at wavelengths longer than 10.0 z_i. Only the shortest decade or less of this subrange was sampled by the Phoenix aircraft flight legs. This sampling is insufficient for any study of the dynamics of the mesoscale energy containing subrange.

The spectral gap region between the mesoscale energy containing subrange and the microscale energy production subrange contains variance contributions from both scales. The depth, width and exact location of this gap are both controlled by the relative magnitude of variances in these two energy containing regions. However, a wavelength of 10 z_i falls within the deepest part of the gap and was, therefore, selected as a boundary between the mesoscale and microscale within the CBL.

5. Variability of Normalized CBL Trubulence Statistics

5.1 Sources of Variability in Normalized CBL Turbulence Statistics

Turbulence statistics for the bulk of the CBL above the surface layer are generally normalized using mixed layer scaling and presented as functions of normalized height, z/z_i (Deardorff, 1970; Lenschow, 1974; Kaimal et al., 1976; Caughey and Palmer, 1979; Lenschow et al., 1980; Hildebrand and Ackerman, 1984 and others). As discussed in Chapter 3.1, this approach will result in universal profiles for each of the turbulence statistics if there are no sampling errors and the assumptions of mixed layer scaling are completely valid. Neither of these conditions is ever satisfied completely. Sampling errors are inherent in turbulence statistics averaged over less than an infinite number of actualizations (Lenschow and Stankov, 1986) and even in the best of conditions the assumptions of mixed layer scaling are violated to some small degree. The effects of these limitations on the applicability of mixed layer scaling and, therefore, on the universality of the results of this study will be discussed in the remainder of this chapter.

The terrian of Phoenix 78 experimental site might also affect the trubulence structure of the CBL. This possibility is checked by comparing the profiles of turbulence statistics from Phoenix 78 with those of other experiments. It will be shown that the terrain of the Phoenix 78 experimental site did not bias the results away from those obtained over more uniform terrain.

The effects of sampling errors will be discussed in Section 5.2. Section 5.3 extends the discussion of mixed layer scaling found in Chapter 3.1 to include various unaccounted for factors which can affect CBL turbulence. Section 5.4 is an intercomparison of the Phoenix 78 profiles of turbulence statistics with those from previous studies. This intercomparison shows the degree of variation in turbulence statistics between experiments. The intercomparison also provides an opportunity to discuss the origins of these variations and the occurrence of terrain induced biases.

5.2 The Effects of Sampling Errors on CBL Turbulence Statistics

Lenschow and Stankov (1986) discuss the importance of the integral length scales to the sampling errors for CBL turublence statistics. They present approximate formulas which can be used to estimate the accuracy expected from the ratio of the length of aircraft flight legs to the depth of the CBL. In general, the longer the sample length relative to the CBL depth, the greater the accuracy of the estimates of the turbulence statistics. This method will be used to estimate the expected leg to leg scatter of estimates of the buoyancy flux for the Phoenix 78 experiment. This method will also be used to estimate the expected experiment to experiment scatter in composite buoyancy flux profiles. The effect of sampling length on buoyancy flux estimates is typical of the effect for the other statistics discussed in Lenschow and Stankov (1986). The effects of sample length limitations affect both the turbulence statistics and the estimates of the mixed layer scaling parameters which are used to normalize them. Therefore, in practice, sample length limitations affect normalized turbulence statistics more severely than they would

if the estimates of the scaling parameters were error free. The degree of sample size induced scatter predicted by this theory will be compared with the total scatter of the buoyancy flux measurements within the Phoenix experiment and between this and other experiments. The experiments are discussed in Section 5.4.

The lengths of the horizontal flight legs of the Phoenix 78 experiment were in the range of 10 to 100 times the boundary layer depth. For these leg lengths, the expected standard deviation of the single leg estimates of buoyancy flux around the bin averaged profile ranges from 6 to 32 percent for the lower half of the CBL. For a typical leg length of 30 times the boundary layer depth the leg to leg scatter is expected to be 10 to 19 percent. These values are similar to the degree of leg to leg scatter actually observed (Figure 5.1). The observations appear to scatter somewhat more than predicated by the theory, suggesting that there was some degree of change in the turbulence structure of the CBL during the experiment.

The total length of flight contributing to each of the bin averages in the mean Phoenix 78 buoyancy flux profile is about 300 times the boundary layer depth. This is typical of most of the experiments disucssed in this chapter. The scatter between the experimental mean profiles of buoyancy flux would be expected to correspond to such sampling lengths. This scatter is estimated at 3 to 6 percent by the method of Lenschow and Stankov (1986). The observed scatter between the results of differenct experiments is of this order in the lower third of the CBL but is somewhat larger in the mid CBL because of variations in the height of the zero crossing. Therefore, the scatter between experiments is closer to that expected

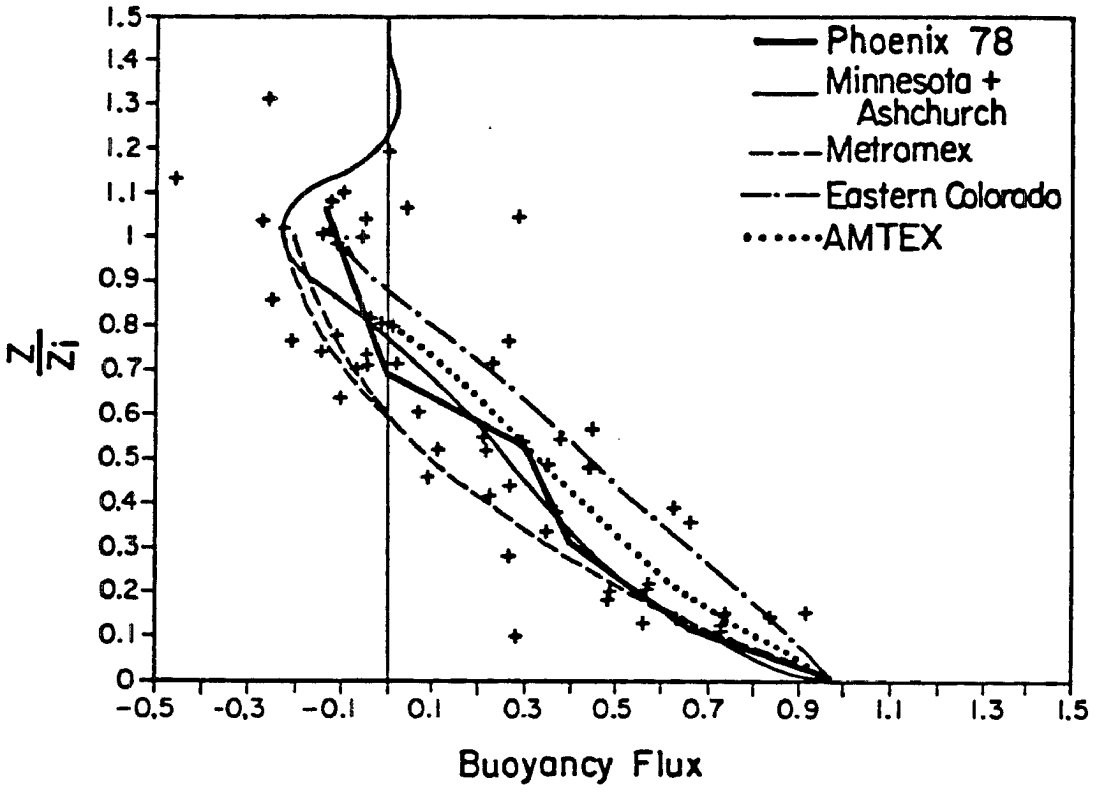

Fig. 5.1 Buoyancy flux profiles from Phoenix 78 and other observational studies. The heavy curve is the bin averaged profile fit to the plotted Phoenix 78 data points. The profiles from the other studies are drawn as light curves. The vertical axis is the height scaled by the depth of the convective boundary layer. The horizontal axis is nondimensionalized by mixed layer scaling.

from the theory of sampling errors in the lower CBL than in the mid CBL. This result suggests that while mixed layer scaled buoyancy flux profile is nearly universal in the lower CBL, differences in entrainment effects cause significant departures from this profile in the mid and upper CBL. Such a result is in accordance with the generally held beliefs about the validity of mixed layer scaling (Kaimal et, al., 1976).

The theory discussed in Lenschow and Stankov (1986) provides a basis for estimating what fraction of the observational scatter is caused by sample size limitations and what fraction is caused by the neglect of certain physical processes from mixed layer scaling. For Phoenix 78, the sample size limitation makes the most significant contribution to the leg to leg scatter. Sample size limitations also account for much of the observed variation between the composite profiles from different experiments as well.

5.3 The Physical Processes Excluded from Mixed Layer Similarity

Mixed layer scaling is based on the assumption that CBL turbulence is controlled by four parameters: the height, boundary layer depth, surface buoyancy flux and the buoyancy parameter, $g/\bar{T}$. Several of the physical processes which can occur in the planetary boundary layer are not accounted for by these assumptions. These processes can cause the boundary layer to depart from the ideal CBL structure to some degree. Mixed layer scaling is completely valid only when all of these other factors are negligible. However, mixed layer scaling has been found to give good results under a broad range of conditions (Lenschow, 1974; Kaimal et al., 1976; Coulman, 1978; Caughey and Palmer, 1979; Lenschow et al., 1980; Hildebrand and Ackerman, 1984 and others).

The weakest assumption of mixed layer scaling is that the surface buoyancy flux, Q_o, completely determines the forcing of CBL turbulence. This assumption can be violated in several ways.

The relative importance of the shear production of turbulence caused by the mean horizontal wind contacting the earth's surface can be measured by the ratio, $-z_i / L$. This ratio is proportional to the fraction of the depth of the CBL through which this shear production dominates buoyant production of turublence kinetic energy. If $-z_i / L \gg 1$ then the surface buoyancy flux is more important than the surface momentum flux in controlling turublence in the bulk of the CBL. The values of $-z_i / L$ range from 10 to 300 for the periods studied in Phoenix 78 so buoyant production of turbulence dominates surface shear production throughout most of the CBL.

Less clearly understood is the relationship between the surface buoyancy flux and the downward entrainment buoyancy flux at z_i, Q_e (Driedonks and Tennekes, 1984). While Q_e is driven in part by Q_o, Q_e does not depend solely on Q_o. Even if Q_o were negligible, vertical shear of the horizontal wind, dU/dz, could induce turublence and thus a downward buoyancy flux at the inversion.

The magnitude of the downward buoyancy flux at the inversion produced by the surface buoyancy flux and the wind shear across the inversion depends upon the thermal stratification of the capping inversion across which air is being entrained. For example, if the CBL is growing into air with the same virtual potential temperature there can be no downward buoyancy flux generated by mixing of this air with air from the CBL. Experimental uncertainity has so far thwarted attempts to derive a precise relationship between the entrainment buoyancy flux and these other factors.

Furthermore, very little work has been reported on effects of variations in Q_e/Q_o on the profiles of other turbulence statistics. Sampling errors in the observational data have severely limited it's contribution to solution of this problem. The results from numerical large eddy simulations (LES models) and from water tank experiments have, however, shed some light on this effect. These model results will be discussed below as part of the comparison of Phoenix 78 turbulence profiles with those reported in the literature.

Shear producation of turbulence across the inversion and within the mixed layer can be important in strongly baroclinic conditions. In addition, large shear within the CBL can stabilize all modes of buoyant convection except those aligned parallel to the shear (Asai, 1970a, b). Shear across the inversion has been observed to generate wave motions on the inversion which contribute to the turbulence statistics. All of these effects are minor for the present study because low wind speed and low shear were criteria for selection of periods for analysis. Most other CBL experiments have also been conducted so as to minimize these effects.

Unevenness of the underlying terrain, large scale environmental subsidence and any effects of clouds or cloud shadows are also neglected in the present formulation of mixed layer scaling. Lack of data has so far made description of the effects of these factors on CBL turublence impossible. Thus, there are several unknown effects which are excluded from mixed layer scaling. Mixed layer scaling of observational or model results can yield universal profiles of turbulence statistics only when these excluded effects are negligible.

5.4 Comparison of Turbulence Statistics for Phoenix 78 and Previous Studies

5.4.1 Description of Previous Studies

A comparison of the vertical profiles of the statistics of CBL turublence from various studies including Phoenix 78 is undertaken below. The goal is to determine how much variability is introduced into the results by sampling errors and by the physical effects not accounted for in mixed layer similarity. In some cases, the qualitative effects of individual physical processes can be determined from such a comparison or hypothesized based on physical and dimensional arguments. Emphasis is placed on determining whether or not the environment of the Phoenix 78 CBL experiment biased the results of that experiment.

The results compared come from the observational and modelling studies listed in Table 5.1. The observational studies were conducted in a wide variety of locations, some with less than ideally smooth terrain or with potentially significant cloud or wind conditions.

The Eastern Colorado field experiment was conducted in the spring of 1968 over nearly flat terrain. The data were collected in moderate winds and scattered stratocumulus a few hours after the passage of a cold front.

The Minnesota experiment was conducted over very smooth terrain during periods of northerly winds and clear skies in the fall of 1973. $-z_i / L$ ranged from 30 to 367 for that study. These values are large enough to ensure that buoyancy dominated shear production of turbulence.

Table 5.1 CBL Turbulence Studies Included in the Intercomparison

Experiment	Date	Published Results
EASTERN COLORADO	1968	Lenschow (1974)
MINNESOTA AND ASHCHURCH	1973 1976	Kaimal et al. (1976) Caughey and Palmer (1979)
MOREE, AUSTRALIA	1974	Coulman (1978)
WATER TANK	1974	Willis and Deardorff (1974)
L.E.S.	1974	Deardorff (1974 a,b)
AMTEX	1975	Lenschow et al. (1980)
METROMEX	1975	Hildebrand and Ackerman (1984)
PHOENIX 78	1978	Present study
L.E.S.	1984	Moeng (1984) Moeng and Wyngaard (1984)

The Ashchurch experiment was carried out in Worchestershire, England during generally clear weather in the summer of 1976. The region around Ashchurch is comprised of farms and hedgerows with a 250 m scarp to the southwest. In this respect the Ashchurch site is more like the BAO site than the site of the Minnesota experiment with which it's results are generally combined.

The Moree, Australia field experiment was conducted over very flat featureless terrain in the grasslands of New South Wales during the fall of 1974.

The AMTEX experiment was conducted during cold air outbreaks over the East China Sea. The conditions of moderate surface windspeed, scattered to broken stratocumulus and strong baroclinicity provided a test of the limits of applicability of mixed layer scaling. Lenschow et al. (1980) report that these conditions had little effect on the budgets of the second moment turbulence statistics.

The METROMEX field study was conducted to compare CBL turublence over rolling urban and rural sites. Wind speeds during METROMEX were 2 to 5 m/s; more than during Phoenix 78 but not high enough to change the character of CBL convection. The cloud cover was 0.1 to 0.4 of fair weather cumulus. Some differences were noted between the turbulence over urban and rural sites, suggesting that large variations in surface characteristics can influence CBL turublence somewhat.

The conditions during Phoenix 78 have been described in detail in Chapter 2. The light winds and nearly clear conditions were close to the ideal assumed for mixed layer scaling. The rolling terrain at the Boulder Atmospheric Observatory site and the mountains to the west are features not taken into account in mixed layer scaling.

Further details of these field experiments and of the model studies can be found in the papers referenced in Table 5.1.

All of the results presented in this section have been normalized using the mixed layer scaling parameters, z_i, w_* and θ_*. The Phoenix 78 results are presented on each figure in two forms, the data points for the individual horizontal flight legs and the bin averaged profile. The profile is created by connection of the points which represent the bin averages of z_* (z/z_i) and the turbulence statistic for the following z_* bins; 0.1 to 0.2, 0.2 to 0.4, 0.4 to 0.6, 0.6 to 0.8, 0.8 to 1.0 and 1.0 to 1.2. The profiles from previous studies are taken from the published mean profiles when possible. In the cases where only scatter plots of the data were published, smooth profiles were drawn by eye to fit the data. It is important to remember that there is a scatter of the data around these profiles in all the observational experiments. The extent of this scatter is generally similar to that seen in the Phoenix 78 data as the theory in Lenschow and Stankov (1986) would suggest.

5.4.2 Buoyancy Flux

The fundamental turbulence statistic of the CBL is the buoyancy flux. This flux is the only source of turbulence kinetic energy for a purely convective boundary layer. Figure 5.1 shows the buoyancy flux profiles for six field experiments (AMTEX, Ashchurch, Eastern Colorado, METROMEX, Minnesota and Phoenix 78). All of the experiments were conducted in highly convective boundary layers although wind shear varied from negligible for Phoenix 78 to significant for AMTEX.

The general shape of the profiles is similar for all of the experiments. The buoyancy flux decreases above the surface and becomes

negative (downward) at a height of from 0.6 to 0.9 z_i. The buoyancy flux reaches a minimum of -0.1 to -0.2 times the surface buoyancy flux at z_i where the entrainmnet of warm air across the inversion is largest. These values fall within the -0.1 to -0.3 range commonly reported (Stall, 1976). All of the bouyancy flux profiles except that from Eastern Colorado are concave upwards. In fact, the Eastern Colorado data points also indicate a concave upwards buoyancy flux profile but a linear approximation to the profile was published.

The curvature of the buoyancy flux profile has been explained by Wyngaard and Broost (1984) in terms of top-down and bottom-up diffusion. They show that large downward entrainment fluxes result in considerable curvature of the profile of a mean scalar in the CBL. To maintain such a curved profile of virtual potential temperature in a growing CBL, the buoyancy flux convergence must vary with height, thus requiring a curve buoyancy flux profile such as that observed. A nonzero mean vertical velocity would also require a curved buoyancy flux profile for the maintenance of a steady shape for the virtual potential temperature profile. The Phoenix 78 buoyancy flux profile falls near the middle of the range of the previously reported observations.

The buoyancy flux profiles for Phoenix 78, a tank experiment (Willis and Deardorff, 1974), and two large eddy simulations (Deardorff, 1974a, b and Moeng, 1984) are shown in Figure 5.2. The model profiles of buoyancy flux are generally similar to those observed in the atmopshere except that the curvature is very much smaller. This suggests either that the models lack the mechanism by which entrainment fluxes lead to curved flux profiles or that mean

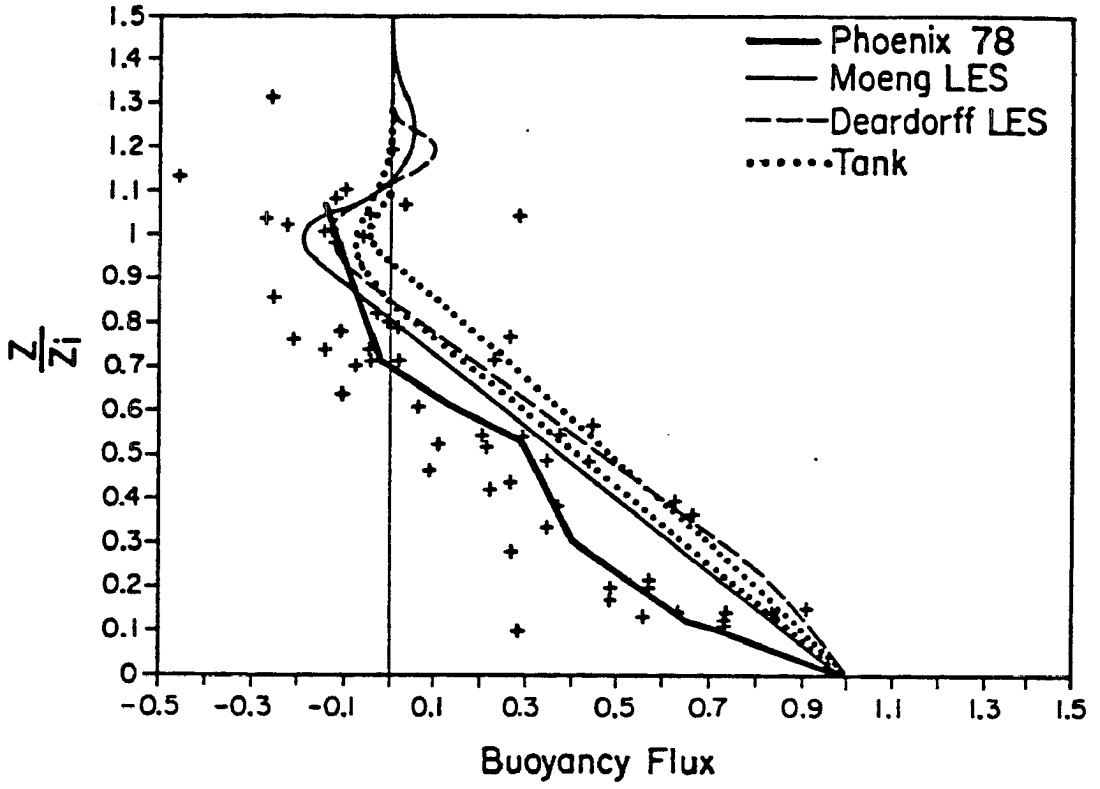

Fig. 5.2 Buoyancy flux profiles from Phoenix 78 and three modelling studies. The heavy curve is the bin averaged profile fit to the plotted Phoenix 78 data points. The profiles from the modelling studies are drawn as light curves. The vertical axis is the height scaled by the depth of the convective boundary layer. The horizontal axis is nondimensionalized by mixed layer scaling.

vertical velocity is the chief cause of curvature in the atmospheric buoyancy flux profiles. In the latter case, the models, having no mean vertical velocity, would not display flux profile curvatures. Both LES models show a second area of upward buoyancy flux above z_i which neither the tank model or the atmospheric observations show. This may be a result of an inability of the models to properly resolve the very small scale motions near the inversion. The lack of curvature in the model buoyancy flux profiles results in their falling to the right of the observed profiles.

The differences between the buoyancy flux profiles for the various observational studies are smaller than the scatter of the individual data points in these studies. The greatest differences between studies occurred in the upper CBL where differences in the entrainment flux are most important. The model results are also very similar to each other except in the magnitude of the entrainment flux. However, the buoyancy flux profiles derived from the models are all much more linear than those determined from atmospheric observations.

5.4.3 Vertical Velocity Variance

The vertical velocity variance profiles for six field experiments (AMTEX, Ashchurch, Australia, Eastern Colorado, Minnesota and Phoenix 78) are shown in Figure 5.3. The profiles are all similar with zero values at the surface, small values above z_i and single maxima near the middle of the CBL. This maxima has a value of 0.4 to 0.55 at heights from 0.3 to 0.5 z_i. The Phoenix 78 vertical velocity variance profile lies near the middle of the range of previous observations. The vertical veloicty variance profile reported for the Australian experiment by Coulman (1978) differs from other observations. The

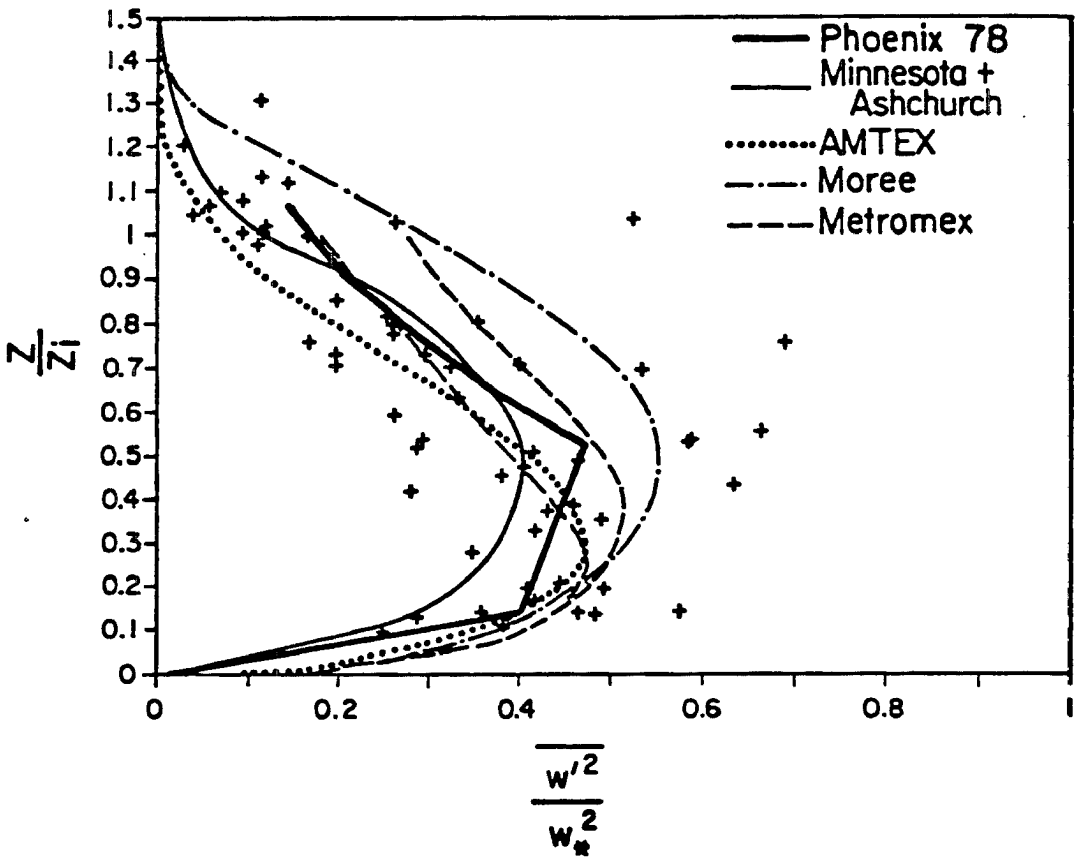

Fig. 5.3 Vertical velocity variance profiles from Phoenix 78 and other observational studies. The heavy curve is the bin averaged profile fit to the plotted Phoenix 78 data points. The profiles from the other studies are drawn as light curves. The vertical axis is the height scaled by the depth of the convective boundary layer. The horizontal axis is non-dimensionalized by mixed layer scaling.

amplitude of the maximum is larger, the maximum occurs at a greater hieght and the variance is significant well above z_i. These differences suggest that z_i has been underestimated in Coulman (1978). This is also apparent from the temperature variance and vertical velocity skewness profiles presented below.

The vertical velocity variance profiles for Phoenix 78, a tank experiment (Willis and Deardorff, 1974) and an LES (Moeng and Wyngaard, 1984) are shown in Figure 5.4. These profiles are very similar to those from the atmospheric observations. The maximum values range from 0.4 to 0.58 at hieghts from 0.3 to 0.5 z_i. Again the Phoenix 78 profile is near the center of the range of the other results.

The vertical velocity variance profiles for the observational and modelling studies are quite similar. These mean profiles differ from each other by less than the scatter of the individual data points.

5.4.4 Temperature Variance

The profiles of temperature and virtual temperature variance differ more between experiments than do the profiles of vertical velocity variance. Figure 5.5 shows the temperature or virtual temperature variance profiles for five field experiments (AMTEX, Ashchurch, Australia, Minnesota and Phoenix 78). The surface maxima of temperature variance is caused by the surface buoyancy flux and is well normalized by mixed layer scaling. The other maxima of temperature variance at z_i is caused by the downward entrainment buoyancy flux. This maxima is not as well normalized by mixed layer scaling because, as discussed in Chapter 5.3, other factors besides those included in mixed layer similarity affect the downward

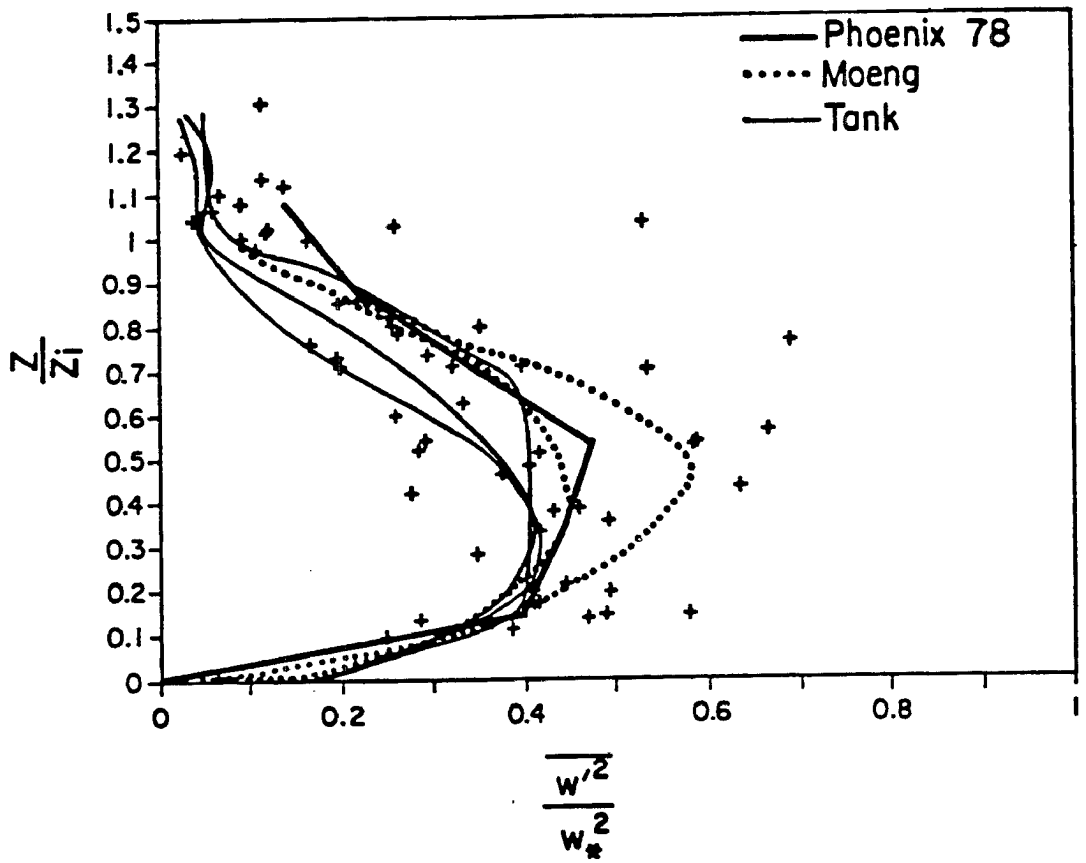

Fig. 5.4 Vertical velocity variance profiles from Phoenix 78 and two modelling studies. The heavy curve is the bin averaged profile fit to the plotted Phoenix 78 data points. The profiles from the modelling studies are drawn as light curves. The vertical axis is the height scaled by the depth of the convective boundary layer. The horizontal axis is nondimensionalized by mixed layer scaling.

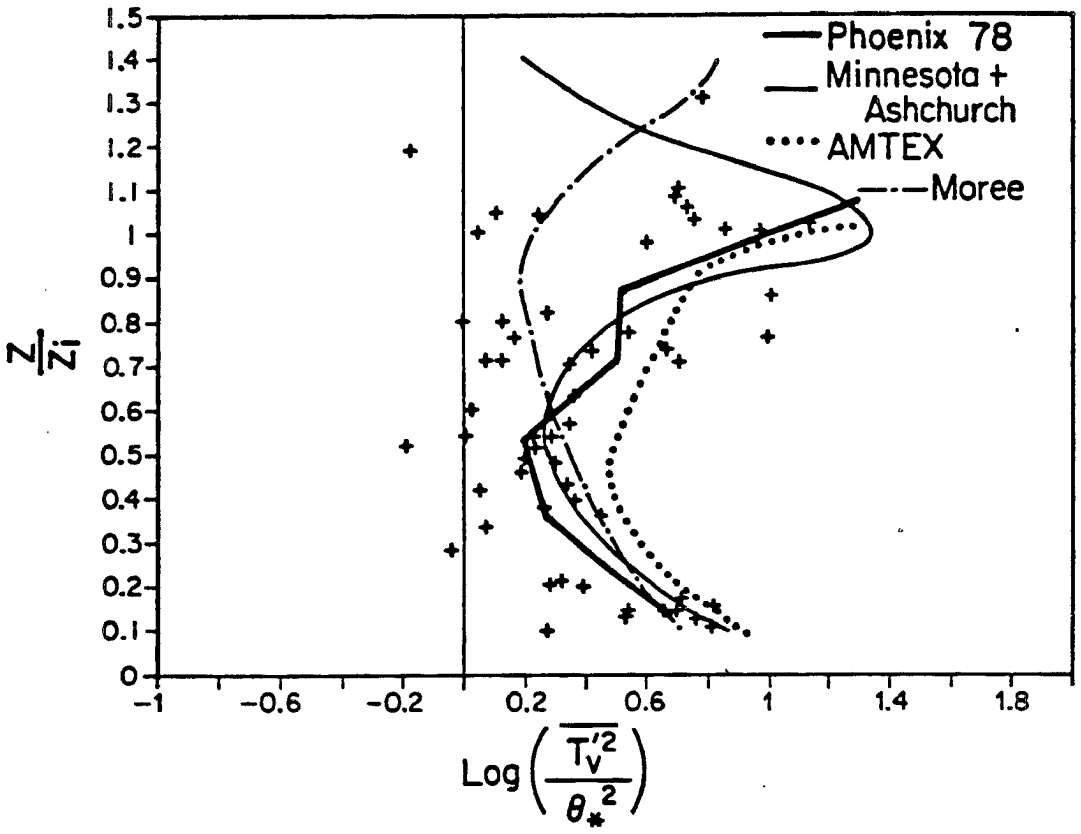

Fig. 5.5 The logarithm of temperature or virtual temperature variance profiles from Phoenix 78 and other observational studies. The heavy curve is the bin averaged profile fit to the plotted Phoenix 78 data points. The profiles from the other studies are drawn as light curves. The vertical axis is the height scaled by the depth of the convective boundary layer. The horizontal axis is nondimensionalized by mixed layer scaling.

entrianment buoyancy flux at z_i. The profiles from the various experiments agree well except for that from Australia which appears to have been influenced by an underestimate of z_i by about one third. The Phoenix 78 virtual temperature variance profile matches that from the Minnesota-Ashchurch composite quite well and is similar in form to those reported for Australia and for AMTEX. The minimum of temperature variance is observed at heights around 0.5 z_i, well below the zero crossing of buoyancy flux at 0.6 to 0.9 z_i. Thus, the influence of entrianment across the inversion extends through a much greater depth than does the downward buoyancy flux caused by this entrainment. This is a key insight for the understanding of CBL turbulence and the differences between observations and models of this turbulence as discussed in the next paragraph.

Model derived temperature variance profiles are compared with the Phoenix 78 virtual temperature variance profile in Figure 5.6. The Deardorff (1974b) LES results shown that the amplitude of the temperature variance maxima at z_i varies with the thermal stratification above z_i. The results from a tank model, (Willis and Deardorff, 1974), are similar in form but have a much more pronounced minima in the upper CBL than do the LES results or the atmospheric observations. The LES profiles generally exhibit a minimum in temperature variance of about 0.2 at 0.7 to 0.8 z_i while the observations including Phoenix 78 give a minimum of 0.2 to 0.5 at 0.4 to 0.5 z_i. The models, as well as the observations, have the minimum in temperature variance located lower in the CBL than the zero crossing of buoyancy flux. The height difference between these two features is, however, much smaller for the models than for the

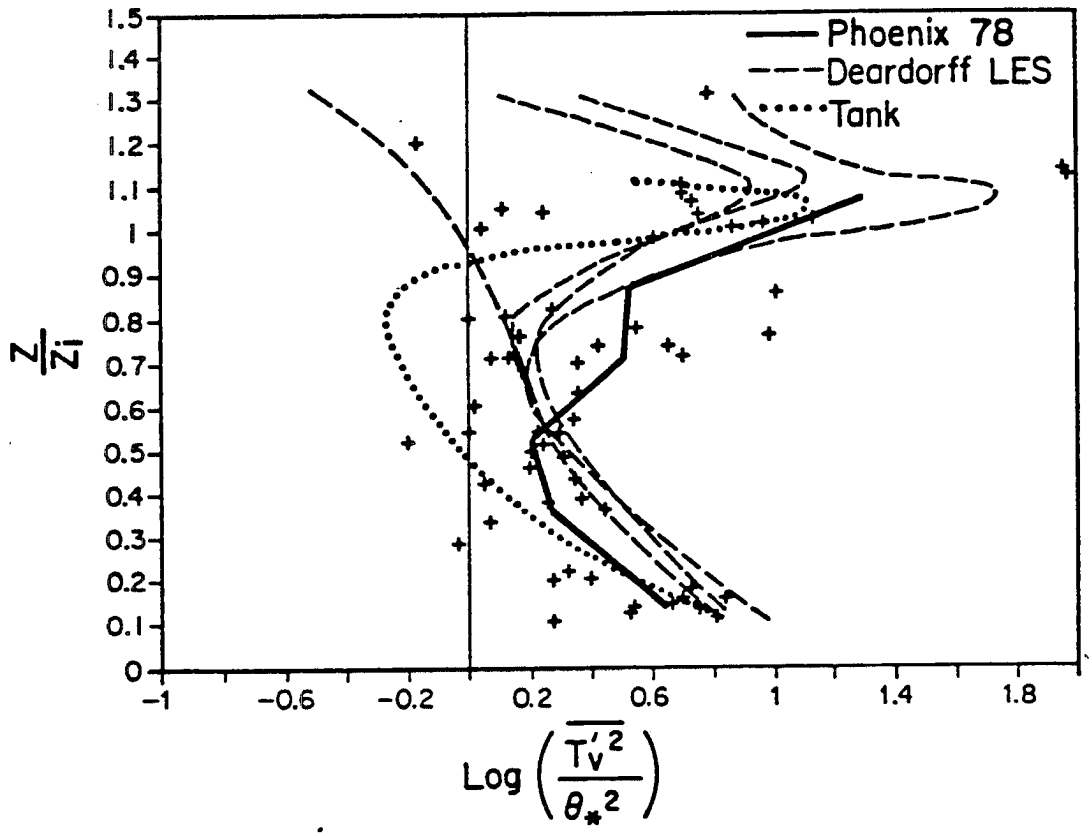

Fig. 5.6 The logorathm of temperature or virtual temperature variance profiles from Phoenix 78 and two modelling studies. The heavy curve is the bin averaged profile fit to the plotted Phoenix 78 data points. The profiles from the modelling studies are drawn as light curves. The vertical axis is the height scaled by the depth of the convective boundary layer. The horizontal axis is nondimensionalized by mixed layer scaling.

atmosphere. These differences, along with the lack of curvature of the buoyancy flux profiles indicates that the effects of entrainment fluxes at z_i are not extending as far down into th CBL in the models as in the atmosphere.

As with buoyancy flux and vertical velocity variance, the differences between the observed profiles of temperature variance are smaller than the scatter in the data. The model derived profiles are however systematically different from the observed profiles.

5.4.5 Horizontal Velocity Variance

Comparison of the variances of the horizontal velocity components is complicated by the smallness of the mean wind during Phoenix 78. Most previous studies have separated the horizontal wind into a component along the mean wind, u, and one perpendicular to the mean wind, v. This distinction is meaningless for the nearly calm conditions which were selected for analysis in Phoenix 78. Therefore, the Phoenix 78, u will be defined as component of the wind towards the east, nearly parallel to the climatological winds aloft, and v will be defined as the northward component of the wind. This somewhat arbitrary definition has no effect on the qualitative results of the comparison because there are no qualitative differences between the variance profiles of u and v for most CBL studies.

The u variance profiles from four field experiments (AMTEX, Ashchurch, Minnesota and Phoenix 78) are shown in Figure 5.7. The Phoenix 78 profile is of the same general form as the Minnesota--Ashchurch composite profile. Both have a maxima at the surface caused by the surface stress and by the convergence into convective updrafts and a maxima in the upper CBL caused by momentum entrainment across

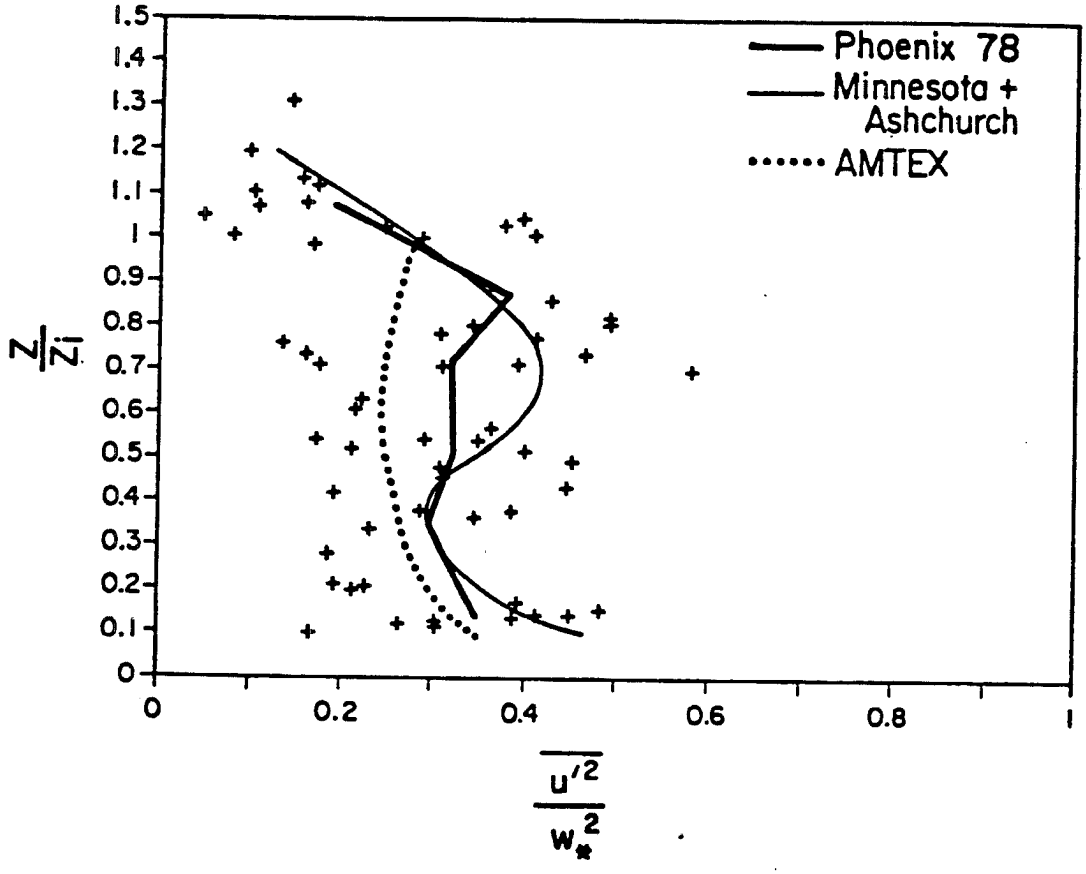

Fig. 5.7 Profiles of the variance of the u component of the horizontal wind from Phoenix 78 and other observational studies. The heavy curve is the bin averaged profile fit to the plotted Phoenix 78 data points. The profiles from the other studies are drawn as light curves. The vertical axis is the height scaled by the depth of the convective boundary layer. The horizontal axis is nondimensionalized by mixed layer scaling.

the inversion and by the divergence from convective updrafts. The AMTEX profile is similar but with the maximum at or above z_i. The maxima of the u variance profiles are 0.35 to 0.5 while the minima are between 0.25 and 0.3. The heights of the minima in u variance correspond to the heights of the maxima of w variance as would be expected if divergent flows associated with convection were an important source of u variance.

The u variance profiles from the tank experiment of Willis and Deardorff (1974) are shown in Figure 5.8. These profiles have shapes similar to those observed in the atmosphere but they have lesser amplitudes. This difference could result from the lack of a horizontal mean flow in the tank model. These profiles could just as well be considered as v variance profiles because there was no mean wind in the tank. The u variance profiles from two LES models (Moeng 1984 and Deardorff, 1974b) shown in Figure 5.9 are very similar.

The v variance profiles for four field experiments (AMTEX, Ashchurch, Minnesota and Phoenix 78) are shown in Figure 5.10. They are very similar in form to the u velocity profiles. Therefore the same comments apply.

The horizontal velocity variance profiles from the LES model of Deardorff (1974b) could apply equally well to u or v because the model has no mean wind. These profiles are shown in Figure 5.11. There is a maximum of horizontal velocity variance at the surface and then a nearly steady variance up to z_i. The values are smaller than those observed in other studies as well. These two characteristics suggest that the impingement of convective elements against the inversion was a less significant source of horizontal velocity variance for this model than for the atmosphere or the other models.

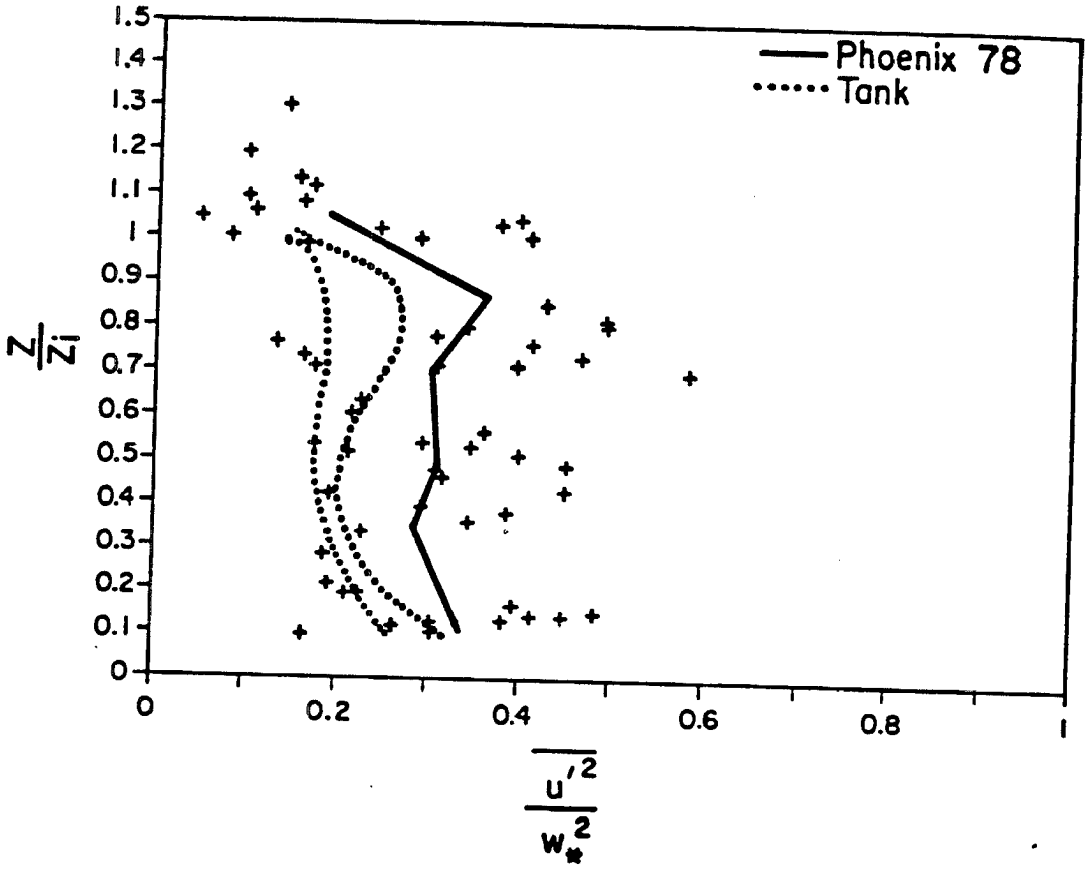

Fig. 5.8 Profiles of the variance of the u component of the horizontal wind from Phoenix 78 and a water tank study. The heavy curve is the bin averaged profile fit to the plotted Phoenix 78 data points. The profiles from the water tank are drawn as light curves. The vertical axis is the height scaled by the depth of the convective boundary layer. The horizontal axis is nondimensionalized by mixed layer scaling.

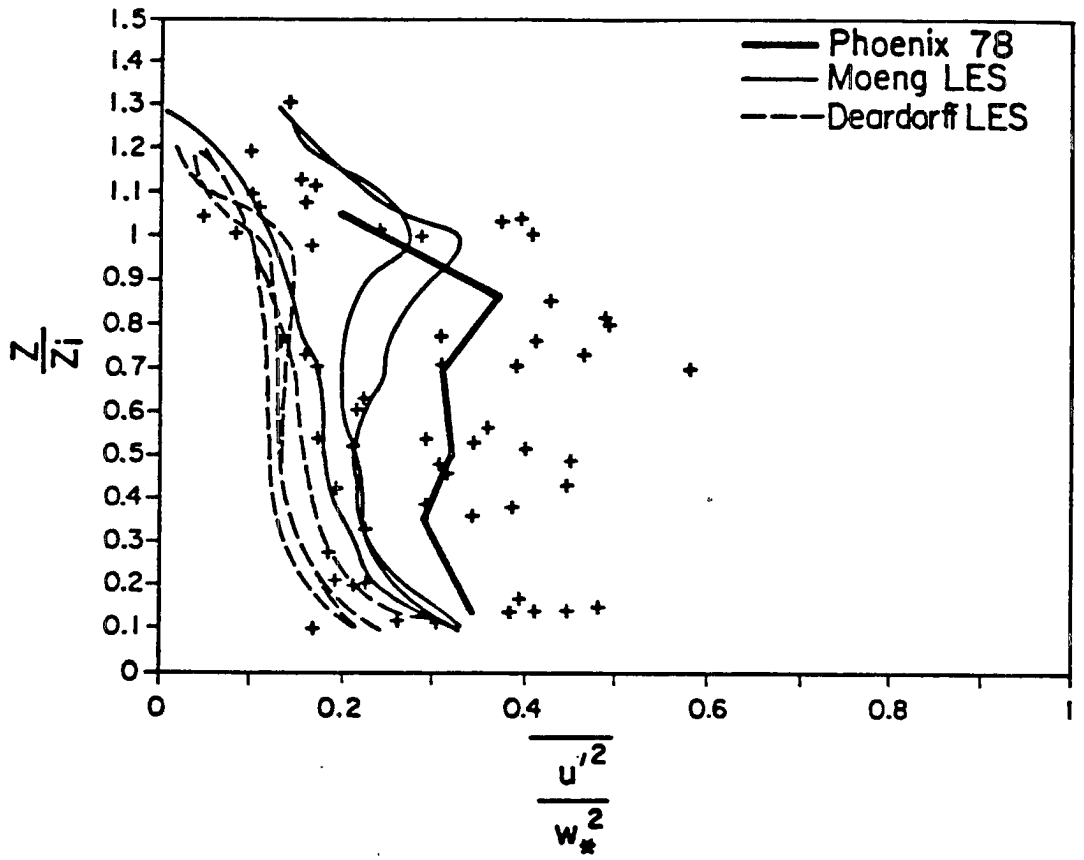

Fig. 5.9 Profiles of the variance of the u component of the horizontal wind from Phoenix 78 and two large eddy simulation studies. The heavy curve is the bin averaged profile fit to the plotted Phoenix 78 data points. The profiles from the modelling studies are drawn as light curves. The vertical axis is the height scaled by the depth of the convective boundary layer. The horizontal axis is nondimensionalized by mixed layer scaling.

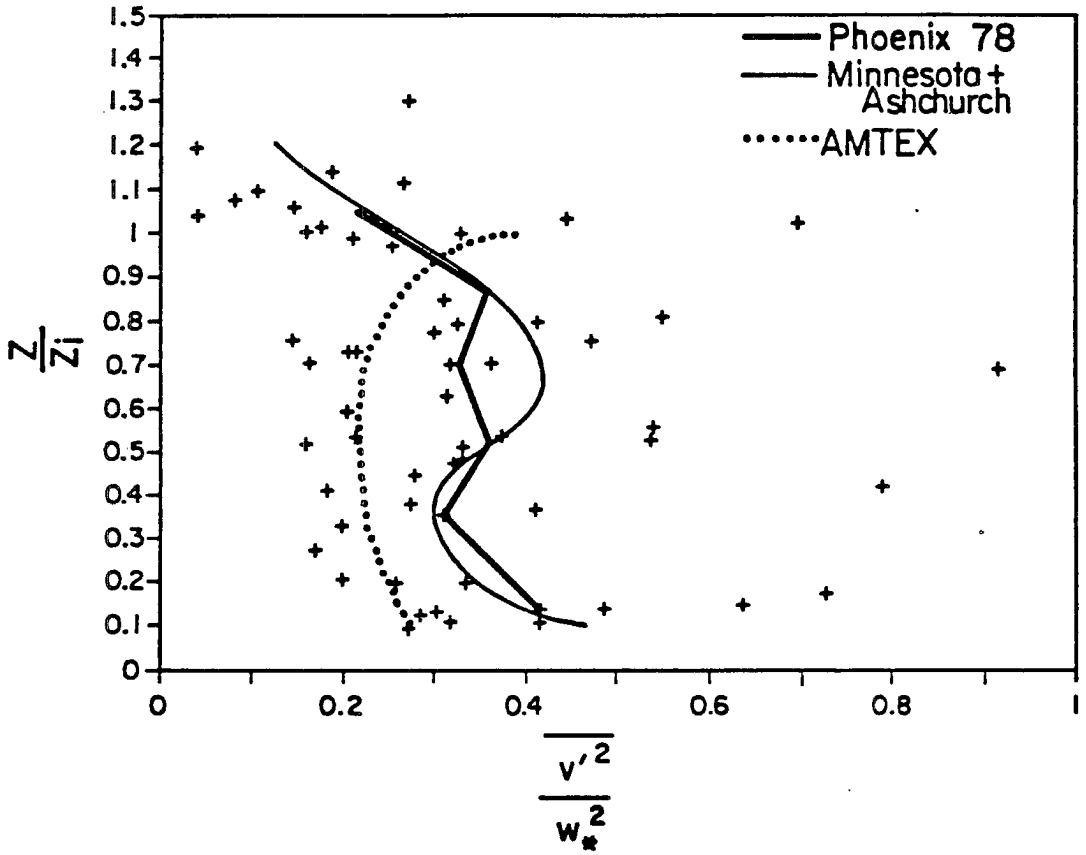

Fig. 5.10 Profiles of the variance of the v component of the horizontal wind from Phoenix 78 and other observational studies. The heavy curve is the bin averaged profile fit to the plotted Phoenix 78 data points. The profiles from the other studies are drawn as light curves. The vertical axis is the height scaled by the depth of the convective boundary layer. The horizontal axis is nondimensionalized by mixed layer scaling.

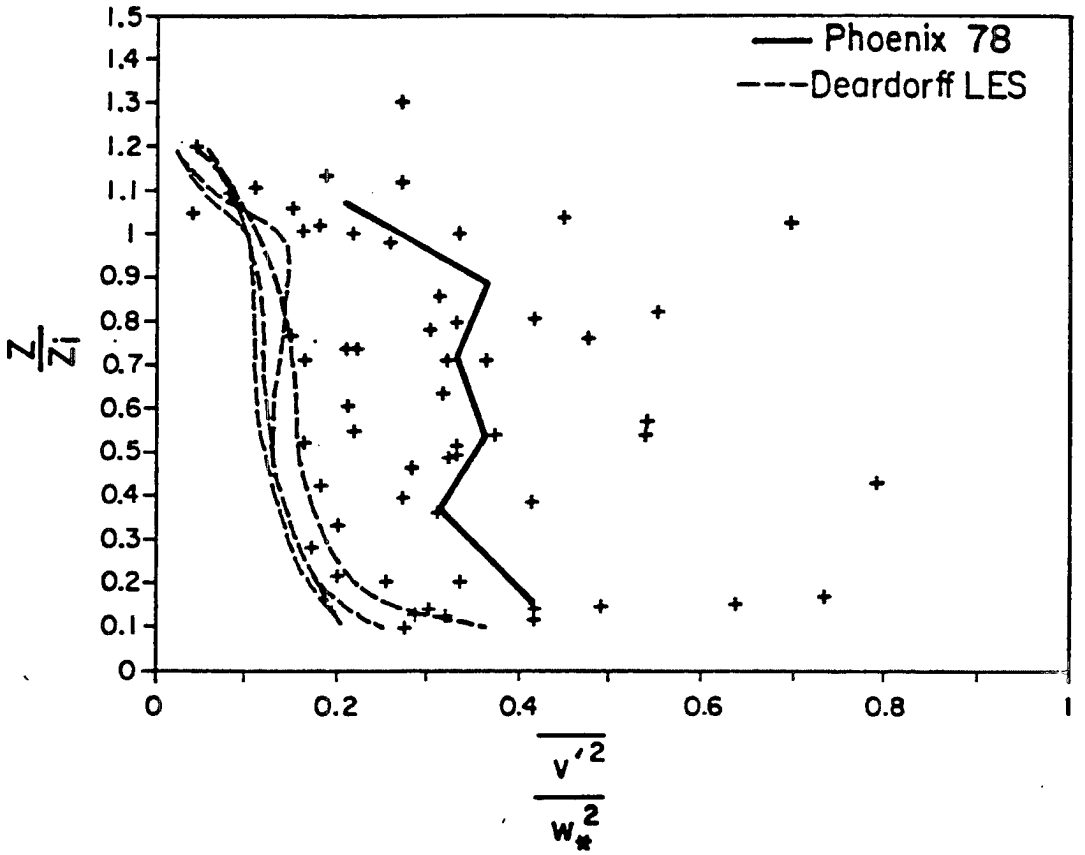

Fig. 5.11 Profiles of the variance of the v component of the horizontal wind from Phoenix 78 and a large eddy simulation. The heavy curve is the bin averaged profile fit to the plotted Phoenix 78 data points. The profiles from the modelling study are drawn as light curves. The vertical axis is the height scaled by the depth of the convective boundary layer. The horizontal axis is nondimensionalized by mixed layer scaling.

The differences between the various observed and model derived profiles of horizontal velocity variance are less than the scatter in the data. These differences and the scatter in the data are large enough to suggest that the profile of the mean wind may be important to the profile of the horizontal velocity variance. The possible existence of two dimensional convective rolls in the higher wind speed situations could also affect the variances of u and v.

5.4.6 Buoyant Production of Turbulence Kinetic Energy

The normalized buoyancy flux profiles described above are equivalent to normalized profiles of the buoyant production of turbulence kinetic energy, TKE. Two other terms in the TKE budget can be measured from the Phoenix 78 aircraft data; turbulenct transport and dissipation. The pressure transport term is unmeasurable because of the problems of determining small pressure deviations from a horizontal average by an aircraft.

5.4.7. Dissipation of Turbulence Kinetic Energy

Profiles of the dissipation of TKE for five field experiments (AMTEX, Ashchurch, Eastern Colorado, Minnesota and Phoenix 78), an LES model (Deardorff, 1974b) and a tank experiment (Willis and Deardorff, 1974) are shown in Figure 5.12. The Phoenix 78 dissipation rates were determined from the amplitude of the inertial subrange w spectra as described in Chapter 4.2. The experimental results show the TKE dissipation decreasing rapidly through the lower CBL and then slowly up to z_i before again decreasing sharply at z_i. The Minnesota-Ashchurch composite TKE dissipation values are somewhat larger than the average and the Phoenix 78 values larger still. Difficulties in measuring dissipation may have caused some of the differences.

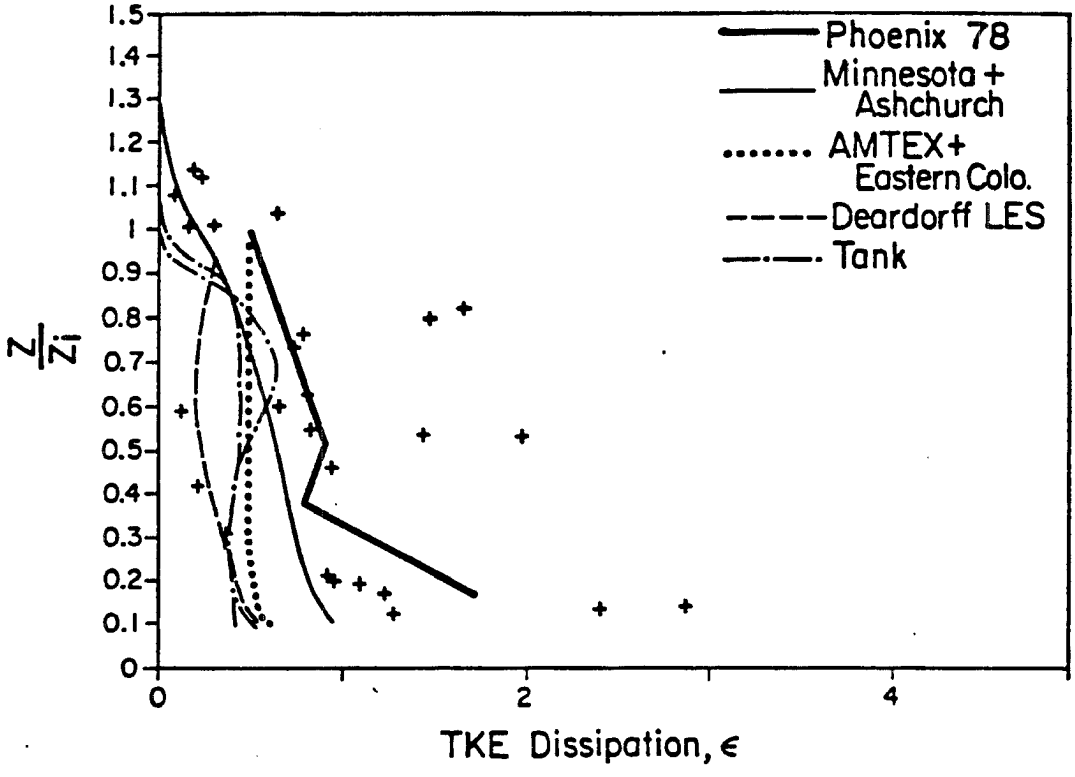

Fig. 5.12 Profiles of the dissipation of turbulence kinetic energy, ε, from Phoenix 78 and other observational and modelling studies. The heavy curve is the bin averaged profile fit to the plotted Phoenix 78 data points. The profiles from the other studies are drawn as light curves. The vertical axis is the height scaled by the depth of the convective boundary layer. The horizontal axis is nondimensionalized by mixed layer scaling.

However, results from the Minnesota experiment suggest that while the scaled dissipation profiles have a fairly universal shape, their amplitude varies considerably from case to case.

5.4.8 Turbulent Transport of Turbulence Kinetic Energy

Profiles of the turbulent transport of TKE for three field experiments (AMTEX, Eastern Colorado and Phoenix 78) and a tank experiment (Willis and Deardorff, 1974) are shown in Figure 5.13. All of the profiles are of the same general form with samll values near the surface and near z_i and large values in the middle of the CBL. The maximum values are 0.12 to 0.17 and occur at heights of from 0.4 to 0.5 z_i. The Phoenix 78 profile lies near the center of the range of reported results. The differences between the profiles are less than the scatter of the data.

5.4.9 Turbulent Transport of Buoyancy Flux

As seen for TKE, turbulent transport by convection can make a significant contribution to the budgets of turbulence statistics. Figure 5.14 shows the profiles of turbulent transport of buoyancy flux for three field experiments (AMTEX, Minnesota and Phoenix 78). All the profiles are zero at the surface, near zero at z_i and have a maximum near 0.1 z_i. The AMTEX and Phoenix 78 profiles match while the Minnesota profile has an amplitude about half as great and a maxima somewhat closer to the surface. Both the Phoenix 78 and AMTEX profiles are nearly linear above 0.1 z_i indicating that turbulent transport provides a uniform source of buoyancy flux throughout the bulk of the CBL. The profile for the Minnesota experiment lies outside the range of the Phoenix 78 data points while the AMTEX profile fits these data well.

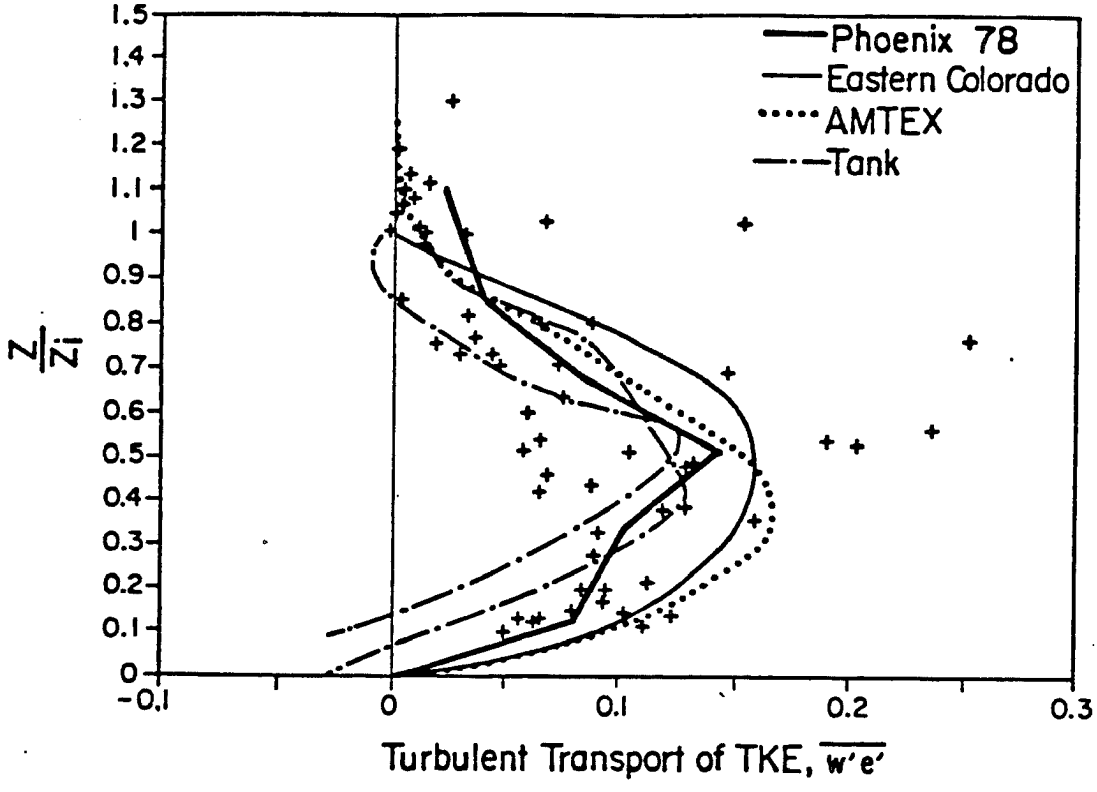

Fig. 5.13 Profiles of the turbulent transport of turbulence kinetic energy, $\overline{w'e'}$, from Phoenix 78 and other observational and modelling studies. The heavy curve is the bin averaged profile fit to the plotted Phoenix 78 data points. The profiles from the other studies are drawn as light curves. The vertical axis is the height scaled by the depth of the convective boundary layer. The horizontal axis is non-dimensionalized by mixed layer scaling.

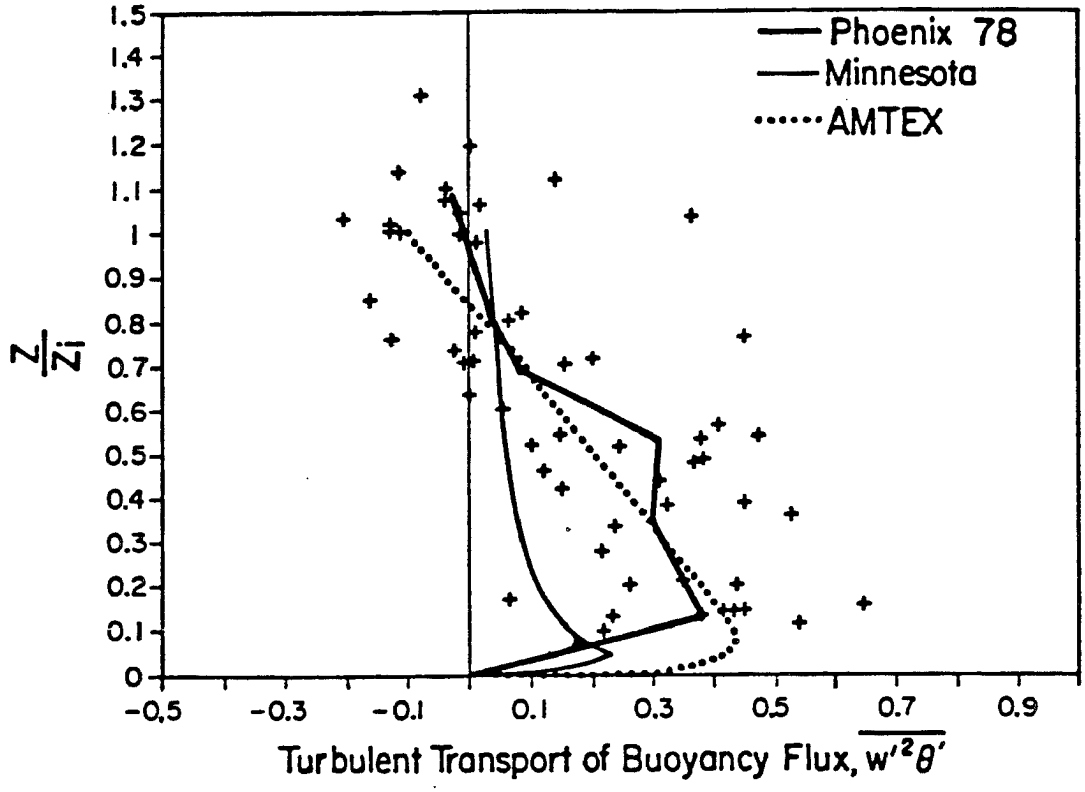

Fig. 5.14 Profiles of the turbulent transport of buoyancy flux, $\overline{w'^2\theta'}$, from Phoenix 78 and other observational studies. The heavy curve is the bin averaged profile fit to the plotted Phoenix 78 data points. The profiles from the other studies are drawn as light curves. The vertical axis is the height scaled by the depth of the convective boundary layer. The horizontal axis is nondimenionalized by mixed layer scaling.

5.4.10 Turbulent Transport of Temperature Variance

Figure 5.15 shows the turbulent transport of temperature or virtual temperature variance for the same three field experiments. Again the Phoenix 78 and AMTEX profiles are very similar while the Minnesota values are smaller in the lower CBL. All three profiles are concave upwards with a maximum at the surface and small values near z_i. It is interesting to note that despite the large temperature variances at z_i in all three experiments there is little turbulent transport of temperature variance near that level. This observation shows that the temperature variance is produced and dissipated locally throughout the upper CBL and inversion rather than being advected from a single source level at the inversion level. This is an important result for our conceptual understanding of how entrainment affects CBL turbulence.

5.4.11 Skewness of the Vertical Velocity Distribution

The skewness of the vertical velocity distribution $(\overline{w'^3}/(\overline{w'^2})^{3/2})$ is a measure of the asymmetry of the vertical velocity distribution. A positive vertical velocity skewness indicates that the updrafts are stronger than the downdrafts; a common feature of turbulence forced primarily by a buoyancy flux from the lower boundary. Figure 5.16 shows the vertical velocity skewness for three field experiments (AMTEX, Australia and Phoenix 78). The three profiles show the same general features, small values near the surface, larger values within the CBL and small values above z_i. The Australian profile of vertical velocity skewness shows the effects of an underestimate of z_i, the maxima is located too high in the scaled CBL and has too great and amplitude. The AMTEX profile is displaced equally on the other side

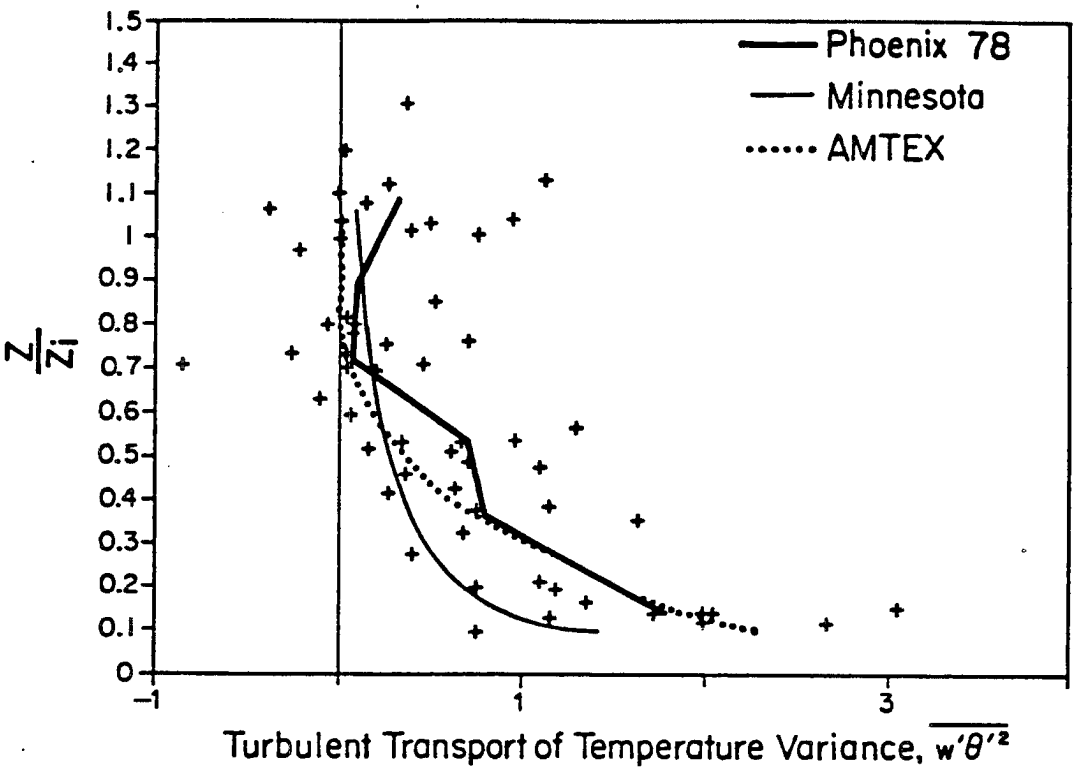

Fig. 5.15 Profiles of the turbulent transport of temperature or virtual temperature variance, $\overline{w'\theta'^2}$, from Phoenix 78 and other observational studies. The heavy curve is the bin averaged profile fit to the plotted Phoenix 78 data points. The profiles from the other studies are drawn as light curves. The vertical axis is the height scaled by the depth of the convective boundary layer. The horizontal axis is nondimensionalized by mixed layer scaling.

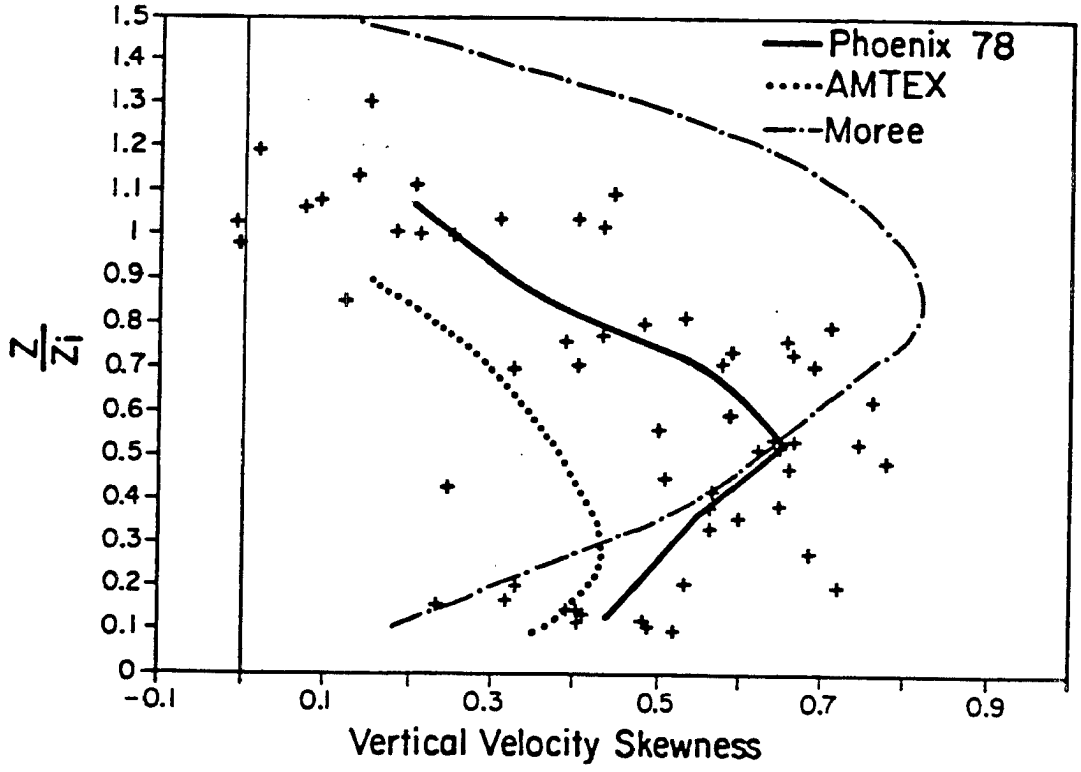

Fig. 5.16 Profiles of the skewness of the vertical velocity distributions from Phoenix 78 and other observational studies. The heavy curve is the bin averaged profile fit to the plotted Phoenix 78 data points. The profiles from the other studies are drawn as light curves. The vertical axis is the height scaled by the depth of the convective boundary layer. The horizontal axis is nondimensional.

of the Phoenix 78 profile. These profiles indicate considerable positive skewness of the vertical velocity distributions in all three experiments. These profiles also show that some effect, probably stable thermal stratification caused by cross inversion entrainment, leads to a decrease in the difference between updraft and downdraft velocities above the mid CBL.

5.5 Conclusions

The conditions of the observational studies described above range from cold air outbreaks over warm oceans to rolling terrain a few tens of kilometers from a major mountain range. These conditions are less than ideal for application of mixed layer scaling and yet this scaling has been found to work well for the individual experiments. There is very little variation in the forms of the vertical profiles of most turbulence statistics between these studies. Variations in the location of maxima and minima in the observed profiles of turbulence statistics between experiments are about plus or minus 10 percent of the inversion height. The locations of some features such as the zero crossing of buoyancy flux are more variable while the locations of others such as the maximum in downward buoyancy flux differ little between experiments. In general the profiles of turbulence statistics cluster to within about plus or minus 20 percent of the peak value. There are exceptions such as the value of temperature variance near z_i which are very poorly scaled by mixed layer similarity.

The LES and tank model results generally resemble the field observations rather closely. There are, however, some important differences. The models exhibit a linear buoyancy flux profile between the surface and the level of zero buoyancy flux whereas the

earth's atmopshere exhibits curved buoyancy flux profiles in this height range. This difference indicates either a significant difference in the handling of cross inversion entrainment of virtual potential temperature between the models and the atmosphere or the lack of mean vertical motions in the models. This difference is found to a lesser degree in some other statistics such as virtual temperature variance. Most of the turbulence statistics compared show no detectable difference from this source.

The most obvious source of variation between CBL experiments is the cross inversion entrainment flux of buoyancy. This quantity has been observed to vary from -1.0 to 0.0 of the surface bouyancy flux between individual atmospheric profiles (Stull, 1976) and from -0.2 to -0.1 between the mean profiles published for these experiments. Scatter of the data prohibit tracing the effects of these variations in the observations. However, the models show that increased downward fluxes of buoyancy at z_i lead to proportionality larger increases in the maximum of virtual temperature variance at z_i. Increased entrainment flux also leads to a lowering of the minimum of virtual temperature variance in the models as the source of variance at the inversions dominates the surface source for a greater fraction of the CBL depth. As the height of this minimum decreases it's magnitude increases.

The observed turbulence profiles for experiments in more uniform terrain and the results from CBL models cluster on both sides of the Phoenix 78 profiles. Thus, the rolling terrain and nearby mountains at the BAO site used for Phoenix 78 have not biased these turbulence statistics away from those which are observed in more ideal conditions.

The intercomparison of the profiles of CBL turublence statistics described above shows that mixed layer similarity can be applied under a variety of less than ideal conditions with only a moderate degradation of results. In addition, several of the sources of variation between observations can be accounted for at least qualitatively. The Phoenix 78 results do not show any bias compared with other CBL experiments except for dissipation of TKE.

6. Phoenix 78 Aircraft Observations of Thermals and Their Environment

6.1 Introduction

This chapter is part II of a series on the turbulence structure of the convective boundary layer. The focus of this part is on aircraft observations of the turbulence structure of thermals and their environment from the Phoenix 78 convective boundary layer experiment.

Previous chapters include a more detailed description of the setting and aircraft operations of the experiment. An intercomparison of the profiles of turbulence statistics from a number of observational and modelling studies makes up the core of Chapter 5. It is shown in Chapter 5 that the effects of the terrain at the BAO site do not alter these profiles away from those observed over more ideal surfaces.

An observational study of the budgets of buoyancy, convective mass flux and vertical velcoity in thermal updrafts and environmental downdrafts is reported in Chapter 7. All of the terms in these budgets are either measured or diagnosed from the observed turbulence profiles. The resulting description of the dynamics of thermals helps to explain the results of this chapter.

Thermals are the buoyantly driven convective eddies which generate most of the turbulence in the unstable planetary boundary layer. These eddies are composed of thermal updrafts and their

compensating environmental downdrafts, both of which span the depth of the convective boundary layer (CBL). The horizontal scales of thermal circulations range around 1.5 times the depth of the CBL, z_i (Caughey and Palmer, 1979). Thermals are both the result of and the primary controlling mechanism for the mean CBL stability profile (Lenschow and Stephens, 1982; Wyngaard and Brost, 1984). The earth's surface is the buoyancy source for the CBL, providing heat and/or moisture to its lower boundary (Deardorff, 1970; Kaimal et al. 1976, Lenschow and Stephens, 1980). The structure and dynamics of the eddies which arise from this addition of buoyancy are important controlling factors for diffusion within the CBL (Lamb, 1978). These thermal circulations help drive entrainment across the capping inversion (Caughey and Palmer, 1979; Raymont and Readings, 1974).

A conditional sampling technique is needed to distinguish thermals from their environment in data series. By conditional sampling, the turbulence in thermal updrafts and environmental downdrafts can be studied separately and compared. Such a technique should have a physical basis in the dynamics of CBL turbulence. The more closely the technique is based on universal characteristics of CBL turbulence the more general will be its applicability. The conditional sampling criteria developed for this study are based on the spectral dynamics of CBL turbulence. The advantages of this basis will be discussed in the procedures section. Using this technique, the size, number density[1], buoyancy and vertical velocity profiles

---

[1]The number density of thermals is the number of thermals encountered in a flight segment of length equal to the depth of the CBL. This quantity is a measure of the average separation between thermals.

of thermal updrafts and environmental downdrafts are determined. The contributions of the convective circulations to the variances of buoyancy and the three components of velocity are computed from the aircraft data. Their contributions to the budget of turbulence kinetic energy are also determined.

The most extensive sets of atmospheric observations of the structure and dynamics of thermals have been obtained from maritime situations. Lenschow and Stephens (1980, 1982) reported observations from the Air Mass Transformation Experiment (AMTEX) which was conducted in the East China Sea during Feburary of 1975. Khalsa and Greenhut (1982) and Greenhut and Khalsa (1985) reported observations from the equatorial central Pacific Ocean. The conditional sampling techniques used in these maritime studies were based either directly or indirectly on the strong moisture signatures provided by the thermals. The present study provides similar information about the structure and dynamics of thermals over continental plains. However, it has been necessary to develop a new conditional sampling technique because of the relatively dry conditions that exist over land.

The conditional sampling criteria used in this study simplify the comparison of observational and numerical model results. The numerical model results of Lamb (1978), Deardorff (1974a, b), Moeng (1984) and Moeng and Wyngaard (1984) will be compared with the Phoenix 78 observations. The laboratory model results of Willis and Deardorff (1974) will also be compared with the Pheonix 78 observations where possible.

Section 6.2.1 outlines the data collection procedures. The theory and practice of conditional sampling of data series to

distinguish thermals is discussed in section 6.2.2. The Phoenix 78 observations of the thermodynamic and kinematic structure of thermals and their environment are reported in section 6.3. These results are compared with those of previous observational studies. The results are summarized in section 6.4.

6.2 Procedures

6.2.1 Data Collection

The turbulence data used in this study were collected by NCAR Queenair aircraft during the September 1978 Pheonix CBL experiment. This experiment was carried out at the Boulder Atmospheric Observatory (BAO) on the Colorado high plains 25 km east of the Front Range of the Rocky Mountains. The aircraft observations are limited to altitudes above 0.1 z_i because of flight restrictions over populated terrain. Thus, these observations do not extend down into the surface layer. Data from 58 horizontal flight legs distributed more or less evenly from 0.1 to 1.3 z_i were used to produce each of the turbulence profiles presented in this study. The flight legs were approximately 35 km long: 20 or more times the CBL depth. These data cover the depth of the mixed layer and the capping inversion. The experiment is described in more detail in the procedures chapter.

The Phoenix 78 aircraft operations are described in Hildebrand (1979). Details of the aircraft and sensors are given in Kelley and Lackman (1976), Lenschow and Spyers-Duran (1982), NCAR (1977, 1981), and Spyers-Duran and Baumgardner (1983). Temperature and the three components of velocity were sampled at wavelengths ranging from 8 m to 35 km. Temperature was measured by a Rosemont platinum resistance thermometer while the three components of velocity were

measured with a fixed vane gust probe/inertial navigation system combination.

The weather conditions during the Phoenix 78 experiment are summarized in Wolfe (1979). The data presented in this paper were collected from nearly clear undisturbed convective boundary layers. The ratio of boundary layer depth to Monin-Obukov length ranged from -15 to -131, indicating the dominance of buoyant convection over shear-produced turbulence. For this study, the time scale for changes in the controlling parameters of CBL turbulence was much longer than the time scale of the turbulence itself. Therefore, the turbulence should have been quasi steady state and the normalized turbulence profiles should have been independent of time (Kaimal et al., 1976).

6.2.2 Distinguishing Thermals from their Environment

6.2.2.1 Conditional sampling methods of previous studies

A number of conditional sampling methods have been used in the past to distinguish thermals from their environment. These techniques specify conditions for determining whether a segment of the data series should be included in the sample series for thermals or the sample series for their environment. Thresholds on the amplitude and spatial extent of some turbulence event are generally used to distinguish thermals from their environment in this manner. The amplitude threshold is the basic criteria for distinguishing thermals. The spatial extent requirement is included to keep small scale perturbations on thermals from being interpreted as breaks between separate thermals. This approach requires that the horizontal scales of thermals be known a priori and that a type of turbulent event uniquely associated with thermals be identified. Because of the type of

indicator event used, many of the previously used methods are applicable only in limited regions of the CBL or over certain types of surfaces. In addition, the thresholds were often arbitrarily selected. A more generally applicable method for distinguishing thermals from their enviornment will be developed in this section.

Positive buoyancy is a good indicator of thermals in the surface layer, the free convection layer and the lower parts of the mixed layer (Grant, 1965; Warner and Telford, 1967; Manton 1977; Coulman, 1978; Greenhut and Khalsa, 1982). However, in the upper third of the CBL, thermals become negatively buoyant as they penetrate into more stably stratified air. Therefore, the positive buoyancy criterion is inapplicable through at least a third of the depth of the CBL.

Positive moisture perturbations can be used as thermal indicators in situations where the turbulent moisture flux is significant and upward throughout the depth of the CBL (Lenschow and Stephens, 1980; Greenhut and Khalsa, 1982). This criterion is inapplicable over relatively dry land surfaces such as that of eastern Colorado where the current study was conducted.

Upward-directed vertical velocity is the most generally applicable indicator of thermal updrafts. The choice of a w threshold and the minimum thermal size depends on what scales of turbulent phenomena are to be counted as thermals. Greenhut and Khalsa (1982) and Khalsa and Greenhut (1985) used different w thresholds to distinguish up and downdrafts from the environment. These thresholds were related to w variances so that they automatically adjusted for varying levels of turbulence. A minimum thermal size of 40 m was used. These criteria were selected to retain small vertical velocity

perturbation events with well defined temperature and humidity perturbations. Nonetheless, the selection of thresholds was basically arbitrary.

6.2.2.2 Conditonal sampling method of the current study

The technique for distinguishing thermals used in the present study is also based on identification of w perturbation events. Determination of physically meaningful minimum and maximum horizontal scales for thermal circulations has eliminated much of the arbitrariness in threshold selection. Thermals occur at scales between the mesoscale and the inertial subrange. Thus, the maximum horizontal scale of thermal circulations should be the short wavelength limit of the mesoscale and the minimum horizontal scale of thermal circulations should be the long wavelength cutoff of the inertial subrange. These scales have been determined from the variance spectra of the linearly detrended series of temperature, vertical velocity and horizontal wind speed shown in Figures 6.1 and 6.2. These spectra show the distribution of variance in the various wavelength bands sampled, from 8 m to 35 km. The times and heights of the flight legs included in the composite spectra for vertical velocity and horizontal wind speed were listed in Table 4.1. The eight temperature spectra shown are a representative subset of these.

The spectra were normalized for ease of comparison. The normalization aligns the spectra from different flight legs but does not change their shape. The alignment of the spectra results from the scaling of wavelength by the depth of the CBL which aligns the peaks and from the scaling of the spectral density by the dissipation rate which collapses the spectra onto a single curve in the inertial

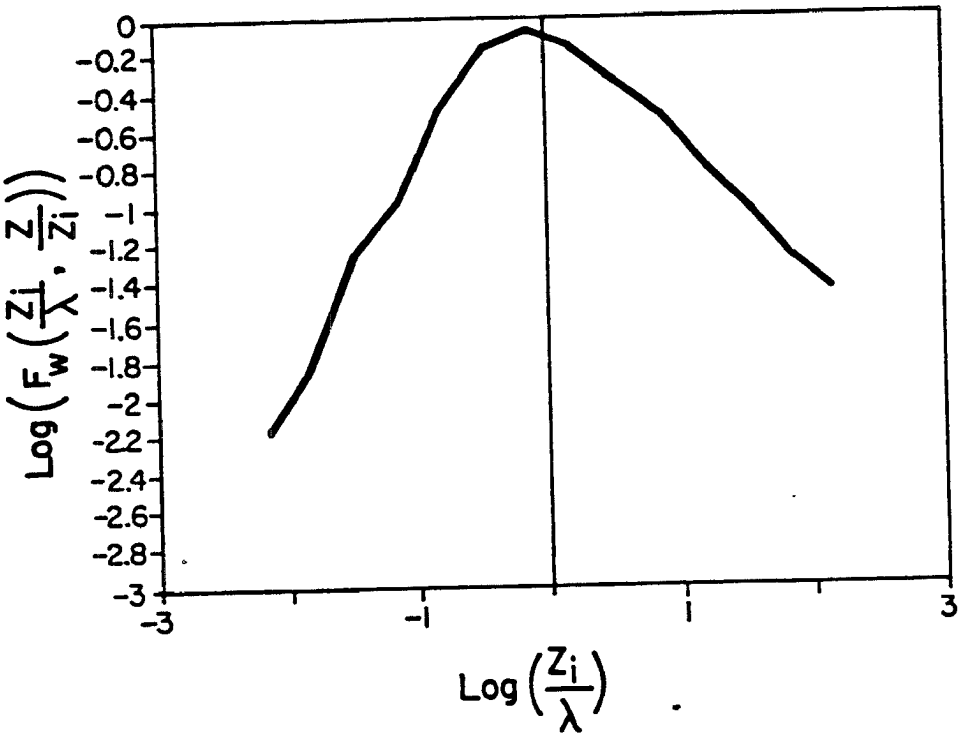

Fig. 6.1a The normalized vertical velocity spectrum for levels between 0.2 and 0.8 Zi. Mixed layer scaling was used for the normalization. This composite spectrum was computed from the spectra of 15 horizontal flight legs from Phoenix 78. The horizontal axis is the logarithm of convective boundary layer depth divided by wavelength. The vertical axis is the logarithm of the normalized spectral density.

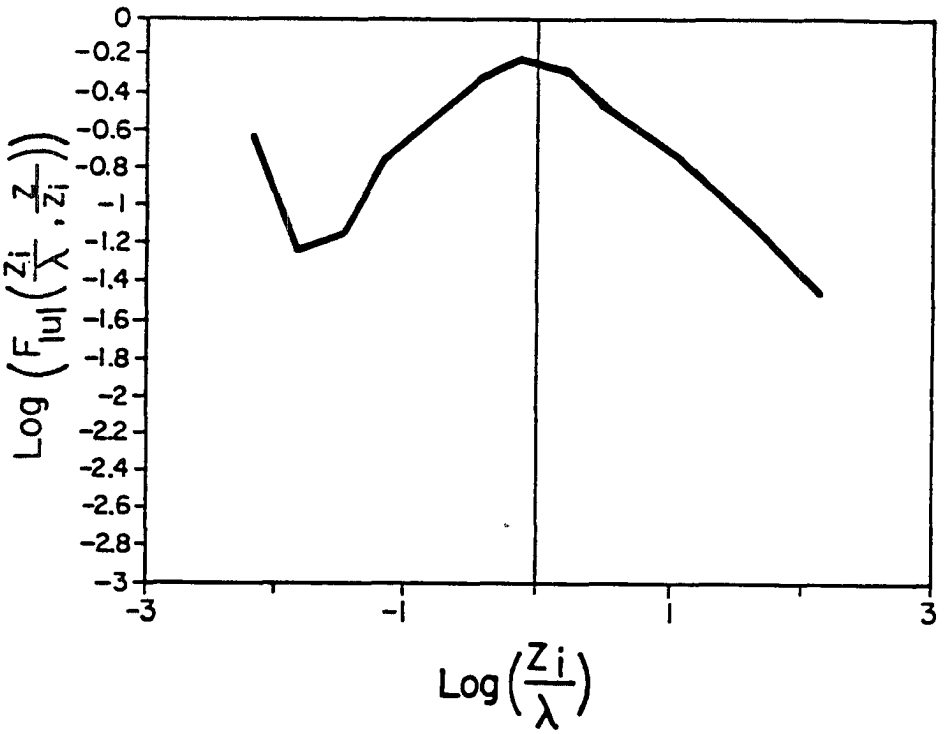

Fig. 6.1b The normalized horizontal wind speed spectrum for levels between 0.2 and 0.8 Zi. Mixed layer scaling was used for the normalization. This composite spectrum was computed from the spectra of 15 horizontal flight legs from Phoenix 78. The horizontal axis is the logarithm of convective boundary layer depth divided by wavelength. The vertical axis is the logarithm of the normalized spectral density.

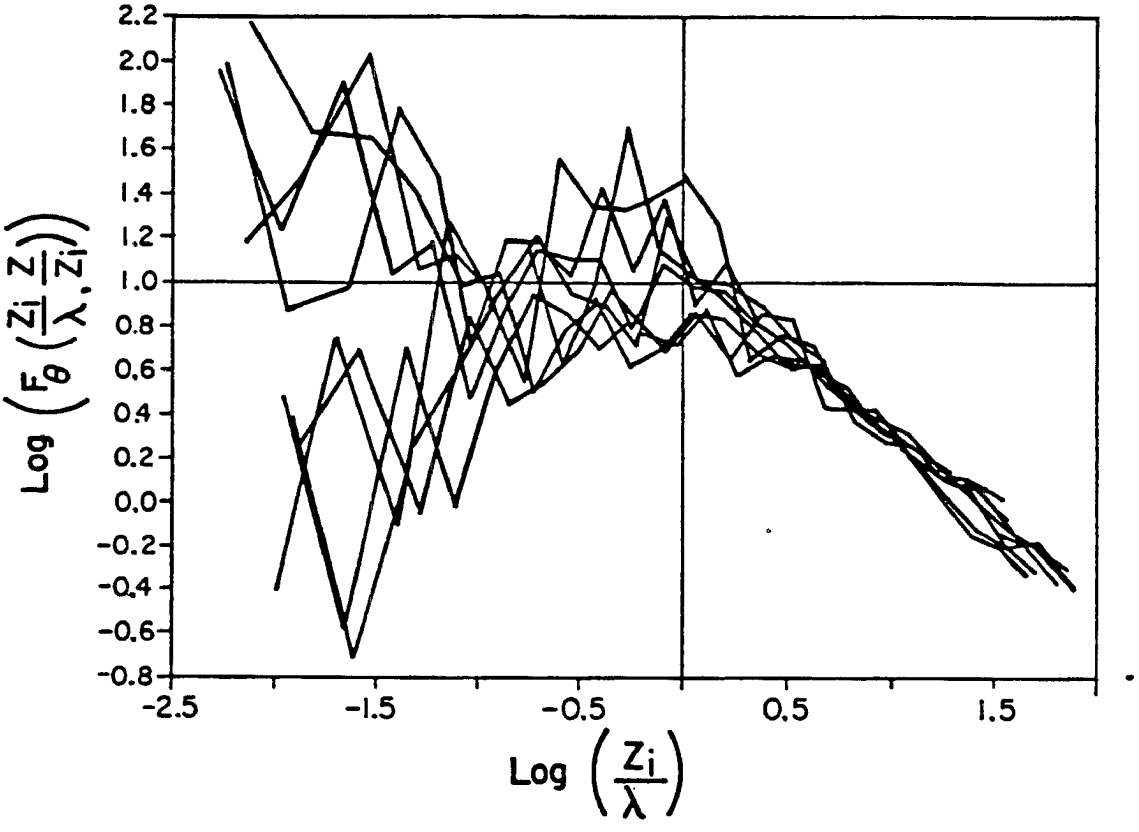

Fig. 6.2 Eight normalized temperature spectra for levels between 0.2 and 0.8 Zi. Mixed layer scaling was used for the normalizaiton. The horizontal axis is the logarithm of convective boundary layer depth divided by wavelength. The vertical axis is the logarithm of the normalized spectral density.

subrange. The spectral variance densities and wavelengths have been normalized by the mixed layer scaling parameters following Kaimal et al. (1976). Normalized mixed layer turbulence spectra take the form:

$$\frac{(2\pi)^{2/3}\ \lambda S_Q(\lambda)}{c\alpha Q_*^2 \psi_Q} = F_Q(z_i/\lambda,\ z/z_i)$$

$$= \left(\frac{z_i}{\lambda}\right)^{-2/3}, \text{ in the inertial subrange}$$

where z_i = mixed layer depth, c is the sampling direction correction, α is the inertial subrange constant, $S_Q(\lambda)$ is the spectral variance density for variable Q, ψ_Q is the nondimensionalized variance dissipation rate factor, and λ is the wavelength. The values of c and α and the form of ψ_Q depend on the variable, Q.

At the largest scales sampled, quasi two-dimensional mesoscale eddies dominate. These eddies have much more horizontal wind speed variance than they do vertical velocity variance. The contribution of these mesoscale eddies can be eliminated from the turbulence data by high pass filtering with a cutoff wavelength of 10 z_i, less than a third of the flight leg length. This cutoff is within the spectral gap between the mesoscale and microscale contributions to the variance of horizontal wind speed and temperature (Figures 6.1 and 6.2). This cutoff wavelength scales with boundary layer depth and so remains proportional to the dominant horizontal scale of thermals (Kaimal et al. 1976). This mesoscale cutoff wavelength is $6.\bar{6}$ times the dominant wavelength of thermals.

The microscale variance which remains after the highpass filtering is composed of two components. At horizontal scales larger

than 0.1 z_i there is variance created by buoyant production of these scales. Variance is not produced at smaller scales. Instead, a downscale inertial cascade from the production scales towards the dissipation scales occurs. Thermals are the upward legs of the buoyantly driven circulations which occupy the scales at which buoyant production of variance occurs. Therefore, a physically meaningful criterion for distinguishing thermals from their environment is that w be positive on these longer horizontal scales. This criterion was implemented by lowpass filerting the w data with a cutoff wavelength of 0.1 z_i and then disignating as part of the sample of thermals those points whose filtered vertical velocities were positive. The dominant horizontal scale for thermals is 15 times this inertial subrange cutoff wavelength.

This set of cirteria is based entirely on the spectral dynamics of CBL turbulence and thus has a physical basis. However, the exact choice of the two cutoff wavelengths remains somewhat arbitary. The transition from mesoscale to microscale turbulence occurs in a broad spectral gap. The exact location of the bottom of this gap varies with the relative intensity of mesoscale and microscale turbulence (Figure 6.2). Therefore, the wavelength above which mesoscale turbulence dominates the spectra varies about the cutoff wavelength of 10 z_i. The transition from the microscale variance producing subrange to the inertial variance cascade surbange of the spectra is also gradual. The cutoff wavelengths used in this study were selected so that all the microscale eddies which contribute to the buoyant production of vertical velocity occurred were included in the series which was used to identify thermal updrafts. These criteria are less

restrictive of thermal updrafts than some of those used in the past because the expected vertical velocity at the thermal boundaries is zero rather than some positive value (Greenhut and Khalsa, 1982; Khalsa and Greenhut, 1985).

6.3 Observations

6.3.1 Fractional Coverage, Size and Spacing of Thermals

The conditional sampling criteria developed in the previous section are used to distinguish thermal updrafts from the intervening environmental downdrafts. The data from each of 58 horizontal flight legs are partitioned between these two categories using these criteria. This partitioning permits the separate computation of turbulence statistics for the regions in thermal updrafts and those in environmental downdrafts.

A fundamental feature of a field of thermal updrafts is the fractional area coverage. A smooth vertical profile, drawn to fit the 58 measured values of this quantity, is shown in Figure 6.3. The fraction of the area covered by thermal updrafts decreases from approximately 50 percent near the surface to a minimum of less than 43 persent at 0.52 z_i. The fraction of the area covered by thermal updrafts increases again above this level to reach 48 percent at z_i and 50 percent at the level where turbulence ceases.

Previous observational studies have yielded a vareity of values for the fractional area coverage by thermals. Manton (1977) reported a value of 0.42 for the lower CBL. Coulman (1978) found fractional coverage by thermals to range from 0.36 to 0.40 with a minimum at intermediate levels in the CBL. Lenschow and Stephens (1982) give the value as 28 percent for the entire depth of the AMTEX CBL. Greenhut

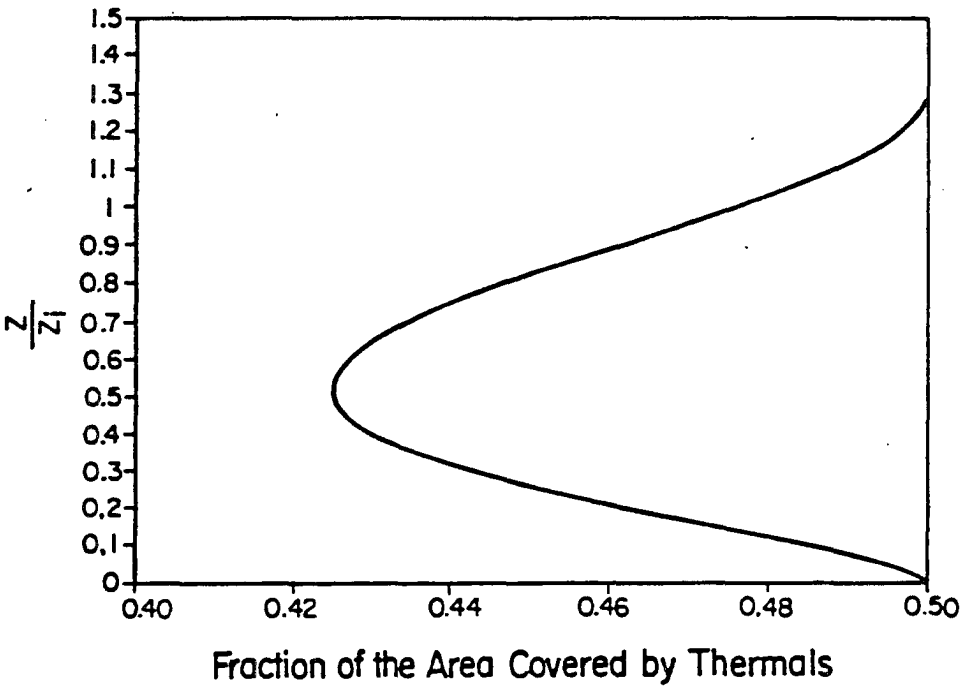

Fig. 6.3 The vertical profile of the fraction of the area covered by thermals. The vertical scale is the height divided by the depth of the convective boundary layer.

and Khalsa (1985) computed 16 percent coverage by updrafts, 24 percent coverage by downdrafts and designated the remaining 60 percent as environment. Their observtions were taken at 0.3 z_i over the central equatorial Pacific Ocean. The two studies with the largest fractional coverage by thermals used temperature thresholds selected such that the expected value of w at the threshold would be zero. The other studies used more restrictive thresholds.

Lamb (1978) used large eddy simulation (LES) methods to estimate the fractional area coverage by thermals. The limited horizontal resolution of the numerical model acted as a minimum horizontal scale for thermals. The amplitude threshold was zero w. The fractional area coverage profile had values approaching 50 percent near the surface, a minimum of about 37 percent near 0.8 z_i and returned to values near 50 percent above z_i. This profile is qualitatively similar to that of the present study. The large amount of data available from a LES increases the precision permitting resolution of structural details of the profile which could have been lost in the data scatter of previous observational studies.

These results show that the fractional area coverage by thermals is less than 50 percent throughout most of the CBL. Fractional area coverages approach 50 percent only in the lowest and highest layers. Estimates of the minimum coverage range from 0.36 to 0.43 for the studies which used a zero expected vertical velocity threshold.

Thermals and the environmental regions between them come in a variety of sizes. The size distribution of thermals can be approximated by the distribution of the length of flight path segments inside thermals. This measured distribution is presented in Figure 6.4 for

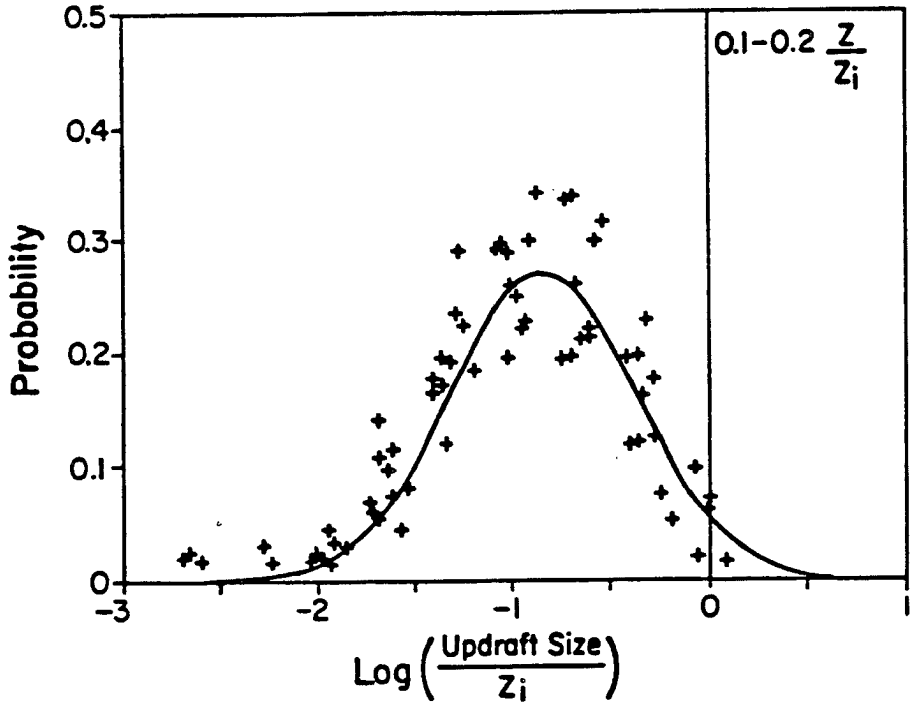

Fig. 6.4a-f Normalized histograms of thermal updraft size for six height bands in the convective boundary layer and capping inversion. The horizontal axis is the logarithm of thermal size divided by the depth of the convective boundary layer. The vertical axis is frequency of occurrence normalized so that the area under the curve equals unity. The observations are marked as +. The solid lines are lognormal distributions plotted for comparison.

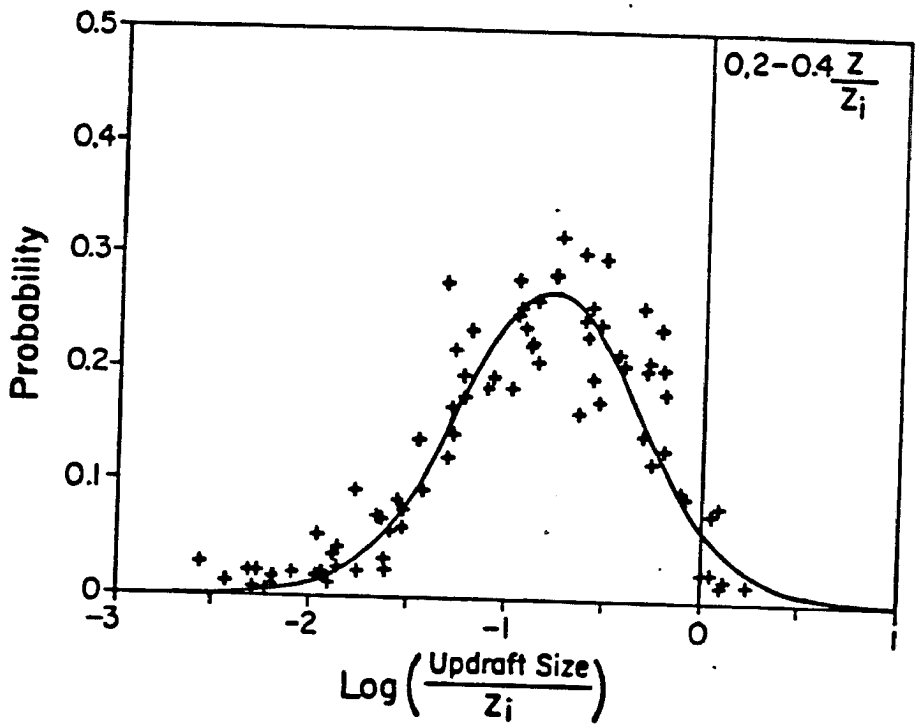
0.5
0.4
0.3
0.2
0.1
0
Probability
0.2-0.4 Z/Zi
-3
-2
-1
0
1
Log (Updraft Size / Zi)

Fig. 6.4b

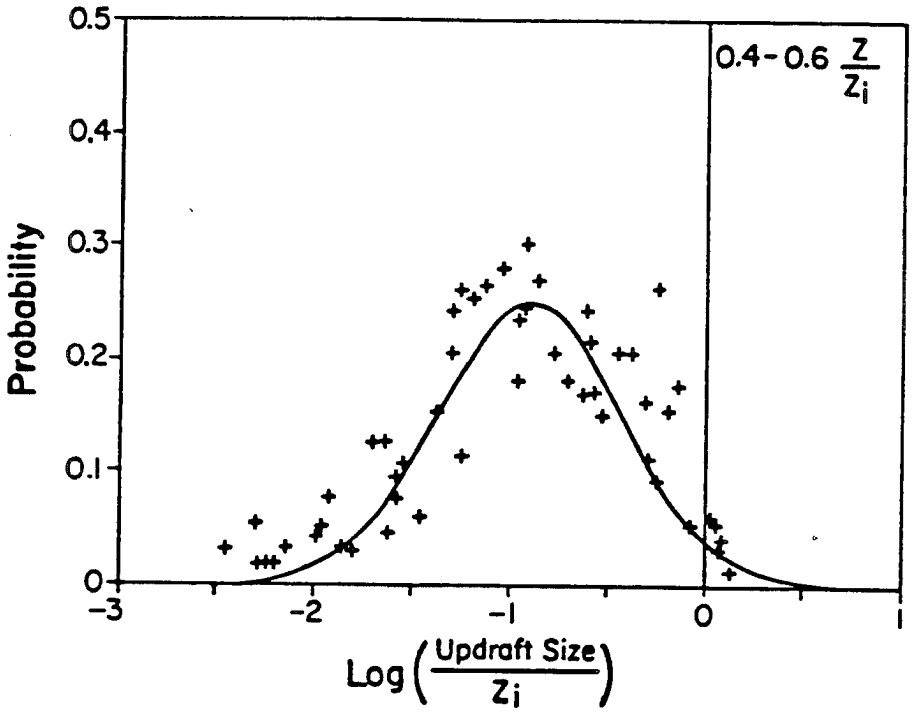
0.5
0.4
0.3
0.2
0.1
0
Probability
0.4-0.6 Z/Zi
-3
-2
-1
0
1
Log (Updraft Size / Zi)

Fig. 6.4c

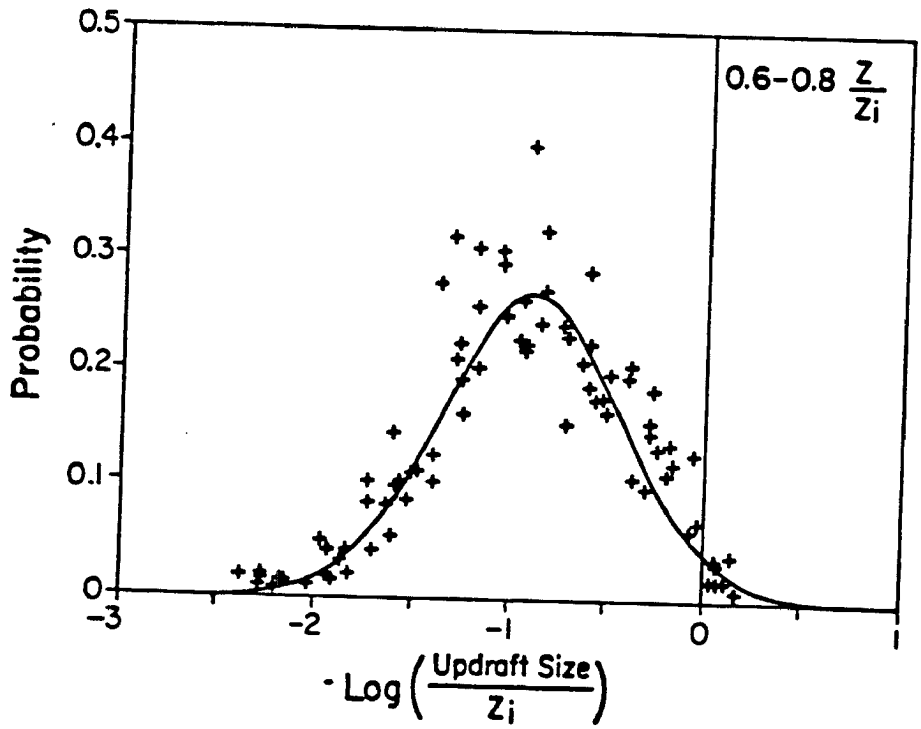
0.5
0.4
0.3
0.2
0.1
0
Probability
0.6-0.8 Z/Zi
-3
-2
-1
0
1
- Log (Updraft Size / Zi)

Fig. 6.4d

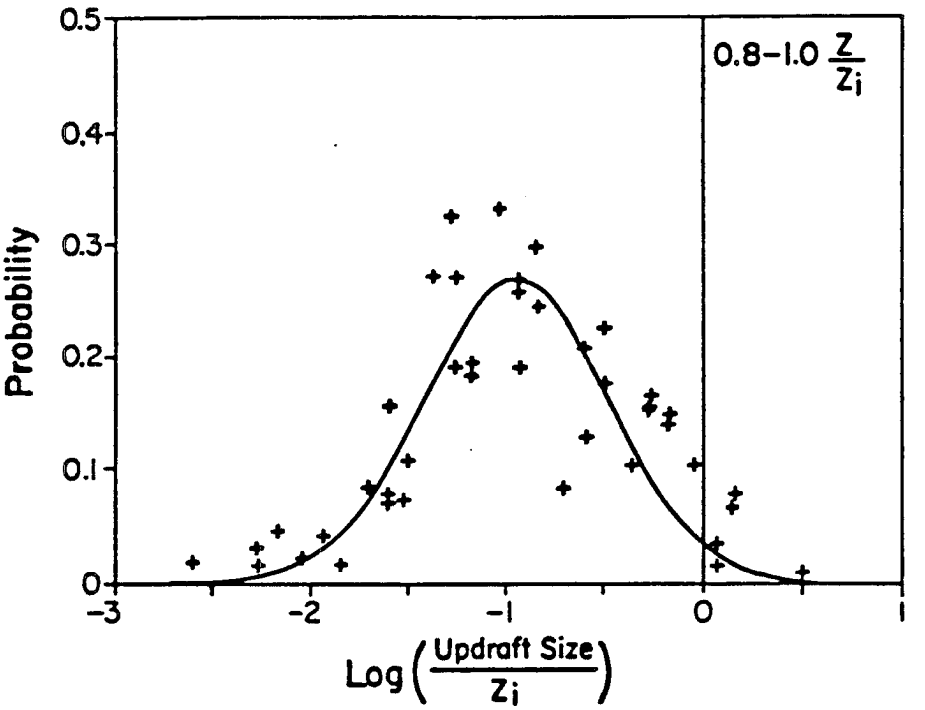
0.8–1.0 Z/Zi
Probability
0.5
0.4
0.3
0.2
0.1
0
-3
-2
-1
0
1
Log (Updraft Size / Zi)

Fig. 6.4e

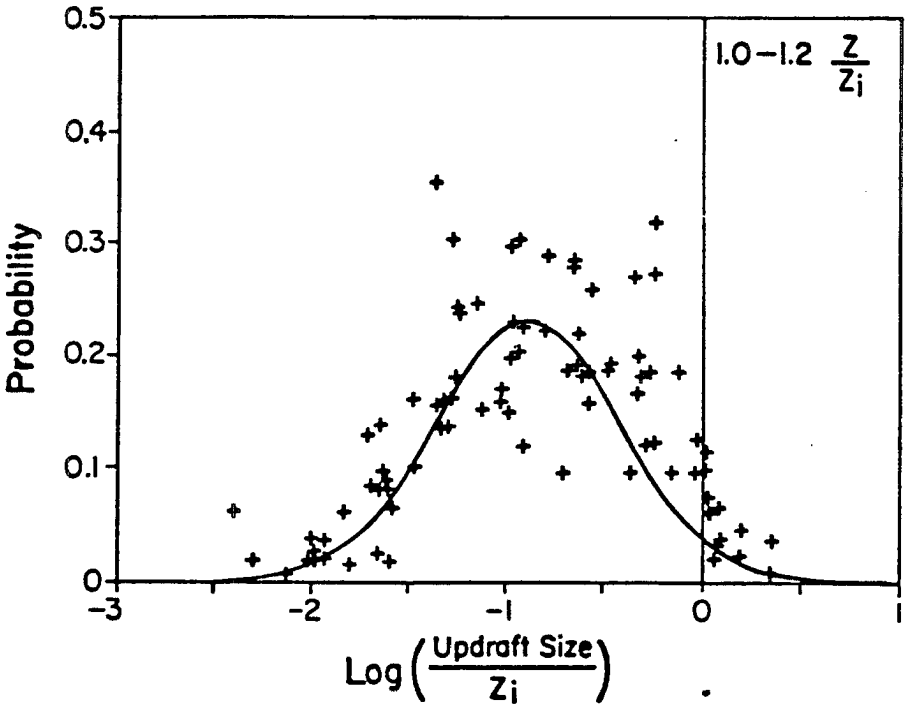
0.5
0.4
0.3
0.2
0.1
0
Probability
1.0–1.2 Z/Zi
-3
-2
-1
0
1
Log (Updraft Size / Zi)

Fig. 6.4f

six contiguous height ranges within the CBL and the capping inversion. These distributions reflect both the size distribtuion of the thermals and the random nature of the intersection of the flight paths with their boundaries. If the environment surrounds thermals, this distribution would be biased toward shorter lengths. However, if the thermals surround regions of downdrafts, this distribution would be biased towards longer lengths. These biases result from the geometry of the thermals as they are intersected by the aircraft flight path. The observed thermal size distributions are approximately lognormal. The environmental downdraft size distributions are shown in Figure 6.5. These distribtions are also approximately lognormal.

Lopez (1977) showed that convective cloud sizes are lognormally distributed as well. Lopez proposed two mechanisms for the genesis of lognormal distributions for convective element sizes. The first mechanism is stochastic growth in which entrainment is a random variate proportional to size of the convection element. The second mechanism is stochastic formation, in which merger of small elements leads to the final lognormal distribution. Both of these mechansims are compatible with what is known of the formation of thermals.

The observed distribution of the sizes of updrafts may, however, be an artifact of the limited resolution of any observational method. If the actual distribution of sizes were exponential, smoothing during the observational process would result in a distribution which approximates the gamma. The scatter in the current data prohibits distinction between the gamma distribution and the similarly shaped lognormal distribtion. The fact that the observed modes of the thermal size distributions are within a factor of two of the cutoff

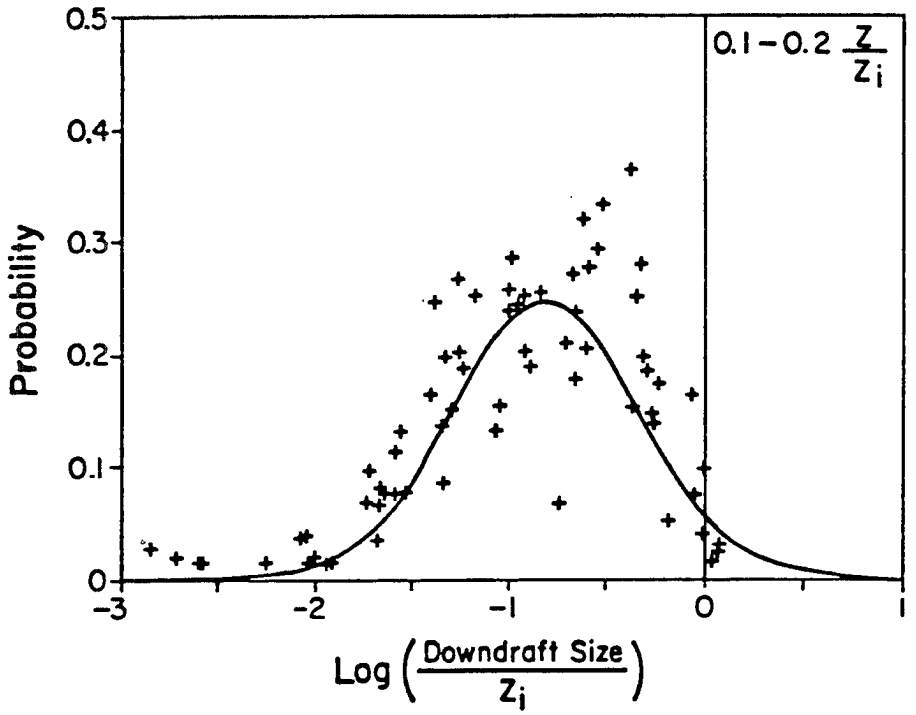

Fig. 6.5a-f Normalized histograms of environmental downdraft size for six height bands in the convective boundary layer and capping inversion. The horizontal axis is the logarithm of downdraft size divided by the depth of the convective boundary layer. The vertical axis is frequency of occurrence normalized so that the area under the curve equals unity. The observations are marked as +. The solid lines are lognormal distributions plotted for comparison.

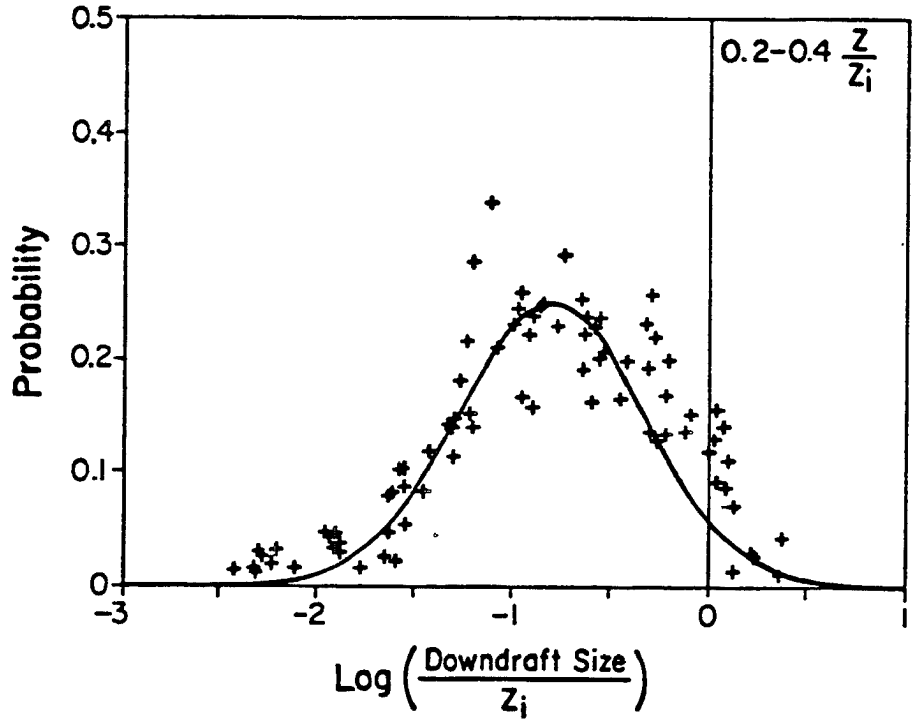
0.5
0.4
0.3
0.2
0.1
0
Probability
0.2-0.4 Z/Zi
-3
-2
-1
0
1
Log (Downdraft Size / Zi)

Fig. 6.5b

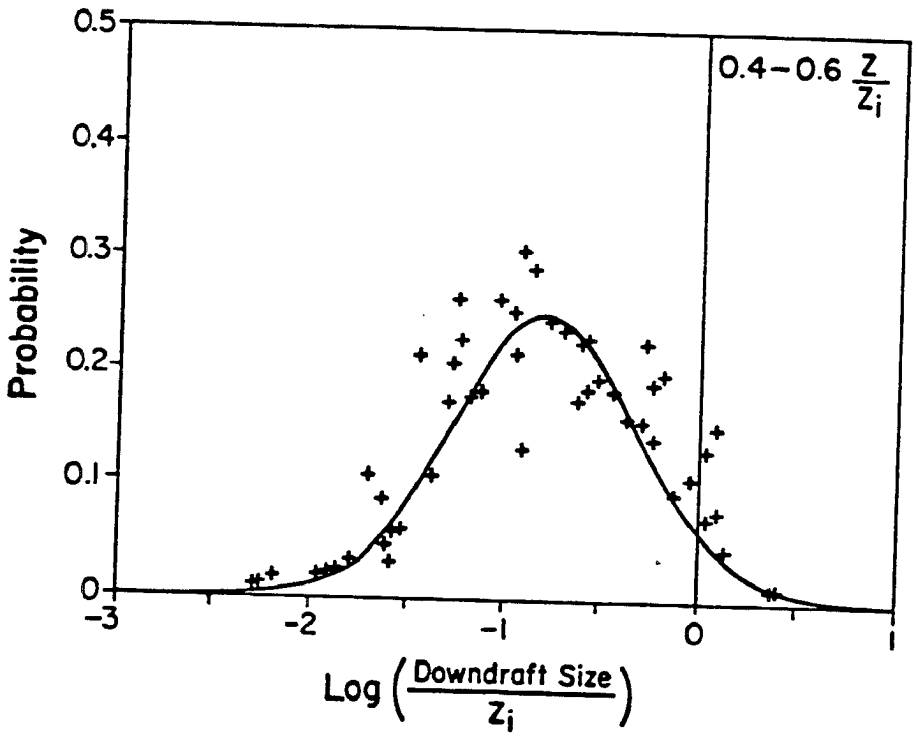
0.5
0.4
0.3
0.2
0.1
0
Probability
0.4–0.6 Z/Zi
-3
-2
-1
0
1
Log (Downdraft Size / Zi)

Fig. 6.5c

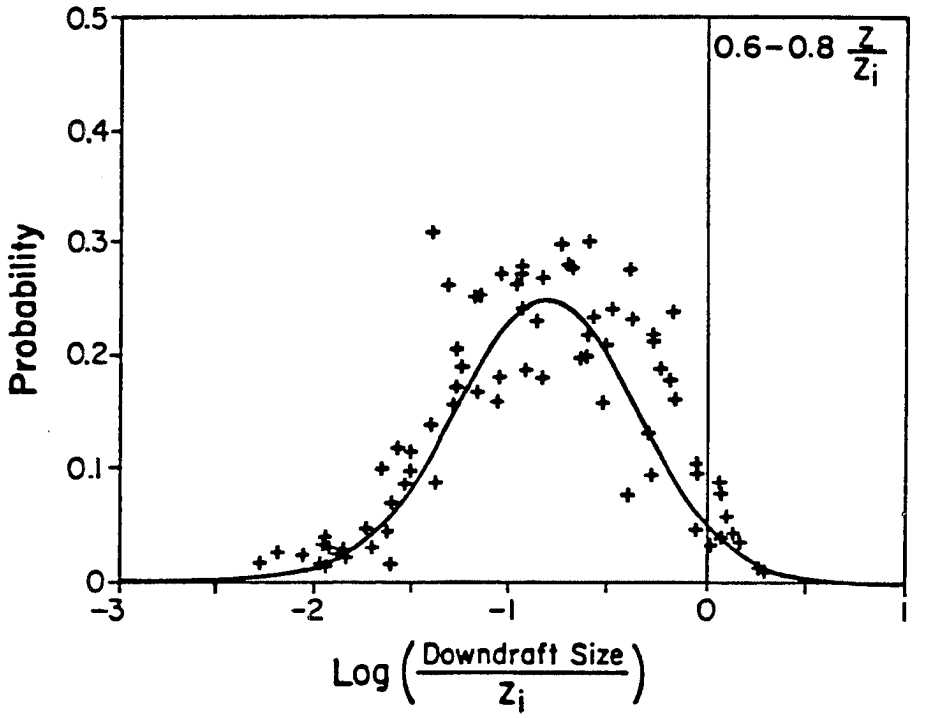
0.6-0.8 $\frac{Z}{Z_i}$
Probability
0.5
0.4
0.3
0.2
0.1
0
-3
-2
-1
0
1
Log $\left(\frac{\text{Downdraft Size}}{Z_i}\right)$

Fig. 6.5d

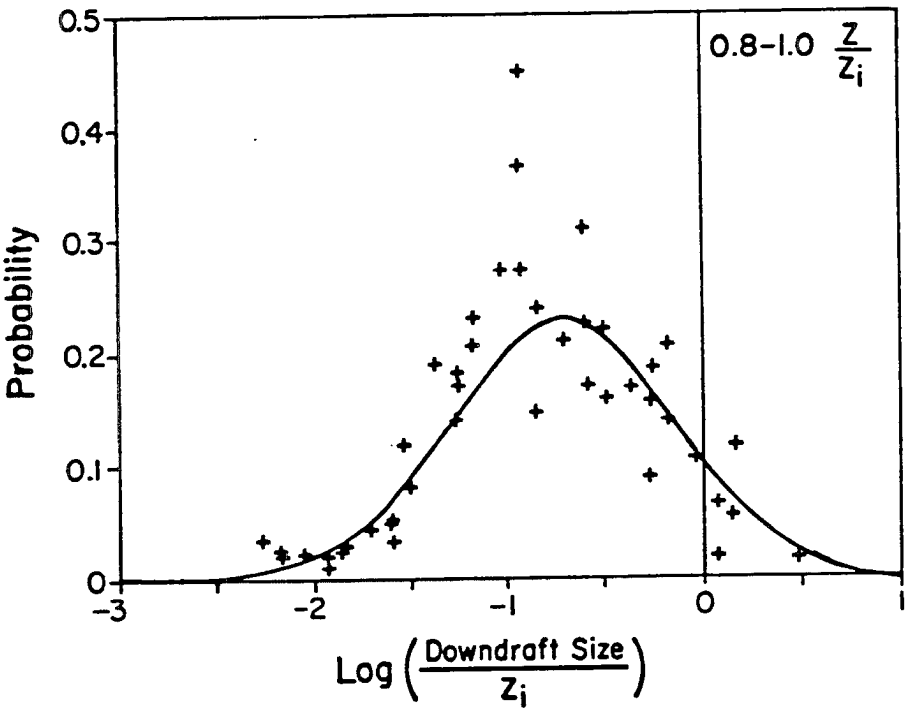
0.5
0.4
0.3
0.2
0.1
0
Probability
0.8-1.0 $\frac{z}{z_i}$
-3
-2
-1
0
1
Log $\left(\frac{\text{Downdraft Size}}{z_i}\right)$

Fig. 6.5e

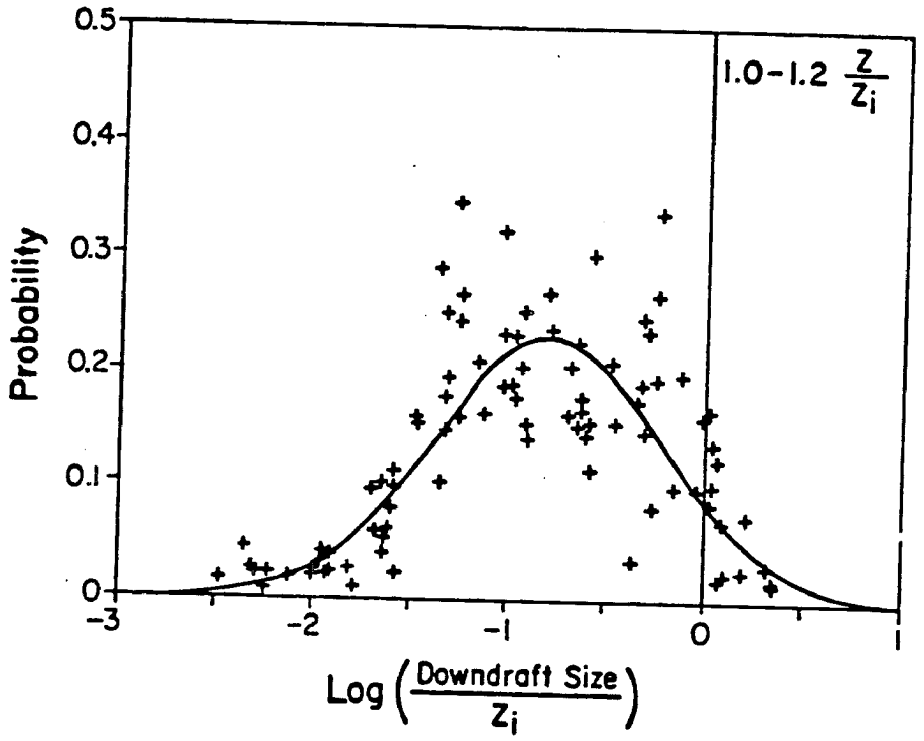
0.5
0.4
0.3
0.2
0.1
0
Probability
1.0-1.2 Z/Zi
-3
-2
-1
0
1
Log (Downdraft Size / Zi)

Fig. 6.5f

wavelength of the filter used to identify thermals suggests that the number of small updrafts has been greatly reduced by the identification process. Therefore, it is possible that the actual distribution of updraft sizes is exponential. However, the distribution of buoyantly driven eddy sizes is not the same as that of updraft sizes because the smaller scales of eddies are driven by the inertial cascade of kinetic energy rather than by buoyancy. The distributions of thermal and gap sizes shown here should reflect this distinction because of the physcial significance of the filter cutoff wavelengths.

The geometric mean of a lognormal distribution is the value which is observed most frequently, the mode of the distribution. It is computed as the exponential of the arithmetic mean of the logarithms of the data.

The geometric mean thermal updraft size ranges from 0.11 to 0.16 z_i while the geometric mean environmental downdraft size ranges from 0.16 to 0.2 z_i. This size difference is consistent with the smaller area occupied by thermals as the number of thermal updrafts and environmental downdrafts encountered on each flight leg is equal to within one. The scatter in the observed distribtuions is such that no vertical profile of geometric mean size can be determined.

The size of thermal which occupies tha largest fraction of the CBL area ranges from 0.36 to 0.50 z_i. The size of environmental downdraft which occupies the largest fraction of the CBL area ranges from 0.63 to 1.12 z_i. The sum of these two lengths is between 0.99 and 1.62 z_i. This size mode for updraft/downdraft pairs is consistent with the turbulence spectra which show a dominant wavelength of approximately 1.5 z_i for the bulk of the CBL (Kaimal et al., 1976).

The arithmetic mean thermal sizes for the individual flight legs are shown in Figure 6.6. The values range from 0.15 to 0.35 z_i with a tendency to increase slightly with height. Lenschow and Stephens (1980) present AMTEX estimates of the arithmetic mean thermal size. The vertical increase is similar, although the AMTEX values are about half as large because of the more restrictive criteria used. Khalsa and Greenhut (1985) report a similar vertical pattern with values midway between those of the other two studies.

The arithmetic mean number density of thermals ranges from 1.4 to 2.8 as shown in Figure 6.7. This means that the average spacing between thermals is about 0.5 z_i whereas the dominant horizontal length scale in the CBL is 1.5 z_i. This implies that the thermals cluster or equivalently that small downdrafts often occur in the midst of thermals. Thermals were packed about twice as closely in Phoenix as in AMTEX (Lenschow and Stephens, 1980). Thermals were found to be more numerious at heights below 0.1 z_i than above in both studies. The observations of Khalsa and Greenhut (1985) are again midway between those of the other two studies. They report thermal number density values ranging from 1.2 at approximately 0.06 z_i down to 0.9 at approximately .32 z_i.

The results of this and previous studies indicate that the horizontal scales of thermals increases much more slowly in the mixed layer than in the layer below 0.1 z_i. Also, the primary decrease in the number of thermals with height is confined to the layer below 0.1 z_i. These results suggest that most merger or early dissipation events in the life cycles of thermals occur at heights below 0.1 z_i.

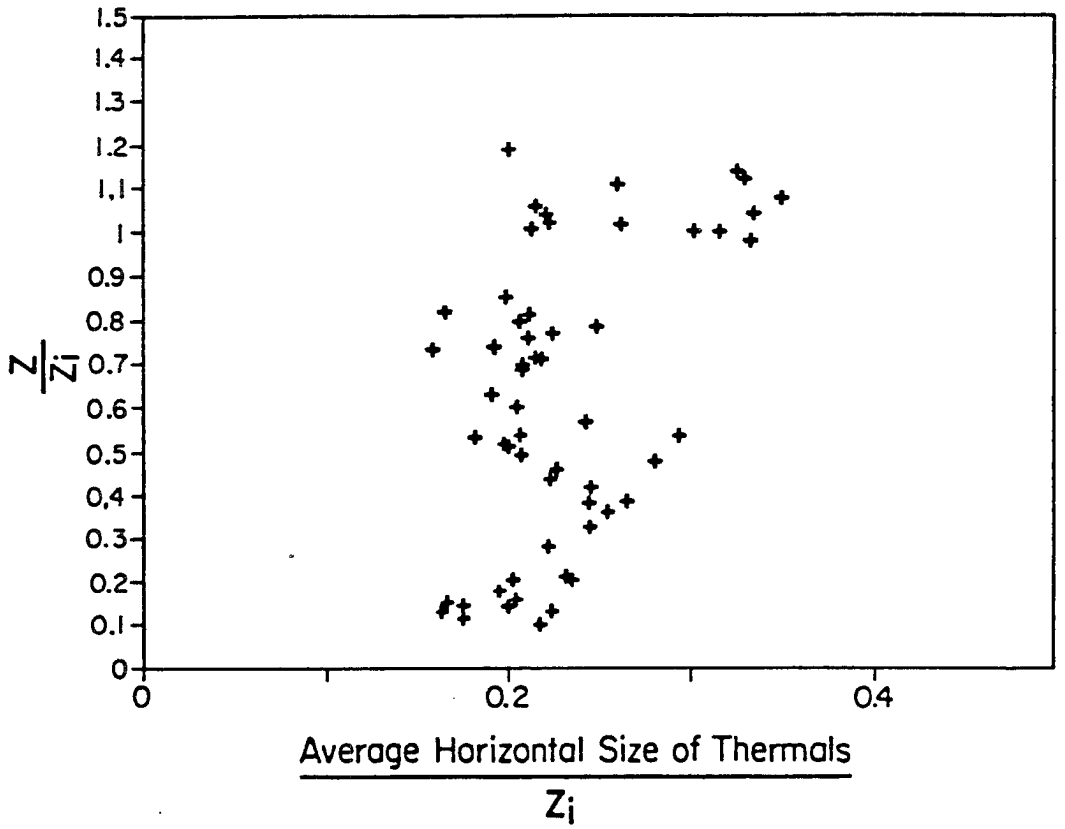

Fig. 6.6 The arithmetic average thermal updraft size. The horizontal scale is thermal updraft size divided by the depth of the convective boundary layer. The vertical scale is height divided by the depth of the convective boundary layer. Each + represents the estimate from one horizontal flight leg.

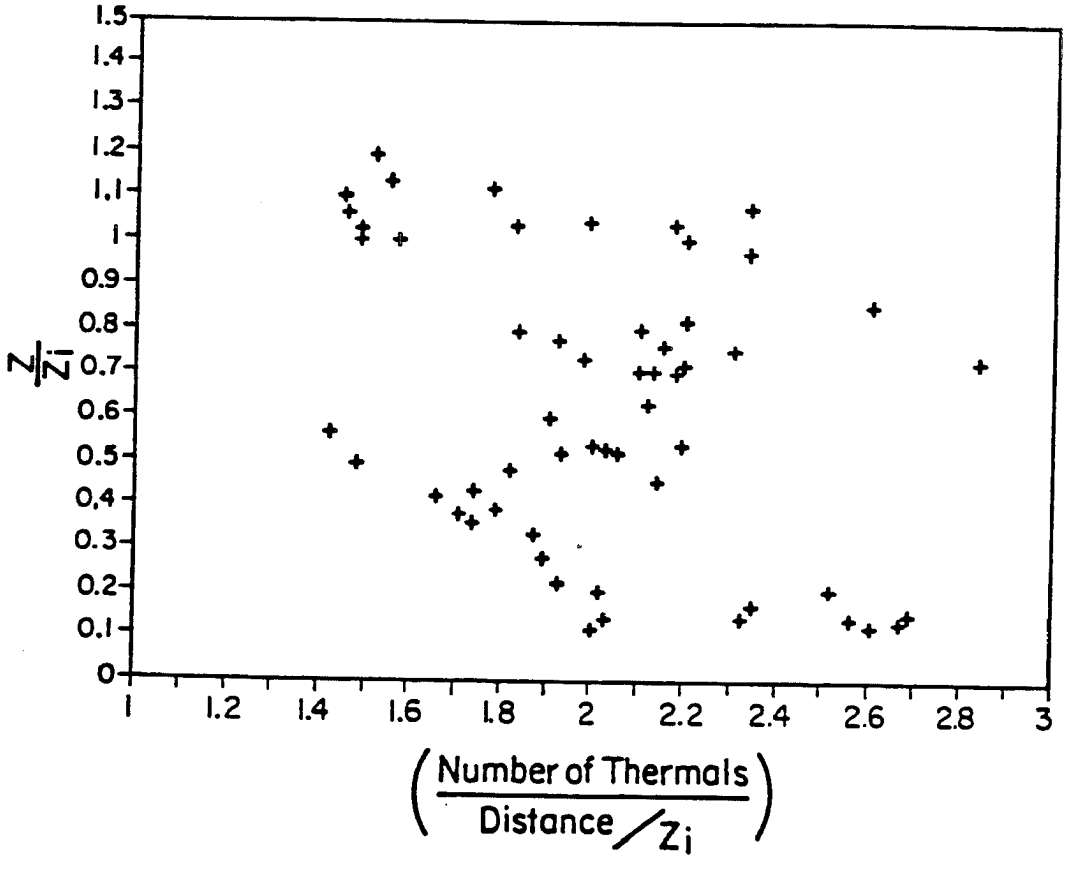

Fig. 6.7 The arithmetic average number density of thermals. The horizontal scale is the number of thermals per flight segment of length equal to the depth of the convective boundary layer. The vertical scale is height divided by the depth of the convective boundary layer. Each + represents the estimate from one horizontal flight leg.

A review of the literature shows just how sensitive the quantitative results are to the criteria used to distinguish thermals from their environment. Therefore, the use of a physically meaningful set of cirteria is essential if the statistics computed from the conditional samples are to have maximum physical meaning.

6.3.2 Plume Mean Buoyancy and Vertical Velocity Profiles

Conditional sampling of CBL turbulence data permits the calculation of separate profiles for turbulence statistics in thermal updrafts and environmental downdrafts. Profiles of the mean buoyancy perturbation and mean vertical velcoity in thermals and their environment will be presented in this section. The profiles are nondimensionalized with the mixed layer scaling parameters.

The nondimensionalized θ_v perturbations are equivalent to nondimensionalized buoyancy. This quantity is the fundamental energy source for the motions of thermals and their environment. The profiles of buoyancy in thermals and their environment are shown in Figure 6.8. The buoyancy of thermals is about 1.0 at 0.1 z_i and decreases almost linearly to zero at 0.65 z_i and on to approximately -0.3 just below z_i before tending back to zero above z_i. This is the pattern expected for buoyantly driven thermals penetrating into layers with greater static stability. The buoyancy profile in the environment is of similar shape and opposite sign as required to achieve zero mean buoyancy at each level.

Lenschow and Stephens (1980) present a buoyancy profile for AMTEX thermals which has a value of 3.0 at 0.1 z_i, more curvature in the lower and mid CBL and no negative area at all. The addition of buoyancy by convective clouds during AMTEX may explain the lack of a

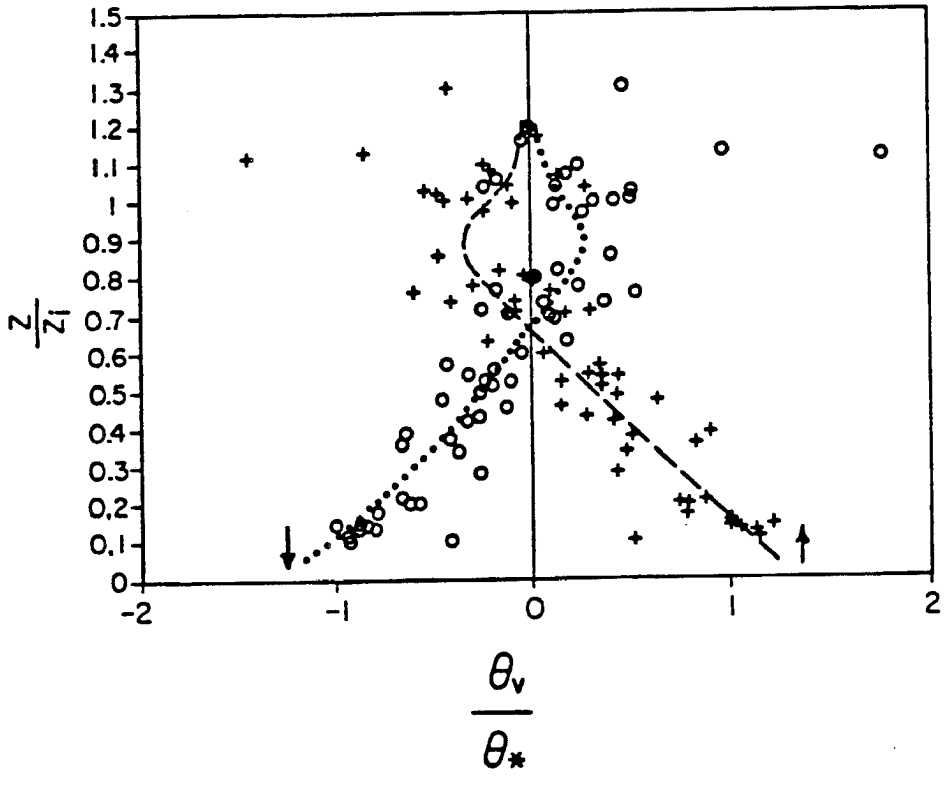

Fig. 6.8 The vertical profiles of the normalized plume mean virtual potential temperatures. The horizontal scale has been normalized by θ_*. The vertical scale is height divided by the depth of the convective boundary layer. The dashed curve is the profile for thermal updrafts and the dotted curve is the profile for environmental downdrafts. The estimates of the plume mean virtual potential temperature from the individual flight legs are plotted as + for thermal updrafts and o for environmental downdrafts.

negatively buoyant area. Khalsa and Greenhut (1985) also show a decrease in buoyancy with height through their limited observational range of 0.1 to 0.3 z_i. Their values are similar to those measured in AMTEX. The larger buoyancies reported in these two studies are consistent with the more restrictive definitions of thermals used. Neither of the previous studies which used a zero expected vertical velcoity threshold reported normalized buoyancy values. Those studies which did report buoyancy profiles used more restrictive conditional sampling criteria. Therefore, the universality of the present result cannot be tested by comparson with past results.

Because θ_*, which was used to nondimensionalize the θ_v perturbations, is of order 0.1 degrees C, stabilities of less than a degree C across the depth of the boundary layer would be sufficient to eliminate thermals. Boundary layers with such stabilities have traditionally been considered well mixed. Such boundary layers are not well mixed from the point of view of the dynamics of thermals. Therefore, because thermals are dominant mixing eddy in the CBL, a slight change in the mean stability of the boundary layer would have a large effect on the diffusive transports of momentum and scalar contaminants. The extent to which buoyancy flux convergence can adjust to damp out changes in the CBL stability profile has yet to be determined. This feedback loop between the vertical velocity of thermals, the stability of the CBL and the buoyancy flux convergence may be important in determining the degree of diffusion in CBLs with non zero mean vertical motion or differential θ_v advection.

The mean w in thermals is the primary measure of the strength of the buoyantly driven vertical circulations in the CBL. The profiles

of mean w in thermals and their environment are shown in Figure 6.9. The mean w in thermals increases from zero at the surface to approximately 0.56 at 0.33 z_i. The value then decreases to approximately 0.25 at z_i and on to zero a short distance above that. Because the profile of fractional area coverage by thermals has a minimum in the mid CBL, the maximum magnitude of the mean environmental downdraft is located lower than that of the mean thermal updraft. This extremum is located at 0.19 z_i and has a value of -0.46. Above this level the mean environmental downdraft weakens to -0.23 at z_i and then on to zero.

Lenschow and Stephens (1980) found similar profile shapes with the maximum amplitudes decreased and lowered slightly. The greater restrictiveness of their definition of thermals reduced the maximum of the mean thermal updraft strength by 20 percent but resulted in a 60 percent decrease in the maximum environmental downdraft strength. This suggests that not only were the normalized vertical circulations weaker during AMTEX than during Phoenix 78 but also that the part of the circulations which they included in the the environment and the present study included in thermals had vertical velocities more nearly similar to those of the thermals than to those of the environment. Khalsa and Greenhut (1985) report mean vertical velocities in thermals of about 1.0 near 0.2 z_i. These values are significantly greater than those reported elsewhere because the 60 percent of the CBL air with the least vertical motion was not included in the averages for either thermals or downdrafts.

Lamb (1978) used large eddy simulation (LES) techniques to estimate the profile of mean w in thermals and their environment. The

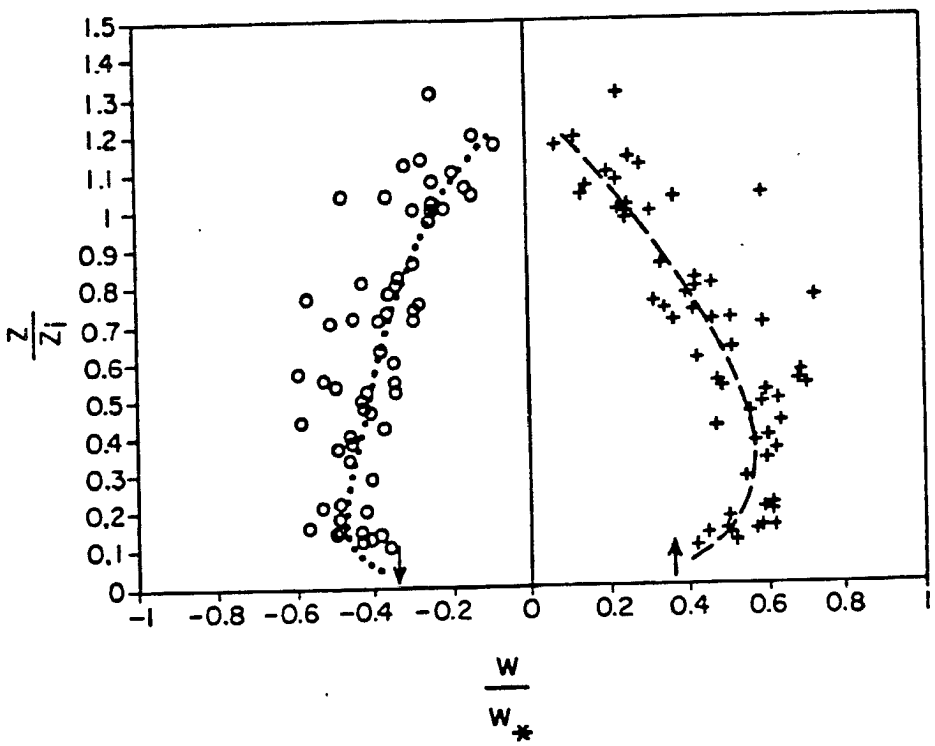

Fig. 6.9 The vertical profiles of the normalized plume mean vertical velocities. The horizontal scale has been normalized by w_*. The vertical scale is height divided by the depth of the convective boundary layer. The dashed curve is the profile for thermal updrafts and the dotted curve is the profile for environmental downdrafts. The estimates of the plume mean vertical velocity from the individual flight legs are plotted as + for thermal updrafts and o for environmental downdrafts.

maximum of environmental downdraft strength was 0.47 at 0.2 z_i. The maximum thermal updraft strength was 0.61 at 0.3 z_i. These model derived values are very close to those measured in the CBL during Phoenix.

The observed maximum value of mean vertical velocity in thermals during Phoenix 78 was smaller than the vertical velocity which would be achieved by a parcel freely accelerating to that level under the influence of the observed mean buoyancy profile. This suggests that the net effect of drag by lateral mixing between thermals and their environment and any pressure forcing is to reduce the rate of acceleration in the lower CBL. These effects will be addressed more fully and more rigorously in Chapter 7.

6.3.3 Contribution of Thermals to Turbulent Variances and Fluxes

Knowledge of the contribution of thermal updrafts and environmental downdrafts to turbulence in the CBL is fundamental to the understanding of the dynamics of the CBL. In addition, the degree to which motions on this scale dominate the turbulence structure of the CBL determines the degree of accuracy needed for the subgrid turbulence parameterizations of an LES. The contribution of these eddies to the variances of θ_v and w as well as to their covariance will be discussed in this section.

There are two ways to measure the contribution of thermal updrafts and environmental downdrafts to turbulence variances and fluxes. First, these turbulence statistics can be computed from plume mean quantities. This type of calculation yields the fraction of the total statistic which is accounted for by the simple two plume conceptual model. This type of model approximates the vertical

circulations of the CBL as two flows, one upward and the other downward, each of which is horizontally homogeneous but is permitted to vary in the vertical. This has traditionally been called the tophat model. The tophat model has been popular because of its simplicity. The fraction of a turbulence statistic which can be explained by the tophat model will be called the tophat contribution to that statistic.

The second way of estimating these statistics is to include all of the scales of thermal motions in the calculation, eliminating only the inertial surbange contribution. This is analogous to computing resolvable scale turbulence statistics from the results of an LES. The resulting statistics will be referred to as the thermal scale contribution.

In this section, these two estimates of the contribution of thermals to fluxes and variances in the CBL will be compared to the total values of these quantities. The profiles of total, tophat contribution and thermal scale contribution to the variance of θ_v are shown in Figure 6.10. The profiles were created by connection of the points which represent the bin averages of z/z_i and the turbulence statistic for the following z/z_i bins: 0.1 to 0.2, 0.2 to 0.4, 0.4 to 0.6, 0.6 to 0.8, 0.8 to 1.0 and 1.0 to 1.2. This procedure yields profiles which are somewhat less smooth than those fit by eye to the data. The total θ_v variance profile has the surface and inversion level maxima which have been observed in past studies (Deardorff, 1974b; Willis and Deardorff, 1974; Coulman 1978; Caughey and Palmer, 1979; Lenschow et al., 1980). The surface maximum is caused by the buoyant production of θ_v variance by surface based convection.

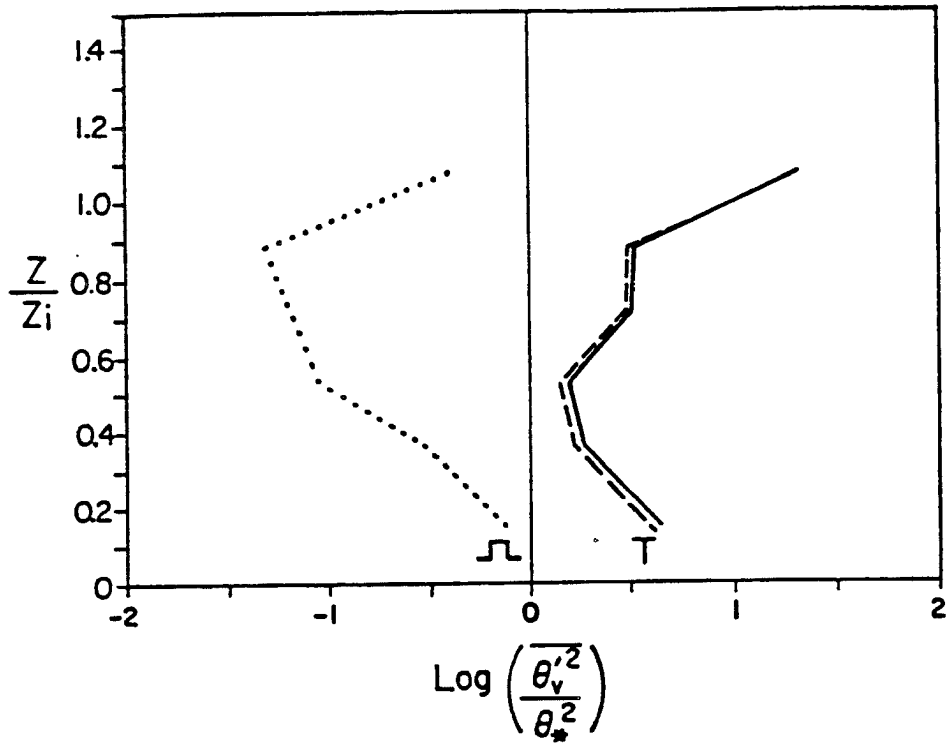

Fig. 6.10 The vertical profiles of the logarithm of normalized virtual potential temperature variance. The horizontal scale has been normalized by θ_*^2. The vertical axis is height divided by the depth of the convective boundary layer. The solid curve is the profile for total variance, the dashed curve, marked by a T, is the profile for the thermal scale contribution to variance and the dotted curve, marked by a ⊓ is the profile for the tophat contribution to variance.

Production of θ_v variance by turbulent entrainment across the inversion causes the maximum at that level. The profile of the thermal scale contribution to the θ_v variance is very similar to that of total variance. The thermal scale variance is less than the total variance in the low and mid levels and nearly identical in the inversion as shown in Figure 6.11. This variation with height is a result of variations in the spectra with height. Caughey and Palmer (1979) showed θ spectra for the CBL and for the stable air above it. The observed spectral slope at horizontal scales less the 0.1 z_i was much steeper in the stable air than in the CBL. Thus, in the inversion, a relatively larger portion of the variance is contributed by the thermal scales than by the smaller scales.

The profile of the tophat contribution to θ_v variance is very different from that of the thermal scale contribution. The tophat contribution to the variance is an order of magnitude less than the thermal scale contribution in the lower CBL and up to two orders of magnitude less in the upper CBL as shown in Figure 6.11. This upper CBL minimum in the ratio of the tophat contribution to θ_v variance relative to the thermal scale contribution to θ_v variance can occur only if the positive and negative thermal scale θ_v perturbations are equally likely to be found in either thermal updrafts or in environmental downdrafts. Thus, while the θ_v perturbations generated by entrainment across the capping inversion are on the same horizontal scale as the thermals they are not in phase with their primary updraft and downdraft structure. This same pattern can be found by computing the tophat contributions to temperature variance from the AMTEX results reported by Lenschow and Stephens (1980) and Lenschow et al., (1980).

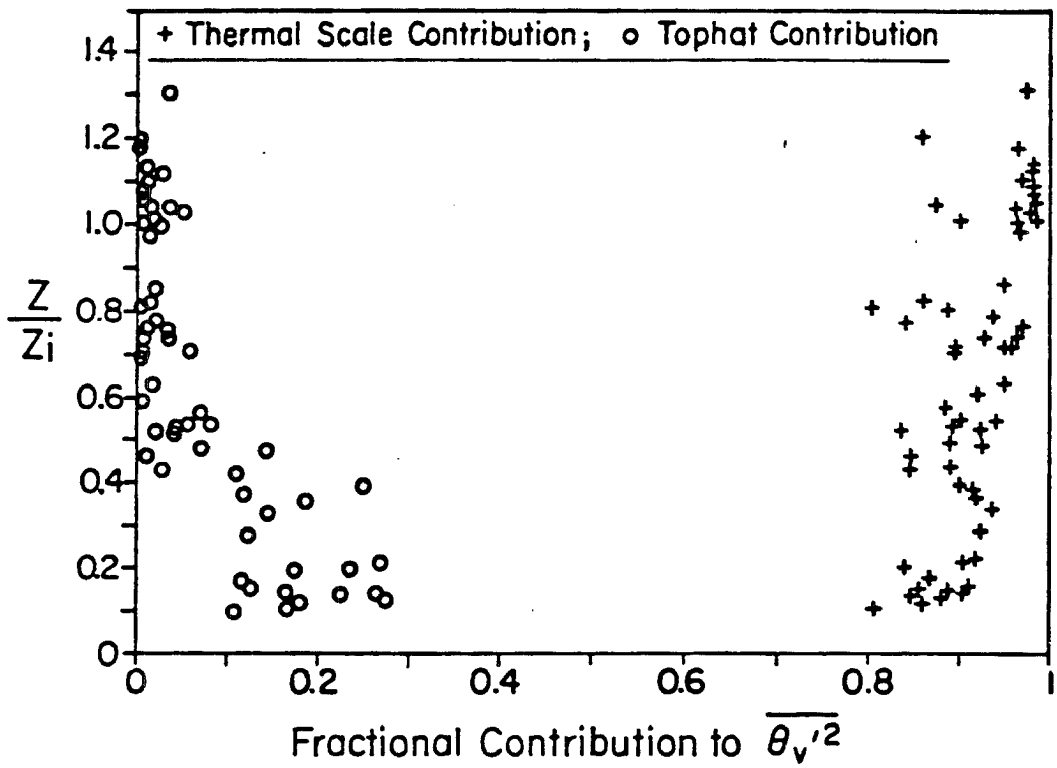

Fig. 6.11 The fractions of the total virtual potential temperature variance contributed by two scales of motion are shown as functions of height. The vertical axis is height divided by the depth of the boundary layer. Each point represents an individual flight leg. The ratios of the thermal scale contribution to the variance to the total variance are plotted as +. The ratios of the tophat contribution to the variance to the total variance are plotted as o.

The relative contributions of the updraft and downdraft regions of thermal scale circulations to the θ_v variance are compared with their net contirbution in Figure 6.12. The ratio of the area weighted contributions of the updraft and downdrafts regions of thermal scale circulations to the θ_v variance is shown in Figure 6.13. In the lower two thirds of the CBL, the variance level is greater in thermal updrafts than in environmental downdrafts. The difference is large enough for the contribution from thermal updrafts to contribute more to the total despite the smaller area occupied by thermals. In the upper CBL, the thermal scale θ_v variance levels are similar in updrafts and downdrafts. This supports the idea that entrainment generated θ_v perturbations are not well correlated with the primary thermal updraft and environmental downdraft structure. This same pattern occurs for total θ variance in thermals versus total θ variance in their environment during AMTEX (Lenshow and Stephens, 1980) and for total θ_v variance in thermals versus downdrafts and the environment over the central equatorial Pacific Ocean (Khalsa and Greenhut, 1985).

The profiles of total, tophat contribution and thermal scale contribution to the w variance are shown in Figure 6.14. The w variance profile is similar to that reported in previous observational, tank and LES studies (Deardorff, 1974a; Willis and Deardorff, 1974; Coulman, 1978; Caughey and Palmer, 1979; Lenschow et al., 1980; Hildebrand and Ackerman, 1984; Moeng and Wyngaard, 1984). The thermal scale contribution to w variance is within 15 percent of the total as shown in Figure 6.15. This is approximately the same fraction as observed for θ_v.

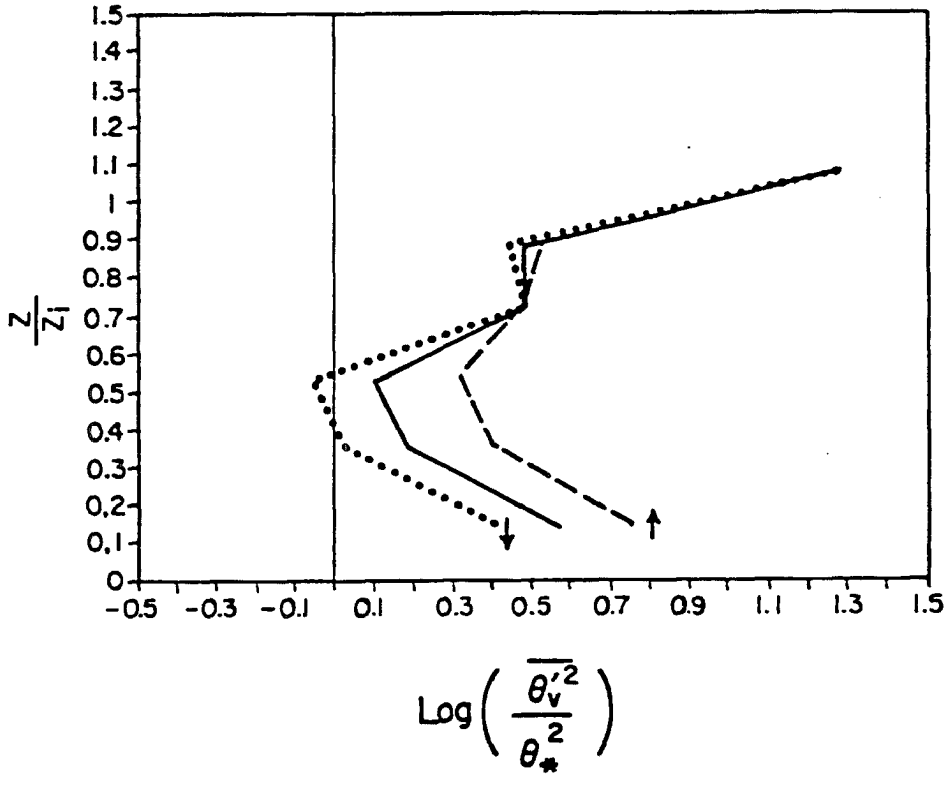

Fig. 6.12 The vertical profiles of the logarithm of the normalized thermal scale contributions to the virtual potential temperature variance. The horizontal scale has been normalized by θ_*^2. The vertical axis is height divided by the depth of the convective boundary layer. The solid curve is the profile for the net thermal scale contribution, the dashed curve, marked by a $\uparrow$, is the profile for the thermal scale updraft contribution and the dotted curve, marked by a $\downarrow$, is the profile for the thermal scale downdraft contribution.

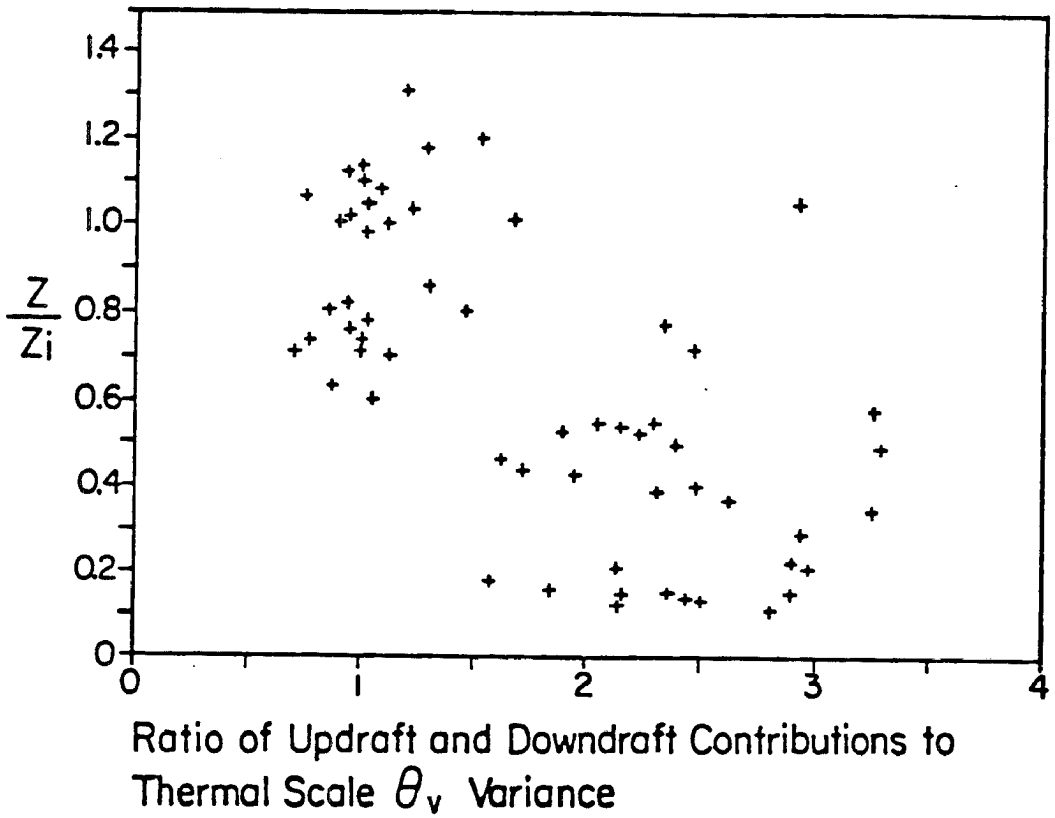

Fig. 6.13 The ratio of the contributions of thermal updrafts and environmental downdrafts to the thermal scale virtual potential variance are plotted as a function of height. The vertical axis is height divided by the depth of the boundary layer. Each point represents an individual flight leg.

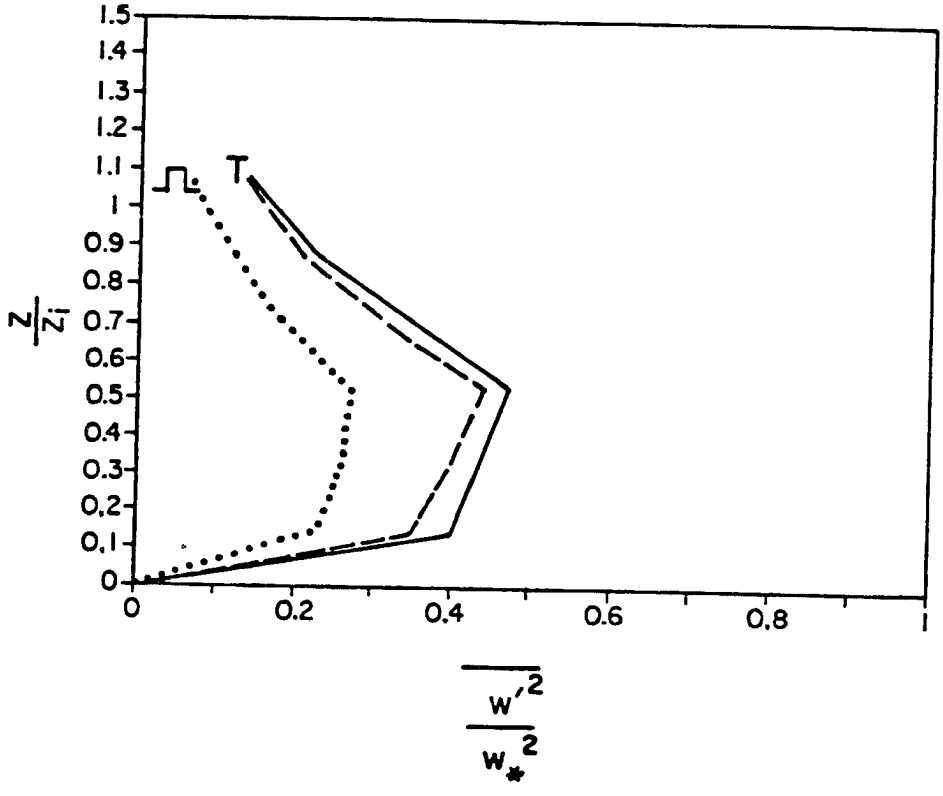

Fig. 6.14 The vertical profiles of the normalized vertical velocity variance. The horizontal scale has been normalized by w_*^2. The vertical axis is height divided by the depth of the convective boundary layer. The solid curve is the profile for total variance, the dashed curve, marked by a T, is the profile for the thermal scale contribution to variance and the dotted curve, marked by a ⊓, is the profile for the tophat contribution to variance.

The tophat contribution to w variance is approximately 55 percent of the total throughout the CBL as shown in Figure 6.15. This is in sharp contrast to the case for θ_v variance for which the tophat contribution becomes negligible in the upper CBL. The constancy of the tophat contribution to w variance reflects the nearly constant form of the w spectra (Kaimal et al., 1976) and the conditional sampling method which was based on those spectra. The AMTEX results reported by Lenschow and Stephens (1980) and Lenschow et al., (1980) show the tophat contributions to w variance decreasing with height. This difference could be related to their use of conditional sampling cirteria based on a variable other than w.

The relative contributions of the updraft and downdraft regions of thermal scale circulations to the w variance are compared with their net contribution in Figure 6.16. The ratio of the area weighted contributions of the updraft and downdraft regions of the thermal scale circulations to the w variance is shown in Figure 6.17. Throughout the CBL the w variance level is greater in the thermal updrafts than in the environmental downdrafts. The difference is large enough for the contribution from thermal updrafts to dominate the total despite the smaller area occupied by them. This difference is largest in the mid CBL. The maximum thermal scale w variance is not only much greater in thermals than in their environment but also occurs at a higher level. This difference could be caused by differences in nature of the buoyant forcing on the updrafts and downdrafts. The buoyant acceleration of environmental downdrafts begins only after they have descended into the unstable lower CBL while thermal updrafts are buoyantly accelerated until they rise above the lower CBL.

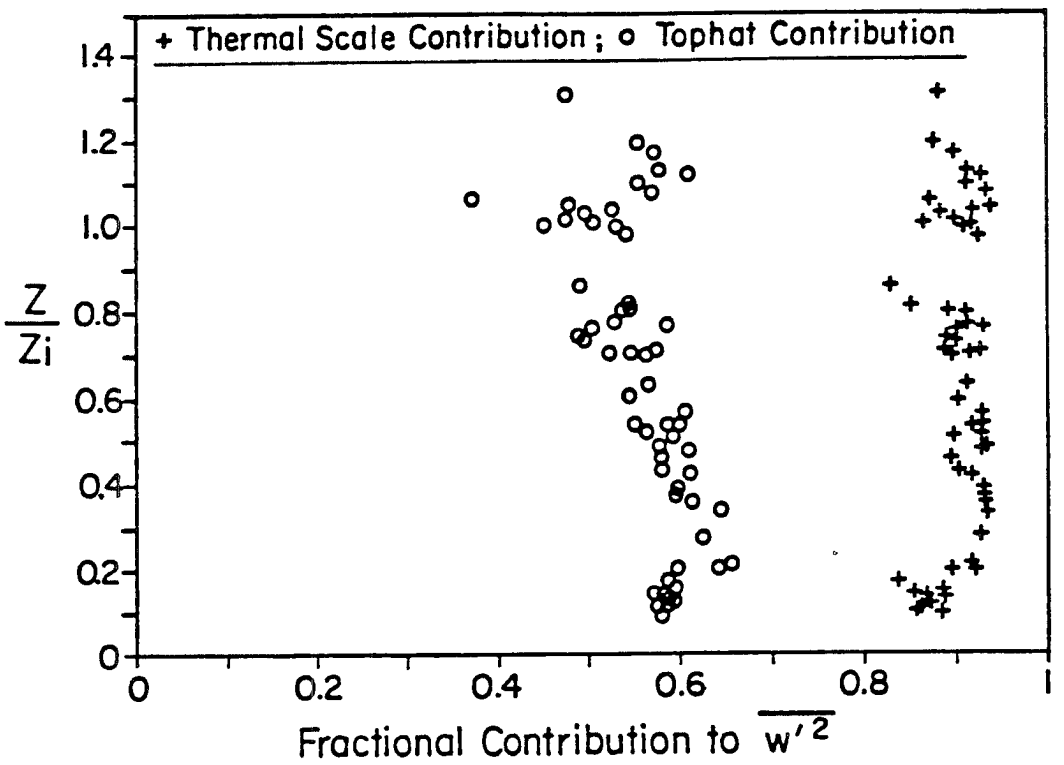

Fig. 6.15 The fractions of the total w variance contributed by two scales of motion are shown as functions of height. The vertical axis is height divided by the depth of the boundary layer. Each point represents an individual flight leg. The ratios of the thermal scale contribution to w variance to the total w variance are plotted as +. The ratios of the tophat contribution to w variance to the total w variance are plotted as o.

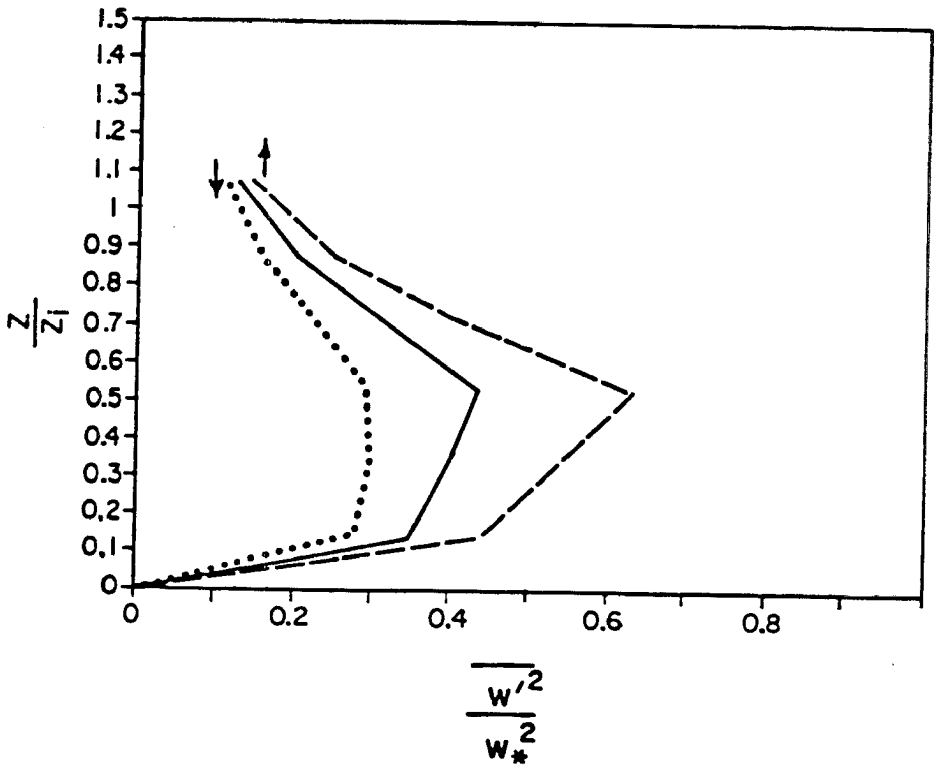

Fig. 6.16 The vertical profiles of the normalized thermal scale contributions to the vertical velocity variance. The horizontal scale has been normalized by w_*^2. The vertical axis is height divided by the depth of the convective boundary layer. The solid curve is the profile for the net thermal scale contribution, the dashed curve, marked by a ↑ , is the profile for the thermal scale updraft contribution and the dotted curve, marked by a ↓ , is the profile for the thermal scale downdraft contribution.

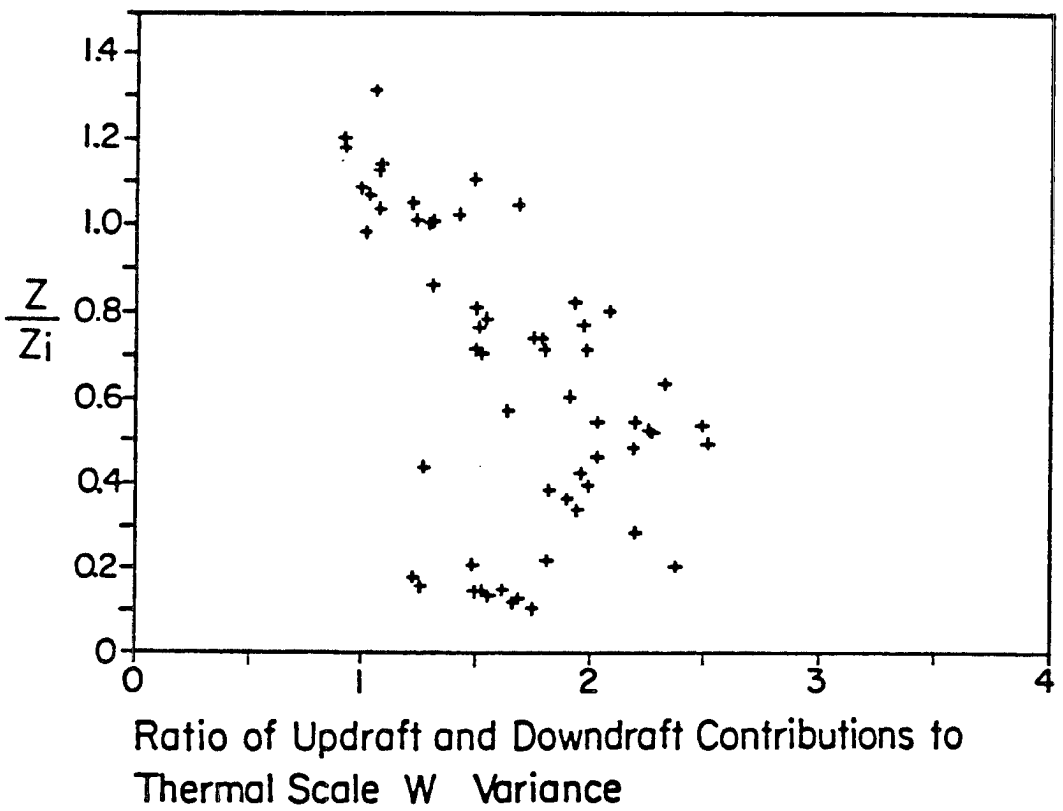

Fig. 6.17 The ratio of the contributions of thermal updrafts and environmental downdrafts to the thermal scale w variance are plotted as a function of height. The vertical axis is height divided by the depth of the boundary layer. Each point represents an individual flight leg.

Therefore, downdrafts experience maximum net buoyant acceleration at the surface while updrafts experience maximum net buoyant acceleration in the mid CBL. Similar differences in magnitude occur for total w variance in thermals versus total w variance in their enviornment during AMTEX (Lenschow and Stephens, 1980) and for total w variance in thermals versus downdrafts and the environment over the central equatorial Pacific Ocean (Khalsa and Greenhut, 1985).

The profiles of total, tophat contribution and thermal scale contribution to the covariance of θ_v and w are shown in Figure 6.18. This nondimensionalized covariance is equivalent to the nondimensional buoyancy flux and the nondimensional buoyant production of turbulent kinetic energy. The shape of the covariance profile is similar to those reported in previous observational, tank and LES studies (Deardorff, 1974a; Willis and Deardorff, 1974; Caughey and Palmer, 1979; Lenschow et al., 1980; Hildebrand and Ackerman, 1984 and Moeng, 1984). The thermal scale contribution to the buoyancy flux is almost identical to the total buoyancy flux as shown in Figure 6.19. The thermal scale motions contribute a much larger fraction of the covariance than of the two variances. This difference is a result of the difference between the -5/3 slopes of w and θ_v variance spectra in the inertial subrange and the -7/3 or steeper slopes for the covariance spectra of w and θ_v (Kaimal et al., 1972, 1976) in the inertial subrange.

The tophat contribution to buoyancy flux is approximately 60 percent of the total as shown in Figure 6.19. This fraction is much greater than that for θ_v variance in the upper CBL but only slightly greater than that for w variance. Thus, the tophat motions contribute

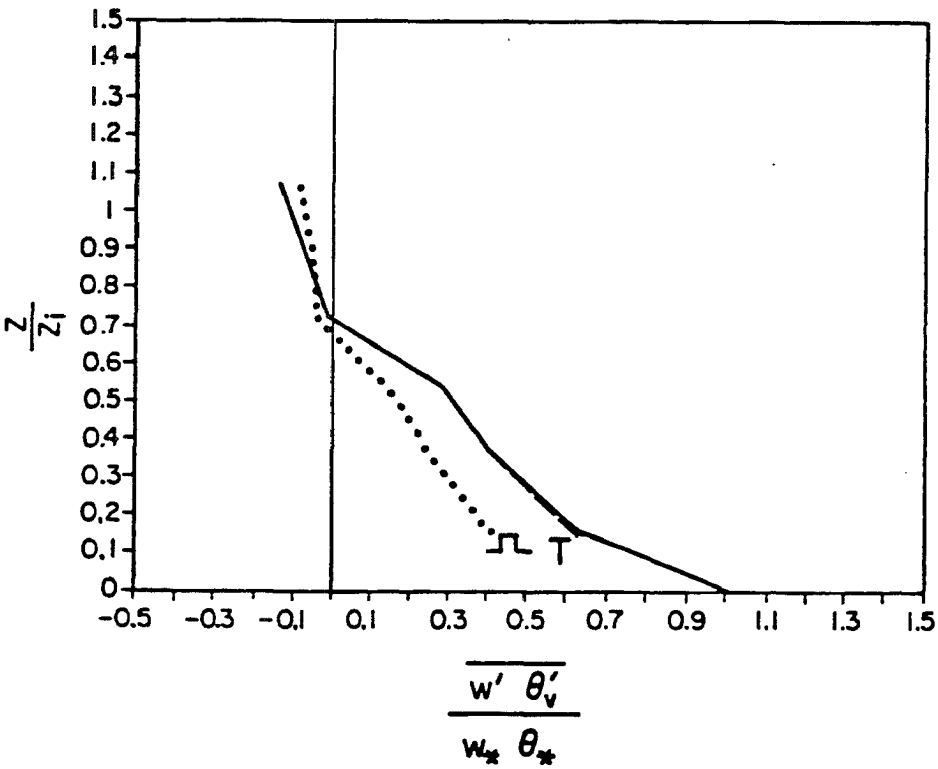

Fig. 6.18 The vertical profiles of the normalized covariance of virtual potential temperature and vertical velocity. This normalized buoyancy flux is equivalent to the normalized buoyant production of turbulence kinetic energy. The horizontal scale has been normalized by θ_* times w_*. The vertical axis is height divided by the depth of the convective boundary layer. The solid curve is the profile for total variance, the dashed curve, marked by a T, is the profile for the thermal scale contribution to variance and the dotted curve, marked by a ⎍, is the profile for the tophat contribution to variance.

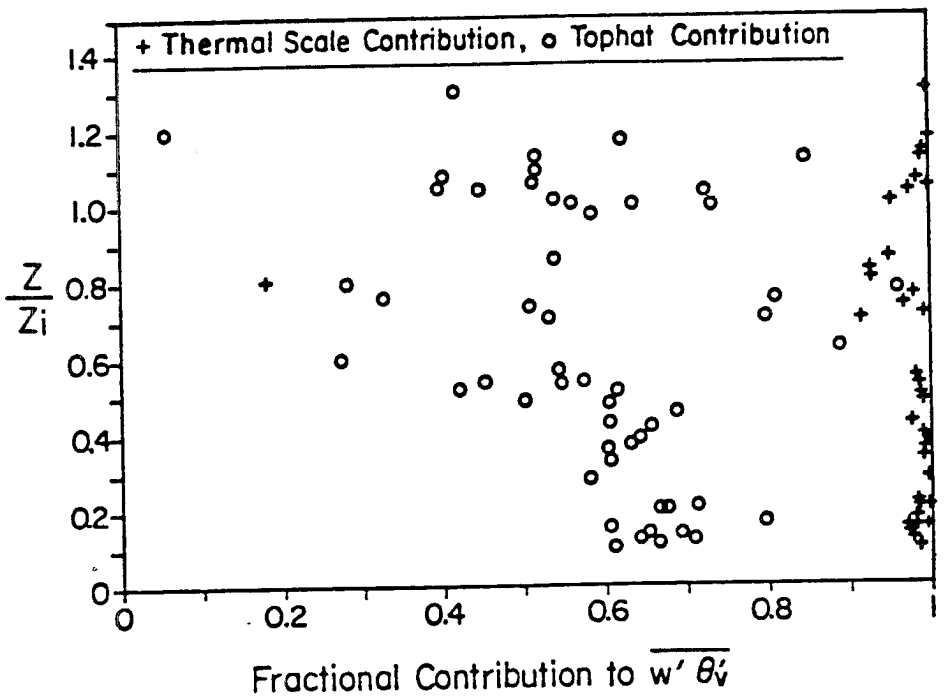

Fig. 6.19 The fractions of the total buoyancy flux contributed by two scales of motion are shown as functions of height. The vertical axis is height divided by the depth of the boundary layer. Each point represents an individual flight leg. The ratios of the thermal scale contribution to buoyancy flux to the total buoyancy flux are plotted as +. The ratios of the tophat contribution to buoyancy flux to the total buoyancy flux are plotted as o.

significantly to the buoyancy flux in the upper CBL despite their negligible contribution to the buoyancy variance. This observation suggests that the remaining bulk of the buoyancy variations in the upper CBL are much less well correlated with w variations than are the tophat buoyancy variations. Indeed, the correlation coefficient of buoyancy with w ranges from 0.3 to 0.5 in the lower CBL but is approximately -0.1 in the stable upper levels of the CBL. The buoyancy variations induced by vertical mixing of the capping inversion are not nearly as efficient at moving buoyancy vertically as are buoyancy variaitons caused directly by surface based convection. This poor correlation of w and buoyancy in the upper CBL can be observed in the results of previous observational, tank and LES studies (Deardorff, 1974a, b; Willis and Deardorff, 1974; Caughey and Palmer, 1979; Lenschow et al., 1980).

The relative contributions of the updraft and downdraft regions of thermal scale circulations to the covariance of θ_v and w are compared with their net contribution in Figure 6.20. The ratio of the area weighted contributions of the updraft and downdraft regions of the thermal scale circulations to covariance is shown in Figure 6.21. Throughout the lower CBL the variance level is greater in thermal updrafts than in environmental downdrafts. This differnce is largest in the mid CBL. The covariances in thermals and their environment are equal in the stable upper CBL. Similar differences in magnitude occur for total covariance of θ_v and w in thermals versus downdrafts and the environment over the central equatorial Pacific Ocean (Khalsa and Greenhut, 1985).

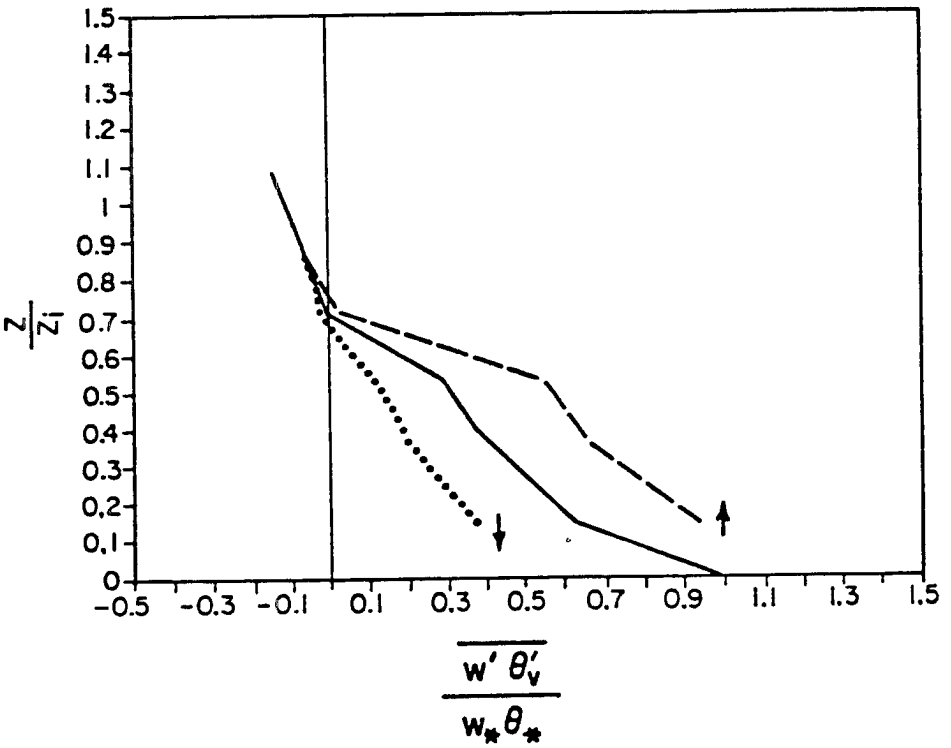

Fig. 6.20 The vertical profiles of the normalized thermal scale contributions to the covariance of virtual potential temperature and vertical velocity. This normalized buoyancy flux is equivalent to the normalized buoyant production of turbulence kinetic energy. The horizontal scale has been normalized by θ_* times w_*. The vertical axis is height divided by the depth of the convective boundary layer. The solid curve is the profile for the net thermal scale contribution, the dashed curve, marked by a ↑, is the profile for the thermal scale updraft contribution and the dotted curve, marked by a ↓, is the profile for the thermal scale downdraft contirbution.

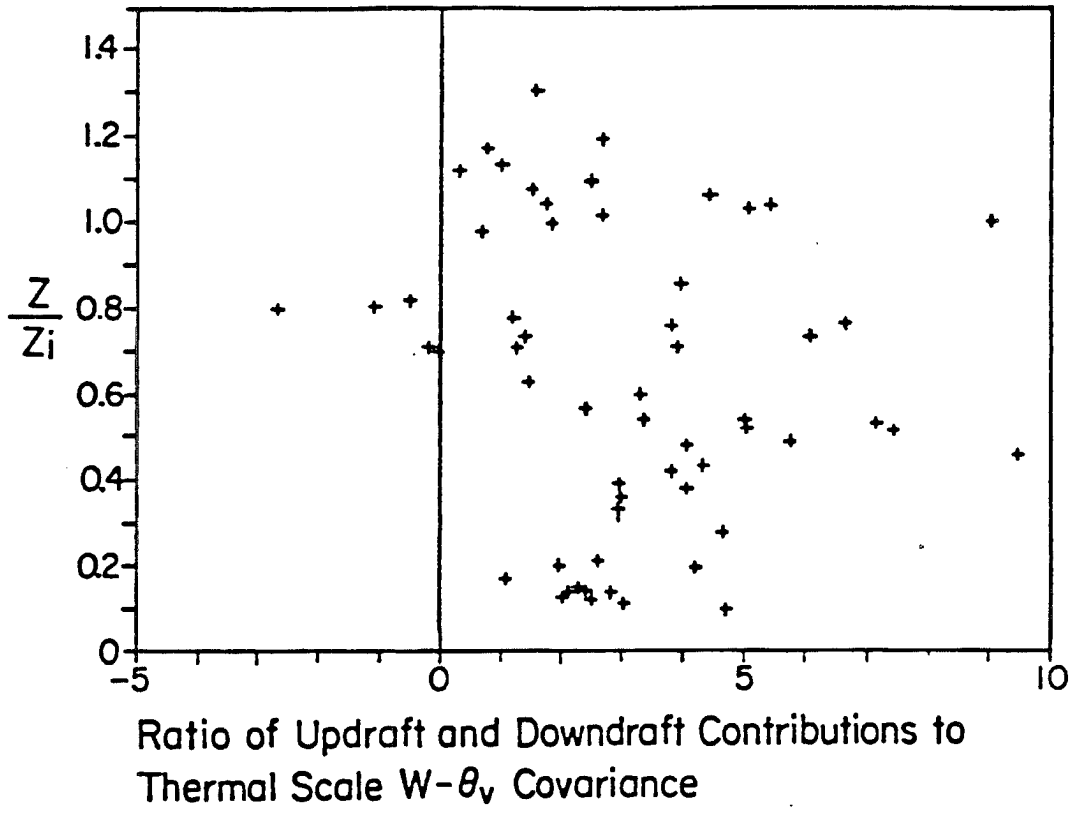

Fig. 6.21 The ratio of the contributions of thermal updrafts and environmental downdrafts to the thermal scale buoyancy flux are plotted as a function of height. The vertical axis is height divided by the depth of the boundary layer. Each point represents an individual flight leg.

The contribution of thermal scale motions to turbulence variances and covariances depends on the form of the variance and covariance spectra respectivley. The θ_v-w covariance spectra have steeper slopes in the inertial subrange than do the variance spectra of θ_v and w. Therefore, thermal scale motions account for almost all of the θ_v-w covariance but as little as 85 percent of the θ_v and w variances. These results suggest that the buoyancy flux profile is easier to model with LES methods than are the θ_v and w variance profiles.

The simple tophat model of thermals and their environment fits the data best in the lower CBL where surface based buoyant convection dominates the variances and covariances of θ_v and w. In the upper CBL, the tophat model continues to account for a significant fraction of the variance of w and the covariance of θ_v and w. However, in this region, mixing of the stable air of the capping inversion is the primary source of θ_v variance. The failure of the simple tophat model to account for a significant fraction of the upper CBL θ_v variance suggests that while crossinversion entrainment produces variance on the thermal scales, it does not produce it in phase with the thermal plumes.

6.3.4 Contribution of Thermals to the Turbulence Kinetic Energy Budget

The contribution of thermal updrafts and environmental downdrafts to the budget of turbulence kinetic energy (TKE) can be estimated from both the theraml scale statistics and the tophat statistics. The TKE budget for the CBL is:

$$\frac{\partial e'}{\partial t} = \frac{g}{T_o}\,\overline{w'T_v'} - \frac{\partial}{\partial z}\,(\overline{w'e'}) - \varepsilon - \overline{w'u_i'}\,\frac{\partial u_i}{\partial z} - \frac{1}{\rho}\,\frac{\partial}{\partial z}\,(\overline{w'p'})$$

where e' is the turbulence kinetic energy and u_i is the ith component of velocity. The first three terms on the right hand side of the TKE budget are buoyant production, turbulent transport and dissipation. These three terms can be calculated directly from the aircraft turbulence data. The fourth term, shear producion, can be estimated from the magnitude of the mean wind and the w variance. The fifth term, pressure transport, cannot be measured because of the difficulty of measuring turbulent pressure fluctuations from an aircraft.

The w variance profile presented in the previous section is only one of the three components of TKE. The eastward wind component (u variance) and the northward wind component (v variance) are shown in Figures 6.22 and 6.23 respectively. The contribution of thermal scale motions to the u variance ranges from 85 percent in the lower CBL to 95 percent in the upper CBL. The u variance in thermal updrafts averages 10 to 25 percent greater than the u variance in environmental downdrafts with some variability as shown in Figure 6.24. The profiles of thermal scale contirbutions to v variance are similar to those for u variance. Figure 6.25 shows the ratio of the updraft and downdraft contributions to thermal scale v variance. The pattern of this ratio is similar to that seen for u. The light and variable mean winds during this study account for this similarity and were the reason a coordinate system aligned with the mean CBL wind was not used.

The tophat contribution to the variances of u and v is less than 3 percent throughout the CBL. This negligibility reflects the dominantly radial nature of the horizontal branches of the thermal circulations under the light mean wind conditions of this study. If

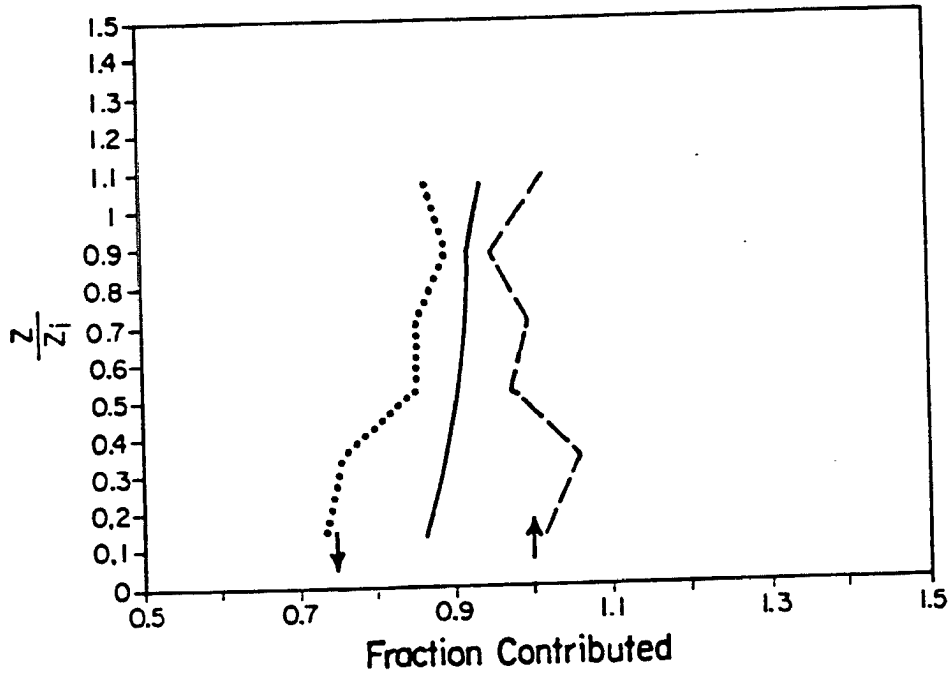

Fig. 6.22 The vertical profiles of the fraction of the normalized variance of the eastward component of the wind contributed by thermal scale motions. The vertical axis is height divided by the depth of the convective boundary layer. The solid curve is the fraction contributed by all thermal scale motions, the dashed curve, marked by a ↑ , is the fraction contributed by the thermal scale updrafts and the dotted curve, marked by a ↓ , is the fraction contributed by the thermal scale downdrafts contribution.

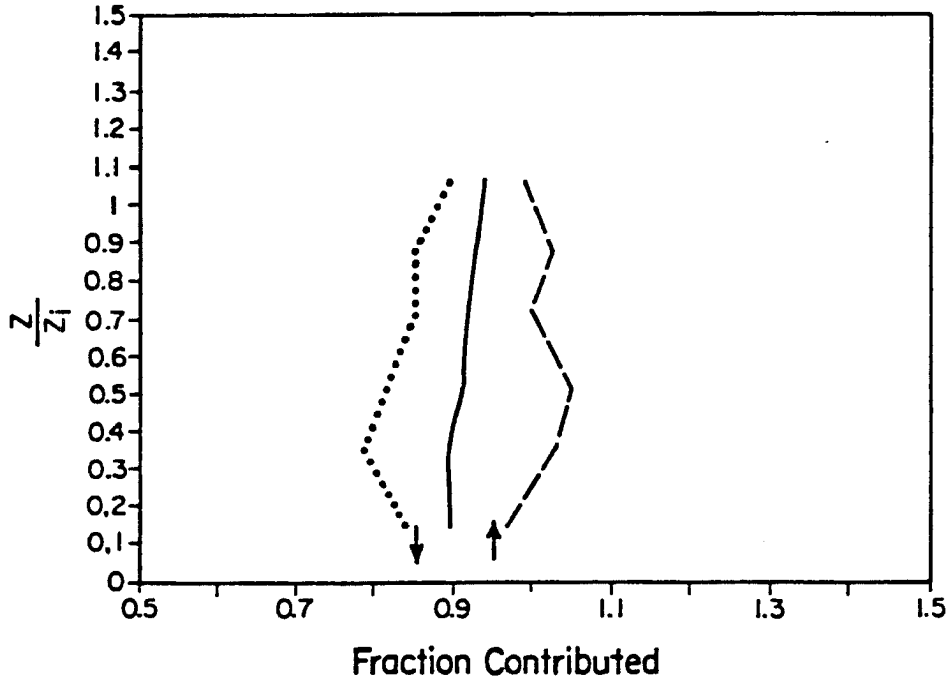

Fig. 6.23 The vertical profiles of the fraction of the normalized variance of the northward component of the wind contributed by thermal scale motions. The vertical axis is height divided by the depth of the convective boundary layer. The solid curve is the fraction contributed by all thermal scale motions, the dashed curve, marked by a ↑ , is the fraction contributed by the thermal scale updrafts and the dotted curve, marked by a ↓ , is the fraction contributed by the thermal scale downdrafts contribution.

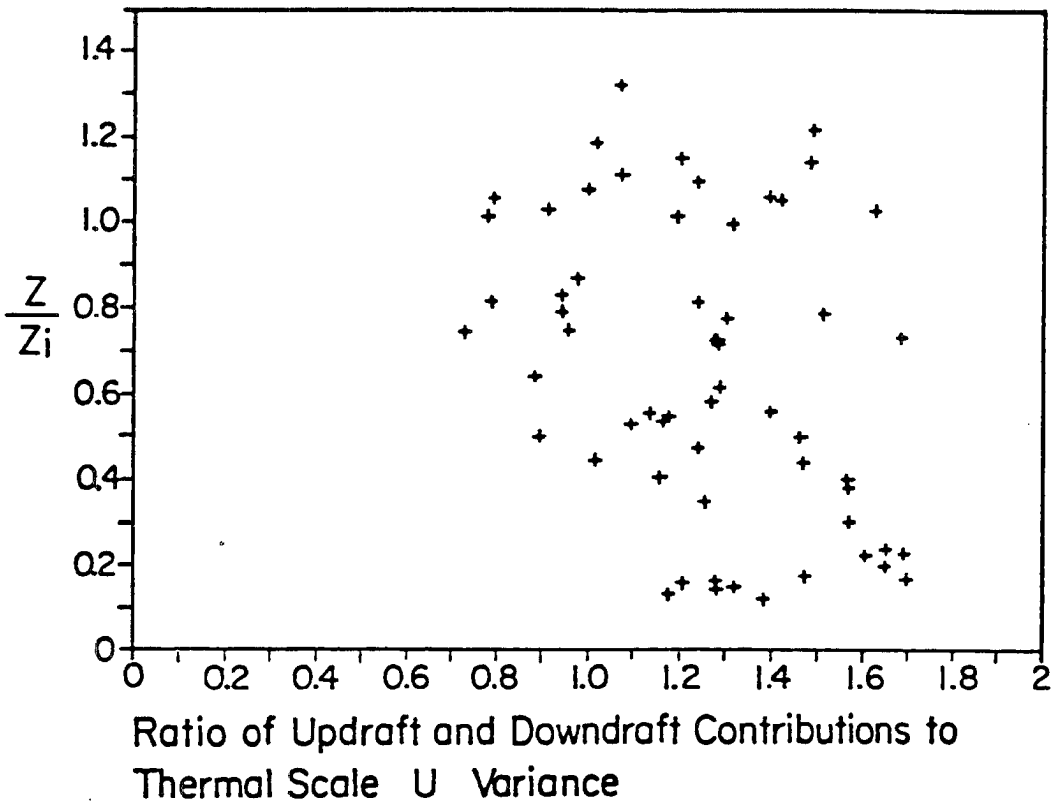

Fig. 6.24 The ratio of the contributions of thermal updrafts and environmental downdrafts to the thermal scale u variance are plotted as a function of height. The vertical axis is height divided by the depth of the boundary layer. Each point represents an individual flight leg.

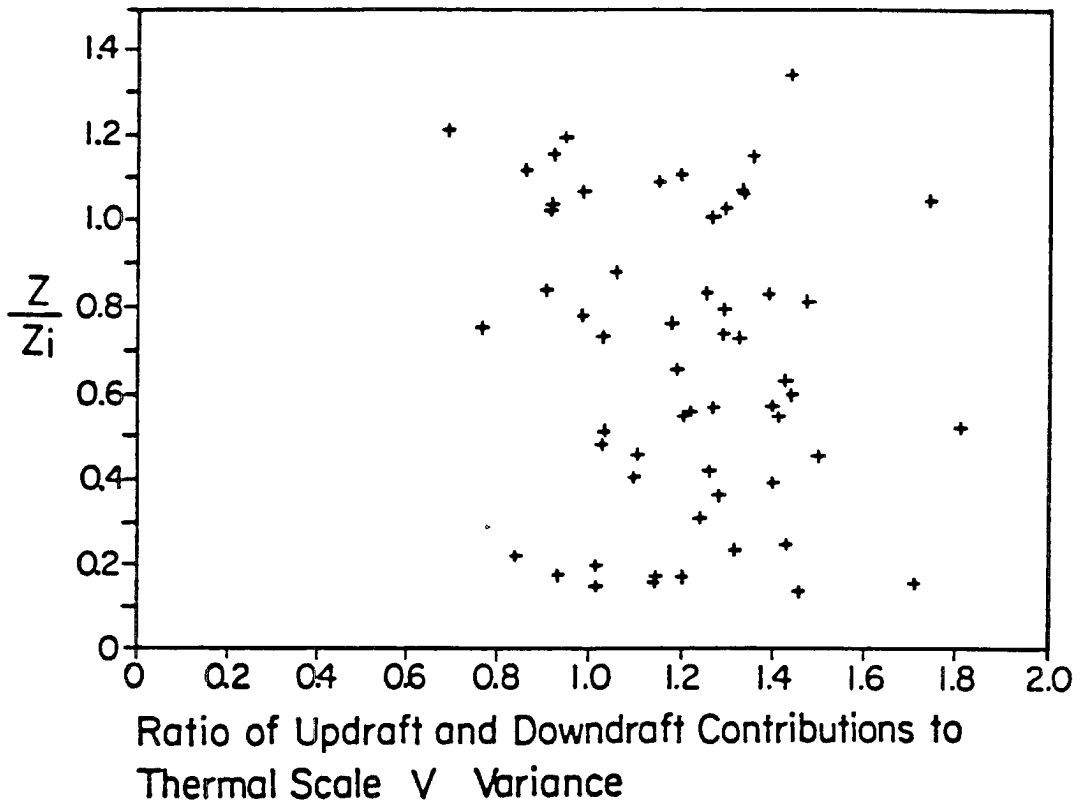

Fig. 6.25 The ratio of the contributions of thermal updrafts and environmental downdrafts to the thermal scale v variance are plotted as a function of height. The vertical axis is height divided by the depth of the boundary layer. Each point represents an individual flight leg.

the radial inflow were perfectly symmetric, the mean horizontal velocity in both thermal updrafts and environmental downdrafts would be exactly zero. This would give a tophat contribution of zero to the variances of u and v. The observed values of less than 3 percent are rather close to this ideal value of zero.

The profiles of tophat contribution, thermal scale contribution and total buoyant production of TKE were presented Figure 6.18. Thermal scale motions accout for nearly 100 percent of the buoyant production of TKE. The tophat model, however, acounts for only about 60 percent of the buoyant production of TKE. Buoyant production of TKE dominates the shear production of TKE at all heights within the CBL above 0.6 times the Monin-Obukov length (Wyngaard and Cote, 1971). The height above the earth's surface to which shear production dominates buoyant production varied from 0.4 to 4.2 percent of the CBL depth for the current study. The shear production of TKE could also be important in the capping inversion. Throughout the bulk of the CBL the mean winds during the study were light and variable. The resulting shears within the CBL were too small by an order of magnitude to produce a significant contribution to the TKE budget.

Dissipation of TKE occurs primarily at the samll scale end of the inertial subrange. Therefore, thermals do not contribute significantly to the dissipation of the TKE which they produce.

The fraction of the turbulent transport of TKE contributed by thermal scale motions is shown in Figure 6.26. This fraction ranges from about 75 percent in the lower CBL to as much as 90 percent in the mid and upper CBL. The thermal scales are not nearly as dominant in the turbulent transport of TKE as they are in the vertical advection

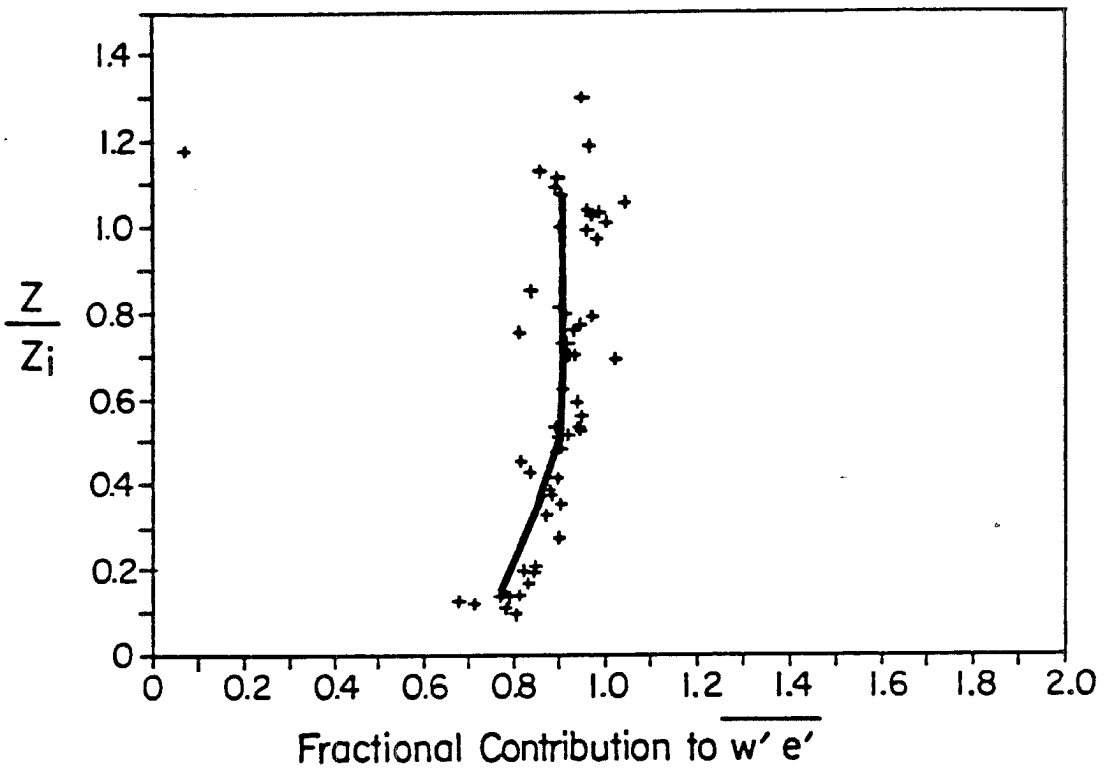

Fig. 6.26 The fraction of the total turbulent transport of turbulence kinetic energy, $\overline{w'e'}$, contributed by thermal scale motions. The vertical axis is height divided by the depth of the boundary layer. Each point represents an individual flight leg. The solid curve is the bin averaged profile.

of buoyancy. This difference can be explained in terms of the spectra of TKE and of buoyancy flux. The tendency towards isotropy at small scales results in the small contribution of inertial subrange turbulence to the buoyancy flux (Kaimal et al., 1972, 1976). However, inertial subrange TKE is not negligible and may be advected vertically by all scales of turbulence. Therefore, inertial subrange turbulence is significant to turbulent transport of TKE. The tophat contribution to the turbulent transport of TKE comes almost entirely from the turbulent transport of w variance because the tophat contribution to the variances of u and v is negligible. Therefore, because the total turbulent transport of the vrainces of u and v are not negligible, the tophat model is a poor approximation to the total turublent transport of TKE.

Thermal scale motions are of primary importance to the production and turbulent transport terms of the TKE budget. Thermal scale motions contribute almost 100 percent to the buoyant production term. This is the dominant production term throughout the bulk of the CBL. The thermal scale motions contribute 75 to 90 percent of the turbulent transport of TKE. The tophat model is observed to yield a poor approximation to the TKE budget of the CBL.

6.4 Summary

Conditional sampling of CBL turublence to distinguish thermals from their environment has been developed and applied to aircraft observations from a continental plains site. Some aspects of the turbulence structure and dynamics of thermals and their environment were measured and discussed.

A conditional sampling technique for distinguishing thermal updrafts from environmental downdrafts, which is based on the spectral dynamics of CBL turbulence, has been developed. This technique removes the inertial subrange turbulence from consideration when the determining of the boundaries between thermal updrafts and environmental downdrafts. The use of the bounding wavelength of the inertial subrange as a cutoff wavelength for the filter provides a universally applicable physical basis for defining the boundaries between thermal and their environment.

The fracitonal area coverage by thermals was found to vary from 50 percent near the surface and in the capping inversion to a minimum of 43 percent of a height of 0.52 z_i. The previous studies which also used a zero expected vertical velocity criteria for distinguishing thermals found similarly shaped profiles with minimum coverages ranging down to 36 percent. As pointed out by Lamb (1978), this observed minimum in thermal coverage has important implications for the diffusion of pollutants in the CBL.

The thermal size distribution was observed to be approximately lognormal. However, the actual updraft size distribution may have been exponential because the filtering used to distinguish thermals from their environment could theoretically modify such a distribution towards one indistinguishable from that observed. The updraft and downdraft size ranges which occupied most of the CBL area corresponded to the wavelength of the peak of the vertical velocity spectra observed in the CBL by Kaimal et al., (1976).

Thermal updrafts were observed to be positively buoyant in the lower two thirds of the CBL and negatively buoyant in the upper third.

The maximum in the profile of mean vertical velocity in thermals occurred at one third the CBL depth, only halfway up to the level of neutral buoyancy. In addition, the observed w maximum was less than that which would result from free convection driven by the observed buoyancy profile. These two observations suggest that lateral entrainmnet drag and pressure gradient forces are important factors in the vertical velocity budget of thermals.

Thermal scale turbulence contributed 75 percent or more of the variances of u, v, w and θ_v. Thermal scale turublence contirbuted nearly 100 percent to the buoyant production of TKE and 75 to 90 percent to the turbulent transport of TKE. The contribution of thermal scale turbulence to each of these quantities increased with height. These results suggest that 75 percent or more of the turbulence variances in the CBL are on scales resolvable by LES models. The observations confirm the LES results of Moeng (1984) that buoyant production of TKE is nearly 100 percent resolvable by such a model.

The tophat contribution to these same quantities is much smaller than the thermal scale contribution. The tophat contribution to w variance is 50 percent. However, it was negligible for θ_v variance in the upper CBL and for u and v variances throughout the CBL. The tophat contribution to the buoyant production of TKE was 60 percent. The tophat contribution to the turbulent transport of TKE was also much smaller than the thermal scale contribution. While the tophat model provides a useful description of the simpler bulk characteristics of thermals such as buoyancy and vertical velocity it is inappropriate for estimation of the higher order turbulence statistics of the CBL.

The observations reported in this paper and elsewhere suggest that there are qualitative differences in the structure of thermal updrafts and environmental downdrafts between the lower, unstable, part of the CBL and the upper, stable, part of the CBL. The primary indication of this difference is the decrease in magnitude of the correlation coefficient between θ_v and w in the upper CBL. This decrease in correlation is found for the total, tophat and thermal scale estimates.

More insight into the dynamical processes which control the turbulence characteristics of thermals and their environment may be gained from diagnostic models of the budgets of buoyancy, convective mass flux and vertical velocity. This approach yields the coefficients of lateral mixing between thermals and their environment and the pressure forces acting upon them. This further analysis of the Phoenix 78 aircraft data is undertaken in Chapter 7.

7. Diagnosis of Lateral Mixing and Pressure Forcing in Thermals and their Environment

7.1 Introduction

The convective circulations which arise when buoyancy is supplied to the lower boundary of the atmosphere are commonly called thermals. These circulations are composed of updrafts and downdrafts with a dominant horizontal scale of approximately 1.5 times depth of the boundary layer, z_i. The thermal updrafts and compensating environmental downdrafts span the depth of the Convective Boundary Layer (CBL) as either bubbles or plumes extending from the surface layer to the capping inversion (Richter et al., 1974, Hall et al., 1975; Kaimal et al., 1976; Kunkel et al., 1977; Emmitt, 1978; Gaynor and Mandics, 1978; Caughey and Palmer, 1979; Taconet and Weill, 1983).

The structure of thermal convective elements in the CBL has been discussed in a number of previous studies (Grant, 1965; Manton, 1977; Coulman, 1978; Lamb, 1978; Lenschow and Stephens, 1980 and 1982; Khalsa and Greenhut, 1982; Greenhut and Khalsa, 1985). These studies have been primarily descriptive, focusing of the structure of thermals and their effects on the budgets of turbulence kinetic energy and other second order turbulence statistics. Conditional sampling was used to divide the CBL into two or more regions with thermal updrafts and environmental downdrafts being of primary interest. Chapter 6 describes the use of conditional sampling of Phoenix 78 aircraft

turbulence data to characteristize the turbulence structure of thermal updrafts and environmental downdrafts of a continental plains site in eastern Colorado.

The two plume conceptual model divides the entire CBL into two plumes, thermal updrafts and environmental downdrafts. This type of model approximates the vertical circulations of the CBL as two flows, one upward and the other downward; each of which is horizontally homogeneous but is permitted to vary in the vertical. This has traditionally been called the tophat model. The tophat model has been popular because of its simplicity. In this study the effects of perturbations on the plume means will be taken into account, yielding a model with far fewer simplifying assumptions than the simplest tophat models which retain only first order terms. The tophat model has been popular not only for descriptive studies of thermals but also for descriptive and diagnostic studies of convective clouds (Fraedrich, 1973; Betts, 1973 and 1975, Lenschow and Stephens, 1982). The mean buoyancy and vertical velocity profiles of the thermal updrafts and environmental downdrafts are the most basic features of the tophat model. The buoyancy profile is a measure of the external forcing for the convective motions while the vertical velocity profile is a measure of the strength of the resulting convective motions.

Betts (1973, 1975 and 1976) developed a tophat model for the budgets of dry and moist static energy which he eventually adapted to the study of CBL convection under fair weather cumuli. The soundings used by Betts (1976) yielded no vertical velocity data so it was necessary to close the model with assumptions about the heat flux and lateral mass exchange and solve for the convective mass flux. The use

of aircraft observations of turbulence in the current study permits direct measurement of the convective mass flux and other turublence statistics which were neglected, parameterized or dependent variables in Betts' convective budget studies. In particular, the budgets of virtual potential temperature and convective mass flux in thermals can be solved simultaneously to give the coefficients of lateral mass exchange between thermals and their environment.

Lenschow and Stephens (1982) derived a slightly simplified form of the budget equation for plume mean vertical velocity in thermals. Using this equation alone, they were able to diagnose the sum of the lateral mass exchange and the pressure effects. In the current study, these two effects can be distinguished because the lateral mass exchange coefficients are available from the budgets of virtual potential temperature and convective mass flux.

The budget equations for the mean virtual potential temperature, convective mass flux and vertical velocity profiles for thermal updrafts and environmental downdrafts are presented in the next section. In the following sections, the physical interpretation of the terms in these budget equations is discussed. Profiles of the measureable terms are determined from the aircraft and tower observations made during the Phoenix 78 CBL experiment. The observed profiles of the terms in the virtual potential temperature and convective mass flux budgets are then used to diagnose the lateral mixing between the thermal updrafts and environmental downdrafts. This lateral mixing is an important factor in the buoyancy budget of thermals. Its profile has not been masured or diagnosed previously. The pressure forcing on the vertical velocity budgets is determined

from this diagnosed lateral mixing and the observed terms in those budgets. This is the first diagnostic study to separate the pressure effects from the lateral mass exchange effects.

The result of this analysis is the determination of all the terms in the budgets of the two primary parameters of thermal convection, buoyancy and vertical velocity. The importance of lateral mass exchange between thermals and their environment and of pressure effects to these budgets are the primary findings of this study. These findings and their role in the dynamics of thermals are discussed in sections 7.5 and 7.6.

7.2 The Plume Mean Budget Equations for Buoyancy, Convective Mass Flux and Vertical Velocity

In this section, a mathematical model of CBL convection is developed. This mathematical model is based on the two plume conceptual model described in the introduction. The model includes separate budget equations for the buoyancy, convective mass flux and vertical velocity profiles for thermal and environmental plumes. These budgets must account not only for processes occurring within each of the plumes but also for the lateral exchanges between the two plumes.

The derivation of these budgets is contained in Appendix A. The nomenclature used in this section is defined at the beginning of the derivation. The plume mean buoyancy budget for the thermal updrafts is derived from the conservation equation for virtual potential temperature. This equation is averaged horizontally over the thermal area. The vertical variations in this area, σ, necesitates the use of Liebnitz's rule to move the averages inside the spatial derivatives.

The various lateral exchange terms which arise in this equation are parameterized in terms of lateral mass exchange coefficients. The lateral exchange of virtual potential temperature between the thermals and their environment is composed of two components: the rate of mass transfer from the thermals to the environment times the virtual potential temperature of the thermals and the rate of mass transfer from the environment to the thermals times the virtual potential temperature of the environment.

The plume virtual potential temperature budget for thermals must be manipulated further before its terms can be determined from the Phoenix 78 observations. The observations are departures from flight leg means which have been normalized by convectional mixed layer scaling. By this procedure, the plume mean virtual potential temperature budget for thermals becomes (equation 18 of Appendix A).

$$\left(\frac{z_i}{w_* \theta_*}\right)\frac{\partial \theta_*}{\partial t}\left(\frac{\overline{\theta_{vT}} - \overline{\theta_v}}{\theta_{v*}}\right) - \frac{\partial\left(\frac{\overline{w'\theta'_v}}{w_*\theta_*}\right)}{\partial z_*} + \frac{\partial\left[\left(\frac{\overline{w_T} - \overline{w}}{w_*}\right)\left(\frac{\overline{\theta_{vT}} - \overline{\theta_v}}{\theta_*}\right)\right]}{\partial z_*}$$

$$+\left(\frac{\overline{w_T} - \overline{w}}{w_*}\right)\frac{\partial\left(\frac{\theta_v}{\theta_*}\right)}{\partial z_*}\frac{\left(\frac{\overline{w_T} - \overline{w}}{w_*}\right)\left(\frac{\overline{\theta_{vT}} - \overline{\theta_v}}{\theta_*}\right)}{\sigma}\frac{\partial \sigma}{\partial z_*} + \frac{\partial\left(\frac{\overline{w'_T\theta'_{vT}}}{w_*\theta_*}\right)}{\partial z_*} + \frac{\left(\frac{\overline{w'_T\theta'_{vT}}}{w_*\theta_*}\right)}{\sigma}\frac{\partial \sigma}{\partial z_*} \qquad (1)$$

$$-\frac{\left(\frac{z_i E_T}{w_*}\right)\left(\frac{\overline{\theta_{vE}} - \overline{\theta_v}}{\theta_*}\right)}{\sigma} + \frac{\left(\frac{z_i E_E}{w_*}\right)\left(\frac{\overline{\theta_{vT}} - \overline{\theta_v}}{\theta_*}\right)}{\sigma} = 0$$

There is an analogous budget equation for the plume mean virtual potential temperature in the environment.

The first term in equation 1 is time rate of change of plume mean buoyancy. The second term is the regional mean buoyancy flux convergence, which is also the rate of change of the regional mean virtual potential temperature profile. The next five terms are the components of the vertical transport of virtual potential temperature in the thermals. The last two terms are the lateral mixing of virtual potential temperature between the thermal regions and their environment. Equation 1 is therefore a blance of four effects: changes in the thermal buoyancy profile, changes in the regional mean virtual potential temperature profile, vertical transport of virtual potential temperature in thermals and lateral mixing of virtual potential temperature between the thermals and the environment.

The only two quantities in this buoyancy budget which cannot be measured directly from the Phoenix 78 observation are the two lateral mass exchange rates, $(z_i E_T/w_*)$ and $(z_i E_E/w_*)$. The convective mass flux budget for the thermal region contains the same two quantities. The mass budget, equation 2, is a balance between the vertical divergence of the convective mass flux and the net lateral mass exchange rate.

$$\frac{\partial \overline{\sigma w_T}/w_*}{\partial z_*} = \frac{z_i E_T}{w_*} - \frac{z_i E_E}{w_*} \qquad (2)$$

Equations 1 and 2 can be solved as a pair of simultaneous linear algebraic equations for these two lateral mass exchange coefficients. The observed terms in these budgets along with the diagnosed lateral mass exchange coefficients will be discussed in section 7.3.

The plume mean vertical velocity budgets for thermals and their environment can be derived in a manner analogous to that used to derive the plume mean virtual potential temperature budgets. This derivation is contained in the latter half of Appendix A. The resulting plume mean vertical velocity budget for thermals is (equation 33 of Appendix A).

$$\left(\frac{z_i}{w_*^2}\right)\frac{\partial w_*}{\partial t}\left(\frac{\overline{w_T}-\overline{w}}{w_*}\right)+\frac{\partial'}{\partial z_*}\left(\frac{\overline{(w_T-\overline{w})^2}}{w_*^2}\right)+\frac{\left(\frac{\overline{w_T}-\overline{w}}{w_*}\right)^2}{\sigma}\frac{\partial\sigma}{\partial z_*}+\frac{\partial}{\partial z_*}\left(\frac{\overline{w_T'^2}}{w_*^2}\right) \qquad (3)$$

$$+\frac{1}{\sigma}\left(\frac{\overline{w_T'^2}}{w_*^2}\right)\frac{\partial\sigma}{\partial z_*}-\frac{1}{\sigma}\left[\left(\frac{z_i E_T}{w_*^2}\right)\left(\frac{\overline{w_E}-\overline{w}}{w_*}\right)-\left(\frac{z_i E_E}{w_*^2}\right)\left(\frac{\overline{w_T}-\overline{w}}{w_*}\right)\right]+\left(\frac{z_i}{w_*^2}\right)P_T$$

$$-\left(\frac{\overline{\theta_{vT}}-\overline{\theta_v}}{\theta_*}\right)=0$$

is an analogous budget equation for the profile of plume mean vertical velocity in the environment.

The first term is time rate of change of plume mean vertical velocity perturbation. The next four terms are the components of the vertical divergence of the vertical velocity flux. The next two terms are the lateral exchange of vertical velocity between the thermals and their environment. The next to last term, P_T, represents the pressure effects. The last term is the buoyant forcing. Equation 1 is therefore a balance of four effects: changes in the thermal vertical velocity profile, vertical divergence of the vertical velocity flux, lateral mixing of vertical velocity between the thermals and the environment and buoyant forcing.

The time tendency term and the four vertical flux divergence terms can be determined directly from the Phoenix 78 aircraft turbulence data. If the two lateral mixing terms in equation 3 are computed using the lateral mass exchange rates determined from equations 1 and 2, then the only unknown term in equation 3 is that representing the pressure effects. Thus, equation 3 is a linear algebraic equation in one unknown. The pressure effects on the mean vertical velocity in thermals can be diagnosed as this residual. The environmental vertical velocity budget can be used in an identical manner to diagnose the environmental pressure effects. The observed terms in these budgets along with the diagnosed profiles of the pressure effects will be discussed in section 7.4.

Lenschow and Stephens (1982) derived a similar budget equation which did not separate the components of lateral exchange of pressure.

7.3 Diagnosis of Lateral Mass Exchange from the Plume Mean Buoyancy Budgets

The nondimensional budget equations for the mean virtual potential temperature profile and the convective mass flux profile in thermal updrafts, equations 1 and 2, were discussed in the previous section. In this section, the profiles of the terms in these two budget equations will be presented. The lateral mass exchange coefficients, E_T and E_E, diagnosed from these two equations are also presented. The profiles of these coefficients are of fundamental importance to the dynamics of boundary layer convection.

The terms representing the rate of change of plume mean buoyancy, the regional mean virtual potential temperature change and four of the five parts of the vertical transport of virtual potential temperature

can all be determined directly from the Phoenix 78 turbulence data collected by the Queenair aircraft and the BAO tower. The vertical advection of regional mean virtual potential temperature by the plume scale updrafts can be measured directly in the lower half of the CBL but must be approximated as described below in the upper half of the CBL. Thus, the only terms in the plume mean virtual potential temperature budget which cannot be measured are the lateral mass exchange terms. Within these terms only the coefficients of lateral mass exchange are unmeasured. Therefore, the vertical profiles of the coefficients of lateral mass exchange between the thermal updrafts and environmental downdrafts can be diagnosed from the thermal virtual potential temperature and the convective mass flux budgets.

The lateral mass exchange terms in the budgets can include both lateral mass exchange between steady plumes and the changes in plume characteristics which result from changes in sign of the vertical velocity. The birth and death of nonsteady convective eddies are thus part of this term. For example, the effects of a thermal bubble which stops rising and dissipates are included in this term.

The aircraft observations extend only down to 0.1 z_i because of the restrictions on flight over populated terrain. The profiles below that level are based on extrapolation and free convective similarity as appropriate. The accuracy of the results in bottom ten percent of the CBL are therefore suspect.

This analysis could be done with the results of other CBL experiments or Large Eddy Simulation (LES) models. The differences between the profiles of turbulence statistics measured in this and previous studies were examined in Chapter 5. The differences are

generally quantitative rather than qualitative and the Phoenix 78 results lie near the median. Therefore, it is probable that the results of this study will be a least qualitatively universal for convective boundary layers with $z_i >> -L$.

The profiles used in this study are smooth analytic curves fit by eye to the observed data from the Phoenix 78 field experiment. Positive terms act to decrease θ_v while negative terms act to increase θ_v.

The only time dependent term in the plume mean θ_v budget is the term which includes the rate of change θ_{v*}. The θ_{v*}, w_* and z_i time series followed a similar pattern on each of the days used in this study. Therefore, composite time series were used to determine typical and extreme values of this term.

The profile of the time dependent term at 12:40 pm is shown in Figure 7.1. This profile has the same shape as the plume mean θ_v perturbation profile. The shape of the profile of the time tendency term does not change with time but its amplitude does. As shown in Figure 7.2, the amplitude at 12:40 pm is typical of morning and midday. The amplitude increases into the afternoon. At its largest, the time tendency term is an order of magnitude or more smaller than other terms to be diagnosed. While this term will be included in the budget calculations, its effect is negligible. Therefore, the diagnosed profiles of the lateral mass exchange coefficients are as universal as the mixed layer turbulence profiles which are used to compute them, with negligible time dependence from this term. This result is to be expected because of the mixed layer scaling parameters change slowly relative to the time scale of convective overturning.

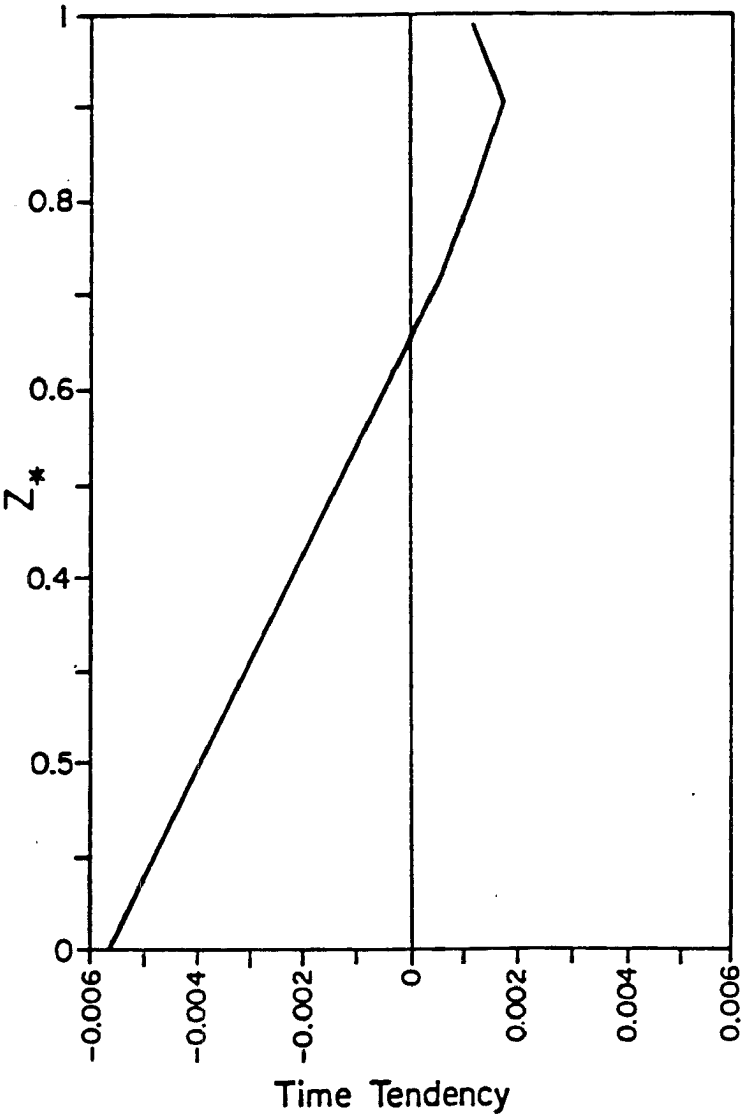

Fig. 7.1 The vertical profile of the time tendency term in the budget of plume mean virtual potential temperature. This is the first term in equation 1. The vertical coordinate is z/z_i, the fraction of the depth of the convective boundary layer. The horizontal scale is nondimensional.

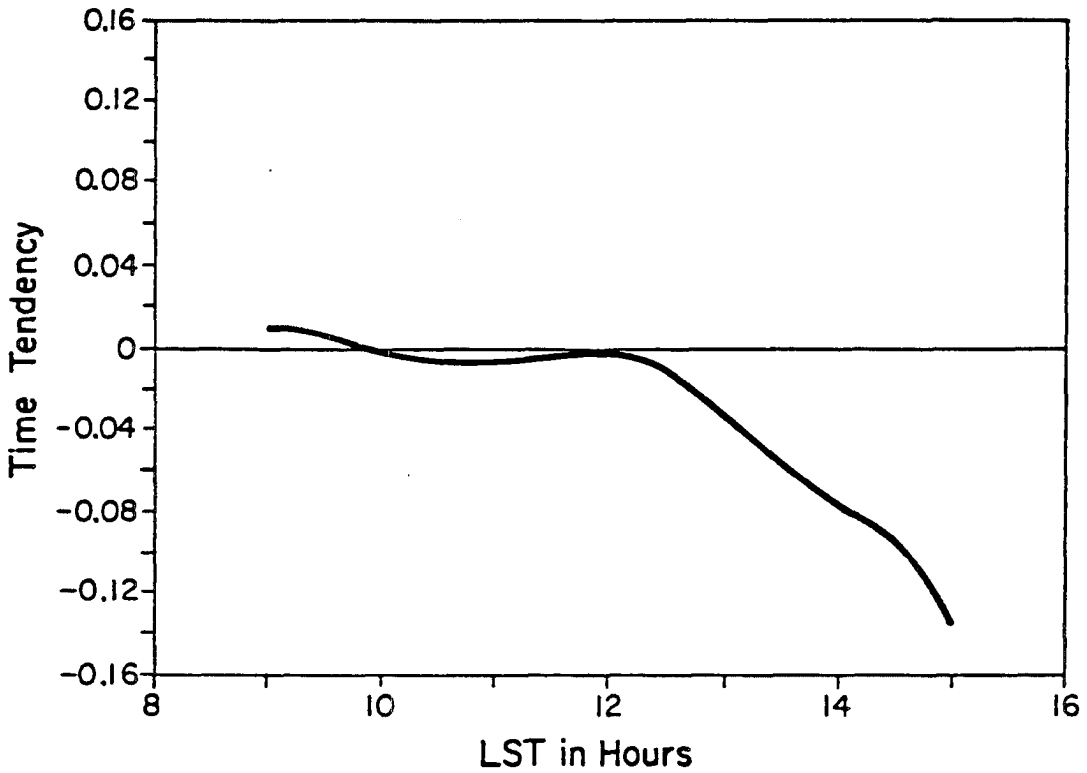

Fig. 7.2 The composite time series of the maximum amplitude of the time tendency term in the budget of plume mean virtual potential temprature. The horizontal coordinate is in hours after midnight local standard time. The vertical scale is non-dimensional.

The rate of change of the regional mean virtual potential temperature profile is shown in Figure 7.3. This term is positive and is one of the dominant terms throughout the depth of the CBL. Because of the observed curvature in the θ_v flux profile, this term is largest near the surface and becomes smaller in the upper CBL.

The two components of the divergence of θ_v flux by plume mean quantities are shown in Figure 7.4. The area change component is small throughout the depth of the CBL. The flux gradient component is large and positive in the lowest levels of the CBL because large eddies become increasing important to the transport as the influence of the surface decreases. This component is significant and negative throughout the bulk of the CBL where plume scale motions carry a significant fraction of the buoyancy flux. Above the level of greatest negative buoyancy in the upper CBL, this component becomes positive again. The total contribution of plume mean motions to the vertical transport of buoyancy is significant. These terms do not however dominate the buoyancy budget as is assumed in the simplest tophat models.

The two components of the divergence of subplume perturbation contribution to θ_v flux are shown in Figure 7.5. The area change component is small and negative throughout the depth of the CBL. The flux gradient component is large and positive in the lowest levels of the CBL because the importance of small eddies to the transport decrease with height near the surface. This component is significant and negative throughout the bulk of the CBL indicating that small scale motions carry roughly as significant a fraction of the buoyancy flux as do plume scale motions. Above the level of greatest negative

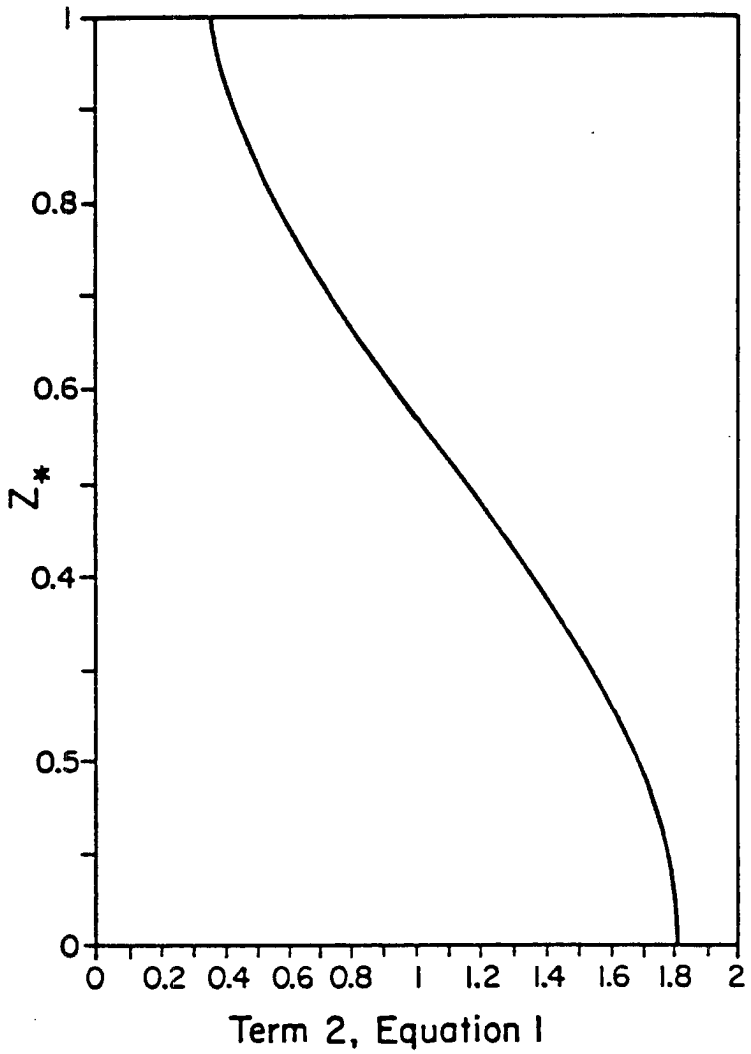

Fig. 7.3 The vertical profile of the rate of change of the regional mean virtual potential temperature. This quantity is the same as the convergence of the regional mean virtual potential temperature flux, the second term in equation 1. The vertical coordinate is z/z_i, the fraction of the depth of the convective boundary layer. The horizontal scale is non-dimensional.

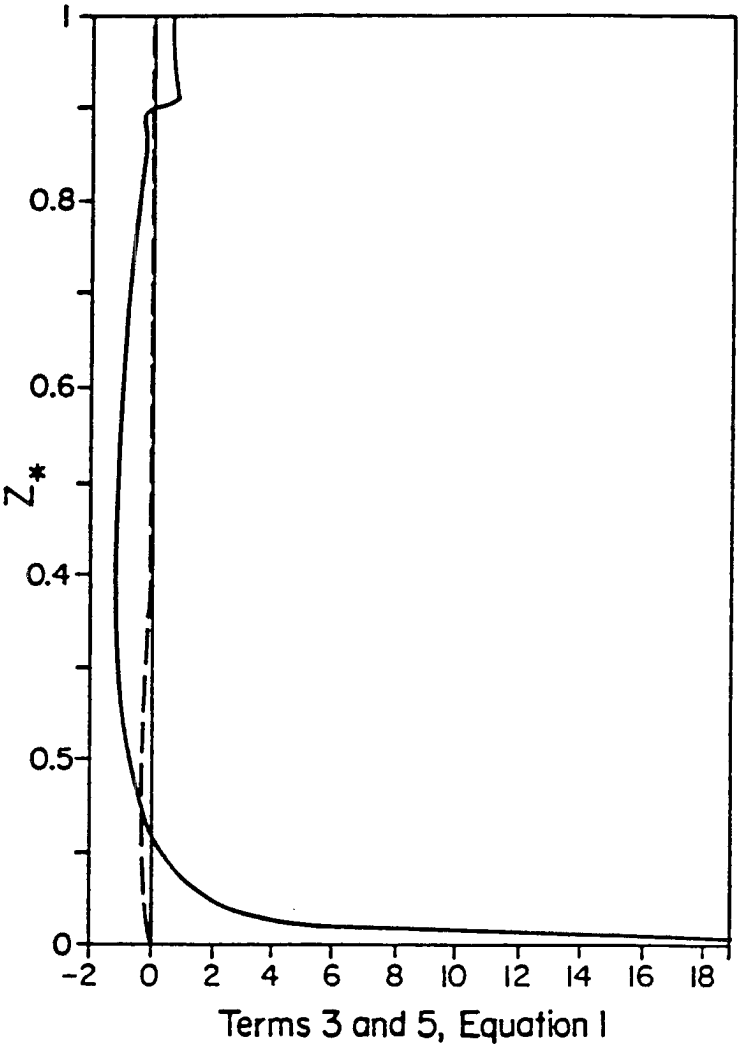

Fig. 7.4 The vertical profiles of the two components of the plume mean contribution to the flux divergence of virtual potential temperature in thermals. The solid curve represents the flux gradient contribution, term 3 in equation 1. The dashed curve represents the plume area change contribution, term 5 in equation 1. The vertical coordinate is z/z_i, the fraction of the depth of the convective boundary layer. The horizontal scale is nondimensional.

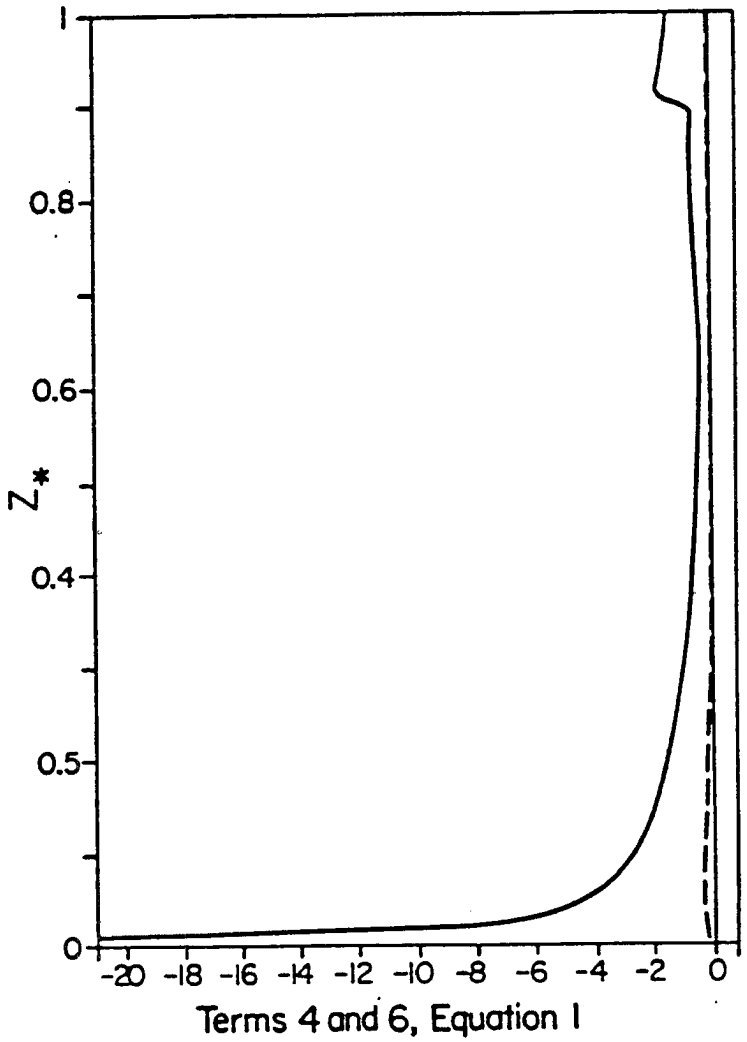

Fig. 7.5 The vertical profiles of the two components of the subplume perturbation contributions to the flux divergence of virtual potential temperature in thermals. The solid curve represents the flux gradient contribution, term 4 in equation 1. The dashed curve represents the plume area change contribution, term 6 in equation 1. The vertical coordinate is z/z_i, the fraction of the depth of the convective boundary layer. The horizontal scale is nondimensional.

buoyancy in the upper CBL, this component becomes even more negative. The total contribution of subplume mean motions to the vertical transport of buoyancy is significant. There terms are not negligible as is assumed in the simplest tophat models.

In the lowest and highest levels of the CBL the plume mean and subplume perturbation contributions to the buoyancy flux divergence partially cancel. However, in the mid CBL there terms are of the same sign, opposite that of the regional mean virtual potential temperature change term.

The vertical advection of the regional mean virtual potential temperature by plume mean motions is the gradient production term for plume mean buoyancy. Computation of this term requires knowledge of the gradient of the regional mean virtual potential temperature profile for the CBL. The gradient of this profile cannot be determined from the aircraft horizontal flight legs because of the change which occurs in the CBL θ_v characteristics during the hour required to complete a set of legs. Therefore, virtual potential temperature profiles from the BAO tower and from Phoenix 78 aircraft soundings are used to estimate the mixed layer profile for virtual potential temperature which is needed for this computation.

The BAO θ_v profiles from all the times for which aircraft flux data were analyzed were composited to give a profile of θ_v from the surface through the mid CBL. The compositing procedure was as follows. The heights of the 8 levels of tower data were first scaled by z_i. Then an offset was added to each of the tower θ_v profiles so that they intersected each other at a height of 0.1 z_i. Next these profiles were scaled by θ_{v*}. Finally the entire set of profiles were offset equally so that the average value above 0.5 z_i was zero.

This procedure results in a profile of the mixed layer scaled departure of θ_v from its mid CBL minimum. The vertical gradient of this profile can be shown to be equivalent to the profile of the mixed layer normalized gradient of θ_v. The θ_v data are shown in Figure 7.6. The points generally lie within one θ_* of a smooth curve. The cluster of points well to the negative side of the curve at heights around 0.2 z_i all come from a single sensor on one day when its data were in disagreement with those of the surrounding sensors. The problem had been corrected before subsequent data collection.

The BAO θ_v profile shows a strong superadiabatic lapse rate in the surface layer which decreases with height. However, this lapse rate does not approach neutrality until 0.4 z_i. Values of the regional mean lapse rate of order θ_*/z_i are dynamically significant because the total buoyancy difference between thermal updrafts and environmental downdrafts is only of order θ_*. Therefore, vertical advection of these mean superadiabatic lapse rates can make a major contribution to the buoyancy budgets of thermal updrafts and environmental downdrafts of the CBL. Because θ_*/z_i is generally of order 10^{-4} degrees C/m, dynamically significant regional mean lapse rates can appear to be neutral unless great care is taken in the data acquisition and analysis. In terms of the dynamics of convective turbulence, the lower third of the CBL is strongly unstable. This failure of the virtual potential temperature profile to be mixed to neutrality through a significant fraction of the CBL depth is a key finding of this study. Mahrt and Paumier (1984) present without comment a similar θ_v profile for the AMTEX study of cold air outbreaks over warm water.

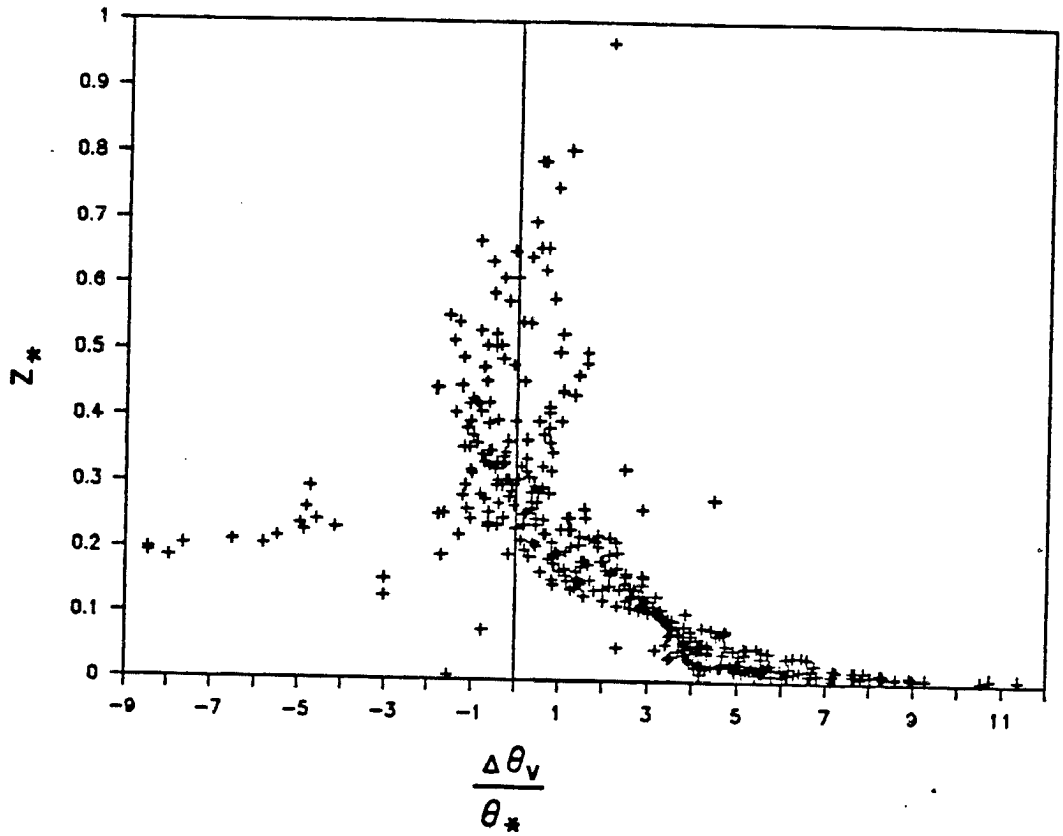

Fig. 7.6 The vertical profile of virtual potential temperature in the convective boundary layer. The absicissa is the departure from the mid CBL θ_v minimum. Each point represents one 20 minute average from a quartz thermomenter at the BAO 300 m tower. The vertical coordinate is z/z_i, the fraction of the depth of the convective boundary layer. The horizontal scale has been scaled nondimensionalized by θ_*, the mixed layer temperature.

Accurate measurements of the lapse rate in the upper CBL are much more difficult to obtain. The BAO tower rarely penetrated these levels with its high accuracy quartz thermometers and the aircraft did not cover a large enough distance in each height interval to obtain averages which were accurate to within less than one θ_* of the true mean as needed.

The composite aircraft θ_v sounding is presented in Figure 7.7. This composite was created by first offsetting the individual soundings so that the mean θ_v between 0.4 and 0.8 z_i was zero and then scaling the remainder by θ_*. This procedure accomplishes the same result as that used on the BAO θ_v profiles, the scaling of the departures from the mid CBL θ_v minimum by θ_*. This scaling is not expected to be appropriate outside the CBL. This profile has been smoothed by a running average 0.03 z_i in depth.

Stability increases by well over an order of magnitude of z_i where there is a very sharp transition from the CBL to the capping inversion. Within the CBL the small sample size results in scatter which ranges up to twice θ_*. This scatter is large enough to hide dynamically significant regional mean lapse rates. The aircraft θ_v profile does, however, put an upper limit on the stability of the upper CBL at approximately 4 θ_*/z_i.

There is one level for which the mean θ_v lapse rate can be computed directly from the plume mean θ_v budget. This is the level of zero mean buoyancy, 0.66 z_i, at which the updraft and downdraft regions have the same plume mean θ_v. At this level, the unmeasured lateral mass exchange effects drop out of the system of equations because there is no lateral θ_v difference to mix. Therefore, at this

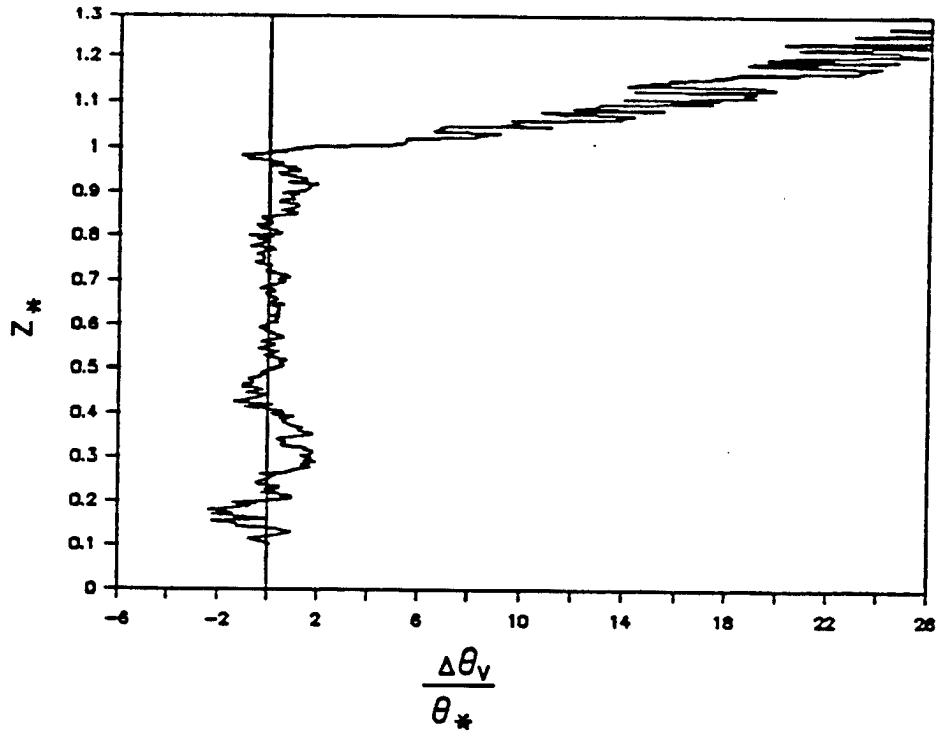

Fig. 7.7 The vertical profile of virtual potential temperature in the convective boundary layer. The abscissa is the departure from the mid CBL θ_v minimum. This profile is a composite data collected on the aircraft sounding legs of Phoenix 78. The profile has been smoothed by a running mean whose length equalled three percent of the boundary layer depth. The base of the capping inversion can be seen as a sharp change in slope of the profile. The vertical coordinate is z/z_i, the fracion of the depth of the convective boundary layer. The horizontal scale has been scaled nondimensionalized by θ_*, the mixed layer temperature scale.

one level the mean lapse rate of θ_v can be computed without knowledge of the lateral mass exchange coefficients. The value of the mixed layer normalized regional mean θ_v lapse rate computed for this level is very near 1.0. This regional mean lapse rate is well within the limit determined from the aircraft and tower measurements.

A smooth analytic profile for the normalized gradient of θ_v which fits the tower data in the lower CBL and has the correct lapse rate at the level of zero buoyancy is shown in Figure 7.8. The shape of the profile above 0.66 z_i is only qualitatively correct. The physical constraint that the diagnosed lateral mass exchange coefficients be non-negative helps to limit the values of the lapse rate in this region. The observational data would not rule out gradients a factor of two larger or smaller in these levels. This uncertainity will be taken into account in the discussion of the results.

The gradient production of buoyancy is computed from this profile and is shown in Figure 7.9. This term is very large and negative in the lower half of the CBL where it is a one of the two dominant terms in the plume mean buoyancy budget. In the upper half of the CBL, this term is positive and significant although not dominant.

Measurements of the convective mass flux are easily made from the Phoenix 78 aircraft data. The profile of the divergence of the convective mass flux will not be shown because it can be determined as the difference between the two lateral mass exchange coefficients which are presented later in this section.

The terms described above are all that are required to solve the plume mean θ_v and convective mass flux budget equations for the lateral mass exchange terms. The sum of the lateral mass exchange

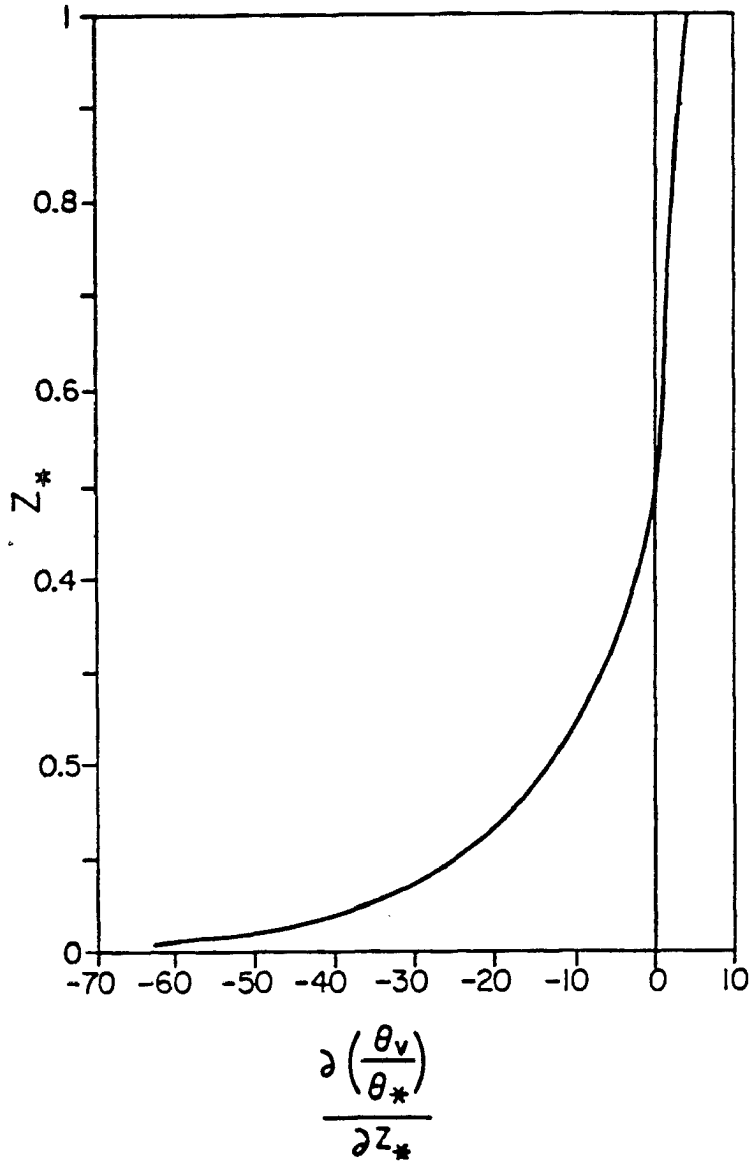

Fig. 7.8 The profile of the vertical gradient of regional mean virtual potential temperature in the convective boundary layer. The lower half of this profile is a smooth curve drawn to fit the BAO tower profile of virtual potential temperature during Phoenix 78. The upper half of the profile was drawn to meet the constraints of the plume mean virtual potential temperature budget for thermals at the level of zero buoyancy as well as the aircraft sounding shown in Figure 7.7. The vertical coordinate is z/z_i, the fraction of the depth of the convective boundary layer. The horizontal scale has been nondimensionalized by θ_*, the mixed layer temperature scale, and z_i, the boundary layer depth.

terms are compared with the vertical advection of regional mean θ_v by plume mean motions in Figure 7.9. These two terms act against each other throughout most of the CBL. Both terms are large in the lower third of the CBL where regional mean superadiabatic lapse rates are large. In the upper CBL, these two terms are significant but not dominant, being of the same order as the vertical transport terms. In this layer, the gradient production term is much smaller than the sum of the lateral mass exchange terms. Therefore, the uncertainty in the gradient production term in the upper thrid of the CBL is not large enough to make a qualitative difference in the lateral mixing terms.

The profiles of the lateral mass exchange coefficients themselves are shown in Figure 7.10. It must be remembered that the profiles used in this computation were based on conjecture for levels below 0.1 z_i. Therefore, the results in the bottom ten percent of the CBL should not be trusted. The values in the upper third of the CBL are only qualitatively correct because of the difficulty in determining the regional mean lapse rate for those levels.

The difference between these two coefficients is the divergence of the convective mass flux as shown in equation 2. The lateral mass exchange coefficients are equal at 0.25 z_i whre the convective mass flux is at a maximum. Below that level, the mass exchange coefficient into updrafts is greater than that into downdrafts. Above that level, the reverse is true. The magnitude of the lateral mass exchange coefficients in the lower half of the CBL is much large than that in the upper half of the CBL. In the lower CBL, the lateral exchange rates are large enough to almost totally exchange the mass of the updrafts before they reach 0.5 z_i. This is the only way the observed

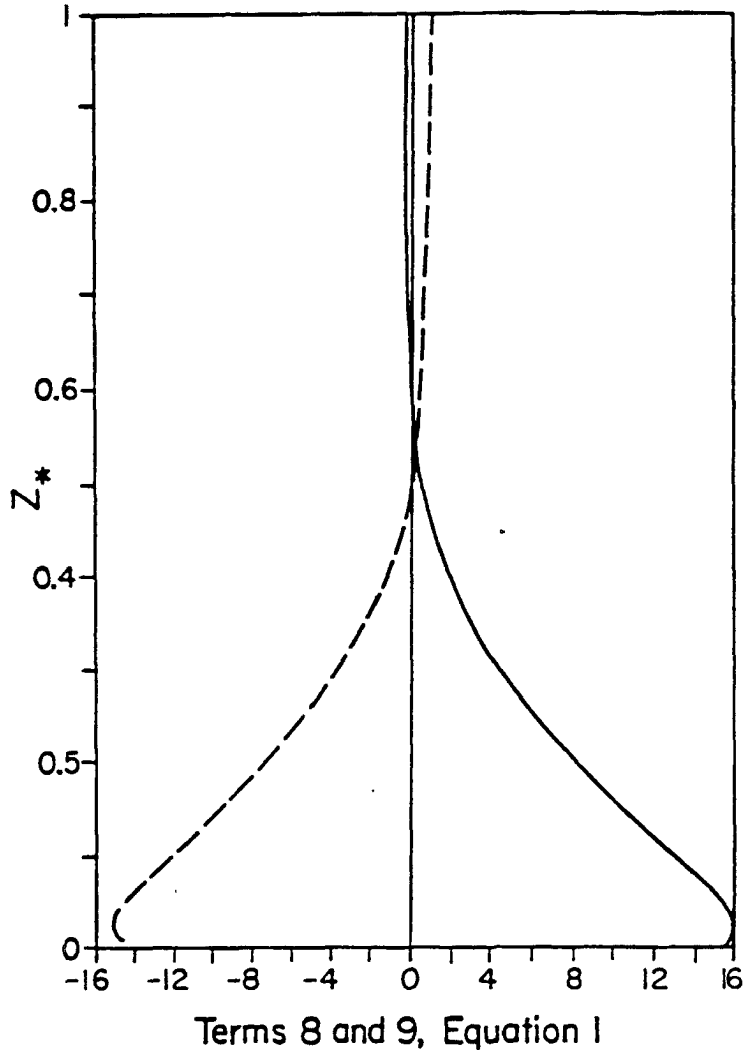

Fig. 7.9 The vertical profiles of the lateral mass exchange and gradient production terms in the plume mean virtual potential temperature budget for thermals. The solid curve represents the sum of the lateral mass exchange terms, 8 and 9, in equation 1. The dashed curve represents the gradient production of buoyancy, term 4 in equation 1. The vertical coordinate is z/z_i, the fraction of the depth of the convective boundary layer. The horizontal scale is non-dimensional.

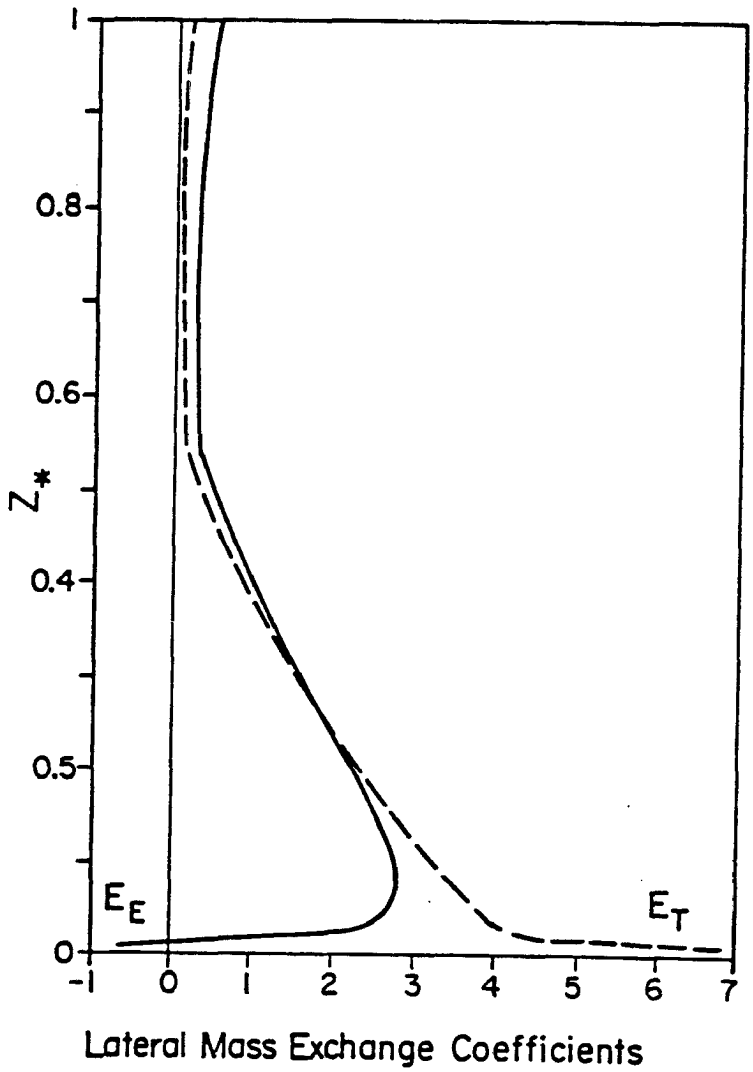

Fig. 7.10 The vertical profiles of the two coefficients of lateral mass exchange as determined from the budgets of plume mean virtual potential temperature and convective mass flux for thermals. The solid curve represents the coefficient for mass exchange from thermals into their environment, the coefficient in term 9 of equation 1. The dashed curve represents the coefficient for mass exchange from the environment into thermals, the coefficient in term 8 of equation 1. The vertical coordinate is z/z_i, the fraction of the depth of the convective boundary layer. The horizontal scale is nondimensional.

large regional mean lapse rates, >10 θ_*/z_i, can be reconciled with the small, > 1 θ_*, updraft buoyancies in the lower CBL. Both of these quantities could be measured accurately during the Phoenix 78 experiment so the order of magnitude of the lateral exchange coefficients in the lower CBL is not in doubt.

In the lower half of the CBL, where the mean superadiabatic lapse rate is large relative to the lapse rate of plume mean perturbation θ_v, lateral mass exchange and vertical advection of the regional mean θ_v are approximately an order of magnitude larger than the other terms in the plume mean θ_v budget. The plume buoyancy is, thus, determined primarily by the interaction of the vertical advection of the regional mean θ_v between updrafts and downdrafts. The magnitude of the lateral mass exchange required to achieve a balance to the budgets is much larger than would be expected if the CBL were thought of as nearly neutrally stratified as it often has been in the past.

In the upper half of the CBL, the situation is different. The difference between the two coefficients of lateral mass exchange is of the same order as the coefficients themselves. The mass exchange into thermals is much less than the mass exchange out of them into the environment. This suggests that in the upper CBL contaminants released in downdrafts will have a much longer in plume residence time than those released in updrafts. Knowledge of the mass flux profile alone is not sufficient to show this. Only knowledge of both components of the lateral mass exchange between updrafts and downdrafts can show how little downdraft air enters updrafts in the upper CBL. These results help explain why the center of mass of a nonbuoyant contaminant released in the upper CBL would immediately

begin to descend towards the mid CBL without waiting for the plume to impinge on the inversion base (Lamb, 1979).

In the upper half of the CBL, all of the terms in the plume mean θ_v budgets except the time tendency and area change terms are roughly the same order of magnitude. The net affect of the advective and flux terms is to decrease θ_v in the thermal updrafts to balance the increase caused by the lateral mass exchange.

7.4 Diagnosis of Pressure Forcing from the Plume Mean Vertical Velocity Budgets

The nondimensional budget equation for the mean vertical velocity profile in thermal updrafts, equation 3, was discussed in section 7.2. A similar budget equation exists for the mean vertical velocity profile of environmental downdrafts. In this section, the profiles of the terms in these two equations will be presented.

The terms representing the nonuniversal time dependency, the buoyancy forcing and the four parts of the divergence of vertical velocity flux can all be determined directly from the Phoenix 78 aircraft and BAO tower turbulence data. The lateral mass exchange terms can be determined from these data and from the lateral mass exchange coefficients derived from the plume mean buoyancy budget in the previous section. The one undetermined term in each of the plume mean vertical velocity budget equations is the pressure forcing.

The pressure effects in this term include not only the plume mean pressure gradient force but also any pressure effects which would cause vertical velocity to mix differently than buoyancy. These effects cannot be separated by the current analysis. However, the diagnosis of the net of these effects provides more information about

the dynamic forcing of CBL convection than has been available previously. Positive terms act to decrease the plume mean vertical velocity while negative terms act to increase it.

The only time dependent term in the plume mean vertical velocity budgets is the term which includes the rate of change w_*. Composite time series were used to determine typical and extreme values of this term.

The 12:40 pm profiles of these terms are shown in Figure 7.11 for the updraft and downdraft regions. These profiles have the same shape as the plume mean vertical velocity perturbation profiles. The shapes of these profiles do not change with time but their amplitudes do. As shown in Figure 7.12, the amplitudes at 12:40 pm are typical of morning and midday. However, the terms change sign and increase in amplitude during the afternoon. At their largest, these time tendency terms are an order of magnitude or more smaller than the diagnosed pressure forcing terms. The smallness of the time tendency terms can be explained by the relative time scales of convective cells and CBL evolution as described above the θ_v budgets. Despite their smallness, these terms are retained in the budget equations.

The plume area change contribution to the divergence of subplume perturbation part of the vertical velocity flux in updrafts and downdrafts is shown in Figure 7.13. These terms act to accelerate the updrafts and downdrafts in the lower CBL and to decelerate them in the upper CBL. These terms are small throughout the depth of the CBL.

The plume area change contribution to the divergence of the vertical velocity flux by plume mean motions in updrafts and downdrafts is shown in Figure 7.14. These terms act to accelerate the

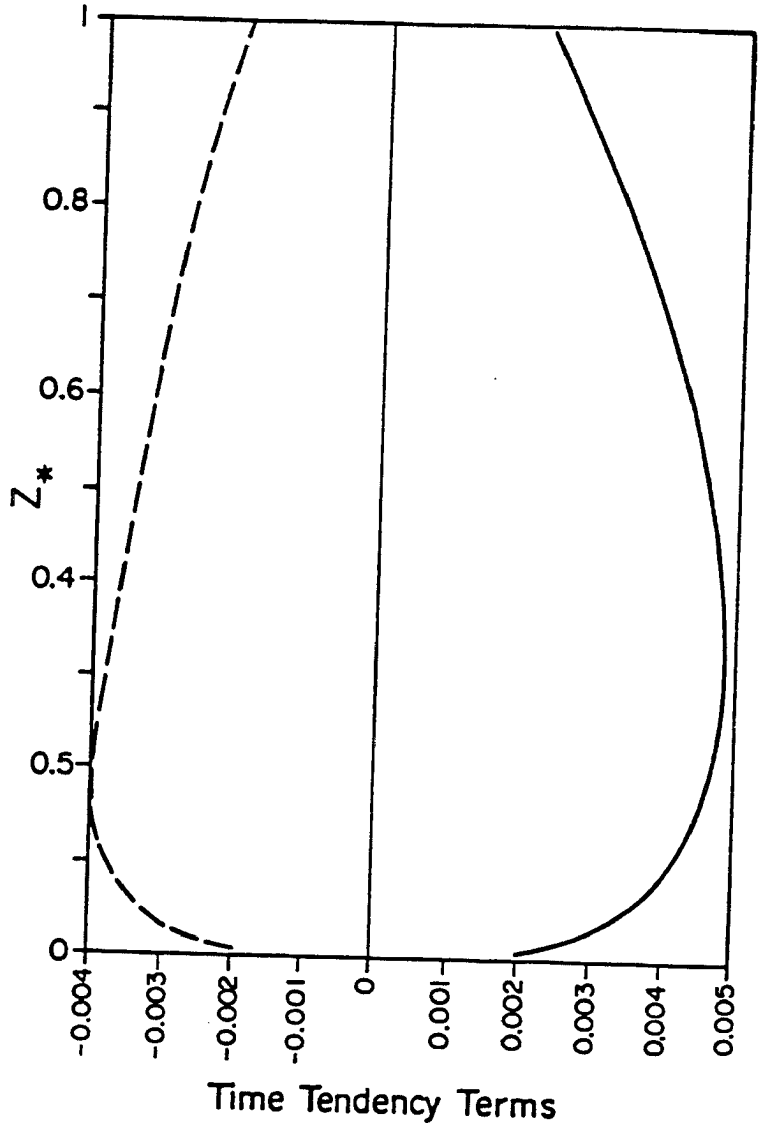

Fig. 7.11 The vertical profile of the time tendency term in the budgets of plume mean vertical velocity for thermals and their environment. This is the first term in equation 3 and the similar equation for the the environment. The solid line represents the profile for thermals while the dashed line represents the profile for their environment. The vertical coordinate is z/z_i, the fraction of the depth of the convective boundary layer. The horizontal scale is non-dimensional.

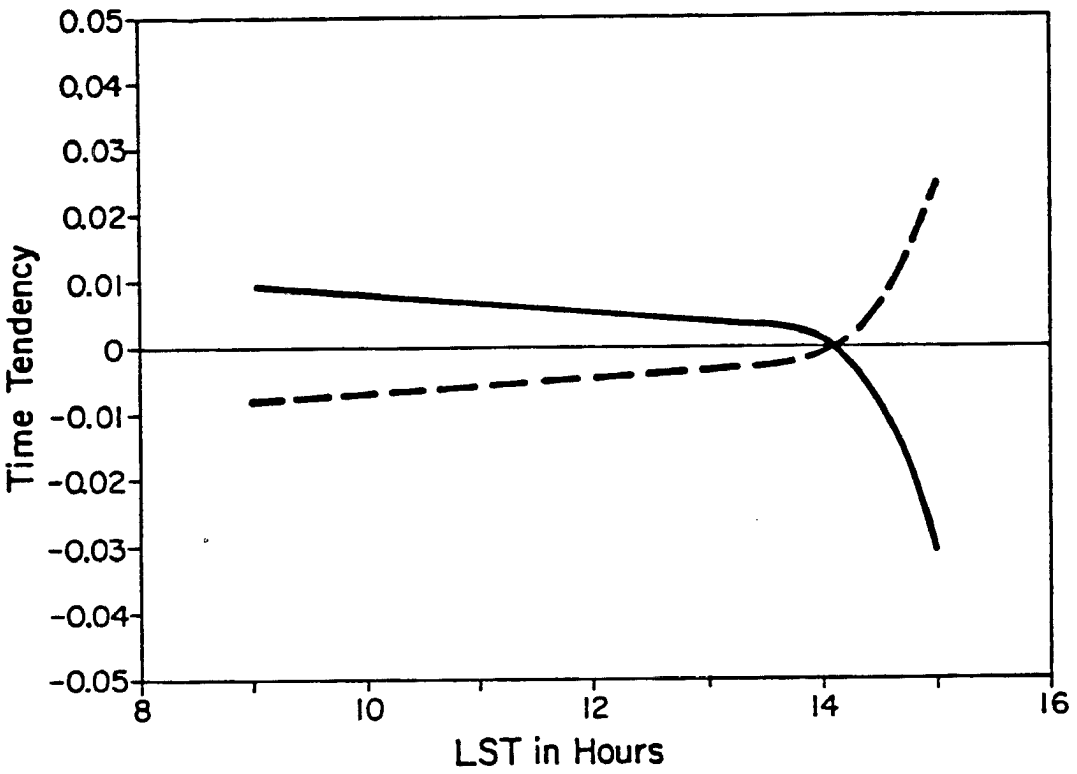

Fig. 7.12 The composite time series of the maximum amplitude of the time tendency term in the budgets of plume mean vertical velocity for thermals and their environment. This is the first term in equation 3 and the similar equation for the environment. The solid line represents the series for thermals while the dashed line represents the series for their environment. The horizontal coordinate is in hours after midnight local standard time. The vertical scale is nondimensional.

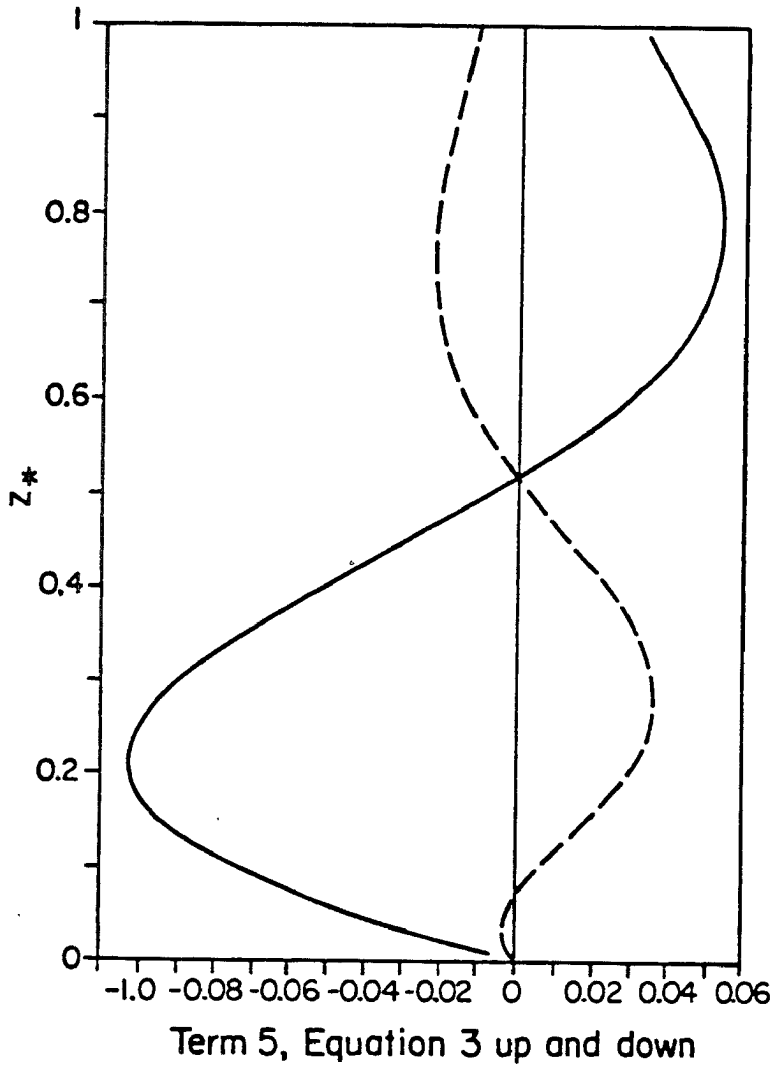

Fig. 7.13 The plume area change contribution to the divergence of the subplume perturbation part of the vertical veloicty flux in updrafts and downdrafts, the fifth term in the plume mean vertical velocity budgets. The solid line represents the profile for thermals while the dashed line represents the profile for their environment. The vertical coordinate is z/z_i, the fraction of the depth of the convective boundary layer. The horizontal scale is nondimensional.

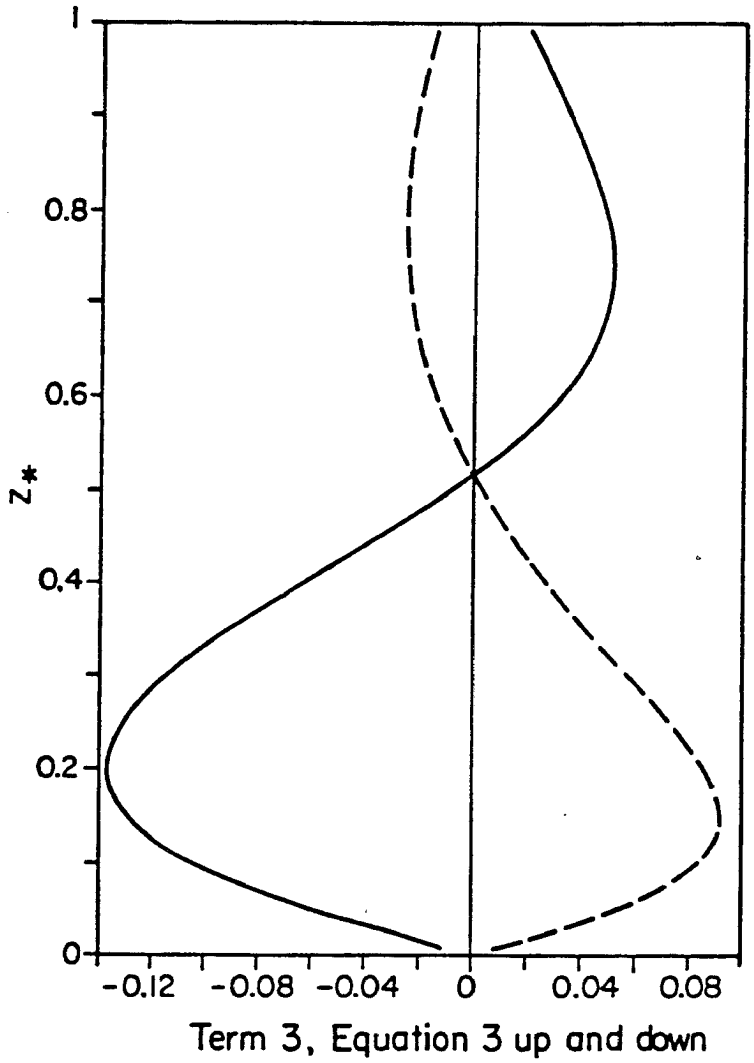

Fig. 7.14 The plume area change contribution to the divergence of the plume mean part of the vertical velocity flux in updrafts and downdrafts, the third term in the plume mean vertical velocity budgets. The solid line represents the profile for thermals while the dashed line represents the profile for their environment. The vertical coordinate is z/z_i, the fraction of the depth of the convective boundary layer. The horizontal scale is nondimensional.

updrafts and downdrafts in the lower CBL and to decelerate them in the upper CBL. These terms are small thoughout the depth of the CBL.

The profiles of the plume mean buoyant forcing and the two flux gradient parts of the divergence of the vertical velcoity flux are shown for thermal updrafts and environmental downdrafts in Figures 7.15 and 7.16 respectively. Because of the mixed layer scaling, the plume mean buoyant forcing profiles are the same as the plume mean perturbation θ_v profiles. Buoyancy acts to accelerate both updrafts and downdrafts in the lower two thirds of the CBL but acts to decelerate both in the top third of the CBL and within the capping inversion. This lack of buoyant forcing for the downdrafts in their upper CBL source region will be discussed below in relation to the other forcing terms.

The flux gradient component of the divergence of the subplume perturbation part of the vertical velocity flux is large and positive in the lower CBL. In the upper CBL, this term is negative and of the same order as the buoyant forcing. This term acts to decelerate updrafts in their lower CBL source region and accelerate them in the upper CBL. Thus, except for a region in the mid CBL, this term opposes buoyant forcing in updrafts. On the other hand, this term acts similarly to buoyancy for downdrafts, decelerating them in their upper CBL source region and accelerating them in the lower CBL. This term acts against the observed acceleration patterns in both updrafts and downdrafts. Therefore, this term cannot provide the inital impetus for downdrafts in the CBL.

The flux gradient component of the divergence of the plume mean part of the vertical velcoity flux is large and positive in the lower

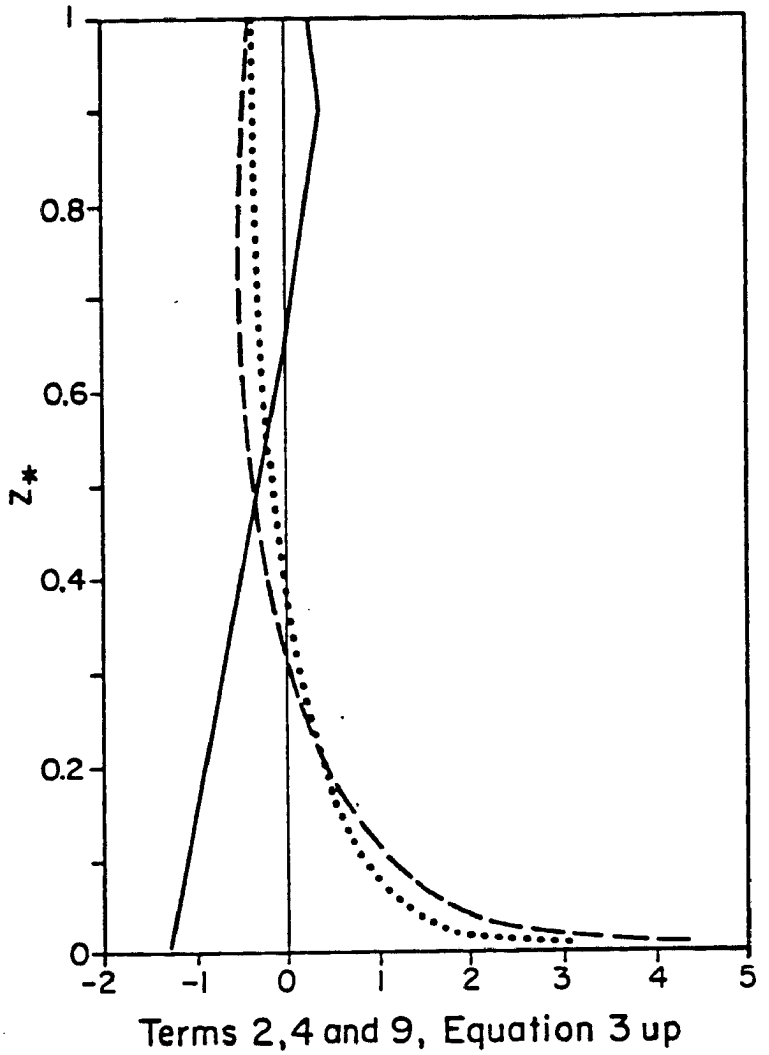

Fig. 7.15 The profiles of the plume mean buoyant forcing and the two flux gradient parts of the divergence of the vertical velocity flux are shown for thermal updrafts. The solid line represents the profile of the plume mean buoyant forcing of the vertical velocity budget for thermals, term 9 of equation 3. The dashed line represents the profile for the plume mean contribution to the flux gradient part of the divergence of vertical velocity flux, term 2 of equation 3. The dotted line represents the profile for the subplume perturbation contribution to the flux gradient part of the divergence of vertical velocity flux, term 4 of equation 3. The vertical coordinate is z/z_i, the fraction of the depth of the convective boundary layer. The horizontal scale is non-dimensional.

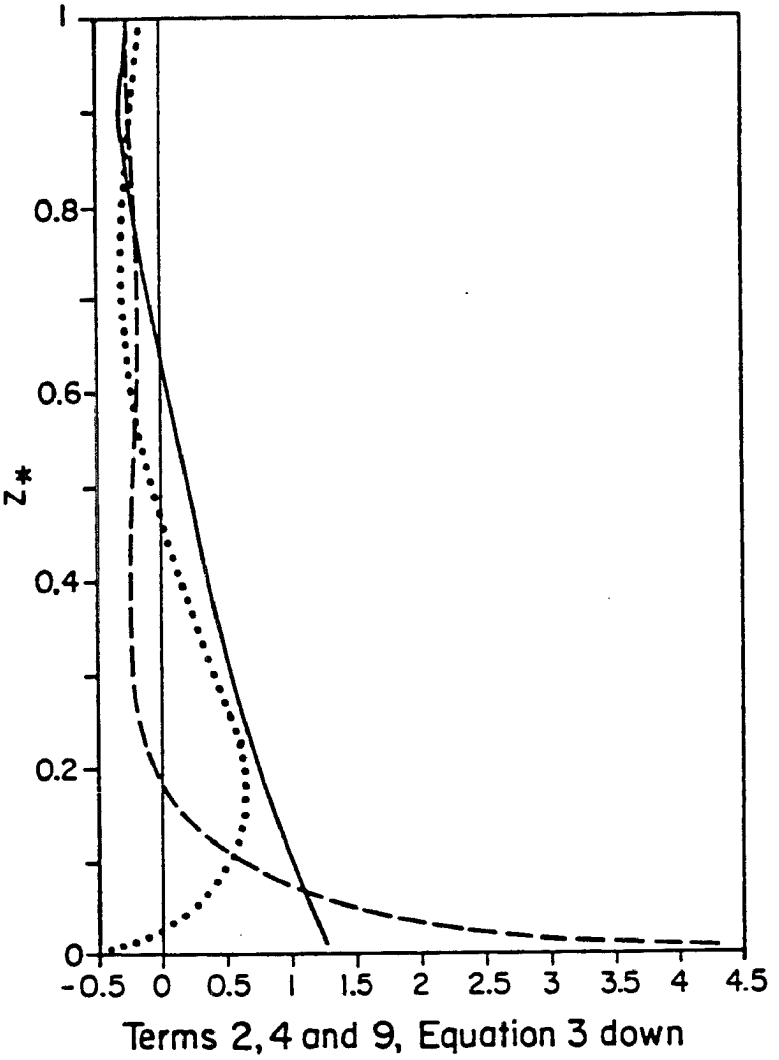

Fig. 7.16 The profiles of the plume mean buoyant forcing and the two flux gradient parts of the divergence of the vertical velocity flux are shown for environmental downdrafts. The solid line represents the profile of the plume mean buoyant forcing of the vertical velocity budget for the environment, the ninth term. The dashed line represents the profile for the plume mean contribution to the flux gradient part of the divergence of vertical velocity flux, the second term. The dotted line represents the profile for the subplume perturbation contribution to the flux gradient part of the divergence of vertical velocity flux, the fourth term. The vertical coordinate is z/z_i, the fraction of the depth of the convective boundary layer. The horizontal scale is nondimensional.

CBL. In the upper CBL, this term is negative. The sign change occurs just below the level of maximum magnitude of plume mean vertical velocity. This level is somewhat lower for downdrafts than for updrafts. This flux divergence term is also of the wrong sign to profide the inital impetus for CBL downdrafts.

The subplume perturbation and plume mean contributions to the divergence of vertical velocity flux are of similar magnitude. Thus, both scales of motion must be accounted for in diagnostic models of CBL convection. The subplume perturbation contribution is equally important in the thermal updrafts and the environmental downdrafts indicating that the amount of small scale turbulence is similar in the updrafts and downdrafts of the CBL.

Only the lateral mass exchange and pressure forcing terms remain to provide the initial impetus for CBL downdrafts. These two terms are compared for updrafts and downdrafts in Figures 7.17 and 7.18 respectively. The lateral mass exchange terms were computed with the mass exchange coefficients which were diagnosed from the plume mean buoyancy and convective mass flux budgets in the previus section. The lateral mass exchange can only act to decelerate both updrafts and downdrafts because it always mixes in air moving in the opposite direction.

This mass exchange induced deceleration is largest in the lower CBL where it is generally larger than any of the previously described terms. In the upper CBL, the deceleration caused by lateral mass exchange between updraft and downdraft plumes is of the same magnitude as the buoyancy and flux divergence terms. Lateral mass exchange is a significant term in these plume mean vertical velocity budgets

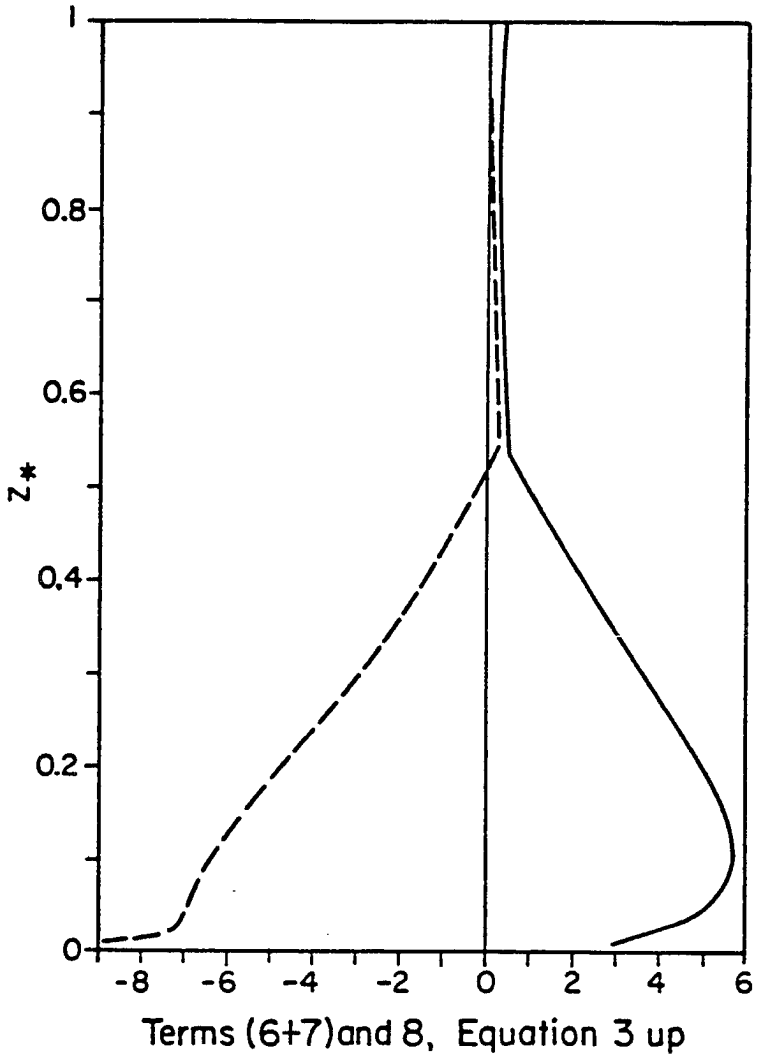

Fig. 7.17 The vertical profiles of the lateral mass exchange and nonhydrostatic pressure effect terms in the plume mean vertical velocity budget for thermals. The solid curve represents the sum of the lateral mass exchange terms, 6 and 7, in equation 3. The dashed curve represents the nonhydrostatic pressure effect, term 8 of equation 3. The vertical coordinate is z/z_i, the fraction of the depth of the ocnvective boundary layer. The horizontal scale is nondimensional.

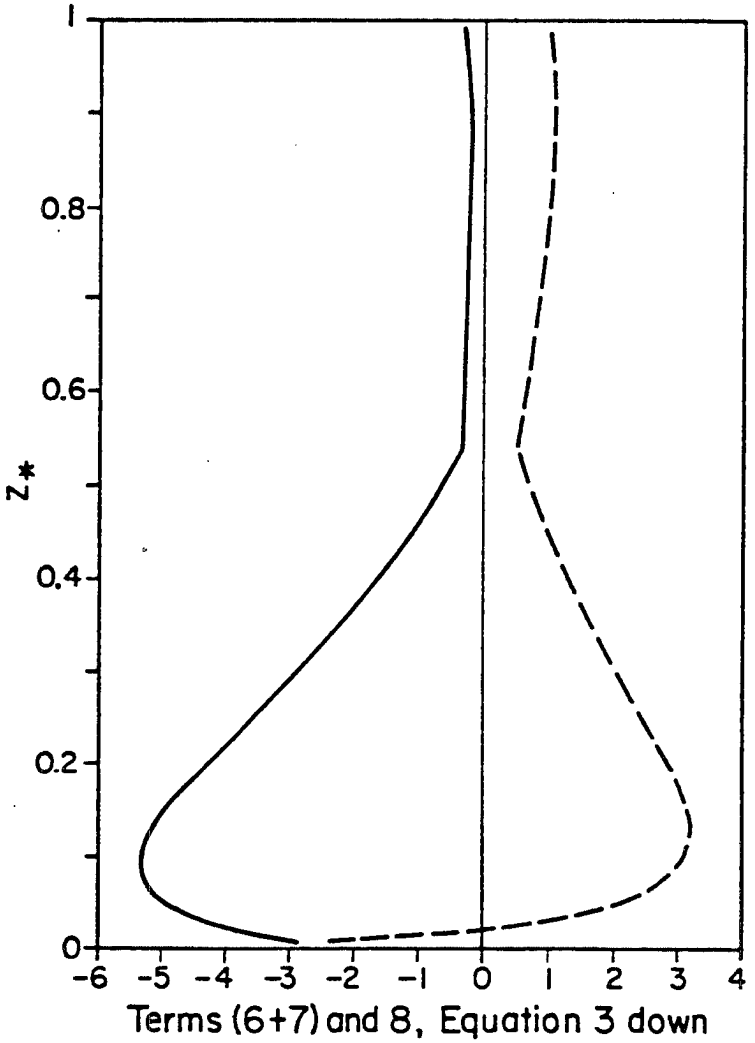

Fig. 7.18 The vertical profiles of the lateral mass exchange and nonhydrostatic pressure effect terms in the plume mean vertical velocity budget for the environment. The solid curve represents the sum of the lateral mass exchange terms. The dashed curve represents the nonhydrostatic pressure effects. The vertical coordinate is z/z_i, the fraction of the depth of the convective boundary layer. The horizontal scale is nondimensional.

throughout the depth of the CBL and is a dominant term in the lower CBL.

Large pressure forcing is required to balance the plume mean vertical velocity budgets. Pressure forcing, along with lateral mass exchange, dominates these budgets in the lower half of the CBL. In the upper CBL these terms are smaller but remain significant.

In the lower CBL, the pressure forcing acts to accelerate both thermals updrafts and environmental downdrafts. In the upper CBL, this term changes sign in updrafts and acts weakly to decelerate them as they approach the capping inversion. Downdrafts, on the other hand, are accelerated significantly by the pressure forcing through out the depth of the CBL. Thus, pressure forcing is the one significant term acting to accelerate downdrafts out of their source region in the upper CBL.

Lenschow and Stephens (1982) found the net of the lateral mass exchange and pressure effects on thermals by using the vertical velocity budget alone. The profile for this term computed from their Airmass Transformation Experiment data has the same shape but twice the amplitude as that computed from the components described above for Phoenix 78. In both experiments, the net of these two terms was two to three times as large in the lower CBL as in the upper CBL and acted as a drag on thermals.

The dominance of the lateral mass exchange and pressure forcing terms in the plume mean vertical velocity budgets of the lower half of the CBL is a direct result of the relative magnitudes of the regional mean θ_v lapse rate and the plume mean perturbation θ_v profiles. Vertical advection of the large observed regional mean θ_v lapse rate

would produce much larger plume mean perturbation θ_v values than are observed if lateral mass exchange did not dilute the plumes in compensation. However, the required amount of lateral mass exchange would result in much weaker plume mean vertical velocities than are observed if the pressure forcing did not act to aid buoyancy in driving the CBL convection. This is a very interesting observation in that the only external forcing on the CBL convection, buoyancy, is not the dominant internal forcing term.

The feedback between the regional mean θ_v lapse rate, the plume mean buoyancies and the plume mean vertical velocities is probably quite complex. The basic chain of cause and effect can, however, be traced. A stronger than normal lapse rate would lead to more buoyant convective plumes. These plumes would rise more rapidly because of their greater than normal buoyancy. This more rapid and more buoyant convection would transport more buoyancy from the lower CBL to the upper CBL thereby reducing the lapse rate. This feedback would continue until the convection weakened enough so that the buoyancy it transported away from the surface equaled that supplied to the atmosphere by the surface. Similar arguments can be used to support a return from weak lapse rates towards the equilibrium lapse rates.

As shown in the plume mean budget equations of buoyancy and vertical velocity, the efficiency of lateral mass exchange between thermal updrafts and environmental downdrafts controls the relationship between the plume mean buoyancy and vertical velocity profiles and the regional mean θ_v profile. Thus, diffusive effects which alter the dynamics of lateral mass exchange between thermal updrafts and environmental downdrafts in either the real CBL or a LES model would

alter the regional mean θ_v profile and the properties of the updrafts and downdrafts. If lateral mass exchange were weak, then less instability in the lower CBL would be required to maintain the convective vertical velocities and buoyancies necessary to produce a given buoyancy flux. Strong lateral mass exchange would, on the other hand, require more unstable lower CBL lapse rates to maintain the convective vertical velocities and buoyancies required to produce a the same buoyancy flux. In the limiting case of instant lateral mass exchange between updrafts and downdrafts, there could be no upward buoyancy flux away from the surface no matter how strong the super-adiabatic lapse rate was because the updraft and downdrafts would have the same θ_v.

The buoyancy fluxes at the surface and the inversion base determine the linear part of the CBL buoyancy flux profile. The diurnal changes in the CBL lapse rate profile determine the departure from linearity of the buoyancy flux profile. Because the observed θ_v variations with height in the CBL are much smaller than the observed diurnal variations in the mean θ_v of the CBL, the buoyancy flux profile is quasilinear between the surface and the inversion base. The CBL lapse rate profile thus has little influence on the buoyancy flux profile and therefore on the plume mean buoyancy and vertical velocity profiles. Thus, while the surface and inversion level buoyancy fluxes dominate the determination of the convective plume buoyancy and vertical velocity characteristics, the lateral mass exchange between these plumes dominates the determination of the regional mean θ_v profile.

This result suggests that it may be easier to predict the turbulence characteristics of the CBL than to predict the regional mean lapse rate profile using an LES model. Prediction of the regional mean lapse rate profile of the CBL is a test of how accurately the lateral mass exchange between thermal updrafts and environmental downdrafts is being modelled. Because vertical diffusion is affected by the lateral mass exchange between thermal updrafts and environmental downdrafts, the prediction of the lapse rate profile of the CBL is also a test of the accuracy of the vertical diffusion predictions of an LES model. Lapse rate profiles for LES models have not generally been published because this importance has gone unrecognized.

7.5 Discussion

Thermal updrafts and environmental downdrafts are buoyantly driven with the surface buoyancy flux and the depth of the CBL being the controlling external parameters as shown in Chapter 6 and in Lenschow and Stephens (1980 and 1982). The budgets of vertical velocity in these two legs of the CBL convective circulation show that buoyancy does not dominate the forcing at any level and is dominated by lateral mass exchange and pressure forcing in the lower half of the CBL. The dynamics of CBL convection can be illustrated by discussing the factors which affect a parcel as it undergoes a cycle of convective rise and decent. These factors are shown schematically in Figure 7.19 and discussed below.

A parcel in the surface layer has its θ_v increased by the surface flux. If it is displaced upwards it will become positively buoyant because of the strongly superadiabatic lapse rate which is observed in

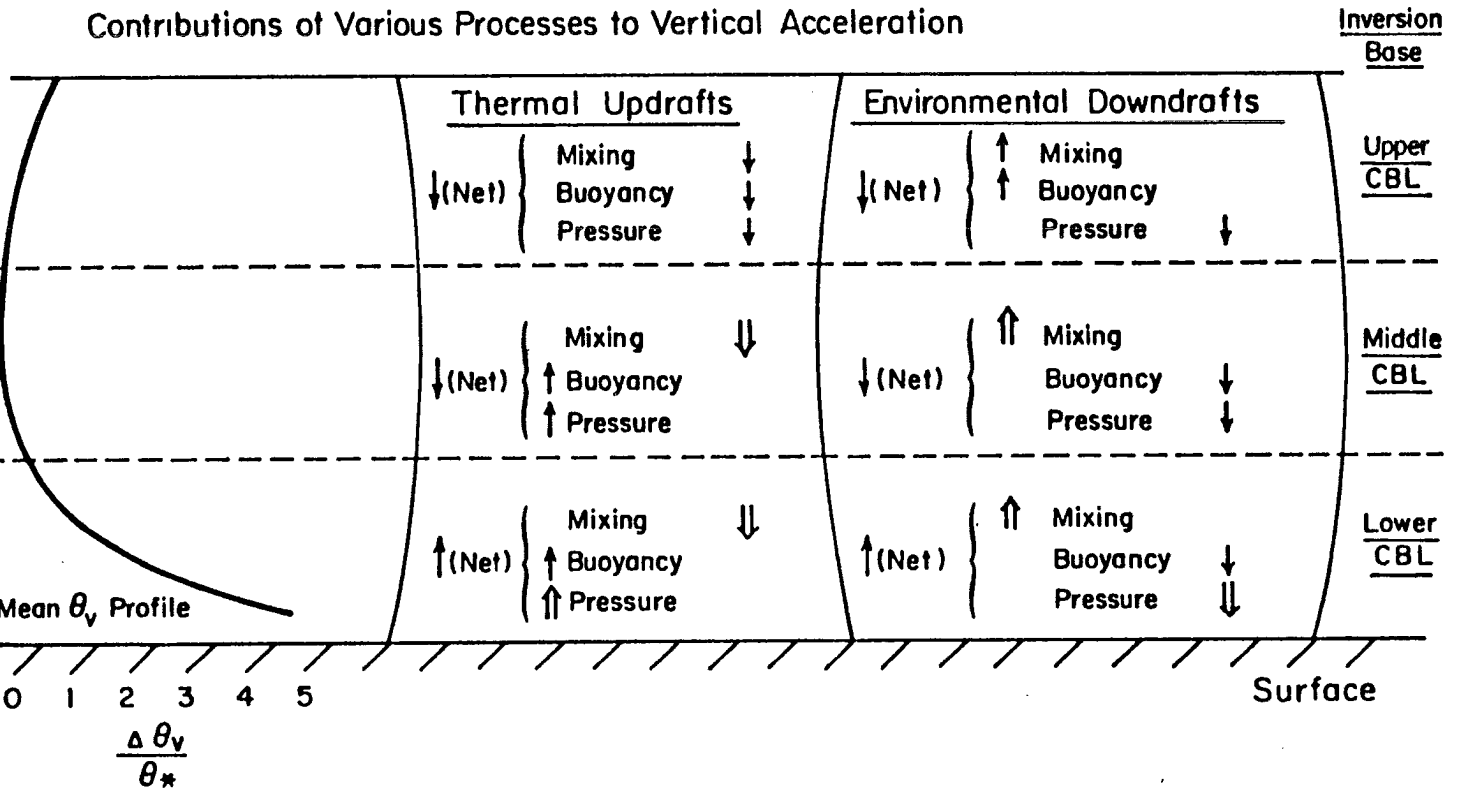
Contributions of Various Processes to Vertical Acceleration
Inversion Base
Thermal Updrafts
Environmental Downdrafts
(Net)
Mixing
Buoyancy
Pressure
Upper CBL
Middle CBL
Lower CBL
Mean θ_v Profile
0 1 2 3 4 5
$\frac{\Delta \theta_v}{\theta_*}$
Surface

Fig. 7.19

the lowest levels of the CBL. Buoyancy acts to accelerate the initial upward motion in classical static instaiblity. Lateral exchange of the positively buoyant rising parcel with negatively buoyant environmental downdrafts limits the buoyancy produced in this manner to approximately a tenth of what it would be without lateral mass exchange.

In the lower third of the CBL, the rising parcel is accelerated by buoyancy and by pressure forces which more than compensate for the drag caused by lateral exchange of downdraft air into the updraft. As the parcel rises into the middle third of the CBL, buoyancy and pressure forcing are no longer able to compensate for the drag of lateral mass exchange so the parcel decelerates. The parcel becomes negatively buoyant as it moves into the more stable upper third of the CBL. The lateral mass exchange between the thermal updrafts and the environmental downdrafts is not sufficient to eliminate this negative buoyancy. Thus, negative buoyancy aids the drag of lateral mass exchange in slowing the updraft in the upper third of the CBL. Pressure forcing is also acting to slow the updraft as it crosses the upper third of the CBL towards the inversion base.

Cross inversion entrainment increases the buoyancy of the parcel at the top of the CBL. Buoyant forcing is thus upward, opposing the inclusion of the parcel into a downdraft. However, pressure forcing is downward throughout the upper third of the CBL. This forcing is strong enough to overcome positive buoyancy and the drag of lateral mass exchange to accelerate the parcel down away from the inversion base. Lateral mass exchange in the upper third of the CBL acts to reduce the positive buoyancy of the downdraft despite the gradient

production from the stable regional mean lapse rate. The downdraft parcel becomes negatively buoyant in the middle third of the CBL. In this layer it is accelerated downwards by increasing buoyant and pressure forces acting against the drag of lateral mass exchange. As the parcel descends through the mid CBL, negative buoyancy production by vertical advection of the regional mean θ_v becomes greater than destruction by lateral mass exchange. This process continues to increase the negative buoyancy throughout the lower third of the CBL. However, in the lower 20 percent of the CBL the lateral mass exchange dominates the buoyant and pressure forcing so the parcel decelerates as it approaches the surface despite increasingly negative buoyancy. This return to rest near the surface closes the cycle.

The Phoenix 78 aircraft data do not extend low enough to permit determination of the role of lateral mass exchange and perturbation pressure in the formation of updrafts and the destruction of downdrafts in the surface layer. This problem could be examined using conditional sampling of tower turbulence data and surface layer scaling.

7.6 Conclusions

The dynamics of thermal updrafts and compensating environmental downdrafts in the CBL have been examined using observations from the Phoenix 78 field experiment and a new diagnostic model consisting of the budget equations for buoyancy, convective mass flux and vertical velcoity in the thermal updrafts and environmental downdrafts. All terms of possible significance were retained in these budgets. Aircraft and tower turbulence data were sufficient for the measurement or diagnosis of all of the terms.

The time tendency terms in these budget equations were found to be negligible. The components of the flux divergences caused by changes in plume coverage with height were also small relative to the other terms in the budgets. The components of the flux divergences caused by vertical gradients of the plume mean and subplume perturbation fluxes were significant. These terms generally acted against the observed acceleration of the convective flows. Gradient production of buoyancy from the regional mean θ_v gradient was observed to be one of the two dominant terms in the plume mean buoyancy budgets for the lower half of the CBL. The other dominant term was the lateral mass exchange between updrafts and downdrafts. These terms had similar magnitudes to the other significant terms in the upper half of the CBL.

The lateral mass exchange between updrafts and downdrafts and the pressure forcing dominated the plume mean vertical velocity budgets in the lower CBL. These two terms were of similar magnitude to the buoyancy and the flux gradient components of the vertical velocity flux in the upper CBL.

The importance of the lateral mass exchange between updrafts and downdrafts and the pressure forcing is directly related to the strength of the superadiabatic lapse rates observed from the BAO tower in the lower half of the CBL. The extreme nonneutrality of the stratification observed up to 0.4 z_i has a major impact on the dynamics of CBL convection. Lateral mass exchange between updrafts and downdrafts and pressure forces cannot be small in the presence of such strongly unstable lapse rates without giving rise to vertical motions which would remove buoyancy from the surface layer much faster

than it is supplied from the surface. The choice of conditional sampling criteria is not apt to influence these results qualitatively because the observed imbalance between total gradient production of buoyancy and the observed buoyancy is an order of magnitude larger than the observed buoyancy.

Thermal updrafts were found to be accelerated away from the surface by buoyancy and pressure gradients and to be decelerated primarily by lateral mass exchange and negative buoyancy as they approached the inversion base. Drag from lateral mass exchange was most important in the lower CBL. Environmental downdrafts were found to be accelerated away from the inversion base by the pressure forces which acted against both the drag of lateral mass exchange and buoyancy. The downdrafts continued to accelerate down to 0.2 z_i. In the lowest layers of the CBL the drag of lateral mass exchange begins to slow the environmental downdrafts. The aircraft data did not extend low enough to permit study of the role of pressure forces in halting downdrafts as they entered the surface layer.

Lateral mass exchange between plumes and pressure forces are observed to be very important to the dynamics of the CBL. Therefore, any model of CBL dynamics and diffusion should include these effects as accurately as possible. Because of the constraints imposed by the forcing from the surface and inversion base buoyancy fluxes, the buoyancy and vertical velocity characteristics of the convective plumes cannot be greatly altered by inaccuracies in the modelling of lateral mass exchange. However, the vertical diffusion of scalar contaminants and the regional mean profile θ_v are very dependent on the accuracy of the modelling of the lateral mass exchange between updrafts and downdrafts.

Lamb (1979) reported LES results which showed a lowering of the center of nonbuoyant contaminant plumes released in the upper CBL. Lamb suggested that this lowering of the plume center could be explained by the fact that the thermal updrafts cover a smaller fraction of the area than do environmental downdrafts. The Phoenix 78 observations support this hypothesis. However, the diagnosed dominance of lateral mass exchange into downdrafts over that into updrafts would also contribute to this lowering. This dominance would cause much of the contaminant released into thermal updrafts to reverse it's direction and decend before reaching the inversion while relatively little of the contaminant released into the environmental downdraft would reverse direction before decending to the mid CBL.

The dominance of lateral mixing in the budgets of buoyancy and vertical velocity for thermals and their environment poses a potential problem for studies which diagnose buoyancy and pressure fields from remote sensing observations of the velocity fields, such procedures require the parameterization of that fraction of the lateral mixing which occurs at scales which are too small to resolve in the observations. The currently available sensors cannot resolve most of the scales at which lateral mixing occurs, the perturbations on the thermal plume structure. Therefore, much of the lateral mixing terms would have to be parameterized. The diagnosed buoyancy and pressure fields would be quite sensitive to the parameterization used.

8. Conclusions

The objective of this research is to advance the understanding of the structure and dynamics of thermals in the convective boundary layer. This objective has been met by the combination of observational data with a new diagnostic model of the dynamics and thermodynamics of the CBL. The data were acquired by NCAR Queenair aircraft and the BAO tower during the 1978 Phoenix experiment. Turbulence profiles were computed from these data for the entire CBL and for two subregions, thermal updrafts and environmental downdrafts.

Intercomparisons of the profiles of turbulence statistics for the entire CBL from Phoenix 78 and from previous field and laboratory experiments indicated that the rolling terrain around the BAO site did not alter the CBL turbulence structure away from that observed over more uniform terrain. Thus, the results of the present study should be applicable to the dynamics of thermals over any flat or gently rolling site.

A conditional sampling technique was needed to distinguish the thermal updrafts from the compensating environmental downdrafts. Previous methods of conditional sampling of thermals were dependent upon the existence of upward fluxes of heat or moisture at the levels studied. These methods could not be applied at the BAO site because neither of these fluxes was positive at all heights in this continental environment. Therefore, a new conditional sampling

technique based on the universal spectra of vertical velocity was developed. The spectra show that buoyant production of vertical velocity variance occurs primarily at horizontal scales of from 0.1 to 10.0 times the depth of the convective boundary layer. Therefore, thermals are defined as those regions in which vertical velocity is upwards at these horizontal scales. This procedure eliminates the contributions of mesoscale and inertial subrange eddies to the vertical velocity series which is used to determine the boundaries between thermal updrafts and environmental downdrafts. The form of the vertical velocity spectra has been observed to be nearly constant with height in the bulk of the mixed layer. The form is also insensitive to changes in the underlying topography from smooth to rolling terrain. Therefore, this new conditional sampling method is applicable at any level of the CBL over any smooth or rolling surface.

A new diagnostic model was developed which permits the determination, from observations, of the vertical profiles of the lateral mass exchange rates between thermal updrafts and environmental downdrafts and of the pressure forces acting on the vertical velocity in these two regions. This model consists of the budget equations for the horizontal averages of buoyancy, convective mass flux and vertical velocity. These averages are computed separately over the updraft and downdraft regions so that the processes affecting the two legs of the convective circulation can be examined separately. This separation of the CBL into updraft and downdraft regions results in the appearance of lateral mixing terms in the budget equations to account for the exchanges between the two regions. One of the primary results of this work is the documentation of the importance of these lateral

mass exchanges to the dynamics and diffusive characteristics of the CBL.

The lateral mixing of mass between thermal updrafts and environmental downdrafts was found to dominate the budgets of buoyancy and vertical velocity in the lower half of the CBL. The diagnosed lateral mass exchange includes two components at each level, one into thermals and the other out of thermals. These two components of lateral mixing are commonly called lateral entrainment and detrainment respectively in studies of moist convection. The sum of the two components of the lateral mass exchange rate must equal the vertical divergence of the convective mass flux.

In the lower CBL, the two components are much larger than their difference so that far more lateral mixing occurs than would be required to account for the observed gradient of the vertical profile of convective mass flux. The existence of this large lateral mixing is required to explain the relative smallness of the observed buoyancies compared with the gradient production of buoyancy in the lower half of the CBL. This important finding would not be affected qualitatively by the exact choice of conditional sampling criteria because it is a result of the order of magnitude difference between the observed buoyancy and the total gradient production of buoyancy at levels between 0.1 and 0.4 times the boundary layer depth. This difference is a result of the large lapse rate in this layer. The variations in the observed buoyancy profiles between various field experiments which used different sampling criteria are much smaller than the imbalance upon which this finding is based.

The dominance of the lateral mixing has important implications for both LES models of the CBL and for studies which diagnose the mass and buoyancy fields from the observed velocity field. Because the lapse rate profile is very dependent on the lateral mixing rates, the correct simulation of the observed profile by an LES model would be a good test of the model performance as regards lateral mixing and pollution dispersion. This test is more demanding than the correct simulation of the turbulence profiles because they do not depend so strongly on the lateral mixing rates.

In the upper CBL, the two components of lateral mixing are of the same order as their difference. However, the mixing into thermals is significantly smaller than the mixing out of thermals. This difference in the two lateral mixing rates has important implications for the diffusion of nonbuoyant contaminants in the upper CBL. The fraction of a contaminant residing in downdrafts would initially increase with time because of this effect. This temporary migration of the contaminant into downdrafts would contribute to the initial decent of plume centers seen in LES studies such as Lamb (1979).

The perturbation pressure forcing of the updrafts and downdrafts was also diagnosed from the Phoenix 78 observaions. The pressure forcing is important in compensating for the large drag imposed by the lateral mass exchange in the lower CBL. Without this help, the buoyancy is not able to overcome this drag to generate the observed vertical velocities. In the upper CBL source region of environmental downdrafts, the pressure forcing is the only factor acting to accelerate parcels downwards. The pressure acts against both buoyancy and the drag imposed by the lateral mixing to generate the observed acceleration of downdrafts away from the inversion base.

References

Betts, A.K., 1973: Nonprecipitating cumulus convection and its parameterization. Quart. J. Roy. Meteor. Soc., 99, 178-196.

Betts, A.K., 1975: Parametric interpretation of tradewind cumulus studies. J. Atmos. Sci., 32, 1934-1945.

Betts, A.K., 1976: Modeling the subcloud layer structure and interaction with a shallow cumulus layer. J. Atmos. Sci., 33, 2363-2382.

Burris, R.H., J.C. Covington and M.N. Zrubek, 1973: Beechcraft Queen Air aircraft. Atmos. Technol., 1, 25-30, National Center for Atmospheric Research, Boulder, Colorado.

Busch, N.E. and H.A. Panofsky, 1968: Recent spectrum of atmospheric turbulence. Quart. J. Roy. Meteor. Soc., 94, 132-148.

Caughey, S.J. and S.G. Palmer, 1979: Some aspects of turbulence structure through the depth of the convective boundary layer. Quart. J. Roy. Meteor. Soc., 105, 811-827.

Charney, J.G., 1948: On the scale of atmospheric motions. Geof. Publ., 17, 3-17.

Clark, R.H., A.J. Dyer, R.P. Brook, D.G. Reid and A.J. Troup, 1971: The Wangara experiment: Boundary layer data. Tech. Pap. 19, Dir, Meteor. Phys., CSIRO, Australia, 316 p.

Corrsin, S., 1951: On the spectrum of isotropic temperature fluctuations in an isotropic turbulence. J. Appl. Phys., 22, 469-474.

Coulman, C.E., 1978: Boundary-layer evolution and nocturnal inversion dispersal, Part II. Bound. -Layer Meteor., 14, 493-513.

Deardorff, J.W., 1970: Convective velocity and temperature scales for the unstable planetary boundary layer and for Rayleigh convection. J. Atmos. Sci., 27, 1211-1213.

Deardorff, J.W., 1974a: Three-dimensional numerical study of the height and mean structure of a heated planetary boundary layer. Bound. Layer Meteor., 7, 81-106.

Deardorff, J.W., 1974b: Three-dimensional numerical study of turbulence in an entraining mixed layer. Bound.-Layer Meteor., 7, 199-226.

Deardorff, J.W., 1976: Discussion of 'Thermals over the sea and gull flight behavior' by A.H. Woodcock, Boundary Layer Met., 10, 241-246.

Donelan, M. and M. Miyake, 1973: Spectra and fluxes in the boundary layer of the trade-wind zone. J. Atmos. Sci., 30, 444-464.

Driedonks, A.G.M. and H. Tennekes, 1984: Entrainment effects in the well-mixed atmospheric boundary layer. Bound. Layer Meteor., 30, 75-105.

Emmitt, G.D., 1978: Tropical cumulus interaction with and modification of the subcloud region. J. Atmos. Sci., 35, 1485-1502.

Fraedrich, K. 1973: On the parameterization of cumulus convection by lateral mixing and compensating subsidence. Part 1. J. Atmos. Sci., 30, 408-413.

Gaynor, J.E. and P.A. Mandics, 1978: Analysis of the tropical marine boundary layer during GATE using acoustic sounder data. Mon. Wea. Rev., 106, 223-232.

Grant, D.R., 1965: Some aspects of convection as measured from aircraft. Quart. J. Roy. Meteor. Soc., 91, 268-281.

Greenhut, G.K. and S.J.S. Khalsa, 1982: Updraft and downdraft events in the atmospheric boundary layer over the equatorial Pacific Ocean. J. Atmos. Sci., 39, 1803-1818.

Hall, F.F., Jr., J.C. Edinger and W.D. Neff, 1975: Convective plumes in the planetary boundary layer investigated with and acoustic sounder. J. Appl. Meteor., 14, 513-523.

Hardy, H.G. and H. Ottersten, 1969: Radar investigation of convective patterns in the atmosphere. J. Atmos. Sci., 26, 666-672.

Hildebrand, R.H., 1979: Phoenix operations of the NCAR Queen Air research aircraft, in Project Phoenix: The September 1978 field operation, BAO Bulletin 1, NCAR and NOAA/ERL, Boulder, Colorado, W.H. Hooke (ed), 57-68.

Hildebrand, P.H. and B. Ackerman, 1984: Urban effects on the convective boundary layer. J. Atmos. Sci., 41, 76-91.

Huffaker, E.C., 1897: On soaring flight. Smithosonian Institution, Annual report of the Board of Regents, 183-206.

Kaimal, J.C., Z. Izumi, O.R. Cote, 1972: Spectral characteristics of surface layer turbulence. Quart. J. Roy. Meteor. Soc., 98, 563-589.

Kaimal, J.C. and D.E. Wolfe, 1979: Tower instrumentation, and Phoenix operations: The September 1978 Field Operation, BAO Buoletin 1, NCAR and NOAA/ERL, Boulder, CO, W.H. Hooke (ed.), 57-68.

Kaimal, J.C., J.C. Wyngaard, D.A. Haugen, O.R. Coté, Y. Izumi, S.J. Caughey and C.J. Readings, 1976: Turbulence structure in the convective boundary layer. J. Atmos. Sci., 33, 2152-2169.

Kaimal, J.C. and J.E. Gaynor, 1983: The Boulder Atmospheric Observatory. J. Clim. Appl. Meteor., 22, 863-880.

Kelley, N.D. and R.L. Lackman, 1976: Description of standard output data produces from NCAR Research Aviation Facility aircraft, RAF Bulletin No. 9, National Center for Atmospheric Research, Boulder, Colorado.

Khalsa, S.J.S. and G.K. Greenhut, 1985: Conditonal sampling of updrafts and downdrafts in the marine atmospheric boundary layer. J. Atmos. Sci., 42, 2550-2562.

Konrad, T.G., 1970: Dynamics of convective processes in the clear air as seen by radar. J. Atmos. Sci., 27, 1138-1147.

Konrad, T.G. and F.L. Robinson, 1973: Development and characteristics of free convection in the clear air as seen by radar and aircraft. J. Appl. Meteor., 12, 1284-1294.

Kunkel, K. E., E.W. Eloranta and S.T. Shipley, 1977: Lidar observations of the convective boundary layer. J. Appl. Meteor., 16, 1306-1311.

Lamb, R.G., 1978: A numerical simulation of dispersion from an elevated point source in the convective planetary boundary layer. Atmos. Environ., 12, 1297-1304.

Lamb, R.G., 1979: The effects of release height on material dispersion in the convective boundary layer. Preprint vol. AMS Fouth Symposium on Turbulence, Diffusion and Air Pollution, Reno, NV.

Lanczos, G., 1956: Applied Analysis, Prentice Hall, 530 pp.

Larson, M.F., M.C. Kelley, K.S. Gage, 1982: Turbulence spectra in the upper troposphere and lower stratosphere at periods between 2 hours and 40 days. J. Atmos. Sci., 39, 1035-1041.

LeMone, M.A., 1973: The structure and dynamics of horizontal roll vorticies in the PBL. J. Atmos. Sci., 30, 1077-1091.

Lenschow, D.H., 1974: Model of the height variation of the turbulence kinetic energy budget in the unstable planetary boundary layer. J. Atmos. Sci., 31, 465-474.

Lenschow, D.H., C.A. Callian, R.B. Friasen and E.N. Brown, 1978: The status of air motion measurements on NCAR aircraft. Preprints for the Symp. Meteorological Observations and Instrumentation. Amer. Meteor. Soc., 433-438.

Lenschow, D.G., and B.B. Stankov, 1986: Length scales in the convective boundary layer. J. Atmos. Sci., 43, 1198-1209.

Lenschow, D.H. and P.L. Stephens, 1980: The role of thermals in the convective boundary layer. Boundary-Layer Meteorol., 19, 509-532.

Lenschow, D.H., J.C. Wyngaard and W.T. Pennel, 1980: Mean-field and second moment budgets in a baroclinic, convective boundary layer. J. Atmos. Sci., 31, 465-474.

Lenschow, D.H. and P.L. Stephens, 1982: Mean vertical velocities and turbulence intensity inside and outside thermals. Atmospheric Environment, 16, 761-764.

Lenschow, D.H. and P. Spyers-Duran, 1985: Measurement Techniques: Air motion sensing, RAF Bulletin No. 23, National Center for Atmospheric Research, Boulder, Colorado

Li, W.H. and S.H. Lam, 1964: Principles of Fluid Mechanics, Addison-Wesley, 374 pp.

Lopez, R.E., 1977: Some properties of convective plume and small fair weather cumulus fields as measured by Aircraft and lidar sounders. J. Appl. Meteor., 16, 861-865.

Lopez, R.E., 1977: The log normal distribution and cumulus cloud populations. Mon. Wea. Rev., 105, 869-872.

Mahrt, L. and J. Paumier, 1984: Heat transport in the atmospheric boundary layer. J. Atmos. Sci., 41, 3061-3075.

Manton, M.J., 1977: On the structure of convection. Bound-Layer Meteor., 12, 491-503.

Moeng, C.-H., 1984: A large-eddy-simulation model for the study of planetary boundary-layer turbulence. J. Atmos. Sci., 41, 2052-2062.

Moeng, C.-H. and J.C. Wyngaard, 1984: Statistics of conservative scalars in the convective boundary layer. J. Atmos. Sci., 41, 3161-3169.

Monin, A.S. and A.M. Obukhov, 1954: Basic laws of turbulent mixing in the ground layer of the atmosphere. Tr. Geofiz. Inst. Akad. Nauk SSR, 151, 163-187.

NCAR, 1976: Airborne humidity measurements, RAF Bulletin No. 22, National Center for Atmospheric Research, Boulder, Colorado.

NCAR, 1977: Flight Planning: Queen Air, RAF Bulletin No. 5, National Center for Atmospheric Research, Boulder, Colorado.

NCAR, 1981: Queen Air: Overview and summary of capabilities, RAF Bulletin No. 2, National Center for Atmospheric Research, Boulder, Colorado.

Noonkester, V.R., 1976: The evolution of the clear air convective layer revealed by surface based remote sensors. J. Appl. Meteor., 15, 594-606.

Obukhov, A.M., 1946: Turbulence in the atmosphere with inhomogeneous temperature. Tr. Geofiz. Inst. Akad. Nauk SSR., 1, 95-115.

Panofsky, H.A. and J.A. Dutton, 1984: Atmospheric Turbulence, John Wiley and Sons, 397 pp.

Pielke, R.A., 1984: Mesoscale meteorological modelling, Academic Press, 612 pp.

Rayment, R. and C.J. Readings, 1974: A case study of the structure and energetics of an inversion. Quart. J. Roy. Meteor. Soc., 100, 221-223.

Richter, J.H., D.R. Jensen, V.R. Noonkester, T.G. Koonrad, A. Arnold and J.R. Rowland, 1974: Clear air convection: A close look at its evolution and structure. Geophys. Res. Lett., 1, 173-176.

Roland, J.R., 1973: Intense probing of a clear air convective field by radar and instrumented drone aircraft. J. Appl. Meteor., 12, 149-155.

Roland, J.R., 1976: Clear air convective behavior revealed by radar chaff. J. Appl. Meteor., 15, 521-526.

Scorer, R.S., 1957: Experiments on convection of isolated masses of buoyant fluid. J. Fluid Mech., 2, 583-594.

Smedman-Hogstrom, A., U. Hogstrom, 1975: Spectral gap in surface layer measurements. J. Atmos. Sci., 32, 340-350.

Spyers-Duran, P. and D. Baumgardner, 1983: In flight estimation of the time response of airborne temperature sensors, Preprints of the 5th Symposium on Meteorological Observations and Instrumentation, April 11-15, 1983, Toronto, Ont. Canada, 352-357, American Meteorological Society, Boston, Mass.

Stull, R.S., 1976: The energetics of entrainment across a density interface. J. Atmos. Sci., 33, 1260-1267.

Taconet, O. and A. Weill, 1983: Convective plumes in the atmospheric boundary layer as observed with an acoustic Doppler sodar. Bound.-Layer Meteor., 25, 143-158.

Tennekes, H., 1978: Turbulent flow in two and three dimensions. Bul. Amer. Meteor. Soc., 59, 22-28.

Tennekes, H. and J.L. Lumley, 1972: A first course in turbulence, MIT Press, 300 pp.

Townsend, A.A., 1958: The effects of radiative transfer on turbulent flow in a stratified fluid. J. Fluid. Mech., 4, 361-375.

Venkatram, A., 1984: Letter in response to comment on "Dispersion from an elevated source in a convective boundary layer. Atmos.Environ., 18, 1493.

Vul'fson, N.L., 1961: Some results of the study of convective activity in the free atmosphere. Studies of clouds, precipitation, and thunderstorm electricity, Boston, Amer. Meteor. Soc., 119-131.

Warner, J. and J.W. Telford, 1963: Some patterns of convection in the lower atmosphere. J. Atmos. Sci., 20, 313-318.

Warner, J. and J.W. Telford, 1967: Convection below cloud base. J. Atmos. Sci., 24, 374-382.

Willis, G.E. and J.W. Deardorff, 1974: A laboratory model of the unstable planetary boundary layer. J. Atmos. Sci., 31, 1297-1307.

Wolfe, D.E., 1979: A brief summary of weather conditions during Phoenix, in Project Phoenix: The September 1978 field operation, BAO Bulletin 1, NCAR and NOAA/ERL, Boulder, Colorado, W.H. Hooke (ed), 176-238.

Woodcock, A.H., 1940: Convection and soaring over the open sea. J. Marine. Res., 3, 248-253.

Woodcock, A.H., 1975: Thermals over the sea and gull flight behavior. Boundary Layer Met., 9, 63-68.

Wyngaard, J.C. and R.A. Brost, 1984: Topdown and bottomup diffusion of a scalar in the convective boundary layer. J. Atmos. Sci., 41, 102-112.

Wyngaard, J.C. and O.R. Coté, 1971: The budgets of turbulence kinetic energy and temperature variance in the atmospheric boundary layer. J. Atmos. Sci., 28, 190-201.

Wyngaard, J.C., O.R. Coté, and Y. Izumi, 1971: Local free convection, similarity, and the budgets of shear stress and heat flux. J. Atmos. Sci., 28, 1171-1182.

Appendix A

Derivation of the Plume Mean Budget Equations

for Virtual Potential Temperature and Vertical Velocity

Definitions

σ = Fractional coverage by thermal updrafts.

$1 - \sigma$ = Fractional coverage by environmental downdrafts.

T subscript denotes values of thermal quantities.

E subscript denotes values of environment quantities.

so $\overline{(\ )}$: a horizontal regional average (the average over both thermals and their environment).

$\overline{(\ )}_T$: a horizontal average in thermals which is referred to as a plume mean for the thermals.

$\overline{(\ )}_E$: a horizontal average in the environment which is referred to as a plume mean for the environment.

$(\ )'_T = (\ )_T - \overline{(\ )}_T$: an instantaneous local perturbation from the plume mean for the thermals.

$(\ )'_E = (\ )_E - \overline{(\ )}_E$: an instantaneous local perturbation from the plume mean for the environment.

where $(\ )_T$ and $(\ )_E$ are instantaneous local values in thermals and environment respectively.

Derivation

The budget equation for $\overline{\theta_{vT}}$, the profile of plume mean virtual potential temperature in thermals is derived below.

One starts by assuming θ_v conservation, thus ignoring radiational effects which are small on the time scale of the CBL convection (Townsend, 1958).

$$(1) \qquad \frac{d\theta_{vT}}{dt} = 0$$

This conservation equation is transformed into the flux form before averaging over the thermal updrafts. This transformation is done so that Liebnitz rule can be used to move the averaging operator inside the vertical derivatives. Expanding the total derivative in equation 1 gives equation 2.

$$(2) \quad \frac{\partial\theta_{vT}}{\partial t} + u_T \frac{\partial\theta_{vT}}{\partial x} + v_T \frac{\partial\theta_{vT}}{\partial y} + w_T \frac{\partial\theta_{vT}}{\partial z} = 0$$

Now assume incompressability in the continuity equation for 3.

$$(3) \quad \frac{\partial u_T}{\partial x} + \frac{\partial v_T}{\partial y} + \frac{\partial w_T}{\partial z} = 0$$

Multipling the continuity equation 3 by θ_{vT} gives equation 4.

$$(4) \quad \theta_{vT}\left(\frac{\partial u_T}{\partial x} + \frac{\partial v_T}{\partial y} + \frac{\partial w_T}{\partial z}\right) = 0$$

Combining equations 2 and 4 and using the product rule of differentation creates the flux form of the θ_{vT} budget equation 5.

$$(5) \quad \frac{\partial\theta_{vT}}{\partial t} + \frac{\partial u_T\theta_{vT}}{\partial x} + \frac{\partial v_T\theta_{vT}}{\partial y} + \frac{\partial w_T\theta_{vT}}{\partial w} = 0$$

Now averaging 5 over the region of thermals gives equation 6.

$$(6) \quad \overline{\frac{\partial\theta_{vT}}{\partial t}} + \overline{\frac{\partial u_T\theta_{vT}}{\partial x}} + \overline{\frac{\partial v_T\theta_{vT}}{\partial y}} + \overline{\frac{\partial w_T\theta_{vT}}{\partial z}} = 0$$

Substituting $\overline{(\ )}_T + (\ )'_T$ for $(\ )_T$ converts equation 6 to equation 7. This is done to separate the plume mean quantities from the sub-plume scale perturbations.

$$(7)\quad \frac{\overline{\partial\theta_{vT}}}{\partial t} + \frac{\overline{\partial\theta'_{vT}}}{\partial t} + \overline{\frac{\partial}{\partial x}\left[(\overline{u_T}+u'_T)(\overline{\theta_{vT}}+\theta'_{vT})\right]} + \overline{\frac{\partial}{\partial y}\left[(\overline{v_T}+v'_T)(\overline{\theta_{vT}}+\theta'_{vT})\right]}$$

$$+ \overline{\frac{\partial}{\partial z}\left[(\overline{w_T}+w'_T)(\overline{\theta_{vT}}+\theta'_{vT})\right]} = 0$$

One next expands the products in 7 and takes the averages inside the time derivatives. This procedure is valid because σ, the region over which the average is taken, does not change with time as "universal" profiles are used for σ and the other measured statistics.

$$(8)\quad \frac{\partial\overline{\theta_{vT}}}{\partial t} + \frac{\partial\overline{\theta'_{vT}}}{\partial t} + \overline{\frac{\partial}{\partial x}\left[\overline{u}_T\overline{\theta_{vT}} + u'_T\theta'_{vT} + \overline{u_T}\theta'_{vT} + u'_T\overline{\theta_{vT}}\right]}$$

$$+ \overline{\frac{\partial}{\partial y}\left[\overline{v}_T\overline{\theta_{vT}} + v'_T\theta'_{vT} + \overline{v_T}\theta'_{vT} + v'_T\overline{\theta_{vT}}\right]}$$

$$+ \overline{\frac{\partial}{\partial z}\left[\overline{w}_T\overline{\theta_{vT}} + w'_T\theta'_{vT} + \overline{w_T}\theta'_{vT} + w'_T\overline{\theta_{vT}}\right]} = 0$$

Distribution of the derivatives over the sums transforms equation 8 into equation 9 which permits simplification of the budget.

$$(9)\quad \overline{\frac{\partial\theta_{vT}}{\partial t}} + \overline{\frac{\partial\theta'_{vT}}{\partial t}} + \overline{\frac{\partial(\overline{u}_T\overline{\theta_{vT}})}{\partial x}} + \overline{\frac{\partial(u'_T\theta'_{vT})}{\partial x}} + \overline{\frac{\partial(\overline{u_T}\theta'_{vT})}{\partial x}} + \overline{\frac{\partial(u'_T\overline{\theta_{vT}})}{\partial x}}.$$

$\overline{\frac{\partial\theta'_{vT}}{\partial t}}$ ↓ 0 by Def.

$\overline{\frac{\partial(\overline{u}_T\overline{\theta_{vT}})}{\partial x}}$ ↓ 0 by H.H.

$$+\overline{\frac{\partial(\overline{v_T}\overline{\theta_{vT}})}{\partial y}}+\overline{\frac{\partial(v_T'\theta_{vT}')}{\partial y}}+\overline{\frac{\partial(\overline{v_T}\theta_{vT}')}{\partial y}}+\overline{\frac{\partial(v_T'\overline{\theta_{vT}})}{\partial y}}$$

$\downarrow$ 0 by H.H.

$$+\overline{\frac{\partial(\overline{w_T}\overline{\theta_{vT}})}{\partial z}}+\overline{\frac{\partial(w_T'\theta_{vT}')}{\partial z}}+\overline{\frac{\partial(\overline{w_T}\theta_{vT}')}{\partial z}}+\overline{\frac{\partial(w_T'\overline{\theta_{vT}})}{\partial z}}=0$$

0 by Def. means zero by the definition of the prime and averaging operators, $\overline{(\ )'}=0$. 0 by H.H. means zero by the assumption of horizontal homogeniety. Equation 9 simplifies to equation 10 when the zero terms are dropped.

$$(10)\quad \overline{\frac{\partial\theta_{vT}}{\partial t}}+\overline{\frac{\partial(u_T'\theta_{vT}')}{\partial x}}+\overline{\frac{\partial(\overline{u_T}\theta_{vT}')}{\partial x}}+\overline{\frac{\partial(u_T'\overline{\theta_{vT}})}{\partial x}}+\overline{\frac{\partial(v_T'\theta_{vT}')}{\partial y}}+\overline{\frac{(\overline{v_T}\theta_{vT}')}{\partial y}}$$

$$+\overline{\frac{\partial(v_T'\overline{\theta_{vT}})}{\partial y}}+\overline{\frac{\partial(\overline{w_T}\overline{\theta_{vT}})}{\partial z}}+\overline{\frac{\partial(w_T'\theta_{vT}')}{\partial z}}+\overline{\frac{\partial(\overline{w_T}\theta_{vT}')}{\partial z}}\quad\overline{\frac{\partial(w_T'\overline{\theta_{vT}})}{\partial z}}=0$$

Moving the averaging operator inside the vertical derivatives requires the use of Liebnitz rule because σ varies with z and hence the region of averaging varies with z. Equation 11 results.

$$(11)\quad \underbrace{\overline{\frac{\partial\theta_{vT}}{\partial t}}}_{A}+\underbrace{\overline{\frac{\partial(u_T'\theta_{vT}')}{\partial x}}+\overline{\frac{\partial(v_T'\theta_{vT}')}{\partial y}}}_{B}+\underbrace{\overline{\frac{\partial(\overline{u_T}\theta_{vT}')}{\partial x}}+\overline{\frac{\partial(\overline{v_T}\theta_{vT}')}{\partial y}}}_{C}$$

$$+ \underbrace{\frac{\partial(\overline{u'_T\theta'_{vT}})}{\partial x} + \frac{\partial(\overline{v'_T\theta'_{vT}})}{\partial y} + \frac{\partial(\overline{\bar{w}_T\theta'_{vT}})}{\partial z}}_{D} + \underbrace{\frac{(\overline{\bar{w}_T\theta'_{vT}})}{\sigma}\frac{\partial\sigma}{\partial z}}_{E} + \underbrace{\frac{(\overline{\bar{w}_T\theta'_{vT}})\big|_B}{\sigma}\frac{\partial\sigma}{\partial z}}_{F}$$

$$\underbrace{\frac{\partial(\overline{w'_T\theta'_{vT}})}{\partial z}}_{G} + \underbrace{\frac{(\overline{w'_T\theta'_{vT}})}{\sigma}\frac{\partial\sigma}{\partial z}}_{H} - \underbrace{\frac{(w'_T\theta'_{vT})\big|_B}{\sigma}\frac{\partial\sigma}{\partial z}}_{I} = 0$$

$$J$$

where $\big|_B$ indicates an average along the boundary between the updraft region and the downdraft region. The differences which occur between the use of Liebnitz rule with integral operators and its use with averaging operators should be noted. When used to move an integral operator inside a derivative, Liebnitz rule gives rise to a boundary term such as $\frac{(w'_T\theta'_{vT})\big|_B}{\sigma}\frac{\partial\sigma}{\partial z}$. However, when Liebnitz rule is used to move an averaging operator inside a derivative another similar term arises via the chain rule. This additional term is an area average such as $\frac{(\overline{w'_T\theta'_{vT}})}{\sigma}\frac{\partial\sigma}{\partial z}$.

The terms have the following physical interpretations:

A = storage

B = the subplume scale lateral flux into the thermal region from the environmental region.

C = advection of cross plume gradients of θ_v by the plume mean horizontal flow.

D = divergence of plume mean θ_v by cross plume gradients of the horizontal flow.

E = the flux gradient part of the divergence of the flux caused by plume mean motions.

F = the plume area gradient part of the divergence of the flux caused by plume mean motions.

G = the area change induced lateral exchange of the flux caused by plume mean motions.

H = the flux gradient part of the divergence of the flux caused by subplume scale motions.

I = the plume area gradient part of the divergence of the flux caused by subplume scale motions.

J = the area change induced lateral exchange of the flux caused by subplume scale motions.

The terms B, C, D, G, and J are all part of the lateral mixing between thermal updrafts and environmental downdrafts. This mixing consists of two components. One component is the mass transferred from the environment into thermals. The other component is the mass transferred from thermals into the environment. Each of these components transfers θ_v between the two regions at a rate proportional to the mass moved and the θ_v of that mass. The lateral mixing terms can therefore be parameterized as

$$- \frac{E_T\overline{\theta_{vE}} - E_E\overline{\theta_{vT}}}{\sigma}$$

where $\frac{E_T}{\sigma}$ is the fractional mass exchange rate into thermals and $\frac{E_E}{\sigma}$ is the fractional mass exchange rate into the environment as denoted by the subscripts. The net lateral mixing into the thermal region equals vertical gradient of the convective mass flux.

$$(14)\quad \frac{\partial \sigma \overline{w_T}}{\partial z} = E_T - E_E$$

This parameterization of the lateral mixing terms converts equation 11 to equation (14).

$$(15)\quad \frac{\partial \overline{\theta_{vT}}}{\partial t} + \frac{\partial(\overline{\bar{w}_T \bar{\theta}_{vT}})}{\partial z} + \frac{(\overline{\bar{w}_T \bar{\theta}_{vT}})}{\sigma}\frac{\partial \sigma}{\partial z} + \frac{\partial(\overline{w'_T \theta'_{vT}})}{\partial z} + \frac{(\overline{w'_T \theta'_{vT}})}{\sigma}\frac{\partial \sigma}{\partial z}$$

$$- \frac{E_T \overline{\theta_{vE}} - E_E \overline{\theta_{vT}}}{\sigma} = 0$$

Equation 14 is the mass budget for the thermal region and equation 15 is the θ_v budget for the thermal region. These two equations can be manipulated into forms which can be solved simultainiously for E_T and E_E, the two lateral mixing coefficients. These diagnosed coefficients can be used to evaluate the importance of lateral mixing in the virtual potential temperature budgets. These coefficients can also be used in the vertical velocity budgets to permit diagnosis of the pressure effects. This formulation permits the lateral mixing coefficients to vary in the vertical.

Next, the θ_v budget equation is put in a form where the Phoenix 78 turbulence data will be sufficient to permit solution for the lateral mixing coefficeints. Using the definition $\overline{(\ )}_T = (\overline{(\ )}_T - \overline{(\ )}) + \overline{(\ )}$ (a simple adding and subtracting of the regional average), the regional average will be separated from the plume mean departure from the regional average. This will aid in the solution of the budget equations using the aircraft data which are perturbations from regional means. Equation 15 expands into equation 16 .

$$(16)\quad \frac{\partial(\overline{\theta_{vT}}-\overline{\theta_v})}{\partial t} + \frac{\partial\overline{\theta_v}}{\partial t} + \frac{\partial}{\partial z}\,[(\overline{w_T}-\bar{w})+\bar{w}][(\overline{\theta_{vT}}-\overline{\theta_v})+\overline{\theta_v}]$$

$$+ \frac{[(\overline{w_T}-\bar{w})+\bar{w}][(\overline{\theta_{vT}}-\overline{\theta_v})+\overline{\theta_v}]}{\sigma}\,\frac{\partial\sigma}{\partial z} + \frac{\partial(\overline{w_T'\theta_{vT}'})}{\partial z}$$

$$+ \frac{(\overline{w_T'\theta_{vT}'})}{\sigma}\,\frac{\partial\sigma}{\partial z} - \frac{E_T[(\overline{\theta_{vE}}-\overline{\theta_v})+\overline{\theta_v}]-E_E[(\overline{\theta_{vT}}-\overline{\theta_v})+\overline{\theta_v}]}{\sigma} = 0$$

Expanding the products in equation (16) gives equation (17).

$$(17)\quad \frac{\partial(\overline{\theta_{vT}}-\overline{\theta_v})}{\partial t} + \frac{\partial\overline{\theta_v}}{\partial t} + \frac{\partial[(\overline{w_T}-\bar{w})(\overline{\theta_{vT}}-\overline{\theta_v})]}{\partial z} + \frac{\partial[\bar{w}\overline{\theta_v}]}{\partial z} + \frac{\partial[(\overline{w_T}-\bar{w})\overline{\theta_v}]}{\partial z}$$

$$+ \frac{\partial[\bar{w}(\overline{\theta_{vT}}-\overline{\theta_v})]}{\partial z} + \frac{[(\overline{w_T}-\bar{w})(\overline{\theta_{vT}}-\overline{\theta_v})]}{\sigma}\,\frac{\partial\sigma}{\partial z} + \frac{[\bar{w}\overline{\theta_v}]}{\sigma}\,\frac{\partial\sigma}{\partial z} + \frac{[(\overline{w_T}-\bar{w})\overline{\theta_v}]}{\sigma}\,\frac{\partial\sigma}{\partial z}$$

$$+ \frac{[\bar{w}(\overline{\theta_{vT}}-\overline{\theta_v})]}{\sigma}\,\frac{\partial\sigma}{\partial z} + \frac{\partial(\overline{w_T'\theta_{vT}'})}{\partial z} + \frac{(\overline{w_T'\theta_{vT}'})}{\sigma}\,\frac{\partial\sigma}{\partial z} - \frac{E_T(\overline{\theta_{vE}}-\overline{\theta_v})}{\sigma} + \frac{E_E(\overline{\theta_{vT}}-\overline{\theta_v})}{\sigma}$$

$$- \frac{(E_T-E_E)\overline{\theta_v}}{\sigma} = 0$$

But $\bar{w}<<(\overline{w_T}-\bar{w})$ for the undisturbed CBL so the terms containing $\bar{w}$ as a factor can be neglected. The three terms containing $\overline{\theta_v}$ as a factor can be collapsed into $(\overline{w_T}-\bar{w})\,\frac{\partial\overline{\theta_v}}{\partial z}$ by use of the product rule of differentation and equation 14 . Equation 17 can be normalized using mixed layer scaling and the fact that w_*, θ_* and z_i depend only upon time not upon height to get equation 18 .

$\frac{\partial\overline{\theta_v}}{\partial t} = -\frac{\partial(\overline{w'\theta_v'})}{\partial z}$ is also used.

$$(18)\quad \left(\frac{z_i}{w_* \theta_*}\right)\frac{\partial \theta_*}{\partial t}\left(\frac{\overline{\theta_{vT}}-\overline{\theta_v}}{\theta_*}\right)-\frac{\partial\left(\frac{\overline{w'\theta'_v}}{w_*\theta_*}\right)}{\partial z_*}+\frac{\partial\left(\frac{\overline{w_T}-\overline{w}}{w_*}\right)\left(\frac{\overline{\theta_{vT}}-\overline{\theta_v}}{\theta_*}\right)}{\partial z_*}$$

$$+\left(\frac{\overline{w_T}-\overline{w}}{w_*}\right)\frac{\partial\left(\frac{\overline{\theta_v}}{\theta_*}\right)}{\partial z_*}+\frac{\left(\frac{\overline{w_T}-\overline{w}}{w_*}\right)\left(\frac{\overline{\theta_{vT}}-\overline{\theta_v}}{\theta_*}\right)}{\sigma}\frac{\partial \sigma}{\partial z_*}+\frac{\partial\left(\frac{\overline{w'_T\theta'_{vT}}}{w_*\theta_*}\right)}{\partial z_*}+\frac{\left(\frac{\overline{w'_T\theta'_{vT}}}{w_*\theta_*}\right)}{\sigma}\frac{\partial \sigma}{\partial z_*}$$

$$-\frac{\left(\frac{z_i E_T}{w_*}\right)\left(\frac{\overline{\theta_{vE}}-\overline{\theta_v}}{\theta_*}\right)}{\sigma}+\frac{\left(\frac{z_i E_E}{w_*}\right)\left(\frac{\overline{\theta_{vT}}-\overline{\theta_v}}{\theta_*}\right)}{\sigma}=0$$

This form of the virtual potential temperature budget for thermals has been normalized using mixed layer scaling so that "universal" turbulence profiles may be used in its solution. The only quantities in this equation which are not directly determined from the Phoenix 78 turbulence data are the lateral mixing coefficients. The first term contains all the time tendency which could cause solutions for lateral mixing to depart from a universal form. The mass budget for thermals, equation 14 , may also be normalized using mixed layer scaling so that aircraft turbulence data may be used in its solution. Equation 19 results.

$$(19)\quad \frac{\partial\left(\frac{\overline{\sigma w_T}}{w_*}\right)}{\partial z_*}=\frac{z_i E_T}{w_*}-\frac{z_i E_E}{w_*}$$

Equations 18 and 19 can be solved as a pair of simultainious linear algebratic equations for the profiles of the two normalized lateral mixing coefficients. A similar budget could be derived for the virtual

potential temperature in the environment. However, such an equation is not needed to find the lateral mixing coefficients.

A similar approach can be applied to the conservation equation for vertical velocity. The result will be equations in which the pressure forces can be realted to lateral mixing and measured turbulence statistics. One starts from the local w equation, and ignores molecular diffusion which is negligibly small on the CBL convective scale.

$$(20)\quad \frac{dw_T}{dt} = -\left(\frac{1}{\rho}\frac{\partial p}{\partial z}\right)_T + \frac{g}{\theta_o}\,(\theta_{vT}-\overline{\theta_v})$$

The change in w is related to the pressure gradient and buoyancy.

Expansion of the total derivative in equation 20 gives equation 21

$$(21)\quad \frac{\partial w_T}{\partial t} + u_T\frac{\partial w_T}{\partial x} + v_T\frac{\partial w_T}{\partial y} + w_T\frac{\partial w_T}{\partial z} = -\left(\frac{1}{\rho}\frac{\partial p}{\partial z}\right)_T + \frac{g}{\theta_o}\,(\theta_{vT}-\overline{\theta_v})$$

Now assume incompressability in the continuity equation for (22).

$$(22)\quad \frac{\partial u_T}{\partial x} + \frac{\partial v_T}{\partial y} + \frac{\partial w_T}{\partial z} = 0$$

Multipling equation 21 by w_T gives equation 22 .

$$(23)\quad w_T\left(\frac{\partial u_T}{\partial x} + \frac{\partial v_T}{\partial y} + \frac{\partial w_T}{\partial z}\right) = 0$$

Combining equations (21) and (23) and use of the product rule of differention creates the flux form of the w_T equation, 24 .

$$(24)\quad \frac{\partial w_T}{\partial t} + \frac{\partial u_T w_T}{\partial x} + \frac{\partial v_T w_T}{\partial y} + \frac{\partial w_T^2}{\partial z} = -\left(\frac{1}{\rho}\frac{\partial p}{\partial z}\right)_T + \frac{g}{\theta_o}\,(\theta_{vT}-\overline{\theta_v})$$

Averaging equation 24 over the region of thermals gives equation 25 .

$$(25)\quad \overline{\frac{\partial w_T}{\partial t}} + \overline{\frac{\partial u_T w_T}{\partial x}} + \overline{\frac{\partial v_T w_T}{\partial y}} + \overline{\frac{\partial w_T^2}{\partial z}} = -\overline{\left(\frac{1}{\rho}\frac{\partial p}{\partial z}\right)_T} + \overline{\frac{g}{\theta_o}\,(\theta_{vT}-\overline{\theta_v})}$$

Substitution of $\overline{(\ )_T} + (\ )'_T$ for $(\ )_T$ converts equation 25 to equation 26 .

$$(26)\ \frac{\overline{\partial w_T}}{\partial t} + \frac{\overline{\partial w'_T}}{\partial T} + \overline{\frac{\partial}{\partial x}\left[(\overline{u_T}+u'_T)(\overline{w_T}+w'_T)\right]} + \overline{\frac{\partial}{\partial y}\left[(\overline{v_T}+v'_T)(\overline{w_T}+w'_T)\right]}$$

$$+ \overline{\frac{\partial}{\partial y}\left[(\overline{w_T}+w'_T)^2\right]} = -\overline{\left(\frac{1}{\rho}\frac{\partial p}{\partial z}\right)_T} + \overline{\frac{g}{\theta_o}(\overline{\theta_{vT}}+\theta'_{vT}-\overline{\theta_v})}$$

Expanding the products in equation 26 and taking the averages inside time derivatives gives equation 27 .

$$(27)\ \frac{\partial \overline{w_T}}{\partial t} + \frac{\partial \overline{w'_T}}{\partial t} + \overline{\frac{\partial}{\partial x}\left[\overline{u_T}\,\overline{w_T} + u'_T w'_T + \overline{u_T} w'_T + u'_T \overline{w_T}\right]}$$

$$+ \overline{\frac{\partial}{\partial y}\left[\overline{v_T}\,\overline{w_T} + v'_T w'_T + \overline{v_T} w'_T + v'_T \overline{w_T}\right]} + \overline{\frac{\partial}{\partial z}\left[\overline{w_T}^2 + w'^2_T + 2\overline{w_T} w'_T\right]}$$

$$- \overline{\left(-\frac{1}{\rho}\frac{\partial p}{\partial z}\right)_T} - \overline{\frac{g}{\theta_o}(\overline{\theta_{vT}}-\overline{\theta_v}+\theta'_{vT})} = 0$$

Distributing the differentiation over the sums and eliminating terms by assuming horizontal homegineity and $\overline{(\ )}'_T = 0$, converts equation 27 into equation 28 .

$$(28)\ \frac{\partial \overline{w_T}}{\partial t} + \overline{\frac{\partial(u'_T w'_T)}{\partial x}} + \overline{\frac{\partial(\overline{u_T} w'_T)}{\partial x}} + \overline{\frac{\partial(u'_T \overline{w_T})}{\partial x}} + \overline{\frac{\partial(v'_T w'_T)}{\partial y}} + \overline{\frac{\partial(\overline{v_T} w'_T)}{\partial y}} + \overline{\frac{\partial(v'_T \overline{w_T})}{\partial y}}$$

$$+ \overline{\frac{\partial(\overline{w_T}^2)}{\partial z}} + \overline{\frac{\partial(w'^2_T)}{\partial z}} + 2\,\overline{\frac{\partial(w'_T \overline{w_T})}{\partial z}} - \overline{\left(\frac{-1}{\rho}\frac{\partial p}{\partial z}\right)_T} - \overline{\frac{g}{\theta_o}(\overline{\theta_{vT}}-\overline{\theta_v})} = 0$$

Using Liebnitz rule the average operators are moved inside the vertical derivative to get equation 29 from equation 28 .

$$(29)\quad \underbrace{\frac{\partial \overline{w_T}}{\partial t}}_{A} + \underbrace{\frac{\overline{\partial (u_T' w_T')}}{\partial x} + \frac{\overline{\partial (v_T' w_T')}}{\partial y}}_{B} + \underbrace{\frac{\overline{\partial (\overline{u_T} w_T')}}{\partial x} + \frac{\overline{\partial (\overline{v_T} w_T')}}{\partial y}}_{C} + \underbrace{\frac{\overline{\partial (u_T' \overline{w_T})}}{\partial x} + \frac{\overline{\partial (v_T' \overline{w_T})}}{\partial y}}_{D}$$

$$+ \underbrace{\frac{\partial (\overline{w_T})^2}{\partial z}}_{E} + \underbrace{\left(\frac{\overline{w_T}}{\sigma}\right)^2 \frac{\partial \sigma}{\partial z}}_{F} + \underbrace{\frac{(\overline{w_T})^2|_B}{\sigma} \frac{\partial \sigma}{\partial z}}_{G} + \underbrace{\frac{\partial \left(\overline{w_T'^2}\right)}{\partial z}}_{H} + \underbrace{\left(\frac{\overline{w_T'^2}}{\sigma}\right)\frac{\partial \sigma}{\partial z}}_{I} - \underbrace{\frac{(w_T'^2)|_B}{\sigma} \frac{\partial \sigma}{\partial z}}_{J}$$

$$\underbrace{-\left(\overline{\frac{-1}{\rho} \frac{\partial p}{\partial z}}\right)_T}_{K} \underbrace{- \frac{g}{\theta_o} (\overline{\theta_{vT}} - \overline{\theta_v})}_{L} = 0$$

The terms have the following physical interpretations:

A = storage

B = the subplume scale lateral flux into the thermal region from the environmental region.

C = advection of cross plume gradients of w by the plume mean horizontal flow.

D = divergence of plume mean w by cross plume gradients of the horizontal flow.

E = the flux gradient part of the divergence of the flux caused by plume mean motions.

F = the plume area gradient part of the divergent of the flux caused by plume mean motions.

G = the area change induced lateral exchange of the flux caused by plume mean motions.

H = the flux gradient part of the divergence of the flux caused by subplume scale motions.

I = the plume area gradient part of the divergence of the flux caused by subplume scale motions.

J = the area change induced lateral exchange of the flux caused by subplume scale motions.

K = pressure effects.

L = buoyancy.

The terms A through J correspond to the similarly lettered terms in the virtual potential temperature budget. It is particularly useful to note the exact correspondence of the lateral mixing terms, B, C, D, G and J. This correspondence suggests that if these terms are parameterized in a similar manner the same lateral mixing coefficients might apply to both budgets. The replacement of the lateral mixing terms by

$$-\frac{E_T\overline{w_E}-E_E\overline{w_T}}{\sigma}$$

and use of the values of the lateral mixing coefficients derived from the virtual potential temperature budget reduces the number of undetermined terms to one. This term, the pressure effect, can then be found as a residual. Any differences in the extent to which a parcels virtual potential temperature and vertical velocity are transferred when its mass is moved between thermals and their environment will give rise to an error in this parameterization of the lateral mixing of vertical velocity and hence an error in the residual. However, pressure effects are the most likely cause of differences in the lateral mixing coefficients for these two properties. Therefore, the grouping of these subplume perturbation pressure effects in with the effect of

the plume mean pressure force yeilds a net pressure effect as the residual of the vertical velocity budget. The contribution of the plume mean and subplume perturbation pressure forces cannot be distinguised by this method. Equation 30 and a similar w_E equation, 31 , result.

$$(30)\ \frac{\partial \overline{w_T}}{\partial t} + \frac{\partial(\overline{w_T})^2}{\partial z} + \frac{(\overline{w_T})^2}{\sigma}\frac{\partial \sigma}{\partial z} + \frac{\partial(\overline{w_T'^2})}{\partial z} + \left(\frac{\overline{w_T'^2}}{\sigma}\right)\frac{\partial \sigma}{\partial z} + P_T$$

$$- \frac{E_T\overline{w_E} - E_E\overline{w_T}}{\sigma} - \frac{g}{\theta_o}(\overline{\theta_{vE}} - \overline{\theta_v}) = 0$$

$$(31)\ \frac{\partial \overline{w_E}}{\partial t} + \frac{\partial(\overline{w_E})^2}{\partial z} + \frac{(\overline{w_E})^2}{\sigma}\frac{\partial \sigma}{\partial z} + \frac{\partial(\overline{w_E'^2})}{\partial z} + \frac{(\overline{w_E'^2})}{\sigma}\frac{\partial \sigma}{\partial z} + P_E$$

$$- \frac{E_E\overline{w_T} - E_T\overline{w_E}}{\sigma} - \frac{g}{\theta_o}(\overline{\theta_{vT}} - \overline{\theta_v}) = 0$$

where P_T and P_E represent the pressure effects. Now noting that $\bar{w} << w_T$ so that $(w_T - w) \cong w_T$ as was done with the virtual potential temperature equation, equation 30 becomes equation 32 .

$$(32)\ \frac{\partial(\overline{w_T} - \bar{w})}{\partial t} + \frac{\partial(\overline{w_T} - \bar{w})^2}{\partial z} + \frac{(\overline{w_T})^2}{\sigma}\frac{\partial \sigma}{\partial z} + \frac{\partial(\overline{w_T'^2})}{\partial z} + \frac{(\overline{w_T'^2})}{\sigma}\frac{\partial \sigma}{\partial z}$$

$$- \frac{[E_T(\overline{w_E} - \bar{w}) - E_E(\overline{w_T} - \bar{w})]}{\sigma} + P_T - \frac{g}{\theta_o}(\overline{\theta_{vT}} - \overline{\theta_v}) = 0$$

This equation can be normalized using mixed layer scaling and the fact that w_*, θ_* and z_i change only with time and not with height to get equation 33 . This normalization is neccessary so that aircraft turbulence data can be used in the solution.

$$(33)\left(\frac{z_i}{w_*^2}\right)\ \frac{\partial w_*}{\partial t}\ \left(\frac{\overline{w_T}-\bar{w}}{w_*}\right)+\ \frac{\partial}{\partial z_*}\left(\frac{\left(\overline{w_T}-\bar{w}\right)^2}{w_*^2}\right)+\frac{\left(\frac{\overline{w_T}-\bar{w}}{w_*}\right)^2}{\sigma}\left(\frac{\partial\sigma}{\partial z_*}\right)+\ \frac{\partial}{\partial z_*}\left(\frac{\overline{w_T'^2}}{w_*^2}\right)$$

$$+\ \frac{1}{\sigma}\left(\frac{\overline{w_T'^2}}{w_*^2}\right)\frac{\partial\sigma}{\partial z_*}\ -\ \frac{1}{\sigma}\left[\left(\frac{z_i E_T}{w_*^2}\right)\left(\frac{\overline{w_E}-\bar{w}}{w_*}\right)-\left(\frac{z_i E_E}{w_*^2}\right)\left(\frac{\overline{w_T}-\bar{w}}{w_*}\right)\right]+\left(\frac{z_i}{w_*^2}\right)P_T$$

$$-\left(\frac{\overline{\theta_{vT}}-\overline{\theta_v}}{\theta_*}\right)=0$$

There is an analogous equation for w_E. The "universal" profiles of the nondimensionallized pressure terms can be found as residuals in these equations.

The Phoenix 78 experiment provides the data needed to solve these two sets to budget euqations from 0.1 z_i up to 1.0 z_i. The results show the contribution of the various effects to maintainence of buoyancy and vertical velocity in a field of thermals.